Synthesis and Characterization of $BiFeO_3$-based Multiferroic Solid Solution Systems

by

Lun Wei Su

M.Sc., University of British Columbia, 2010

B.Sc., Simon Fraser University, 2008

Thesis Submitted in Partial Fulfillment of the
Requirements for the Degree of
Doctor of Philosophy

in the
Department of Chemistry
Faculty of Science

SIMON FRASER UNIVERSITY

Spring 2018

Approval

Name: **Lun Wei Su**

Degree: **Doctor of Philosophy**

Title: ***Synthesis and Characterization of $BiFeO_3$-based Multiferroic Solid Solution Systems***

Examining Committee: **Chair:** Dr. Hua-Zong Yu
Professor

Dr. Zuo-Guang Ye
Senior Supervisor
Professor

Dr. Steven Holdcroft
Supervisor
Professor

Dr. Vance Williams
Supervisor
Associate Professor

Dr. Michael Eikerling
Internal Examiner
Professor

Dr. Ahmad Safari
External Examiner
Professor
Materials Science and Engineering
The State University of New Jersey

Date Defended/Approved: Feburary 9th , 2018

Abstract

Bismuth ferrite $BiFeO_3$ (BFO) is one of the most studied single-phase multiferroic materials with both ferroelectricity and G-type antiferromagnetism above room temperature. It undergoes a ferroelectric-paraelectric phase transition at T_C = 830°C and an antiferromagnetic-paramagnetic phase transformation at Néel temperature T_N = 370 °C. Despite these wonderful properties of BFO, there are some drawbacks associated with this material including the formations of impurity phases, weak magnetic properties, weak magnetoelectric coupling, and large leakage current density. Therefore, the appropriate chemical modifications are required to improve the electrical and magnetic properties of BFO. In this work, the substitutions of rare earth (RE) ions, such as Dy^{3+}, Er^{3+}, Yb^{3+}, etc., for the *A*-site Bi^{3+} ion have been performed and the structures and physical properties of the resulting solid solutions have been investigated.

First, new multiferroic materials (1−*x*)$BiFeO_3$-*x*$DyFeO_3$ (denoted BDF-*x*) and (1-*x*)$BiFe_{(1-y)}Ti_{(y)}O_{(3+y/2)}$-*x*$DyFeO_3$ (denoted BDFT-*x*-*y*) were synthesized by solid-state reactions. Compared with pure BFO, the ferromagnetism in the BDF-*x* solid solution is substantially enhanced by the structural distortion and unpaired electrons due to A-site substitution of Dy^{3+} for Bi^{3+}. The electrical properties, including the ferroelectric and dielectric properties, are further improved by the substitution of Ti^{4+} for Fe^{3+} on the *B*-site, which substantially diminishes the conductivity and consequently the dielectric loss. Well-developed ferroelectric hysteresis loops are displayed in BDFT-*x*-*y* with a large remnant polarization P_r = 23 $\mu C/cm^2$ at room temperature, which is significantly higher than the previously reported P_r = 3.5 $\mu C/cm^2$ in pure $BiFeO_3$ ceramic. Moreover, weak ferromagnetism is found in it at room temperature (Ms = 0.1 μB/f.u.). The structure-composition phase diagram of the $BiFeO_3$-$DyFeO_3$ system is established.

The chemically modified (1-*x*)$BiFe_{(1-y)}Ti_{(y)}O_{(3+y/2)}$-*x*$LuFeO_3$ ceramics exhibit ferromagnetism with a saturated magnetization (Ms = 0.03 μB/f.u) and a remnant polarization of 0.30 $\mu C/cm^2$ at room temperature. In the (1−*x*)$BiFeO_3$-*x*$YbFeO_3$ solid solution, a calculated spontaneous polarization of 7.7 $\mu C/cm^2$ is obtained for the x = 0.11 ceramics which exhibit a weak ferromagnetism with M_s = 0.025 μB/f.u at room temperature. Interestingly, an unusual magnetization reversal behavior is discovered in the (1−*x*)$BiFeO_3$-*x*$ErFeO_3$ solid solution. At x = 0.12, the magnetic pole inversion occurs at 30 K. Lastly, the (1−*x*)$BiFeO_3$-*x*$EuFeO_3$ solid solution is found to exhibit an interesting magnetization behavior, with the magnetic properties undergoing a crossover from an antiferromagnetic to ferromagnetic state at x = 0.12.

Keywords: Perovskite solid solution; bismuth-based complex oxides; ceramics; rare earth multiferroics; ferroelectric and ferromagnetic materials

This thesis is dedicated to my parents, my wife, and my lovely daughters. Thank you for everything.

Acknowledgements

I would like to express my deep and sincere gratitude to my senior supervisor, Dr. Zuo-Guang Ye, for his support, inspiring guidance, and encouragement throughout my graduate studies, and for giving me the opportunity to work on exciting projects. I have been working with Dr. Ye as an undergraduate researcher and then as a graduate student, I have benefited from his guidance in every aspect of my study journey. I deeply appreciate all the time and effort he spent discussing my projects and advising me. It has been marvelous.

I would also like to thank my supervisory committee members, Dr. Vance Williams and Dr. Steven Holdcroft for their guidance, suggestions and thoughtful questions over the years. I would like to thank Dr. Ahmad Safari and Dr. Michael Eikerling to be my external and internal examiners.

I would like to thank the past and present members of Dr. Ye's research group. In particular, I praise the enormous amount of help and teaching by Dr. Hamel Tailor and Dr. Alexei Bokov throughout these years. I also thank Dr. Hua Wu for her general support, and guidance, and also I appreciate all the corrections to my thesis she made. My thanks go to Dr. Nan Zhang for teaching me how to perform structure refinements and editing my thesis. I would like to thank Dr. Jenny Wong and Dr. Zenghui Liu for their contributions to editing Chapter 2 of my thesis. I also recognize the support and help from Mr. Pan Gao for his support of the 3D diagram of the summary phase diagram. I would like to thank Dr. Weimin Zhu, Dr. Jiangtao Wu, Dr. Jian Zhuang, Dr. Bixia Wang, Dr. Zihe Ren, Dr. Alisa Paterson, Dr. Reagan Belan and fellow group members for their thoughtful comments and suggestions that have enhanced this work. Thank you, everyone, from Dr. Ye's lab. Your friendship was irreplaceable.

I would like to acknowledge Dr. Chi-Shun Tu at National Synchrotron Radiation Research Center in Taiwan for establishing a collaboration with Dr. Ye's research group at Simon Fraser University and helping me to perform XAS experiments at XAS beamline lab in Taiwan.

I especially appreciate my grandparents, my parents, my parents in law, and my sisters for their understanding, encouragement, and endless love.

Finally, I heartily thank my lovely wife, Tian Liang, and daughters, Evelyn Su, Tara Su and Cindy Su for all their encouragement and support during these years not only for me to pursue the degree of Ph.D. but for everything in life! I would never have achieved anything without their deep love.

Table of Contents

List of Tables

List of Figures

List of Abbreviations, Acronyms and Symbols

BDF-*x*	$(1-x)BiFeO_3$-$xDyFeO_3$
BDFT-*x*-*y*	$(1-x)BiFe_{(1-y)}Ti_{(y)}O_{(3+y/2)}$-$xDyFeO_3$
BErF-*x*	$(1-x)BiFeO_3$-$xErFeO_3$
BEuF-*x*	$(1-x)BiFeO_3$ -$xEuFeO_3$
BFO	$BiFeO_3$
BLF-*x*	$(1-x)BiFeO_3$-$xLuFeO_3$
BLFT-*x*-*y*	$(1-x)BiFe_{(1-y)}Ti_{(y)}O_{(3+y/2)}$-$xLuFeO_3$
BYF-*x*	$(1-x)BiFeO_3$ -$xYbFeO_3$
C	Curie constant
C_A	ionic charge of A site
C_B	ionic charge of B site
C_s	capacity of the sample
d	sample thickness
d_{33}	piezoelectric coefficient
D_A	A site atom displacement
D_B	B site atom displacements
DM	Dzyaloshinskii–Moriya Interaction
DSC	differential scanning calorimetry
E	electirc field
E_0	ionisation energy
E_b	binding energy of the electron
E_f	final energy of the ejected photoelectron
E_c	coercive field
EXAFS	Extended X-ray Absorption Fine Structure
ε^*	dielectric permittivity
G	free energy
g	gyromagnetic ratio

H_c	coercive field
H_{ext}	external magnetic fields
H_{int}	internal magnetic fields
I	current
I_f	fluorescence X-rays
I_o	incoming intensity of the X-rays
I_t	transmitted intensity of the X-rays
J	total angular momentum
K	electromechanical coupling factor
M	Magnetization
ME	Magnetoelectric
M_{Fe}	magnetization of the canted antiferromagnetism
MPB	Morphotropic Phase Boundary
M_r	remanent magnetization
N_A	numbers of atoms per unit cell for *A* site
N_B	numbers of atoms per unit cell for *B* site
μ_B	Bohr magneton
μ_{eff}	effective magnetic moment
$\mu(E)$	absorption coefficient
μ_S	spin only momentum
P_r	remnant polarization
P_s	spontaneous polarization
PMN-PT	$Pb(Mg_{1/3}Nb_{2/3})O_3$-$PbTiO_3$
PVA	polyvinyl alcohol
PZT	$PbZr_{1-x}Ti_xO_3$
r	shannon ionic radius
RT	room temperature
s	strain
S	spin quantum number
SQUID	superconducting quantum interference device

tan δ	loss tangent
t	tolerance factor
T	temperature
Tc	Curie Temperature
T_N	Néel temperature
T_m	temperature at which the magnetization changes its polarity
V	Voltage
XANES	X-ray Absorption Near Edge Structure
XAS	X-ray Absorption Spectroscopy
XRD	X-ray Diffraction
Z	Impendence
Z_{eff}	atom's effective nuclear charge
a	lattice parameter
α_{rh}	rhombohedral angle
χ	magnetic susceptibility
θ	Weiss temperature
θ	Bragg angle
λ	Wavelength
β	quadratic magnetoelectric coefficient
φ	phase angle

Chapter 1.

Introduction

1.1 Perovskite Structure

Perovskite is known as the most widely studied oxide structure adopted by many functional materials, with a wide range of chemistries possible and thousands of examples known. Many of the piezoelectric and ferroelectric materials used in technological applications crystallize in the complex perovskite structure. A typical perovskite structure was first found in the naturally occurring mineral calcium titanium oxide ($CaTiO_3$) which is named after a Russian mineralogist, Count LevAleksevich von Perovski [1]. In this work, the materials that adopt the crystal chemistry features of the perovskite structure were studied.

The perovskite structure, shown in Figure 1.1, has the general stoichiometry ABO_3, where “A” is a large size cation with a coordination number of 12 that sits at cube corner positions, “B” atom is a small cation in the octahedron site formed by O_6 at the face-centers of the unit cell.

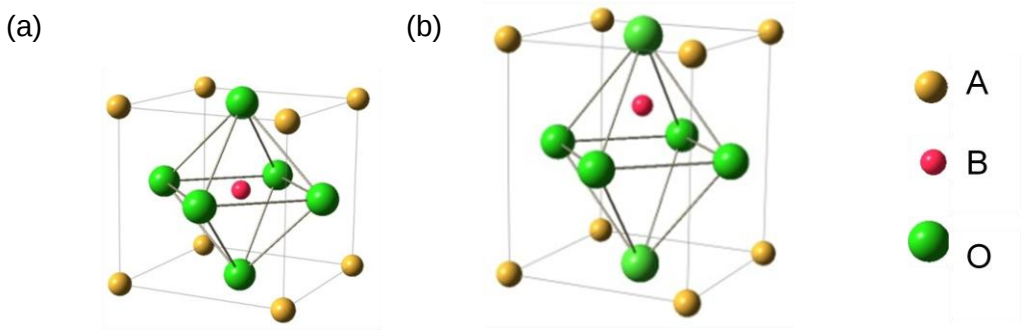

Figure 1.1 The B-cation-centered perovskite structure (ABO_3) for (a) cubic, nonpolar, and (b) tetragonal, polar, unit cells.

Perovskite compounds undergo structural distortions when partial substitution with A and/or B cations to a different oxidation states A' and/or B' cations. The most commonly used parameter for determining the stability of perovskite structure, which is known as the degree of distortion of a perovskite from ideal cubic, is the Goldschmidt tolerance factor, *t*, defined as follows:

$$t = \frac{r_A + r_O}{\sqrt{2}(r_B + r_O)} \quad , \tag{1.1}$$

where r_A, r_B and r_O are ionic radii of A, B and O, respectively [2]. An ideal perovskite structure has a tolerance factor t =1, which indicates a perfect fit and the space group for cubic perovskites is $Pm\bar{3}m$. The coordinates for A cations are (0,0,0), B cation is $(\frac{1}{2}, \frac{1}{2}, \frac{1}{2})$ and O anion are $(\frac{1}{2}, \frac{1}{2}, 0)$, $(\frac{1}{2}, 0, \frac{1}{2})$ and $(0, \frac{1}{2}, \frac{1}{2})$. [3] Any deviation from t = 1 will cause distortion in the structure. A cubic perovskite such as $CaTiO_3$, the tolerance factor is in the range of $0.90 < t < 1$, whereas for a smaller cation *A*, an orthorhombic distortion will occur, the tolerance factor is in the range of $0.85 < t < 0.9$. All perovskite distortions that maintain the *A*- and *B*-site oxygen coordinations involve the tilting of the BO_6 octahedra and an associated displacement of the *A* cation. The perovskite structure is stable if the tolerance factor is in the range of $0.88 \leq t \leq 1.09$, with a selection of a large low valent *A*-site cations and a small high valent *B*-site cations allowing for a distorted polar structure [3,4].

The perovskite structure is an important structure adpoted by a large number of compounds. It has a great variety of structural distortions and modifications because of its flexibility. The perovskite structure can accommodate ions with different sizes and charges (e.g. $A^{I}B^{V}O_3$, $A^{II}B^{IV}O_3$, $A^{III}B^{III}O_3$) and the same site can be occupied by ions with different charges (e.g. $A(B'B'')O_3$). The perovskite structure provides the building blocks for the assembly of other important crystal structures (e.g. $Ca_{n+1}Ti_nO_{3n+1}$) [3]. Materials with perovskite structures constitute important classes of functional materials because of its variety of ferroic properties, which can be used in many practical applications such as high *T*c superconductors, mixed electronic/ionic conduction, oxidation/reduction catalysts, sensors, solid oxides, fuel cells and also the main focus of this work, the

piezoelectric and ferroelectric ceramics. Many of these materials are synthesized through extensive formation of solid solutions [4].

1.2 Ferroic Properties

The prefix “ferro” refers historically to iron (ferrum in Latin). A crystal as being a “ferroic” when it has two or more orientation states in the absence of a magnetic field, electric field, and mechanical stress, and can switch from one to another state with the application of a magnetic field, an electric field, a mechanical stress, or a combination of these. There are three ferroic orders: ferroelectricity (coupling of charge polarization and electric field), ferroelasticity (coupling of stress and strain), and ferromagnetism (coupling of magnetic moment and magnetic field), which are often extended to anti-ferroics: antiferromagnetism and antiferroelectricity [5].

1.2.1 Ferroelectricity

Ferroelectrics are a special sub-group of piezoelectrics (Section 1.3). Ferroelectrics have a spontaneous polarization, P_s, which can be switched with an applied electric field. Ferroelectric materials are polar materials that possess at least two equilibrium orientations of spontaneous polarization P_s in the absence of an electric field. Under the application of the electric filed, the direction of the polarization vector can be reorientated [6]. The most commonly used ferroelectric materials adopt the perovskite crystal structure. In order to classify a material as a ferroelectric, two conditions are required, which are the existence of spontaneous polarization and a demonstrated reorienting of the polarization. Ferroelectricity is characterized by its hysteresis loops which show the polarization (*P)* as a function of the applied electric field (*E*). A typical plot of polarization versus electric field for the ferroelectric state is shown in Figure 1.2. Upon the application of a sufficiently high electric field, the polarization of different domains will reorient along the direction of the field and reach a saturation P_s. Although the polarization decreases with the decreasing applied field, the polarization does not return to the value of zero upon the removal of the electric field, retaining the remnant

polarization P_r at E = 0. The electric field must be reversed in order to obtain a zero polarization state. Therefore, the field required to reduce the polarization to zero is known as the coercive field Ec. Further increase of the field in the negative direction will cause a new alignment of dipoles and saturation in reverse direction. With the field strength being reduced to zero followed by another reversal, a hysteresis loop is produced with the completed cycle [7].

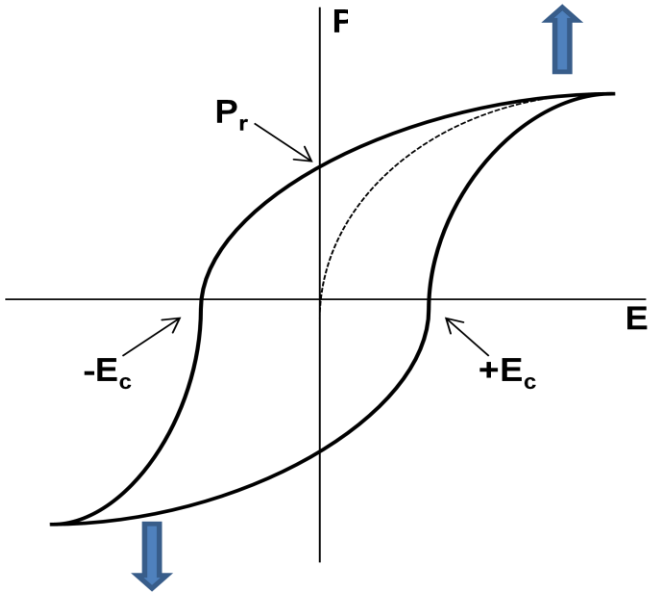

Figure 1.2 Typical polarization versus electric field (*P*-*E*) ferroelectric hysteresis loop displayed in ferroelectric materials. The blue arrows represent the polarization directions of several unit cells.

Accompanied by a symmetry change, ferroelectric materials exhibit a large change in their properties across a critical temperature. Ferroelectric properties are only observed over a certain temperature range that is characteristic to the material. It is typically a lower-temperature state because increasing thermal motion at high temperature often breaks down the common displacements in adjacent octahedra [6]. The temperature at which there is a phase transition between the ferroelectric, polar state and a paraelectric, nonpolar state is known as the Curie temperature, Tc. Such phase transition may be of first or second order [7].

The second-order phase transition is characterized by the continuous change of polarization at the Curie point [8]. For a ferroelectric system, the Gibbs free energy G as a state function can be expressed by choosing polarization, stress components and temperature as independent variables. Figure 1.3 (a) represents the free energy G as a function of polarization at different temperatures for a second order phase transition. At $T < Tc$, there are two equal energy minima for the system which have equal and opposite polarizations with a maximum of free energy at $P = 0$. Either of these two states is energetically more stable than a non-polar state at $P = 0$. At $T = Tc$, the potential curve flattens out with a single minimum at $P = 0$, causing anomalies in the temperature dependences of dielectric, elastic, thermal, and optical properties around the phase transition temperature. At $T > T$c, the crystal is in a nonpolar, paraelectric state with a single free energy minimum at $P = 0$. As the temperature decreases through Tc, most ferroelectric materials undergo a structural phase transition from the paraelectric (nonferroelectric) phase to the ferroelectric phase [8].

For the first-order phase transition, the spontaneous polarization changes discontinuously with temperature at the phase transition temperature. The Gibbs free energy G as a function of polarization at different temperatures for a first-order phase transition is shown in Figure 1.3 (b). At $T \leq T$c the free energy has two minima, similar to that seen in a second-order phase transition. At higher temperatures, a third local minimum appears at $P = 0$ [9]. At this state, the ferroelectric phase is stable, and the paraelectric phase is metastable. At $T = T$c, all three minima have the same depth, therefore the free energies of the paraelectric and ferroelectric phases are equal. Figure 1.3 (c) gives an example of the anomaly in the dielectric properties that occurs at the phase transition. It shows the dielectric constant ε' (or dielectric permittivity) as a function of temperature. At $T > T$c (Fig 1.3 (b)), the central minimum is lower in energy than the other minima, creating a metastable ferroelectric phase. A single minimum appears at $P = 0$ at $T > T$c, and the paraelectric state is stable [7].

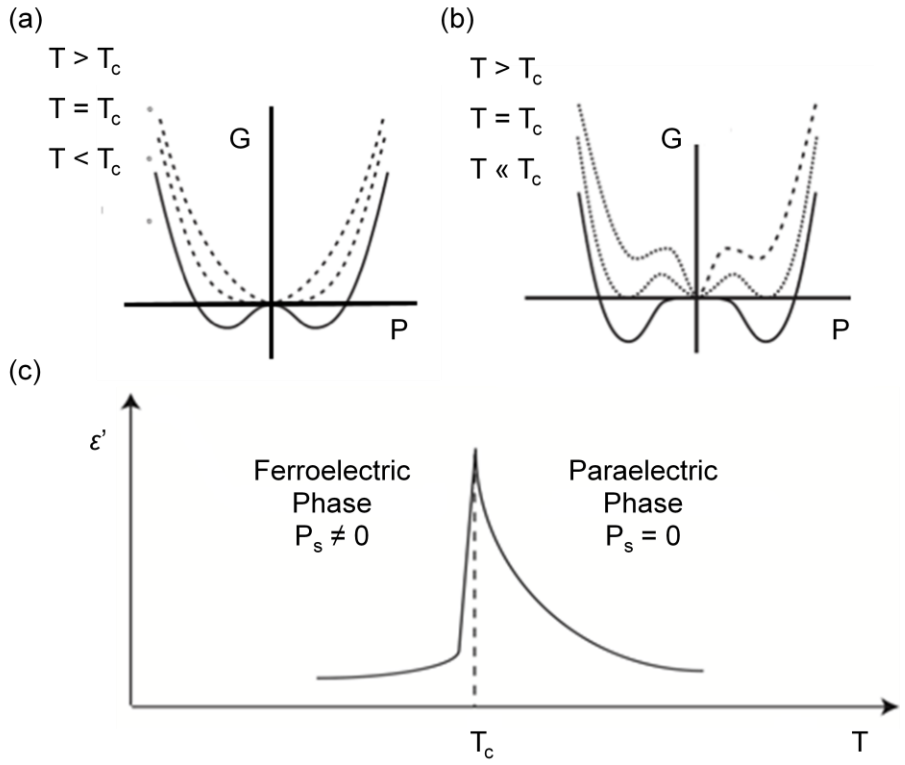

Figure 1.3 **Gibbs free energy as a function of the polarization *P* at various temperatures for (a) a second-order phase transition, and (b) a first-order phase transition. (c) The variation of the dielectric permittivity as a function of temperature for a normal ferroelectric, showing the anomaly in permittivity that occurs at *T*c.**

1.2.2 Ferroelasticity

Ferroelasticity is defined analogously to ferroelectricity, i.e., a crystal is said to be ferroelastic when it possesses two or more orientation states under stress-free conditions, exhibiting a transition between these states upon application of mechanical stress [10]. A typical strain (*s*) versus stress (σ) of a ferroelastic shows a hysteresis loop, similar to the P-E loop in Figure 1.2. Ferroelasticity is a structure-dependent property and is directly inferable from the crystal structure. In the ferroelastic state, the crystal symmetry is reduced to a subgroup of a higher symmetry class by a small distortion which is a measure of the spontaneous strain [11]. For example, as temperature decreases to about 120 °C, $BaTiO_3$ transforms from the non-ferroelastic state with a high

symmetry class (space group $Pm\overline{3}m$) into a ferroelastic state with reduced symmetry (space group *P4mm*), which is a subgroup of the high symmetry class. The onset of ferroelasticity, as a function of temperature or pressure, is often accompanied by additional cooperative phenomena, such as magnetic or ferroelectric ordering [11].

1.2.3 Ferromagnetism and Antiferromagnetism

A magnetic field H produces lines of forces which are known as the magnetic flux density B. When a material is placed in an applied magnetic field, the flux density can either decrease or increase. For example, a diamagnetic material will reduce the density of the lines of force within the material, whereas a paramagnetic material will increase the flux density [12]. As a result, such interactions in the material produce a magnetic field of its own, known as the magnetization *M*, and this is related to the magnetic flux density and applied field as shown in Equation 1.2:

$$B = \mu_0(H + M) \ , \tag{1.2}$$

However, in magnetic materials, the magnetisation is usually discussed in terms of the magnetic susceptibility χ, which is shown as following:

$$\chi = \frac{M}{H} \ , \tag{1.3}$$

An element exhibits magnetic behavior if it possesses an odd number of electrons since electrons carry a spin of $\frac{1}{2}$, as the total spin will not be zero [13]. The magnetic susceptibility χ represents the response of a substance to an applied magnetic field and is temperature dependent. Many paramagnetic materials, in which there is no interaction between moments, follow the Curie Law:

$$\chi = \frac{C}{T} \ , \tag{1.4}$$

where *T* is temperature in K, and *C* is the Curie constant which is defined as

$$C = \frac{N_A \mu_{eff}^2 \mu_B^2}{3k_B} \approx \frac{1}{8}\mu_{eff}^2 \quad , \tag{1.5}$$

where N_A is the Avogrado's number, k_B is the Boltzmann constant, μ_B is the Bohr magneton, and μ_{eff} is spin-only effective magnetic moment:

$$\mu_{eff} = g\sqrt{S(S+1)} \quad , \tag{1.6}$$

where *g* is the gyromagnetic ratio (*g*-factor), which is equal to 2 for spin only systems, and *S* is the total spin quantum number. It should be noted that the contribution of orbital angular momentum is ignored since it is normally quenched by crystal field effects for the first row transition metals [14].

When there are cooperative interactions between the individual electron spins, then different temperature dependences are observed. The typical temperature-dependent susceptibility and inverse susceptibility curves of paramagnetic, ferro- and antiferromagnetic materials are shown in Figure 1.4 [4].

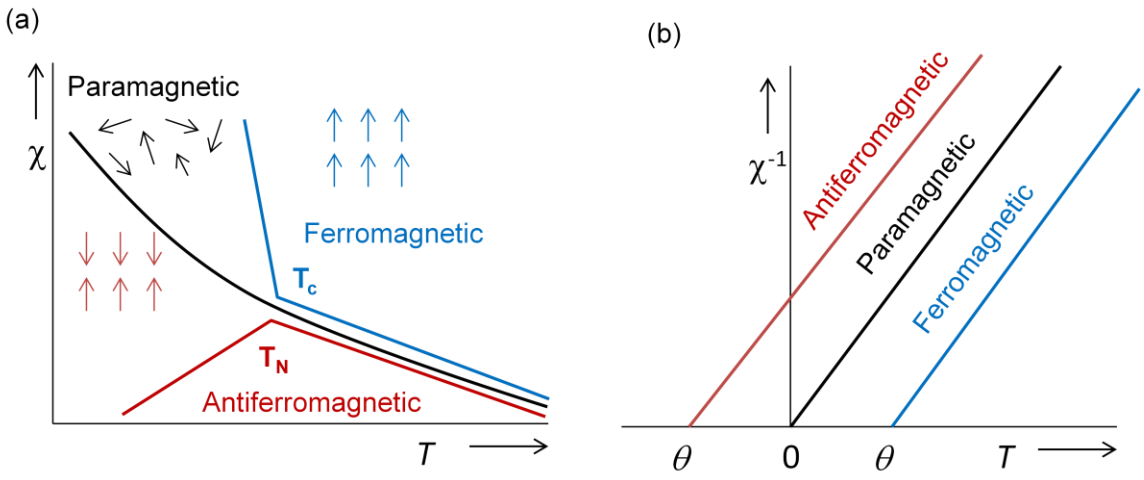

Figure 1.4 **(a) Temperature dependences of the magnetic susceptibilities for paramagnetic, ferromagnetic and antiferromagnetic materials. (b) Inverse susceptibility dependences for each type where ferromagnets give a positive Weiss temperature θ, and antiferromagnets give a negative Weiss temperature θ [16].**

For ferromagnetic materials, all the spins are aligned parallel along the same direction, as seen in Figure 1.4 (a), resulting in a net spontaneous moment in the material, even in the absence of an applied field. This behavior happens below a certain temperature, known as the Curie temperature *T*c, below which quantum mechanical exchange energy causes electrons with parallel spins to have a lower energy than those with antiparallel spins [15]. Above *T*c, the thermal energy ($k_B T$) is larger than that of the exchange energy and the ordered arrangement disappears so that that spins become paramagnetic. Below *T*c, a sharp upturn is observed in the susceptibility due to the alignment of the spins with the applied field [16].

Another common type of spin arrangement is antiferromagnetic, where the moments are ordered antiparallel to each other, resulting in zero net magnetic moment. Similar to ferromagnetism, this behaviour occurs below a phase transition temperature, $T_{N.}$ Above T_N, the susceptibility is nearly independent of the direction of the field relative to the spin axis. However below T_N, the susceptibility of antiferromagets depends strongly on the orientation of magnetic field [16]. Both ferro- and antiferromagnetic materials can be described by a modified version of the Curie law, known as the Curie-Weiss law, shown in Equation 1.7:

$$\chi = C/(T + \theta) \ , \tag{1.7}$$

where θ is the Weiss temperature. It is used to determine the type of magnetic ordering a material exhibits, by fitting the paramagnetic region of the inverse susceptibility data, as shown in Figure 1.4 (b). A positive θ value represents the behavior of the spins are predominately ferromagnetic, whereas a negative θ value indicates the spins are predominately antiferromagnetic [16].

For complex oxides, it is possible to discuss the susceptibility in terms of magnetic moments of the metals that are present. From the microscopic point of view, magnetism is based on the quantum mechanics of electronic angular momentum, which has two distinct sources - (i) orbital motion; the orbital motion of electrons in an orbit of an atom. This orbital moment can be related to the current flowing in a loop of wire of zero (negligible) resistance and gives rise to the orbital magnetic moment; and (ii) spin;

spinning of electrons around its own spin axis gives rise to a spin magnetic moment. Electrons possess both spin and orbital angular momentum, and except for the triply degenerate ground state of d^1 or d^2 electron configurations, the orbital angular momentum is usually negligible for the first row transition metals. Therefore it is possible to determine the theoretical magnetic moment (μ_S) using the spin-only momentum equation as follow [14]:

$$\mu_s = 2\sqrt{s(s+1)} \ , \tag{1.8}$$

where s is the spin quantum number of an atom or ion, the unit of μ_s is in Bohr magnetons. The value of s is related to the number of unpaired electrons ($s = \frac{1}{2}$ for each unpaired electrons; i.e. for 3 unpaired electrons, $s = \frac{3}{2}$).

For heavier elements such as the lanthanides, the orbital angular momentum cannot be neglected, and so must be taken into account in the total angular momentum J, which is the vector sum of the orbital L and spin S angular momenta. The magnetic moment is given by [17]:

$$\mu = g\sqrt{J(J+1)} \ , \tag{1.9}$$

where g is the Landé g -factor and is calculated by:

$$g = 1 + \frac{J(J+1)+S(S+1)-L(L+1)}{2J(J+1)} \ . \tag{1.10}$$

As a result, it leads to a wide range of magnetic moments, particularly for the lanthanides with partially filled f orbitals. For example, 0 μ_B for Eu^{3+} and 10.63 μ_B for Dy^{3+} [18].

1.3 Multiferroics

Multiferroic materials have attracted extensive interest in the past decades because of their exceptional potential for new device applications in multiple-state memory elements, electric field controlled ferromagnetic resonance devices and transducers with magnetically modulated piezoelectricity [19, 20]. Multiferroics are the materials which exhibit two or all three of the ferroic properties: ferroelectricity, ferromagnetism, and ferroelasticity, simultaneously. Multiferroic materials with both the ferroelectric properties and magnetic properties exhibit magnetoelectric effect (ME).

1.3.1 Types of Multiferroics

Multiferroic materials can be divided into two groups. The first group, called type-I multiferroics, contains those materials in which ferroelectricity and magnetism have different sources and are independent of one another, though there is some coupling between them. In these materials, ferroelectricity typically appears at higher temperatures than magnetism and the spontaneous polarization *P* is often large (of order 10 – 100 $\mu C/cm^2$) [19]. The second group, which is called type-II multiferroics, are newly discovered materials [21, 22], in which magnetism can induce ferroelectricity, implying a strong coupling between the two. However, the polarization in type-II multiferroics is usually much smaller (about 10^{-2} $\mu C/cm^2$) [23-27]. Also, multiferroics can be classified into two categories: (a) single phase multiferroics which show ferroelectricity and ferromagnetism simultaneously in one phase, and (b) multiferroic composites which are combinations of ferromagnetic and ferroelectric phases.

1.3.1.1 Single Phase Multiferroic Compounds

There are various multiferroic materials. Some of the most recently studied multiferroics include hexagonal rare-earth manganites with formula $M$$MnO_3$ (M = Y, Ho, Er, Tm, Yb, Lu or Sc) which are single phase multiferroics that exhibit ferroelectricity and frustrated magnetic ordering [28-31]. Also, the compounds Ba$M$$F_4$ (M = Ho Fe, Co, or Ni) have an orthorhombic crystal structure at high temperatures with antiferromagnetic (or weak ferromagnetic) ordering and (anti)ferroelectric properties at low temperatures [32, 33]. Perovskite compounds containing magnetic ions which fully or partially occupy the octahedral positions in the perovskite structure form another group of single phase multiferroic. For example, $BiFeO_3$ has a rhombohedral pseudo-perovskite structure with alternating layers of bismuth and oxygen, and iron and oxygen. Fe^{3+} ions in the octahedral positions cause exchange interaction between the Fe^{3+} ions along the Fe^{3+} - O^{2+} - Fe^{3+} chains [34].

There are a limited number of multiferroics existing in nature and the reasons are discussed below in Section 1.3.3. Some single phase multiferroic materials exhibit multiferroic properties and magnetoelectric coupling at low temperatures (below room temperature), which is not suitable for practical applications. For example, $TbMnO_2$ is a single phase multiferroic material which shows magnetism-induced ferroelectricity and switchable polarization with magnetic field with a small polarization (~ 80 $nCcm^{-1}$) at very low temperature (3 K) [22].

Among all multiferroic materials studied so far, $BiFeO_3$ (BFO) is known to the only single-phase room temperature multiferroic material, which displays ferroelectric behaviour below Tc ~ 1103 K and G-type antiferromagnetic behaviour below T_N ~ 643 K [35]. At room temperature, the structure of BFO is characterized by a rhombohedral distortion with $R3c$ space group in the nearly cubic perovskite cell, in which the cations (Bi^{3+} and Fe^{3+}) are displaced along the [111] direction with FeO_6 octahedra rotating antiphase around the rhombohedral axis. In addition, Bi^{3+} at A-site has a stereochemically active $6s^2$ lone pair, which activates a hybridization of Bi 6p and O 2p states, and causes the off-centering displacement of Bi^{3+} toward O^{2-}, inducing giant spontaneous ferroelectric polarization [36]. In terms of the magnetic properties, BFO

displays a G-type antiferromagnetic ordering with an incommensurately modulated cycloidal spiral spin structure with a modulation period of 62-64 nm and the canted spins arising from the Dzyaloshinskii-Moriya interaction [36]. This unique multiferroic behaviour permits BFO to be an ideal candidate for important multifunctional applications as multiple-state memory elements, sensors and actuators, and electric-field-controlled ferromagnetic resonance devices [19, 23, 24]. A detailed review of the physics and potential applications of $BiFeO_3$ will be discussed in Section 1.6.

1.3.1.2 Multiferroic Composite Systems

Natural single-phase multiferroics are rare, and their magnetoelectric (ME) coupling is usually weak or occurs at low temperatures. In contrast, multiferroic composites, which incorporate both a ferroelectric (piezoelectric/electrostrictive) phase and a ferromagnetic (piezomagnetic/magnetostrictive) phase, yield a giant ME coupling response above room temperature [41]. Figure 1.5 shows the schematic of a multiferroic composite for strain-mediated ME coupling. The distortion of the magnetostrictive phase under the magnetic stimulus is transferred to the piezoelectric phase, resulting in an electrical response [41]. Most multiferroic composites can be achieved in the form of laminates [42, 43] or epitaxial multilayers [44]. $CoFe_2O_4$, $NiFeO_3$, Terfenol-D, and $La_{1-x}Sr_xMnO_3$ have been used for the ferromagnetic phase, and $BaTiO_3$, $Pb(Zr, Ti)O_3$ (PTZ), $BiFeO_3$, and $PbTiO_3$ have been used for the ferroelectric phase [45,46,47,48,49,50]. It was found that the magnetoelectric coefficient in PTZ/Terfenol-D composite material could reach as high as 2 $Vcm^{-1}Oe^{-1}$ = 5 x 10^{-8} $Cm^{-2}Oe^{-1}$ [51]. The converse effect was observed with μ_0 = 2.3 x 10^{-7} $Cm^{-2}Oe^{-1}$ in the $La_{0.67}Sr_{0.33}MnO_3/BaTiO_3$ system [52].

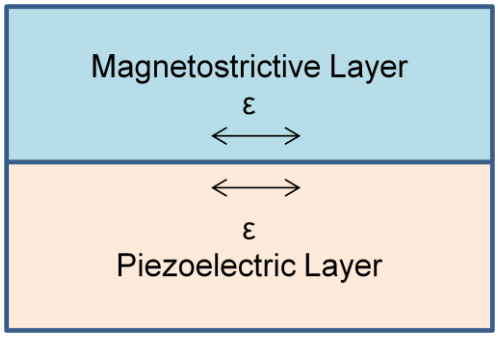

Figure 1.5 Schematic of a multiferroic composite for strain-mediated ME coupling. ε stands for strain.

1.3.2 Magnetoelectric Effects

It is very likely for a multiferroic to exhibit magnetoelectric (ME) effect in which an electric polarization can be induced by a magnetic field, and vice versa, a magnetization can be induced by an electric field [53]. The magnetoelectric effect in a single phase multiferroic is given by Landau theory which is expressed in terms of Gibbs free energy function. It can be expressed as the following equation by using the Einstein summation convention [41]:

$$G = P_i E_i + \mathrm{M}_i \mathrm{H}_i + \frac{1}{2}\varepsilon_0 \varepsilon_{ik} E_i E_k + \frac{1}{2}\mu_0 \mu_{ik} H_i H_k + \alpha_{ik} E_i H_k + \frac{\beta_{ijk}}{2} E_i H_j H_k + \frac{\gamma_{ijk}}{2} H_i E_j E_k \ldots \quad (1.11)$$

Differentiating it with respect to E_i leads to the polarization:

$$P_i(E,H) = \frac{\partial \mathrm{G}}{\partial \mathrm{E}_i} = P_i^s + \frac{1}{2}\varepsilon_0 \varepsilon_{ik} E_k + \alpha_{ik} H_k + \frac{\beta_{ijk}}{2} H_j H_k + \cdots \quad . \quad (1.12)$$

When there is no electric field applied, E = 0, then the polarization becomes:

$$P_i(E,H) = P_i^s + \alpha_{ik} H_i + \frac{\beta_{ijk}}{2} H_j H_k + \cdots \quad , \quad (1.13)$$

where α is the linear magnetoelectric coefficient, that describes both the electric polarization resulting from a magnetic field and the magnetization resulting from an

electric field. β is the quadratic (or bilinear) magnetoelectric coefficient [41]. ME coupling is limited by the relation:

$$\alpha_{ij} \leq \sqrt{\varepsilon_0 \varepsilon_{ij} \mu_0 \mu_{ij}} \quad . \tag{1.14}$$

Since ferroelectric and ferromagnetic materials have particularly high ε and μ, large ME coupling might be expected for ferromagnetic ferroelectrics, which is an important type of multiferroics [41]. In order to enhance the ME coupling for technological applications, a variety of hybrid multiferroic composites have been studied [54]. The typical examples of multiferroic materials exhibiting magnetoelectric effect are Cr_2O_3, $BiMnO_3$, and $BiFeO_3$ [54].

1.3.3 Why Are There So Few Multiferroic Materials

As mentioned previously, despite the advances in the field of multiferroics, few multiferroic materials with a strong coupling of magnetic and electric properties at room temperature have been found. The reason is that ferroelectricity and ferromagnetism (antiferromagnetism) are almost mutually exclusive by nature, which limits the choice of potential multiferroic materials [55].

For example, in the perovskite-structure materials, the *d*-orbital occupancy of the B cation is a requirement for the existence of magnetic moment and the consequent existence of magnetic ordering [15]. Ferroelectricity primarily arises from the additional bonding between the B cation and O^{2-} anion. In other words, the hybridization between the *d* orbitals of the B cation and the *p* orbitals of the O^{2-} anion requires close energy levels between these two sets of orbitals [15]. However, adding electrons to the *d* orbitals will increase the *d* orbital energy significantly, broadening the energy difference between the *d* orbitals of *B*-site cation and *p* orbitals of the O^{2-} anion. As a result, the hybridization of *p* orbital and *d* orbital becomes difficult and thus ferroelectricity and magnetism tend to be mutually exclusive [55].

Structural distortion is another limiting factor that prevents the coexistence of ferromagnetism and ferroelectricity. In some cases, the uneven occupancy of the *d*

orbitals gives rise to magnetic properties, leading to a geometrical distortion of the structure, due to the interaction between the *d* orbitals and the ligand field, which removes the degeneracy of the electronic ground state. This effect is called Jahn-Teller distortion [56]. On the other hand, the hybridization between the B cation and the *p* orbitals of the O^{2-} anion gives rise to off-center distortion. In a partially filled *d* orbital system, the energy can be lowered either by the Jahn-Teller distortion or off-center distortion. However, for cations with certain *d*-orbital occupancies, the tendency to undergo a Jahn-Teller distrtion is strong and will likely be the dominant structural effect. [15,55]. Examples of this effect are seen in lanthanum manganite, $LaMnO_3$, in which the Mn^{3+} ion has a d^4 configuration, and yttrium titanate, $YTiO_3$, in which the Ti^{3+} ion is d^1. Both materials have a *d*-type Jahn-Teller distortion, in which the elongated axes of the oxygen octahedra are oriented parallel to each other along the crystallographic *c* axis [15,57]

Although ferroelectricity and ferromagnetism (antiferromagnetism) are mostly mutually exclusive, which is the main reason why there are so few multiferroic materials. $BiFeO_3$ (BFO) is one of the few multiferroic materials [34,58]. The *A*-site Bi^{3+} has stereochemically active $6s^2$ lone-pair electrons, which results in hybridization of O 2*p* and Bi 6*p* orbitals. As a result, an off-center distortion between Bi^{3+} toward O^{2-} promotes the ferroelectric polarization [36,59].

1.4 Piezoelectricity

Piezoelectricy was discovered in 1880 by French physicists Pierre and Jacques Curies during their study of crystals such as quartz, zinc blende and tourmaline [60]. Piezoelectric materials convert mechanical energy into electrical energy, and vice versa. The direct piezoelectric effect is the electrical charge/polarization generated by a mechanical stress applied to a piezoelectric material, as described in Equation 1.13. The converse piezoelectric effect is associated with an internal strain in the material in response to the application an electrical field and it is described in Equation 1.14 [61, 62].

$$D_i = d_{ijk}\sigma_{jk} \tag{1.13}$$

$$S_{ij} = d_{kij}E_k \tag{1.14}$$

Here, D_i is the resultant charge density, σ_{jk} is the applied stress, S_{ij} is the strain developed in a piezoelectric material with the application of an electric field E_k. d_{ijk} and d_{kij} are the piezoelectric tensor known as the piezoelectric coefficient for the direct and converse effects that are thermodynamically equivalent [7]. The indices i and j are the tensor notation of the physical properties of crystals. The longitudinal coefficients (ij=11, 22, 33) are the piezoelectric coefficients measured in the direction of the applied field. The transverse coefficient (ij =12, 23, 31) are measured in the direction perpendicular to the field. Shear coefficients (ji = 14, 15, 16,… 35, 36) are the remaining piezoelectric coefficients [62]. By using matrix notation, Equations 1.13 and 1.14 can be simplified as follows:

$$D_i = d_{im}\sigma_m \tag{1.15}$$

$$S_m = d_{im}E_i \quad , \tag{1.16}$$

where i = 1, 2, 3 and m = 1, 2, …, 6. The linear and shear components of the strain are represented by the value of m = 1, 2, 3 and m = 4, 5, 6, respectively [7].

The conversion of energy by the ceramic element from electrical to mechanical form or vice versa is described by the electromechanical coupling coefficients k_{33}, k_{31}, k_p, and k_{15}. The electromechanical coupling factor k specifics the conversion efficiency between electrical and mechanical energies which is defined by the following equation:

$$k^2 = \frac{mechanical\ energy\ stored}{electrical\ energy\ applied} \text{ or } k^2 = \frac{electrical\ energy\ stored}{mechanial\ energy\ applied} \quad . \tag{1.17}$$

These subscripts indicate the relative directions of electrical and mechanical quantities and the kind of motion involved. For example, k_{33} is the coupling factor for longitudinal vibrations for a long thin bar with electrode on the ends, polarized along the length, and vibrating in a simple length expansion and contraction. k_{31} relates to a long thin bar but electrode on a pair of long faces. k_p relates to the coupling of electrical and mechanical energy in a thin round disc, whereas k_{15} signifies the energy conversion in a thickness

shear vibration. In order to increase the piezoelectric response to an applied stimulus, large piezoelectric coefficients are desirable and often the piezoelectric coefficient d_{33} attracts more interests due to its same direction piezoelectric coefficient as the applied stress or electric field [63].

1.5 Morphotropic Phase Boundary (MPB)

Ferroelectricity and piezoelectricity are crystallographic symmetry dependent. According to the point group symmetry of lattices, crystals can be classified into seven crystal systems: triclinic, monoclinic, orthorhombic, tetragonal, rhombohedral, hexagonal and cubic. As shown in Figure 1.6, these systems can again be subdivided into 32 point groups according to their lattice systems. 11 of them possess a center of symmetry, and are non-piezoelectric. The remaining 21 non-centro-symmetric crystallographic classes, piezoelectricity exists in 20 of them. Of the 20 piezoelectric crystal classes, only 10 of them (1, 2, m, mm2, 4, 4mm, 3, 3m, 6, and 6m) are polar point groups and can have ferroelectricity, meaning ferroelectric materials are a subclass of piezoelectric materials [64]. Almost all of the high performance piezoelectric materials that have been developed are ferroelectrics. The reason behind this is that the large spontaneous polarization in ferroelectrics promotes space for the change of polarization directions. The space for changing polarization directions is much larger than all the other kinds of dielectric materials. Although large polarization does not necessarily lead to large piezoelectricity, piezoelectricity does depend on the change of polarization by its definition. The large spontaneous polarization in ferroelectrics could possibly accommodate a relatively large change of polarization. Therefore in searching for high performance piezoelectric materials, it is essential to focus on ferroelectrics that can change their spontaneous polarization easily.

The symmetry of the crystallographic structure of ferroelectrics is important for the orientation of the spontaneous polarization. Perovskite ferroelectrics have 6 possible orientations along the <100> directions of the spontaneous polarization in a tetragonal phase, 8 possible orientations along the <111> directions in a rhombohedral phase and 12 possible orientations along the <110> directions in an orthorhombic phase. The

spontaneous polarization can be switched among these orientations in each of the phases under the application of an electric field and/or mechanical force [64, 65].

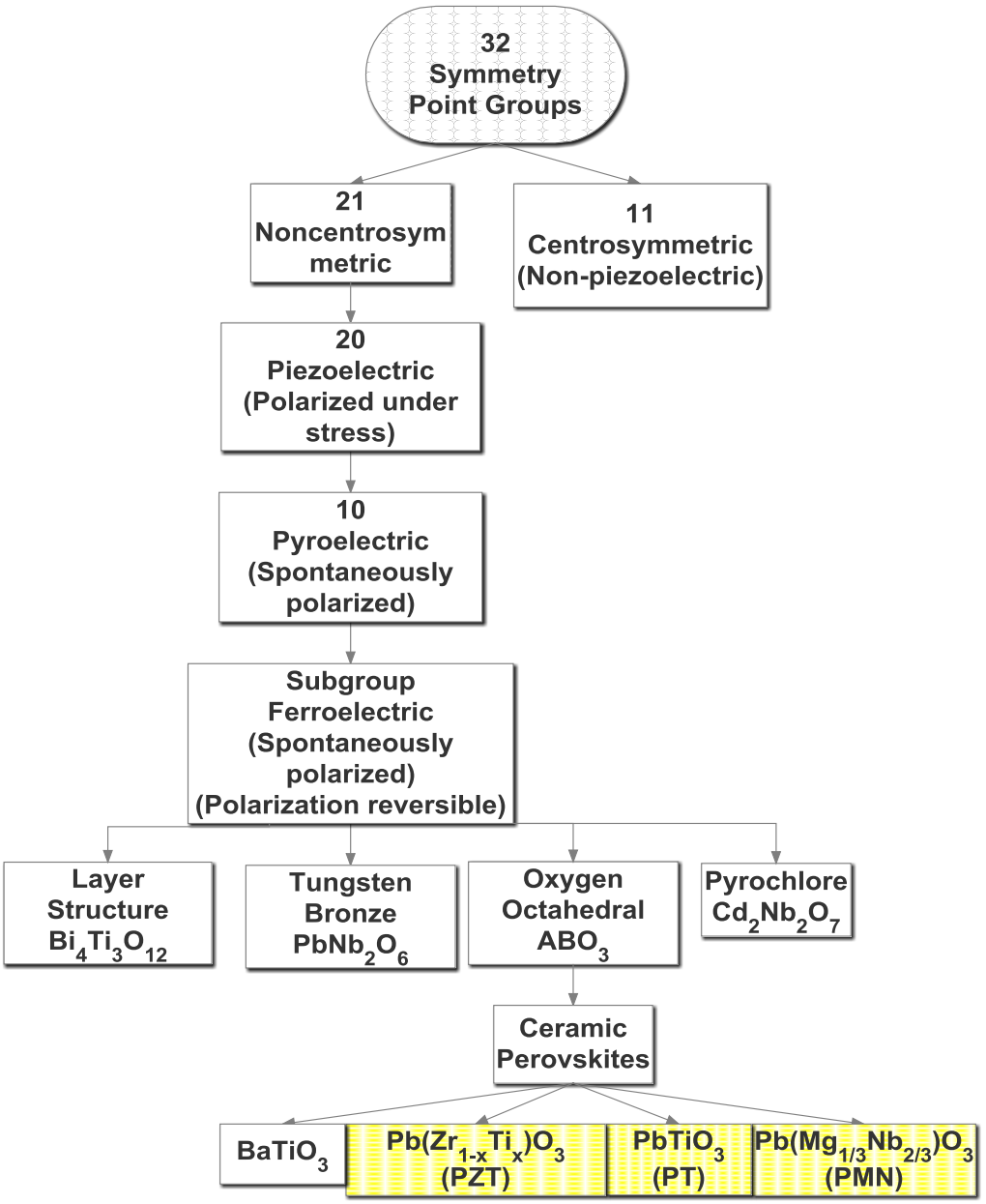

Figure 1.6. Point group flow chart.

The term “morphotropic phase boundary” (MPB) was originally used to refer to phase transitions caused by changes in composition [5]. It is now mainly used in the scientific literature to describe the boundary that separates regions of rhombohedral symmetry with regions of tetragonal or orthorhombic symmetry in the binary phase diagrams of ferroelectric oxide solid solutions. Materials with compositions near this boundary exhibit a greatly enhanced piezoelectric response relative to the compositions far from the boundary [66].

One of the earliest developed complex-structured ferroelectrics that shows an MPB is known as lead zirconate titanate - $PbZr_{1-x}Ti_xO_3$ (PZT) system, where $x \approx 0.45$ - 0.52 [67]. It is a solid solution of $PbZrO_3$ and $PbTiO_3$. The MPB related structures are closely dependent on temperature. Above the transition temperature *T*c, PZT is paraelectric with the cubic perovskite structure. Below the transition temperature, however, the material becomes ferroelectric, with the symmetry of the tetragonal for Ti-rich compositions and rhombohedral for Zr-rich compositions. At the compositions across MPB, the two phases have close free energy and they tend to coexist. Previous experiments have found that the maximum values of the dielectric permittivity, piezoelectric coefficients and the electromechanical coupling factors of PZT at room temperature can be achieved in this MPB region. However, the maximum value of the remanent polarization is shifted to smaller Ti contents [5]. Recent studies using high-resolution X-ray powder diffraction measurements on a homogeneous sample of PZT have shown the existence of a monoclinic phase which “bridges” the tetragonal and rhombohedral phases. Therefore, the high electromechanical response in the MPB region of the phase transition from tetragonal to rhombohedral is related to this intermediate phase of monoclinic symmetry. As a result, the piezoelectric elongation of the unit cell occurs along with the monoclinic distortion [68]. Other renowned examples of enhanced piezoelectric responses at the MPB have been reported in single-crystal relaxor-based solid solution, $Pb(Mg_{1/3}Nb_{2/3})O_3$-$PbTiO_3$ (PMN-PT) by Ye’s research group [69, 70].

1.6 Review of Physics and Applications of Bismuth Ferrite

Multiferroic materials possessing electric, magnetic and/or structure order parameters will exhibit ferromagnetic, ferroelectric, and/or ferroelastic behaviours simultaneously [36]. Among all the multiferroic materials studied so far, Bismuth ferrite, $BiFeO_3$ (BFO) is the most widely studied material and is known to be the only single-phase room temperature multiferroic material.

1.6.1 Structure of $BiFeO_3$

The atomic structure of $BiFeO_3$ was determined by Michel et al. in 1969 based on X-ray diffraction on single crystal and neutron diffraction on powder samples [71]. The crystal structure of bismuth ferrite is characterized as rhombohedral perovskite unit cell with space group *R3c* at room temperature, as shown in Figure 1.7. The perovskite-type unit cell has a lattice parameter, a_{rh} = 3.97 Å and a rhombohedral angle, α_{rh} = 89.3-89.4° at room temperature [72], with ferroelectric polarization along the pseudocubic [111] direction [72]. On the other hand, the unit cell can also be described as hexagonal with lattice parameters, a_{hex} = 5.58 Å and c_{hex} = 13.09 Å. The hexagonal *c*-axis is parallel to the diagonals of the perovskite cube, i.e., $[001]_{hexagonal} \parallel [111]_{pseudocubic}$ [72, 73]. As mentioned earlier in Section 1.1, the Goldschmidt tolerance factor, *t*, can be used to measure how well the ions fit into a perovskite unit cell and $BiFeO_3$ has a tolerance factor *t* of 0.88 [76]. For $BiFeO_3$, the superexchange Fe-O-Fe angle θ = 154 -156° [72]. The Fe-O-Fe angle is important since it controls both the magnetic exchange and orbital overlap between Fe and O, and thus it determines the magnetic ordering temperature and the conductivity [73], which will be discussed in later sections.

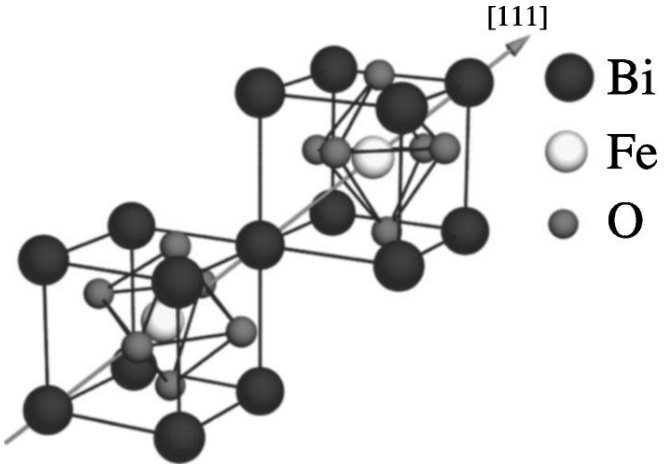

Figure 1.7 Schematic view of the *R*3c structure of $BiFeO_3$ that is built up from two cubic perovskite unit cells. The cations are displaced along the [111] direction relative to the anions, and the oxygen octahedra rotate with alternating sense around the [111] axis.

Note. Reprinted from C. Ederer, N. A. Spaldin, Weak ferromagnetism and magnetoelectric coupling in bismuth ferrite, Phys. Rev. B, 71 (2005) 060401, with the permission of Americal Physical Society [159].

1.6.2 Ferroelectricity of $BiFeO_3$

The ferroelectric polarization of bulk $BiFeO_3$ is along the diagonals of the perovskite unit cell, which is [111] pseudocubic/[001] hexagonal. The $6s^2$ lone-pair orbital of Bi^{3+} stereochemically activates a hybridization of Bi 6*p* and O 2*p* states, and causes an off-centering displacement of Bi^{3+} toward O^{2-} to induce ferroelectricity [36]. It has been reported that the $BiFeO_3$ ceramics have a large polarization of P_r = 60 μCcm^{-2} normal to [001] and P_r = 100μCcm^{-2} along the pseudocubic [111] direction [77]. Thin films of $BiFeO_3$ often have great ferroelectric properties. Previous research [78] reported a rhombohedral crystal class of $BiFeO_3$, but later it has been proved that $BiFeO_3$ displays the monoclinic morphology when grown onto a substrate (e.g. $SrTiO_3$). The in-plane contraction and out-of-plane elongation, as well as the lattice mismatch between the film and the substrate, are responsible for the symmetry-lowering distortion [79]. It was also reported that as the film's thickness was reduced (below 100 nm), there was a further change in symmetry from monoclinic to tetragonal, which was observed on the XRD and Raman spectroscopy data [79]. However, this result does not seem to be consistent with

the result of piezo-response force microscopy (PFM) study. As a result, the external shape of the unit cell maybe tetragonal, but it remains monoclinic with the internal degrees of freedom responsible for the polarization [80]. The relationship between the strain and polarization of $BiFeO_3$ has been confirmed by several researchers, stating that the absolute magnitude of the spontaneous polarization does not change, however, it rotates out-of-plane through the monoclinic symmetry plane [81]. The small sensitivity of $BiFeO_3$ to epitaxial strain may arise from its relatively low piezoelectric coefficient due to the inferior dielectric property. However, its electrostrictive coefficient is not small [73].

1.6.3 Dielectric Properties of $BiFeO_3$

At room temperature, the GHz dielectric constant for $BiFeO_3$ is equal to $\varepsilon_r = 30$, which was reported as the intrinsic dielectric constant at radio frequencies [82]. It peaks at the rhombohedral-orthorhombic phase transition (825 - 840 °C) [82]. This intrinsic dielectric constant $\varepsilon_r = 30$ may seem small for a ferroelectric, but it is reasonable. First, the ferroelectric polarization has already saturated at room temperature, which is far below the ferroelectric Curie temperature of $BiFeO_3$. Since the dielectric constant is a measure of polarizability, the variation of the nearly saturated polarization will be negligible under electric fields, leading to a small dielectric constant. Next, it starts with a strong first-order transition so that there is less phonon softening and thus a low dielectric constant is expected [73].

1.6.4 Ferromagnetism and Magnetoelectric Coupling of $BiFeO_3$

The bulk $BiFeO_3$ is an antiferromagnetic and ferroelectric material with antiferromagnetic Néel temperature and ferroelectric Curie temperature at $T_N \sim 643$ K and $T_C \sim 1103$ K, respectively. The Fe magnetic moments are coupled ferromagnetically within the $(111)_{pseudocubic}$ planes and antiferromagnetically between adjacent planes, forming the so-called G-type antiferromagnetic order [68]. The G-type antiferromagnetism in $BiFeO_3$ is that each Fe^{3+} spin is surrounded by six antiparallel spins on the nearest neighboring Fe ions. A weak ferromagnetism will be produced if the

magnetic moments are oriented perpendicular to the [111] direction. However, these spins are not perfectly anti-parallel and a small canted moment of the antiferromagnetic sublattices results in a macroscopic magnetization due to the Dzyaoshinskii-Moriya interactions [83]. Superimposed on this antiferromagnetic ordering is a spiral spin structure, in which the antiferromagnetic axis rotates through the crystal with a long wavelength period of ~ 620 Å, with the antiferromagnetically ordered sublattices propagating in the $[110]_h$ direction [84]. The plane within which the spins rotate is called the magnetic easy plane, which is defined by the propagation vector (black) and the polarization vector (red) as shown in Figure 1.8. The blue and green arrows represent the canted antiferromagnetic spins which yield a net magnetic moment which is shown as purple arrows. This net magnetic moment is averaged out to zero due to the spiral spin rotation [85].

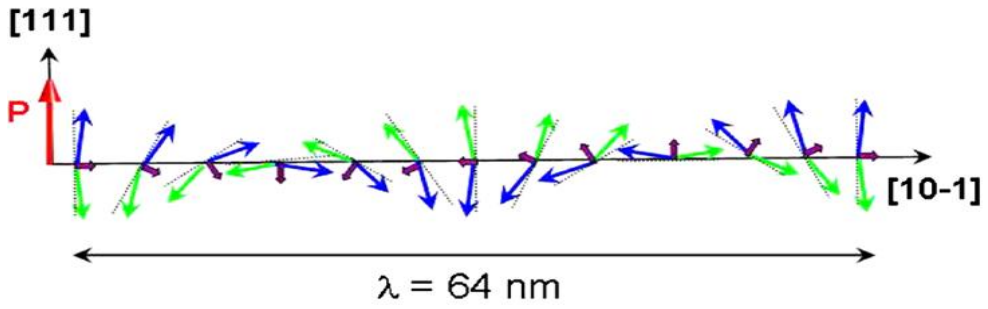

Figure 1.8 Schematic representation of the spiral spin in $BiFeO_3$.

Note. Reprinted from D. Lebeugle, D. Colson, A. Forget, M. Viret, A.M. Bataille, A. Gukasov, Electric-field-induced spin flop for $BiFeO_3$ single crystals at room temperature, Physical Review Letters, 100 (2008) 227602. doi:10.1103/PhysRevLett.100.227602, with the permission of American Physical Society [85].

The spiral spin structure in $BiFeO_3$ can be destroyed by doping [86] or by epitaxial strain [87], disrupting the cancellation of the macroscopic magnetization and also promoting the linear ME effect [68]. The relationship between ferroelectricity and antiferromagnetism in bulk $BiFeO_3$ materials has been studied recently. Figure 1.9 shows the magnetic easy plane that contains the spins, the vector of ferroelectric polarization, and the vector of spiral spin propagation. By applying an electric field E, the magnetic easy plane rotates with the rotation of the polarization.

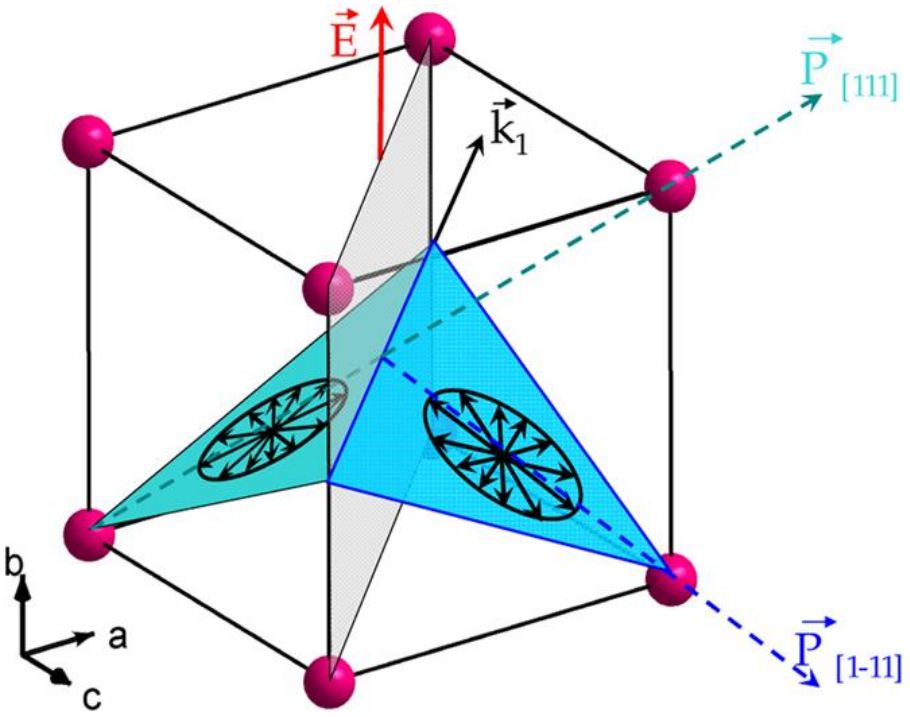

Figure 1.9 Schematic of the planes for the two polarization domains separated by a domain wall in bulk $BiFeO_3$, with cycloids vector k_1.

Note. Reprinted from D. Lebeugle, D. Colson, A. Forget, M. Viret, A.M. Bataille, A. Gukasov, Electric-field-induced spin flop for $BiFeO_3$ single crystals at room temperature, Physical Review Letters, 100 (2008) 227602. doi:10.1103/PhysRevLett.100.227602, with the permission of American Physical Society [85].

However, a significant magnetization and also a strong ME coupling have been observed recently in epitaxial thin films, which suggests that the spiral spin structure is also suppressed in thin films [88]. The reason may arise from the epitaxial constraints or enhanced anisotropy. As mentioned above, thin films have G-type antiferromagnetism with a slighting canting so that the magnetic moments can easily be perpendicular to the ferroelectric polarization. The polarization can be switched by an angle other than 180° so that it changes the magnetic easy plane, and in the case of rhombohedral symmetry, it can be switched by 71°, 109° and also 180° [85]. These epitaxial thin films show large electric polarization which makes them promising candidates for the materials of ME device applications based on voltage-control of magnetization [68, 73].

1.6.5 Limitations of $BiFeO_3$-based Materials

$BiFeO_3$ is the single-phase material that shows multiferroic phenomenon at room temperature, and it has attracted the attention of scientists for its potential applications and the fundamental interest in understanding its properties [19, 20, 23, 24, 89]. Despite the interesting properties of $BiFeO_3$-based materials, several obstacles associated with this compound hinder them from practical applications.

The leakage current behaviour in $BiFeO_3$ arises as a result of domain walls. However, recently researchers have been suggested that the reason for high leakage current falls behind the volatile nature of Bi^{3+} ions during synthesis. $BiFeO_3$ is considered a *p*-type semiconducting material resulting from the loss of Bi^{3+} cations during the high-temperature synthesis process, which causes vacancies to act as p-type centers for accepting electrons [90]. The Fe-O bond length (~ 1.93 Å) is shorter than the Bi-O bond length (~ 2.31 Å), and thus the formation of Bi vacancies is easier than the formation of Fe vacancies [93]. As a result, this leads to a reduction of Fe^{3+} to Fe^{2+} and the formation of cation and anion vacancies [91]. The loss of Bi^{3+} ion also leads to oxygen vacancy formation. As a result, the low electrical resistivity affects the measurement of dielectric and ferroelectric properties at room temperature [92].

In addition to the high leakage current, $BiFeO_3$ also exhibits weak magnetoelectric (ME) coupling. Many researchers have reported the weak magnetoelectric coupling in $BiFeO_3$ [73]. As discussed above, the expected strong linear ME effect is averaged out by the existence of spiral spin, that is, the linear ME effects are forbidden by magnetic symmetry [73]. However, there is a much weaker and higher order quadratic ME effect in $BiFeO_3$ [34]. Many stuides reported the observation of a weak magnetoelectric coupling in A-site rare-earth-doped $(Bi_{1-x}RE_x)FeO_3$ (RE = La, Nd, Sm, Sr) ceramics [94 - 97]. For example, in La-doped $(Bi_{1-x}RE_x)FeO_3$ ceramics, the magnitudes of remanent magnetization (M_r) and coercive field (H_c) increase with increasing La content [97], which may be due to the disruption of the cycloidal spin structure [98] and increased magnetoelectric coupling [93]. The canting of the antiferromagnetic spins by the modification of the antiparallel sublattice magnetization of Fe^{3+} is responsible for the weak ferromagnetism in $(Bi_{1-x}La_x)FeO_3$ ceramics [97].

Another limitation in $BiFeO_3$-based ceramic materials is the low remnant polarization (P_r = 6.0 $\mu C/cm^2$). A large polarization has been observed experimentally in $BiFeO_3$ single crystal and thin films [99,100], however, there is no evidence showing the similar magnitude of remnant polarization in the $BiFeO_3$ ceramics. The reason for low remnant polarization may be related to the difficulties in preparing single-phase materials. The presence of secondary phases results in high leakage currents [34].

1.7 Objectives of This Work and Organization of the Thesis

Recently, the perovskite compound $BiFeO_3$, in which ferroelectricity and antiferromagnetism coexist at room temperature, has attracted a great deal of interest. Despite the unique nature and special properties of $BiFeO_3$, the drawbacks that are discussed in section 1.6 require researchers to make chemical modifications on $BiFeO_3$ in order to achieve better electrical and magnetic properties. In the past decade, different attempts such as rapid liquid phase sintering, leaching the impurity phase with dilute nitric acid, and immediate quenching after sintering have been employed in order to overcome these drawbacks associated with $BiFeO_3$ and to improve its physical properties [101,102]. However, it is still difficult to obtain promising properties of single-phase $BiFeO_3$ ceramics. On the other hand, the physical properties of $BiFeO_3$ could be modulated by the process of ion doping, which has been proved to be an effective method to improve the performance of bulk $BiFeO_3$ [19, 23, 24, 103].

1.7.1 The $(Bi_{1-x}RE_x)FeO_3$ (RE = Dy, Lu, Yb, Er, and Eu) Solid Solutions

To enhance the ferromagnetism in $BiFeO_3$, several researchers have studied the substitution of rare-earth elements for the Bi^{3+} ions on the A site of the perovskite unit cell. The enhanced ferromagnetic behaviour has been observed in A-site doped samples with rare earth elements such as La, Nd, Er, Dy, Eu, and Sm [19, 35, 23, 24, 96,103,104]. Other researchers have studied the substitution of Bi by alkaline earth metals such as Ba, Ca and Sr [105 - 107]. Moreover, in recent studies, improved

magnetic and ferroelectric properties were also found in $BiFeO_3$ co-substituted with rare earth ions and alkaline earth ions [108, 109, 110].

It was found in our previous work of studying the effects of chemical modification on the structure and dielectric and magnetic properties of the (1-x)$BiFeO_3$-x$DyFeO_3$ solid solution [23] that there is a structural change from rhombohedral perovskite to orthorhombic orthoferrite at the morphotropic phase boundary located at $x \approx 0.1$. The ferroelectric and magnetic properties were improved by Dy^{3+} substitution on the *A* site and the simultaneous chemical substitution of Ti^{4+} for Fe^{3+} on the B site. A large saturated magnetization (0.5 μB/f.u.) was realized in 0.92$BiFeO_3$-0.08$DyFeO_3$ with 2% substitution of Ti^{4+} for Fe^{3+}, which was believed to arise from the disruption of the spiral spin modulation and the spin interactions between Dy^{3+} and Fe^{3+}. The aliovalent ionic substitution on the *B*-site of the perovskite structure, namely Ti^{4+} for Fe^{3+}, was found to improve the dielectric and ferroelectric properties of $BiFeO_3$-based solid solutions, by reducing the concentration of oxygen vacancies and thereby decreasing the conductivity [73]. The co-substitutions resulted in the reduction in the leakage current density and the enhanced ferroelectric properties of $BiFeO_3$ to some extent. Therefore, the first part of this project (**Chapter 3**) will extend this subject by focusing on the synthesis, preparation and characterization of the (1-*x*)$BiFeO_3$-*x*$DyFeO_3$ solid solution, with co-substitutions of lanthanide ion for Bi^{3+} on the A-site and Ti^{4+} for Fe^{3+} on the *B* site.

Furthermore, the chemically modified BFO with the *A*-site substitution of RE^{3+} (RE = Dy, Lu, Yb, Er, and Eu) for Bi^{3+} is used in order to improve the electrical and magnetic properties of the pure $BiFeO_3$ ceramics. These chemical modifications have two effects. First, the smaller ionic radius of the RE^{3+} ions can induce the structure distortion and increase the magnetic moment. Second, the shrinkage of the lattice parameters can disrupt the characteristic cycloidal spin structure in the antiferromagnetic $BiFeO_3$. These effects are expected to result in enhanced ferromgnatism and ferroelectricity.

In the following chapters, $BiFeO_3$ is substituted with other rare-earth metal ions: Lu^{3+}, Yb^{3+}, Eu^{3+}, and Er^{3+}, which have different ionic radii and various numbers of unpaired electrons than the Dy^{3+} ion. The ionic radii of the Dy^{3+}, Lu^{3+}, Yb^{3+}, Er^{3+}, and Eu^{3+}

ions are 1.027 Å, 0.977 Å, 0.985 Å, 1.004 Å and 1.066 Å, respectively, and the numbers of unpaired electrons for Eu^{3+}, Dy^{3+}, Er^{3+}, Yb^{3+}, and Lu^{3+} are 6, 5, 3, 1 and 0, respectively.

In order to better undersand the effects of rare-earth substitutions on the strucutral distortions and thereby on the ferromagnetism and ferroelectricity, Lu is chosen to substitute Bi because it has a zero unpaired electrons and smaller ionic raidus (0.977 Å) than that of Bi^{3+} (1.17 Å) and Dy $^{3+}$ (1.027 Å). Therefore, the solid solution system (1-*x*)$BiFeO_3$-x$LuFeO_3$, in which Lu substitutes for Bi^{3+} on the *A*-site, with the simultaneous chemical substitution of Ti^{4+} for Fe^{3+} on the *B*-site, was also studied in **Chapter 4**. The structures of these two co-substituted solid solution systems are investigated by X-ray diffraction (XRD) analysis, along with differential scanning calorimetry, dielectric measurements, ferroelectric measurements, and magnetic characterization by using SQUID.

The Lu-substituted $BiFeO_3$ solid solution system studied in Chapter 4 shows enhanced ferromagnetic and ferroelectric properties. Therefore, the effects of other rare-earth element with different number of unpaired electrons and ionic radii are systematically investigated in the following chapters. With a slightly larger ionic radius and 1 unpaired electron, Yb^{3+} (r = 0.985 Å) is chosen to be studied next and to be compared with Lu^{3+} (0.977 Å, 0 number of unpaired electrons). As such, the effects of chemical modifications on the structures and ferroelectric and ferromagnetic properties of the (1-*x*)$BiFeO_3$-*x*$LuFeO_3$ solid solution are presented in **Chapter 5**. Then, Er^{3+} is chosen and studied in **Chapter 6** because it has a larger ionic radius (1.004 Å) and a larger number of unpaired electrons (3) than that of Yb^{3+} (0.985 Å, 0 numbers of unpaired electrons). An interesting magnetic phenomenon called “magnetic pole inversion” is observed in the (1-*x*)$BiFeO_3$-*x*$ErFeO_3$ solid solution. The terminology “magnetic pole inversion” is defined as a crossover of dc magnetization from a positive value to a negative value as a function of temperature in materials below their magnetic ordering temperature. In most of the ferromagnets, the magnetic moment directions can be significantly changed by applying sufficiently high external magnetic field rather than varying temperature. These solid solution systems containing select rare-earth elements

with different ionic radii and various numbers of unpaired electrons are found to exhibit improved ferromagnetic and ferroelectric properties over the pure BFO system.

The (1-*x*)$BiFeO_3$-*x*$DyFeO_3$ solid solution studied in Chapter 3 is a promising room temperature multiferroic material, however, in order to find a better room temperature multiferroic material, Eu^{3+} is chosen and the (1-*x*)$BiFeO_3$-*x*$EuFeO_3$ solid solution is studied in **Chapter 7**. Eu^{3+} has 6 unpaired electrons, one more than Dy^{3+} (5 unpaired electrons) and it has the largest ionic radius (1.066 Å) compared with Dy^{3+} (1.027 Å), Lu^{3+} (0.977 Å), Yb^{3+} (0.985 Å), and Eu^{3+} (1.004 Å). In order to achieve the same magnitude of the structural distortion, a higher concentration of Eu^{3+} is required. An interesting magnetization behaviour is discovered by the substitution of Eu^{3+} for the Bi^{3+} ion, that with increasing concentrations of $EuFeO_3$, the antiferromagnetic property transforms to ferromagnetic property

Lastly, in **Chapter 8**, we perform a comparative analysis of these five solid solution systems that are formed by the substitutions with different rare-earth ions to reveal the trends in the phase symmetry, phase boundary and phase transformation of the different systems, and the variations of the ferromagnetic and ferroelectric properties with the different substituting RE elements. Also, a preliminary and on-going work is highlighted: the synchrotron spectroscopic studies that reveal some insights on the local structures, coordination number and bonding environments of the solid solutions, useful for understanding the microscopic origins of the structural changes and the enhanced multiferroic properties. Finally this project is concluded with suggestions for some future work.

Chapter 2.

Materials Characterization: Principles and Techniques

2.1 Introduction

This chapter introduces some basic principles and applications of various experimental techniques that are used to characterize the structure, electric and magnetic properties of materials synthesized in this thesis work. These characterization techniques include powder X-ray diffraction (XRD), electric impedance spectroscopy, superconducting quantum interference device magnetometry (SQUID), dielectric spectroscopy, and ferroelectric measurements.

2.2 Powder X-ray Diffraction (XRD)

X-rays are electromagnetic radiation with photon energy in the range of 0.1 keV to 100 keV. They are lying in the region between gamma and ultraviolet in the electromagnetic spectrum. X-rays in the range of 0.01 to 1.0 angstroms are used for diffraction applications. Due to X-rays' comparable wavelength to the size of atoms, they are ideally suited for characterizing the crystallographic structure, grain size, and preferred orientation in polycrystalline or single crystal solid samples. In this work, powder X-ray diffraction (XRD) is used to determine the crystal structure, phase symmetry and lattice parameters of the material studied.

2.2.1 Lab X-ray Source

X-ray diffractors consist of a X-ray source. Electrons are generated by a cathode ray tube and accelerated towards a metal target, usually copper or chromium. These incident electrons have sufficient energy to ionize some of the metal electrons. In the case of copper, upon the collision, the electrons have sufficient energy to dislodge 1*s* (K-shell) electrons (Figure 2.1). The vacancies in Cu 1*s* will be immediately occupied by electrons from an outer orbital (2*p* or 3*p*), resulting in energy release in the form of X-ray radiation during this transition.

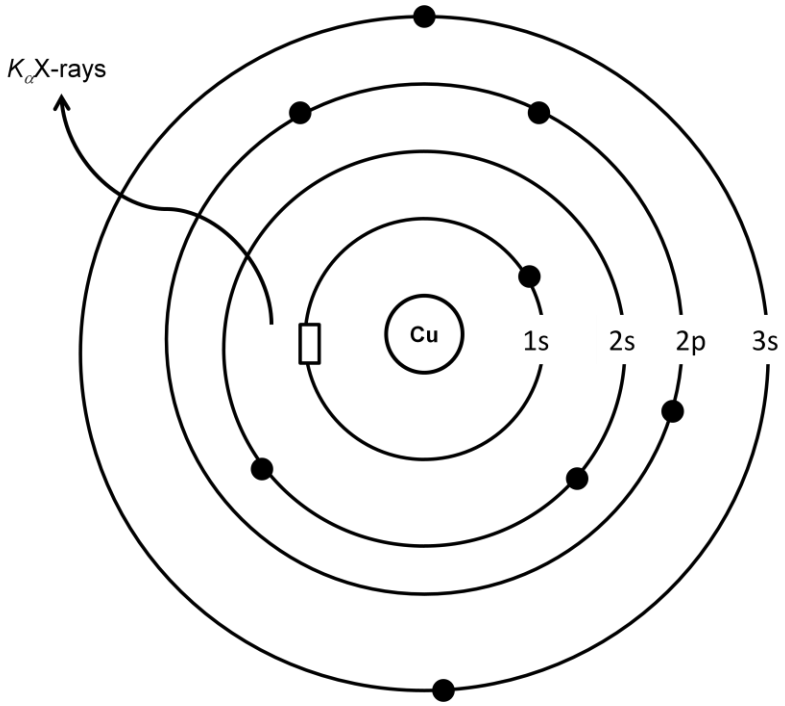

Figure 2.1 Generation of Cu K_α X-rays, arising from the 2*p* → 1*s* transition.

There are several components that a X-ray spectrum has, most commonly being K_α and K_β. For copper, the 2*p* → 1*s* transition produces $K_{\alpha1}$ and $K_{\alpha2}$ X-rays of wavelength 1.54051 Å and 1.54433 Å, respectively, corresponding to the two possible spin states of the 2*p* electron. $K_{\alpha1}$ has a slightly shorter wavelength and twice the intensity as $K_{\alpha2}$. The 3*p* → 1*s* transition produces K_β X-ray of wavelength 1.3922 Å. K_α X-ray is more favourable due to its wavelength comparable or slightly smaller than the atomic or ionic distances of the solid samples, and thus it is more common to be

used as the source of the powder x-ray diffraction. Nickel foil is used to filtered out the K_β X-rays, which allows the K_α X-ray beams to pass through to interact with the sample material [103]. $K_{\alpha1}$ and $K_{\alpha2}$ are sufficiently close in wavelegnth such that a weighted average of the two is commonly used. In this thesis, a copper source with K_α = 1.5418 Å was used for lab diffractometer experiments.

Two instruments that used for a lab diffractometer experiments in this work. Rigaku Rapid Axis (R-AXIS) is an X-ray diffractometer using IPs (imaging plate) and a triple axis goniometer, designed for rapid measurement of diffracted X-rays from crystal line samples. Burker D8 Advance diffractometer was also used for high-resolution powder diffraction, equipped with a Goebel mirror for a parallel X-ray beam. It speeds up data collection and provides additional information about the properties of crystalline samples, such as texture, residual stress, grain size and epitaxial relations.

2.2.2 Bragg's Law

X-ray diffraction is based on constructive interference of monochromatic X-rays with the lattice planes in a crystalline sample. Bragg's law describes the relationship between the spacing of atomic planes in crystals and the angles of incidence at which these planes produce the most intense reflections with the X-rays radiations and particle waves. Bragg's law is given in Equation 2.1:

$$2d_{hkl}sin\theta = \mathrm{n}\lambda \tag{2.1}$$

where d_{hkl} is the inter-planar spacing between crystal planes *hkl* (the *d*-spacing), *hkl* are Miller indices which are a notation system used to describe lattice planes, θ is the Bragg angle between the incident (or diffracted) ray and the associated crystal planes, *n* is an integer, referred to as the order of diffraction, and λ is the wavelength of the X-rays. Several solutions of Bragg's law are possbile with a given set of planes, however *n* is nomally set to unity 1 [6].

Suppose there are two beams diffracted from adjacent planes where an incident X-ray beam makes an angle θ with one of the planes as shown in Figure 2.2, the beam

can be reflected from both the upper and the lower planes. The beam reflected from the lower plane travels further than the beam reflected from the upper plane with a path difference of $2dsin\theta$ which is shown as ABC in Figure 2.2. This path difference must be an integer multiple of λ in order for the two beams to have constructive interference. Therefore, Bragg's law (Equation 2.1) must be obeyed in order for constructive interference to occur. For powdered samples, all possible diffraction directions of the lattice should be attained due to the random orientation of the crystal grain. Since each crystal has its unique set of *d*-spacings, the conversion of the diffraction peaks to *d*-spacings allows identification of the crystal. This can be achieved by comparison of *d*-spacings with standard reference X-ray patterns.

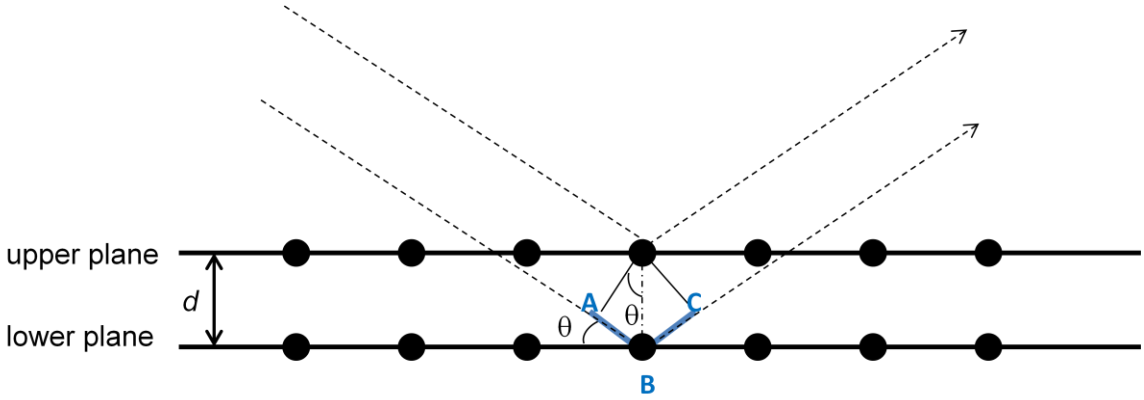

Figure 2.2 Schematic showing Bragg diffraction from a set of lattice planes with an interplanar spacing *d*.

2.2.3 Principles Used for Crystal Symmetry Determination

In principle, each crystal has its own crystal structure, giving rise to a unique X-ray diffraction pattern, like a fingerprint, that provides valuable information on the crystal structure. A crystal structure is composed of a motif, which is a unique arrangement of atoms/molecules. Motifs are located upon the points of a lattice, which is an array of points repeating periodically in three dimensions. The simplest repeating unit in a crystal is called a unit cell, from which the entire lattice can be built up by the repetition in three dimensions. The shape and position of the peaks resulting from the main diffraction are influenced by many factors, such as the size and shape of the unit cell and the position and identity of the atoms. However, the integrated intensity of the diffuse peaks is

unaffected by the size of the atom [6]. Therefore, X-ray diffraction is a useful tool to identify different phases, especially in the morphotropic phase boundary (MPB) region.

The structures of various crystals are classified by seven groups of crystal systems (i.e. cubic, tetragonal, orthorhombic, hexagonal, rhombohedral, monoclinic, and triclinic). The symmetry of each group is described by the relationship between the lattice parameters a, b, and c, and angles α, β, and γ, as denoted in Figure 2.3. The lattice parameters and the axes system for these crystal systems are listed in Table 2.1. The lattice parameters are closely related to phase symmetry and composition, which can be calculated by the Bragg's law from the XRD pattern.

Table 2.1 Unit cell geometries for the seven crystal systems.

Crystal System	Lattice Parameters	Angles
Cubic	$a = b = c$	$\alpha = \beta = \gamma = 90°$
Tetragonal	$a = b \neq c$	$\alpha = \beta = \gamma = 90°$
Orthorhombic	$a \neq b \neq c$	$\alpha = \beta = \gamma = 90°$
Hexagonal	$a = b \neq c$	$\alpha = \beta = 90°, \gamma = 120°$
Rhombohedral	$a = b = c$	$\alpha = \beta = \gamma \neq 90°$
Monoclinic	$a \neq b \neq c$	$\alpha = \gamma = 90°, \beta \neq 90°$
Triclinic	$a \neq b \neq c$	$\alpha \neq \beta \neq \gamma \neq 90°$

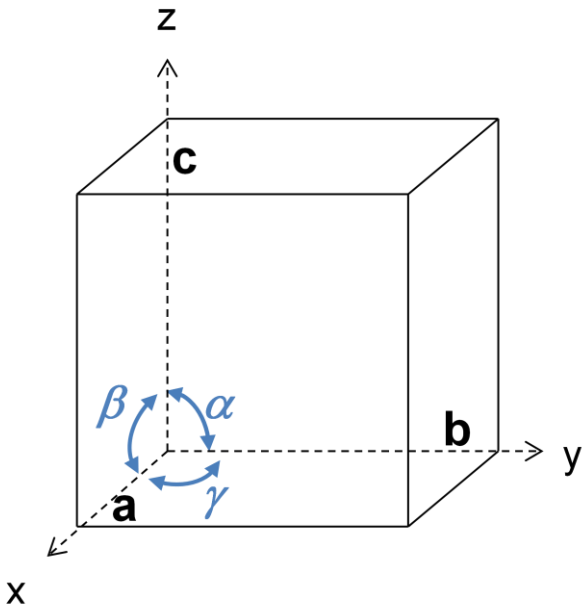

Figure 2.3 Illustration of a unit cell and the corresponding lattice parameters.

An X-ray powder pattern has two characteristics: the *d*-spacings and the intensity of the peaks. In orthogonal crystals ($\alpha = \beta = \gamma = 90°$), the Miller indices are related to the *d*-spacing of the unit cell by:

$$\frac{1}{d_{hkl}^2} = \frac{h^2}{a^2} + \frac{k^2}{b^2} + \frac{l^2}{c^2} \quad , \tag{2.2}$$

where *hkl* are the Miller indices. The *d*-spacings can be calculated from the 2θ value in the diffraction pattern using Bragg's law. Then the lattice parameter can be determined by using Equation 2.2. For a crystal with high symmetry, cubic or tetragonal, the *d*-spacing formulae can be simplified by using the relation of a = b = c or a = b, respectively. As for monoclinic and triclinic crystals, where their angles are not 90°, an additional component is needed to calculate the *d*-spacings [6].

The peak splitting pattern in XRD usually provides information about the crystal symmetry, the thickness of the crystalline layer, roughness, phase transitions, lattice mismatch, chemical composition, and phase purity of a material. It can be affected by the change of *d*-spacing. Figure 2.4 represents the characteristic splitting patterns for the

(111), (200), and (220) reflections for the cubic, tetragonal and rhombohedral symmetries. For a cubic phase, there is only one diffraction peak for all the {100} planes, because the *d*-spacings are all the same for (001), (00-1), (010), (0-10), (100), (-100) planes. On the other hand, a tetragonal phase has two diffraction peaks for the {100} planes since the lattice parameters a (equal to b) and c are different, yielding two *d*-spacings for the {100} planes. For a tetragonal crystal, a peak splitting will be seen in the {200} reflection since (200) = (020) ≠ (002).

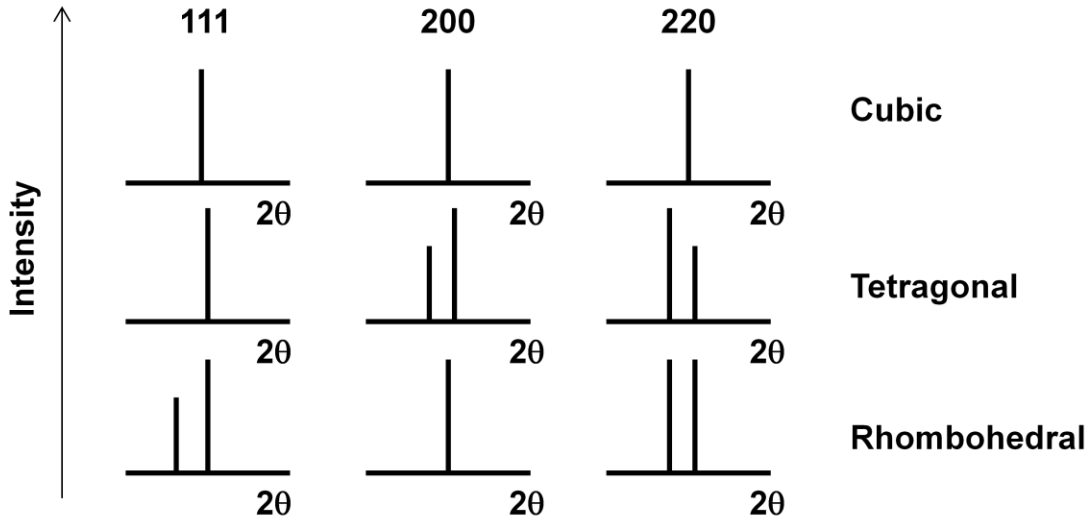

Figure 2.4 Characteristic splitting patterns for the (111), (200), and (220) reflections for the cubic, tetragonal and rhombohedral symmetries.

2.2.4 Rietveld Refinements

The Rietveld method is a technique for refining the crystal structure and lattice parameters of a material. A least-square approach is used to refine a theoretical XRD pattern until it matches the experimental XRD pattern. The crystal structure is then refined from the calculation of the theoretical pattern which includes the space group, lattice parameters, atomic positions, occupancies, atomic displacement parameters. It also can incorporate instrumental information in order to correct any background from the specific instrument used [111]. TOPAS-Academic software is used to refine the Rietveld refinement data in this work. Using this software, the lattice parameters, bond

lengths, bond angles, and atomic displacements of the materials synthesized can be obtained.

2.3 Dielectric Spectroscopy

Dielectric relaxation studies help explain the various mechanisms responsible for polarization. It reveals the time dependence of the frequency response of a group of dipoles when subjected to an external applied field. The dipoles responsible for the polarization do not always follow the oscillations of the electric field at certain frequencies when an alternating voltage is applied to a sample. The complex dielectric permittivity ε^* can be expressed as,

$$\varepsilon^*(\omega) = \varepsilon'(\omega) - i\varepsilon''(\omega) , \qquad (2.3)$$

where ω is the angular frequency, ε' is the real part of the permittivity, which is in phase with the applied field, ε'' is the imaginary part of the permittivity which is in quadrature with the applied field, and $i = \sqrt{-1}$ [113, 114]. The real part of the complex permittivity measures the amount of energy that can be stored in the material when an external electrical field is applied. The imaginary part of the complex permittivity is known as loss factor, which is a measure of the amount of energy lost from the material due to an external field. The loss tangent, $\tan\delta$, is usually used to represent the ratio of the imaginary part to the real part of the complex permittivity as shown below:

$$\tan\delta = \varepsilon''/\varepsilon' \quad . \qquad (2.4)$$

The loss tangent is also called by the terms such as dissipation factor or loss factor as illustrated in Figure 2.5 [114].

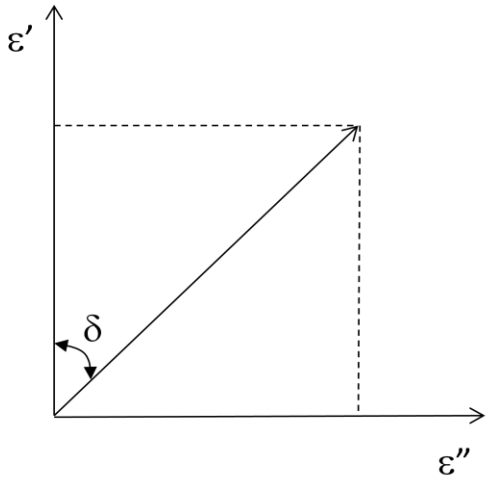

Figure 2.5 The dielectric loss tangent (tan δ) in terms of the real component and the imaginary component of the permittivity.

In this thesis work, Novocontrol Alpha high-resolution broadband dielectric analyzer with a Novotherm heating system was used to perform dielectric measurements. It directly measures the permittivity from impedance. The sample is coated with gold or silver electrodes to form a capacitor and then connected to the instrument through gold wires. The schematic of the circuit used in the dielectric permittivity measurements is shown in Figure 2.6 [115].

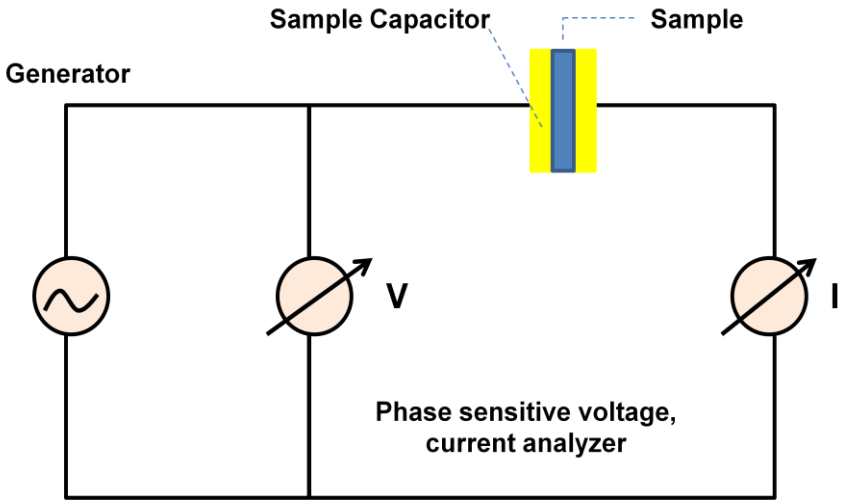

Figure 2.6 Schematic diagram of the circuit used in the dielectric permittivity measurements.

The signal generator applies a voltage (*V*) of a frequency $\omega/2\pi$ to the sample, and simultaneously generates a current (*I*) of the same frequency in the sample. There will be a phase shift of the current from the voltage by the phase angle φ. As shown in Figure 2.6, the complex voltage *V** and the complex current *I** is measured with a phase sensitive voltage-current analyzer. As a result, the impedance Z* of the sample can be calculated by the following equation:

$$Z^* = Z' + iZ'' = V^*/I^* \quad , \tag{2.5}$$

where Z' is the real impendance and Z'' is the imaginary impendance [107]. The impedance of a capacitor can be calculated with Equation 2.6,

$$Z_s^* = -(\frac{i}{\omega C_s}) \quad , \tag{2.6}$$

where C_s is the capacitance of the sampe [107]. Next, dividing the equation of the capacitance of the sampe C_s (Euqation 2.7) by the capacitance of the empty sample apacitor C_0(Equation 2.8) gives rise to the equation for calculating the real permittvity ε' (Equation 2.9).

$$C_s = \varepsilon_0 \varepsilon' \frac{A}{d} \quad , \tag{2.7}$$

$$C_0 = \varepsilon_0 \frac{A}{d} \quad , \tag{2.8}$$

$$\varepsilon' = C_s/C_0 \quad , \tag{2.9}$$

where ε_0 is the permittivity of free space (8.854 x 10^{-12} F/m), ε' is the complex permittivity of the sample, *A* is the area of the electrodes, and *d* is the distance between the electrodes. The magnitude of ε' depends on the degree of polarization of the material. For ferroelectric materials such as $BaTiO_3$, ε' = 10^3 to 10^4 [103].

2.4 Superconducting Quantum Interference Device (SQUID) Magnetometer

In this work, the SQUID magnetometer (MPMS XL, Quantum Design) is capable of measuring a magnetic flux. The magnetic flux produced in the SQUID by the sample is of the order of one-thousandth of a flux quantum, where the flux quantum is 2.07×10^{-7} G/cm^2. A superconducting magnet solenoid incorporated in the system can also generate a magnetic field of 7 Tesla. The SQUID in MPMS (Magnetic Property Measurement System) is the source of the instrument's significant sensitivity and capacity [116]. It does not directly detect the magnetic field from the sample. The sample space is located within a superconducting detection coil. The detection coil is a single piece of superconducting wire wound in a set of three coils configured as a second derivative gradiometer, as shown in Figure 2.7. The upper coil is a single turn wound clockwise, the centre coil comprises two turns wound anti-clockwise, and the bottom coil is again a single turn wound clockwise. In this configuration the detection coil is only sensitive to the magnetic stray fields of the sample, whereas the current induced in the detection coil by the small fluctuation of the magnetic field of the SQUID magnet, if there is any, is canceled out, leaving the current induced by the motion of the magnetic sample within the middle coil of which both turns are anticlockwise. Centred around the detection coil is the superconducting magnet capable of producing a uniform constant magnetic field over the entire coil region.

During the measurement, as the sample is moved vertically through the detection coil, the magnetic moment of the sample induces an electric current in the detection coils. Since the superconducting connecting wires, the superconducting detection coils, and the SQUID superconducting input coil form a closed superconducting loop, any change of magnetic flux in the detection coil produces a change in the persistent current in the detection circuit, which is proportional to the change in magnetic flux. Since the SQUID functions as a highly sensitive current-to-voltage converter, the variations in the current in the detection coil produce corresponding variations in the SQUID output voltage and these variations are proportional to the magnetic moment of the sample [117].

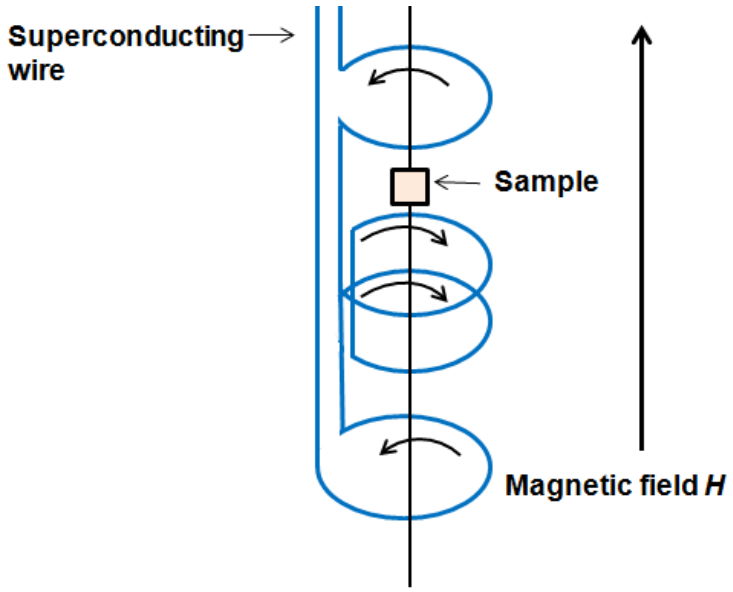

Figure 2.7 Schematic of second derivative gradiometer and sample movement in a SQUID magnetometer.

The sample needs to move upwards for each measurement, and this movement is called a scan. The SQUID picks up the output voltage of the centre of the scan as the SQUID response for the sample. The output peak corresponds to the sample position being in between the two turns of the middle coil that represents the SQUID response of the sample. Therefore, before the magnetic measurement, a procedure called centring is required, in which the sample position needs to be adjusted such that the centre of the scan is in between the two turns of the middle coil. Eventually, the output signal, *V*, is recorded as a function of scan length, in cm as shown in Figure 2.8. The MPMS software of a curve-fitting algorithm fits the measured *V*(cm) data points to the theoretical curve of an ideal dipole and thus extracts the magnetic moment [116].

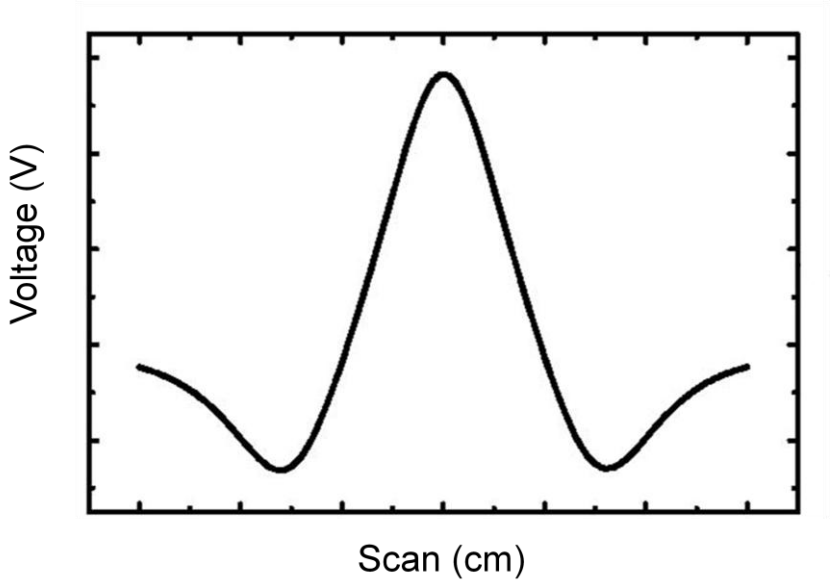

Figure 2.8 Illustration of the SQUID response.

The magnetic field in a SQUID magnetometer is generated by the circular current in the multifilament superconducting wire. Due to the superconducting state of these wires, It is easy to generate a large current which gives rise to a large magnetic field without cooling system, which is required for a conventional magnet due to the heat produced by the large current flowing through the wires with resistance [117, 118].

A MPMS XL SQUID magnetometer that was used in this work can measure a magnetic moment in the range from 10^{-8} to 2 emu (electromagnetic unit, 1 emu = 1.256637 x 10^{-5} Oe), with an operation temperature range from 2 K to 400 K. The operation temperature can be increased to 800 K by using a tube oven with 2 mm diameter inserted into the original sample chamber. Figure 2.9 shows an example of a typical configuration of the sample and the sample holder for high-temperature SQUID measurements, in which the sample is attached to the sample rod then inserted into the oven. The sample is attached to the sample rod by alumina cement which is diamagnetic. However, it is difficult to prepare a sample for the high temperature SQUID measurements due to the small space of the oven (2 mm in diameter). The use of oven will significantly increase the operation temperature, but it will also decrease the measurement sensitivity to a great extent. As a result, in order to obtain strong enough

signal, for samples with small magnetic moment, a high magnetic field is usually needed for high temperature SQUID measurements [117, 118].

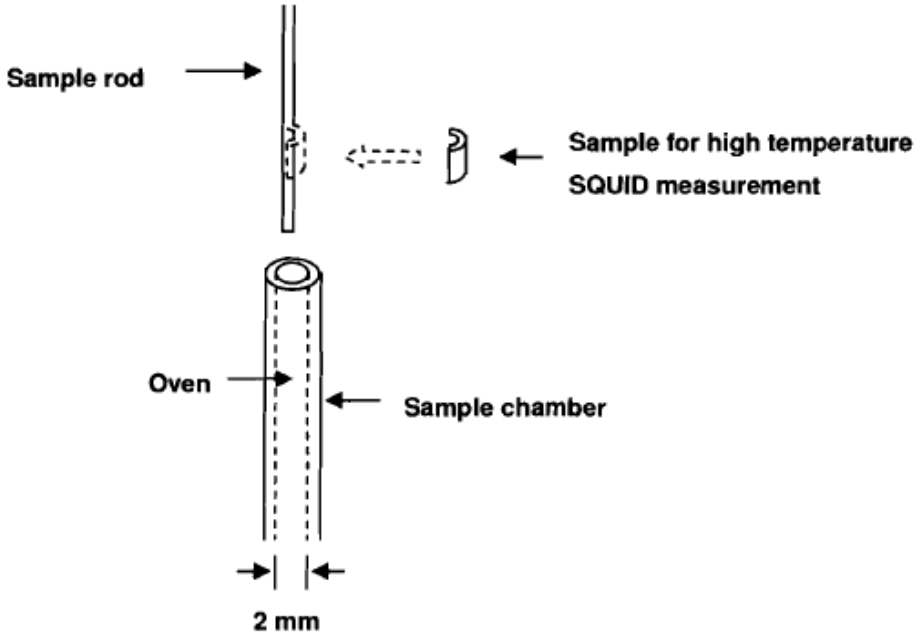

Figure 2.9 Sample for high temperature SQUID measurement by using an oven.

Note. Reprinted from W.-M. Zhu, Synthesis, structural, and properties of perovskite materials for multiferroism and piezoelectricity (Doctoral dissertation). Retrieved from SFU library thesis database, with the permission of W.-M. Zhu [118].

2.5 Ferroelectric Hysteresis Measurements

The ferroelectric properties of the materials prepared in this work are characterized using a RT66A Standard Ferroelectric Testing System (Radiant Technologies), which measures polarization as a function of electric field by using a modified Sawyer-Tower circuit, as shown in Figure 2.10 [119]. In this circuit, an alternating voltage (V) is applied by a signal generator across a pair of electrodes on the surfaces of a sample capacitor (C_s) [119]. A resistor-capacitor circuit is connected in series with the sample, which compensates for the phase shift that is caused by conductivity or dielectric loss in the sample [120]. The sample and reference capacitors (C_r) are connected in series so that the voltage (V_r) across the reference capacitor is

proportional to the polarization of the sample [119]. The charge developed on the surface of the sample, $\mathrm{Q_{sample}}$ can be calculated by the following equation:

$$\mathrm{C_r V_r = Q_r = Q_{sample}} \quad . \tag{2.11}$$

From the charge (Q) on the surface of the sample, the polarization (P) can be determined using the following equation:

$$P = \frac{Q}{A} \quad , \tag{2.12}$$

where A is the area of the electrodes. The applied electric field E is calculated from the sample thickness d, and the voltage across the sample V, as shown in the following equation:

$$E = \frac{V}{d} \quad . \tag{2.13}$$

The ferroelectric hysteresis loop of the sample, as shown in Figure 1.2 in Chapter 1, is then displayed by plotting the field on the *x*-axis and the polarization on the *y*-axis.

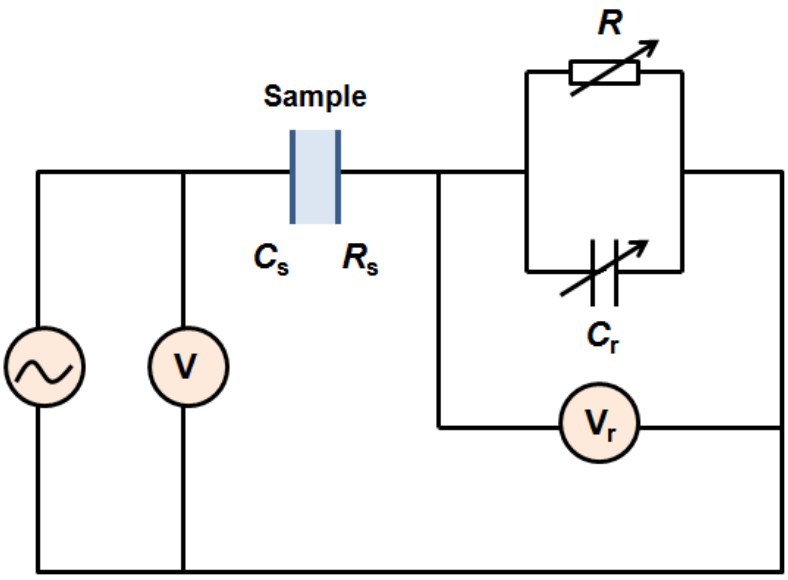

Figure 2.10 Schematic of the modified Sawyer-Tower circuit for the measurement of the ferroelectric hysteresis loop.

2.6 X-ray Absorption Spectroscopy (XAS)

X-ray Absorption Spectroscopy (XAS) is a widely-used technique for determining the local geometric and electronic structure of matter (i.e. solid, liquid or gas). This technique provides information on interatomic distances, oxidation states, and the nature and number of neighbours surrounding the absorbing atom. The strong sensitivity to the neighbours makes XAS the tool of choice, in particular, for coordination chemistry, catalysis, and other nanostructures. Generally, there are two possible types of analyses in XAS: EXAFS (Extended X-ray Absorption Fine Structure) and XANES (X-ray Absorption Near Edge Structure) [121]. In this section, the principle of X-ray absorption, the theory of XANES, as well as its analysis which has been used in this work, will be introduced, followed by a brief introduction of the synchrotron XAS experimental setup.

2.6.1 The Principle of X-ray Absorption

X-rays are electromagnetic radiation with photon energies that range from 0.1 keV to 100 keV. Three types of interactions can be identified when X-rays interact with matter: scattering, elastic and inelastic, and the photoelectric effects. XAS depends on the photoelectric effect in which absorption of a photon leads to the ejection of an electron from a bound level (K, L, M, etc, shells) of the absorbing atom, followed by the emission of a photoelectron. XAS measures X-ray absorption by core-level electrons in atoms of the material being examined. The level that an electron is promoted to is determined by the energy of the incoming photon, $h\nu$, and the binding energy of the electron E_b. The final energy of the ejected photoelectron E_f is given by the following equation:

$$E_f = h\nu - E_b \tag{2.14}$$

The absorbed electron can then be promoted to unoccupied or continuum states by several mechanisms, resulting in fluorescence X-rays, Auger electrons emission, or secondary electrons, as shown in Figure 2.11 [121,122].

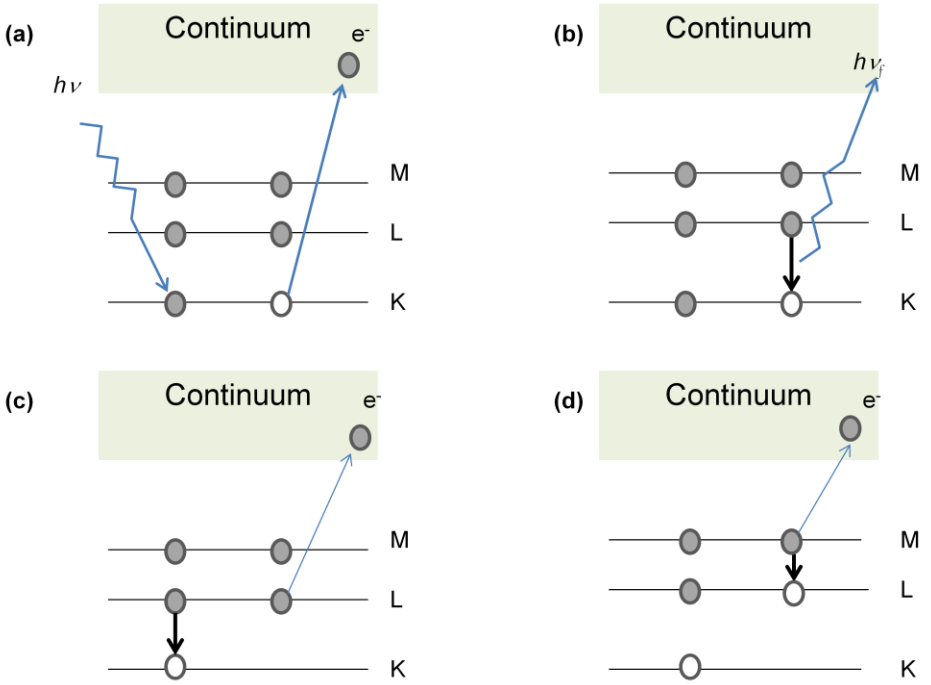

Figure 2.11 Schematic representation of (a) X-ray photoionisation and subsequent ejection of a photoelectron, and the (b) fluorescence, (c) Auger electrons emission, or (d) secondary electrons emission relaxation process of an excited atom.

As a consequence of the absorption, the amount of X-rays transmitted through a material will be decreased, and such decrease can be measured by the intensity of the X-rays transmitted (I_t) relative to their initial intensity (I_0), as described by the Beer-Lambert law. The degree to which a material absorbs X-rays is called the absorption coefficient , $\mu(E)$, and it can be described using the equation:

$$\mu(E) = \log\left(\frac{I_0}{I_t}\right) \quad . \tag{2.15}$$

In addition, the absorption coefficient can also be derived from the X-ray fluorescence following the generation of a core-hole by the excitation of a core electron, as shown in Figure 2.11 (b). This core-hole is then filled by another electron in the atom and an X-ray is released by the decay of the excited state with energy characteristic of

the initially excited core-electron. The following equation describes the relationship between the absorption coefficient and the fluorescence intensity, I_f:

$$\mu(E) \propto (I_f / I_0) \quad . \tag{2.16}$$

The X-ray absorption coefficient depends on the atomic number, atomic mass, and the incident X-ray energy, regardless of the local environment [123]. As the energy of the photon increases, $\mu(E)$ generally decreases until it reaches a certain critical energy called the absorption edge [123]; such energy coincides with the binding energy of the core-electron being excited. Each element has its own unique electron binding energy and absorption edges. Therefore, XAS is especially useful for studying the geometric and electronic structure of the ceramics since it is an element-specific technique as the X-rays can be tuned to the different energies required for promoting core-electrons within different elements [121,122]. In additon, the energies of the absorbed radiation at these edges correspond to the binding energies of the electrons in the specific shells (K, L, M, etc.) of the absorbing elements. They are named according to the principle quantum number of the electron that is excited: K for n = 1, L for n = 2, M for n = 3, etc. The absorption edges are labelled in the order of increasing energy, K, L_I, L_{II}, L_{III}, M_I, etc, corresponding to the excitation of an electron from the 1s ($^1S_{1/2}$), 2s ($^2S_{1/2}$), 2p ($^2P_{1/2}$), 2P ($^2P_{3/2}$), 3S ($^2S_{1/2}$) orbitals, respectively [121], as shown in Figure 2.12.

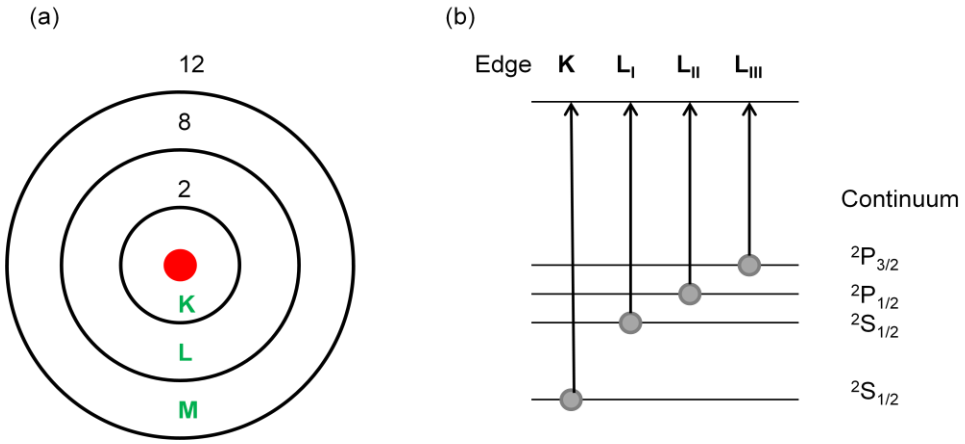

Figure 2.12 Schematic of (a) the Bohr atomic model, (b) the absorption edges with the corresponding continuum.

The main purpose of XAS is to measure the effective absorption coefficient, $\mu(E)$ of the element being studied as a function of the X-ray energy. The absorption behaviour of the element would vary depending on its interaction with the local environment. Therefore, $\mu(E)$ is measured near and above the absorption edge of the element that is being studied, giving rise to a spectrum similar as shown in Figure 2.13. The absorption spectrum can be divided into two main regions: the X-ray absorption near edge structure (XANES), and the extended X-ray absorption fine structure (EXAFS). These two regions provide specific information relative to the absorbing atom.

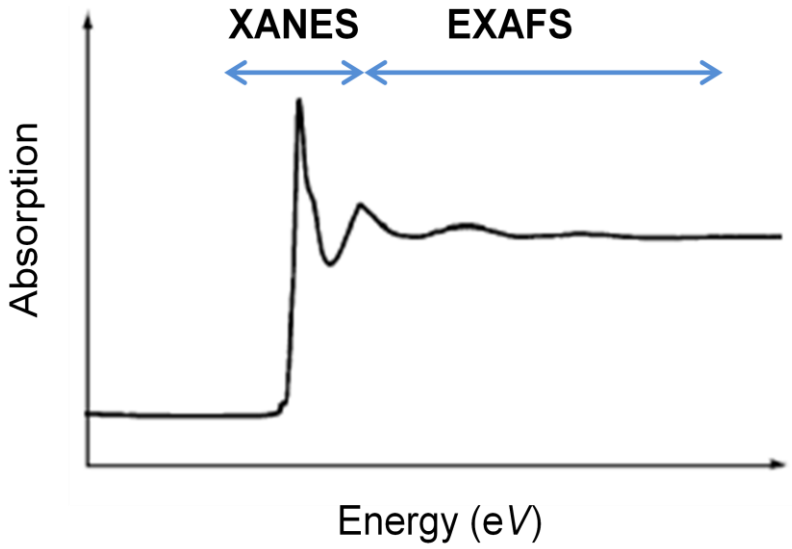

Figure 2.13 Schematic illustration of an X-ray absorption spectrum, showing the structured absorption that is seen both within ca. 50 eV of the edge (XANES) and for several hundred to greater than 1,000 eV above the edge (EXAFS).

2.6.2 X-ray Absorption Near-Edge Structure (XANES)

The XANES region of an XAS spectrum ranges from ± 30 eV from the absorption edge with the energy of the incident X-ray beam $E = E_0 \pm 10$ eV, where E_0 is the ionisation energy (or threshold energy). It consists of three parts: the pre-edge, absorption edge, and post-edge as shown in Figure 2.14. The absorption edge is the most intense region of a XANES spectrum, which is characterized by transitions of the photoelectrons from occupied to unoccupied energy level. However, the electronic

transition can also occur at energies lower than the absorption edge. This can be from an excitation of an electron (1s) of the absorbing atom from the core level to higher vacant orbitals. Orbital hybridization induced by coordinating species can also cause a signal in the pre-edge region [122]. This pre-edge region often provides information about the local electronic structure at short distances (< 3 Å) from the excited atom.

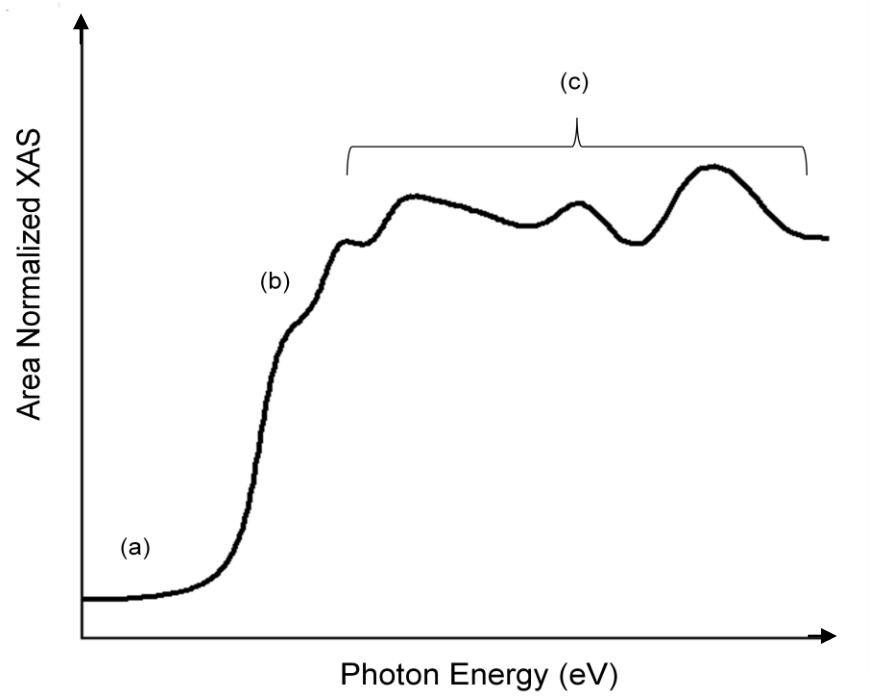

Figure 2.14 Illustration of a XANES spectra showing the (a) pre-edge, (b) absorption edge, and (c) multiple scattering features.

The absorption region is known as the most identifiable and quantifiable feature of XANES, which is the initial intense decrease of transmitted X-rays as a result of their absorption by the element being studied [123]. This region gives information on the coordination number, the electronic configuration, and the oxidation state of the absorbing atom [121-124]. The reason is absorption edge correlates to element-specific and edge-specific electronic transitions, which are sensitive to the atom's effective nuclear charge, Z_{eff} [125]. The oxidation state and ligand interaction can change the Z_{eff} of an atom so that these properties can be characterized using the XANES absorption edge [122]. The K-edge XANES absorption peak position is useful to determine the

oxidation states of various metals [126, 127] since the energy required to promote K-edge transitions is higher in an oxidized metal due to its larger Z_{eff} than in a non-oxidized metal. For example, for the K edge of a first-row transition metal, the 1*s* → 3*d* transitions are often observed for metals that have an open 3*d* shell. Although the 1*s* → 3*d* transition is forbidden by dipole selection rules, it is observed due to 3*d* + 4*p* mixing and the direct quadrupolar coupling [128]. As a result, the intensity of the 1*s* → 3*d* transitions can be used as a probe of geometry. With increasing intensity, the site is progressively distorted from a centrosymmetric environment (i.e. octahedral → square pyramidal → tetrahedral) [129]. Also, it can distinguish between square – planar and tetrahedral sites [130]. For second-row transition metals, the 1*s* → 4*d* transitions are not observed, but by measuring data at the L_{III} and L_{II} edges (2*p* → 4*d* transitions), it is still possible to obtain information about the empty bond states [131]. Similarly, the peak shift can be observed in metal L_{III}-edge XANES spectra, but it is normally related the intensity of the L_{III}-absorption edge to oxidate states, as there is a more direct correlation of its intensity to empty d-orbitals [119,132]. The low energy of L_{III} and L_{II} edges allows 2*p* → 4*d* transitions and results in sharp transitions with narrow lines. Moreover, for excitations into the 3*d* (or 4*d*) shells, the 1*s* → 4*p* transitions are allowed and observed for first-row transition metals. It is found that the 1*s* → 4*p* transition is intense for square-planar complexes (i.e. Cu^{II} and Ni^{II} complexes), but weak for tetrahedral complexes [119]. The reason may be due to the decrease in mixing between the empty 4*p* orbital ($4p_Z$) and the ligand orbitals for square-planar complexes. Moreover, both K-edge and L_{III}-edge of XANES can be influenced by the chemical species attached to the absorbing atom. For example, the metal-ligand systems that contain electronegative atoms, such as S and Cl, will have a greater metal-ligand covalency and often have a smaller Z_{eff}. Thus, a shift in metal K-edge absorption edge position to lower energies is observed [122]. The intensity of the L_{III}-edge will also be changed with the chemical species attached to the absorbing atom since its intensity relates to empty d-orbitals [126, 127]. For example, a more intense L_{III}-absorption edge is often observed in thiolates-attached metal-ligand systems, since thiolates remove electron density from metal d-orbitals, resulting in more electron transitions to the empty d-orbitals [126].

Lastly, the post-edge region of XANES is caused by the scattering of photoelectrons between multiple neighbours, known as multiple scattering. The kinetic

energies of the absorption-induced photoelectrons are low and their mean free paths are large in this energy region. Therefore, the emitted photoelectrons can scatter from multiple atoms and return to the original absorbing atom. These returning photoelectrons then create the spectral oscillations immediately following the absorption edge. Such multiple scattering oscillations can provide qualitative information regarding the structure around the absorbing atoms, including metal lattice type. However, it is difficult to have a comprehensive refinement for multiple scattering within nanomaterials [124]. Therefore, the absorption edge is still the most commonly characterized region of the XANES spectra.

2.6.3 Synchrotron XAS Experimental Setup

The measurement of an X-ray absorption spectrum involves measuring the intensities of incoming and transmitted beam. Various beamlines have different experimental setups, in general, X-ray absorption is measured either by transmission or directly by fluorescence or electron yield, as shown schematically in Figure 2.15 [122].

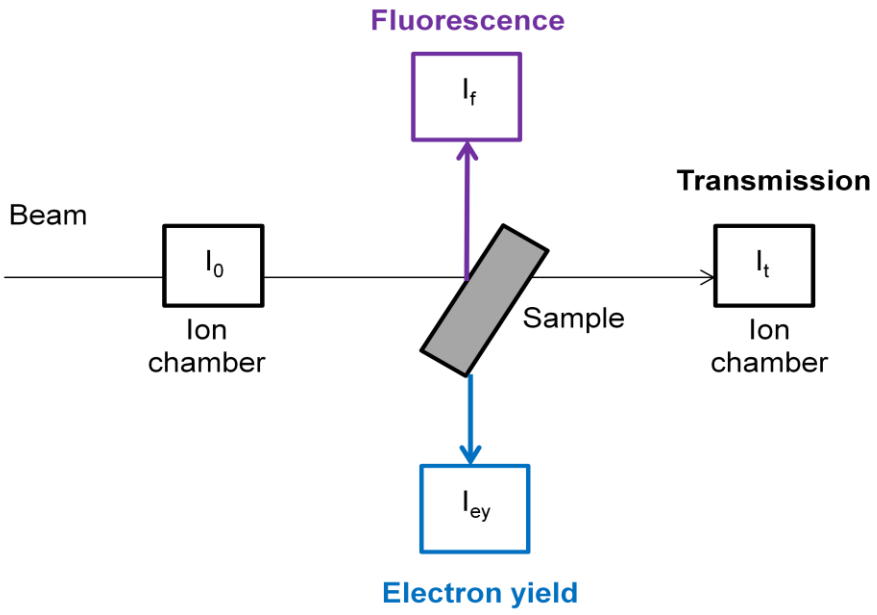

Figure 2.15 Schematic illustrating the various modes of XAS measurements.

In transmission mode, the measurements of the incoming intensity (I_0) and transmitted intensity (I_t) are achieved by using an ionization chamber in front of, and behind, the sample, which are used to directly calculate $\mu(E)$ according to Equation 2.15. This method is often limited to concentrated samples ($>$ ca.10 mM or 500 ppm) [122, 124]. In fluorescence mode, the intensity of the fluorescene X-rays (I_f) is usually detected by a Si or Ge solid-state detector [122, 124]. I_0 and I_f are then used to calculate $\mu(E)$ according to Equation 2.16. This mode is normally used in cases where the sample concentration is high, so that the self-absorption effects can reduce fluorescene and thereby $\mu(E)$ [122, 124]. In electron yield mode, either a liquid or powdered sample is placed onto the sample holder. This mode measures the number of electrons that are lost to the continuum as a result of the absorption process [122, 124]. Both the sample and the sample holder must be sufficiently conductive for meauring the emitted electrons. In addition, the relatviely short mean free path of the electrons causes this to be more surface sensitvie and it does not experience the same self-absorption effect as the fluorescence mode [124, 132].

In this work, the Fe *K*-edge synchrotron X-ray absorption near edge structure (XANES) was obtained in transmission mode at the 01C1 beamline of the National Synchrotron Radiation Research Center (NSRRC) in Taiwan, as illustrated in Figure 2.16. This beamline is a high-resolution X-ray beamline with both collimating and focusing mirrors, which will deliver monochromatic photon beams with energy ranging from 6 keV to 33 keV for XANES, EXAFS, powder diffraction and the related experiments. At the sample position, the expected photon flux is 1 x 10^{11} photon/sec/200 mA with an average energy resolution (ΔE/E) of 1.6 x 10^{-4} and the focused beam size is ~ 0.9 mm x 0.2 mm [133].

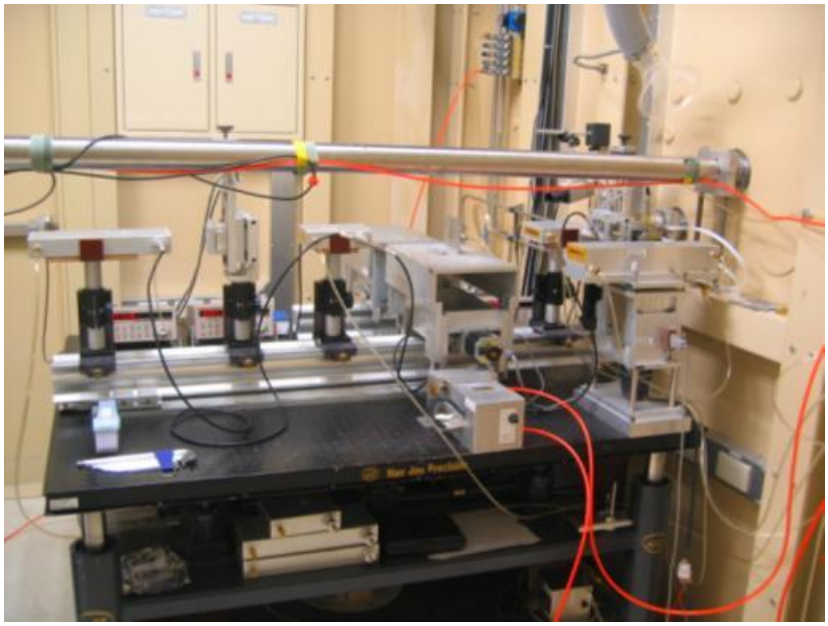

Figure 2.16 Schematic illustrating of beamline 01C1 experimental station.

Note. Reprinted from National Synchrotron Radiation Research Center, Retrieved from http://www.nsrrc.org.tw/english/index.aspx, with the permission of Dr. Chi-Shun Tu [122,133].

Chapter 3.

Synthesis, Structure, and Characterization of the (1-*x*)$BiFeO_3$-*x*$DyFeO_3$ Solid Solution

3.1 Abstract

The Dy-doped BFO ceramics were prepared by solid state reactions. The crystal structure and multiferroic properties of the samples were systematically investigated. The structure of (1−*x*)$BiFeO_3$-*x*$DyFeO_3$ (denoted as BDF-*x*) solid solution was studied by high-temperature X-ray diffraction, in order to understand the effects of the rare-earth ion Dy^{3+} doping on the multiferroic properties of $BiFeO_3$. A morphotropic phase boundary between the rhombohedral perovskite *R*3c phase and the orthorhombic orthoferrite *Pbnm* phase was identified by XRD. For $x < 0.08$, the solid solution is rhombohedral perovskite *R*3*c* phase at room temperature. If the temperature is increased, this solid solution undergoes a first-order phase transition from the rhombohedral to the orthorhombic structure. In the composition range of morphotropic phase boundary, a mixture of two phases was observed and the percentage of each phase was analyzed. The ferroelectric and magnetic properties were improved by Dy^{3+} doping on the *A*-site (Bi site). To further improve the physical properties of BFO, the (Dy-Ti)-co-doped BFO ceramics, (1-*x*)$BiFe_{(1-y)}Ti_{(y)}O_{(3+y/2)}$-*x*$DyFeO_3$ (denoted BDFT-*x*-*y*), were synthesized by solid state reactions, and their structural and multiferroic properties were systematically studied. The chemical substitution of Ti^{4+} for Fe^{3+} on the *B* site led to a large remnant polarization of 23 $\mu C/cm^2$ at room temperature in $Bi_{0.9}Dy_{0.1}Fe_{0.98}Ti_{0.02}O_{3.01}$ solid solution. A high saturated magnetization of 0.8 μ_B/f.u. at 2 K was observed in $Bi_{0.82}Dy_{0.18}Fe_{0.98}Ti_{0.02}O_{3.01}$ solid solution. The coexistence of the ferroelectric and ferromagnetic orders makes these solid solutions truly multiferroic multiferroic materials.

3.2 Introduction

Multiferroic materials can be defined as materials that have different ferroic properties such as ferromagnetism, ferroelectricity, ferroelasticity, and ferrotorodicity coexisting in the same phase. There is a great potential for magnetoelectric applications of multiferroic materials since they simultaneously exhibit ferromagnetism and ferroelectricity [23]. The coupling between ferroelectric and ferromagnetic order parameters allows the switching of the ferroelectric state by a magnetic field and vice versa. However, it is very difficult to obtain both high ferroelectricity and strong ferromagnetism in multiferroic materials since they are mutually exclusive and their magnetoelectric couplings often occur at very low temperatures [85]. Recently, some researches have been focusing on coupling ferroelectric and ferromagnetic properties within a single phase material especially for spintronics applications [132]. Among these multiferroic materials, bismuth ferrite, $BiFeO_3$ (BFO) belongs to the ABO_3 perovskite structure. It has a rhombohedrally distorted perovskite structure with a space group of *R3c,* whose ions are displaced along the [111] direction relative to the ideal centro-symmetric position. The presence of $6s^2$ lone pair electrons on Bi^{3+} ions makes $BiFeO_3$ ferroelectric, whereas the occupancy of unpaired *d* orbital electrons makes it (anti)ferromagnetic [36]. With a three-fold axis along the [111] direction, Bi^{3+} and Fe^{3+} cations are displaced from their symmetric position. Hence a spontaneous polarization is generated by this symmetry along [111] [36]. Spins are aligned along [111] with slightly canted moments from this direction, which results in a weak ferromagnetic moment [85]. However, there are not many reports on the electrical properties of pure BFO [34]. BFO is a G-type antiferromagnet below its Néel temperature (T_N ~ 643 K), which is superimposed by a spiral spin structure with an incommensurate long-wave period of 62 nm in the lattice [84], and a ferroelectric below its Curie temperature (T_C ~ 1103 K) [68]. At room temperature, BFO single crystal has a rhombohedral *R*3*c* structure with a lattice parameter of a_r = 3.96 Å and α_r = 89.4° [72]. Despite those favorable properties of BFO, there are also some major obstacles associated with this compound, such as formations of impurity phases, weak magnetic properties, weak magnetoelectric coupling, and large leakage current density [34, 73, 90, 91, 92, 97, 99, 100], which make pure BFO unfavourable for multiferroic applications.

The electrical and magnetic properties of BFO can be improved by substituting the *A* ion with different rare earth or alkaline earth metal ions, such as the *A* site substitutions of Bi^{3+} by Sm^{3+}, Gd^{3+}, Ca^{2+}, etc. [19, 23, 24, 35, 96, 103, 104], or the *B* site of Fe^{3+} ion by transition metals of Cr^{3+}, Co^{3+}, Mn^{3+}, etc [108-110]. In the previous research of multiferroic compounds $Bi_{0.9}Sm_{0.1}FeO_3$, $Bi_{0.9}Gd_{0.1}FeO_3$, $Bi_{0.9}Ca_{0.1}FeO_3$, $Bi_{0.9}Sm_{0.05}Ca_{0.05}FeO_3$, and $Bi_{0.9}Gd_{0.05}Ca_{0.05}FeO_3$, all XRD patterns indicated the formation of the rhombohedral perovskite BFO structure with a minor impurity phases (about 3% of $Bi_2F_4O_9$) along with the major BFO phase. This phase was reported to form during the synthesis of BFO [135 - 137], and cannot be removed even by longer calcination time which could also lead to more volatilization of Bi_2O_3 [138]. The magnetic hysteresis loops of these compounds at room temperature indicated weak ferromagnetism with no saturation magnetization. The deduced values of the remnant magnetization M_r and coercivity H_c showed similar variation with the ratio of hexagonal *c*/*a*, which revealed that the lattice distortion also had a major effect on the appearance of weak ferromagnetism in these compounds [138]. However, the enhanced values of M_r and H_c for the Gd-containing compounds can be explained by the partial suppression of the spiral spin structure due to the lattice distortion and the stronger interaction between magnetic ions. In addition, there was no significant and systematic difference in magnetic transition temperature T_N for different ionic substitutions and the transition temperatures were found to be in the range of 300-310°C, which was lower than the T_N of BFO (370°C) [138]. Therefore, the solid solutions between BFO and lanthanide ferrites are expected to exhibit interesting and promising properties for magnetoelectric effects.

It was found in our previous work about the effect of chemical modification on the structure, dielectric and magnetic properties of BDF-*x* solid solution [23] that there was a structural change from the rhombohedral perovskite into the orthorhombic orthoferrite structure at the morphotropic phase boundary at $x \approx 0.1$. The ferroelectric and magnetic properties were improved by Dy^{3+} substitution on the *A* site. The BDF-*x* ceramics have some defects present in the lattice which are related to the electronic conduction and ionic conduction. These defects could come from the volatilization of Bi_2O_3 during the preparation process of material, which results in oxygen vacancies and bismuth vacancies. Moreover, Fe^{2+} would occupy the octahedral site in perovskite and the

presence of Fe^{2+} may lead to electron hopping conduction from Fe^{2+} to Fe^{3+} [23]. However, the concentration of oxygen vacancies can be reduced by the substitution of Ti^{4+} for Fe^{3+} on the *B* site because Ti^{4+} has a higher charge and it is about the same size as Fe^{3+}, which leads to a decreased conductivity than the undoped BDF-*x* ceramics. The 2% excessive Bi_2O_3 was introduced to the BDF-*x*-*y* solid solution, in which the excesses of Bi_2O_3 became a liquid phase during sintering and helped to increase the density of ceramics. The chemical substitution of 2% Ti^{4+} for Fe^{3+} on the *B* site resulted in a large saturated magnetization (0.5 μB/f.u.) in BDFT-0.08-0.02, which may arise from the disruption of the spiral spin modulation and the spin interactions between Dy^{3+} and Fe^{3+}. The aliovalent ionic substitution of Ti^{4+} for Fe^{3+} on the *B* site of the perovskite structure is proven to be able to improve the dielectric and ferroelectric properties of $BiFeO_3$-based solid solutions by reducing the concentration of oxygen vacancies and thereby decreasing the conductivity [73].The doping has resulted in the reduction of the leakage current density and the improvement in the ferroelectric properties of BFO to some extent. Therefore, in order to improve the dielectric and ferroelectric properties and to further explore the multiferroic and magnetoelectric properties of BFO-based solid solutions, the effects of chemical modification by means of aliovalent ionic substitution on the structure and properties of BDFT-*x* and the BDFT-*x*-*y* solid solutions will be investigated in this chapter.

3.3 Experimental

3.3.1 Synthesis

The ceramic samples of (1-*x*)$BiFeO_3$-*x*$DyFeO_3$ (denoted as BDF-*x*) solid solution were prepared by conventional solid state reaction method. The starting materials were Bi_2O_3 (99.975%), Fe_2O_3 (99%) and Dy_2O_3 (99.9%), and they were weighed accurately to four significant digits according to the stoichiometric chemical formula:

$$\frac{(1-x)}{2}\mathrm{Bi_2O_3} + \frac{x}{2}\mathrm{Dy_2O_3} + \frac{1}{2}\mathrm{Fe_2O_3} \rightarrow (1-x)\mathrm{BiFeO_3} - x\mathrm{DyFeO_3} \quad (3.1)$$

Each composition was mixed and grounded by ball milling for 24 h. Ball milling container was setup as 25.0 ml bottle with 15.0 ml of ethanol and 40 zirconium oxide balls. The mixed powders were pressed into 10 mm pellets, packed down in a platinum crucible and then calcined in furnace at 820 °C for 4 h. After the calcination, the sample disc was subsequently regrind thoroughly by ball milling for 24 h. The sample powders were then mixed with 0.15 ml of 5% polyvinyl alcohol (PVA) binder. Later, the powders were repressed into pellets with a diameter of 10 mm and then heated at 450 °C for 1 h to evaporate the PVA binder. After the elimination of the binder, the pellets were packed down into a platinum crucible and sealed in a lager Al_2O_3 crucible, and then subsequently sintered at 900 °C for 4 h. The calcination temperature and sintering temperature are increased up to 850 °C and 950 °C, respectively with correspondence of increased concentration of Dy. In addition, the ceramic samples of (1-*x*)$BiFe_{(1-y)}Ti_{(y)}O_{(3+y/2)}$-*x*$DyFeO_3$ (denoted as BDFT-*x*-*y*) with 2% excess of Bi_2O_3 (99.975%) were also prepared by using the same conventional solid-state reactions as the non-Bi_2O_3 excess BDFT-*x*-*y*.

3.3.2 Structural Analysis

X-ray diffractions of the as-sintered ceramics were performed on a Bruker D-8 diffractometer using Cu K_α radiation (40 mA, 40 kV, 0.01° steps and 2θ = 15 - 80°) to analyze the phase purity and to determine the crystal structure. $BiFeO_3$ single crystals were ground into a powder and XRD data were collected and used as a structural reference for $BiFeO_3$. The resulting patterns were analyzed using TOPAS-Academic Software by Rietveld refinements to determine the symmetry, lattice parameters, and atomic positions of the solid solutions.

3.3.3. Differential Scanning Calorimetry Measurement (DSC)

The differential scanning calorimetry (DSC) was carried out by using a Seiko DSC-6200 instrument with a heating rate of 10 °C/min under nitrogen atmosphere from -50 °C to 550 °C. It is used to determine the phase transitions of the solid solutions.

3.3.4 Dielectric, Ferroelectric and Magnetic Measurements

The as-sintered ceramics were polished with a series of silicon carbon sand papers down to 9 μm to achieve parallel and flat surfaces on the circular faces of the ceramics, with various thickness (1000 - 200 μm). The polished ceramics were sputtered with gold layers (Anatech Hummer Sputter-Coater 6.2, 12min., 15 mA plasma discharge current). The gold wires were attached to both surfaces of the samples. The dielectric properties (permittivity, ε', and loss tangent, tanδ) of the (1-*x*)$BiFeO_3$-*x*$DyFeO_3$ ceramics were measured as a function of temperature at various frequencies from 1 -100 kHz, using a Novocontrol Alpha high-resolution broadband dielectric analyzer. Ferroelectric hysteresis loops were measured by a RT66A ferroelectric testing system (Radian Technology), connected to a Trek 609E-6 high voltage bipolar amplifier. Magnetic measurements were performed using a Quantum Design MPMS-XL SQUID magnetometer.

3.4 Results and Discussion

3.4.1 Structural Analysis

The X-ray diffraction patterns of the BDF-*x* (*x* = 0.03 - 0.18) solid solutions are shown in Figure 3.1. The structure of BDF-*x* (*x* = 0.03 - 0.18) solid solutions was studied by high-temperature X-ray diffraction, which can be used to determine the phase transition temperatures and the structures of the BDF-*x* solid solution. For $x < 0.08$, the solid solution is of rhombohedral *R*3*c* phase. At the composition *x* around 0.10, with the increase of $DyFeO_3$ concentration, a structural change from rhombohedral (*R*3*c*) into a mixture of rhombohedral (*R*3*c*) and orthoferrite phase (*Pbnm*) was found, which indicates the presence of a morphotropic phase boundary. In the MPB region, a mixture of two phases was observed in the composition range of *x* = 0.08 - 0.12. The percentage of each phase was analyzed by Rietveld refinements. For *x* > 0.12, the solid solution is orthorhombic perovskite with *Pbnm* space group. $Bi_2Fe_4O_9$ impurity phase was observed in the compounds for $x < 0.1$, which may be due to the kinetics of the $BiFeO_3$ formation and the evaporation of Bi_2O_3 [73]. However, the impurity disappeared with increasing

amount of $DyFeO_3$, which indicates that $DyFeO_3$ can suppress the formation of the undesirable $Bi_2Fe_4O_9$ phase.

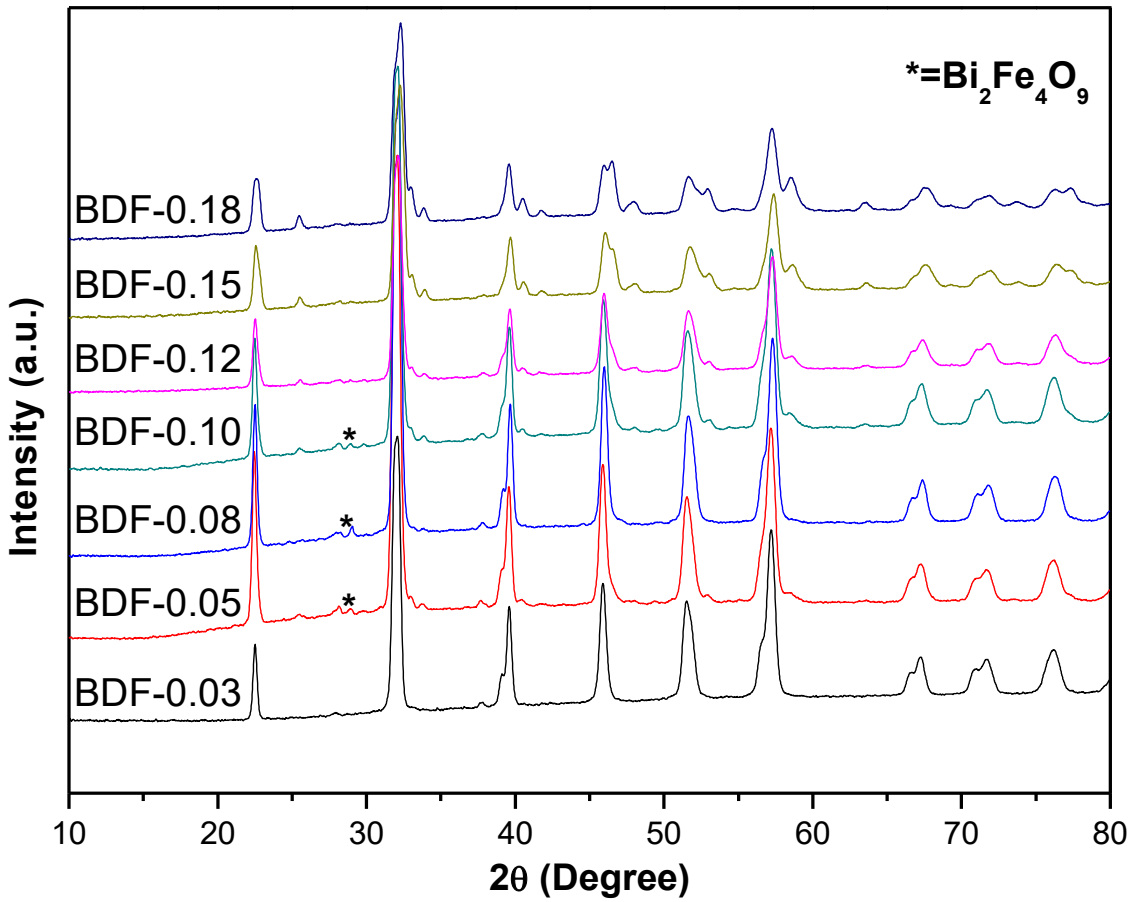

Figure 3.1 **X-ray diffraction patterns of the BDF-*x* (*x* = 0.03 - 0.18) ceramics prepared at optimal sintering temperatures. Stars indicate the peaks of the $Bi_2Fe_4O_9$ impurity phase.**

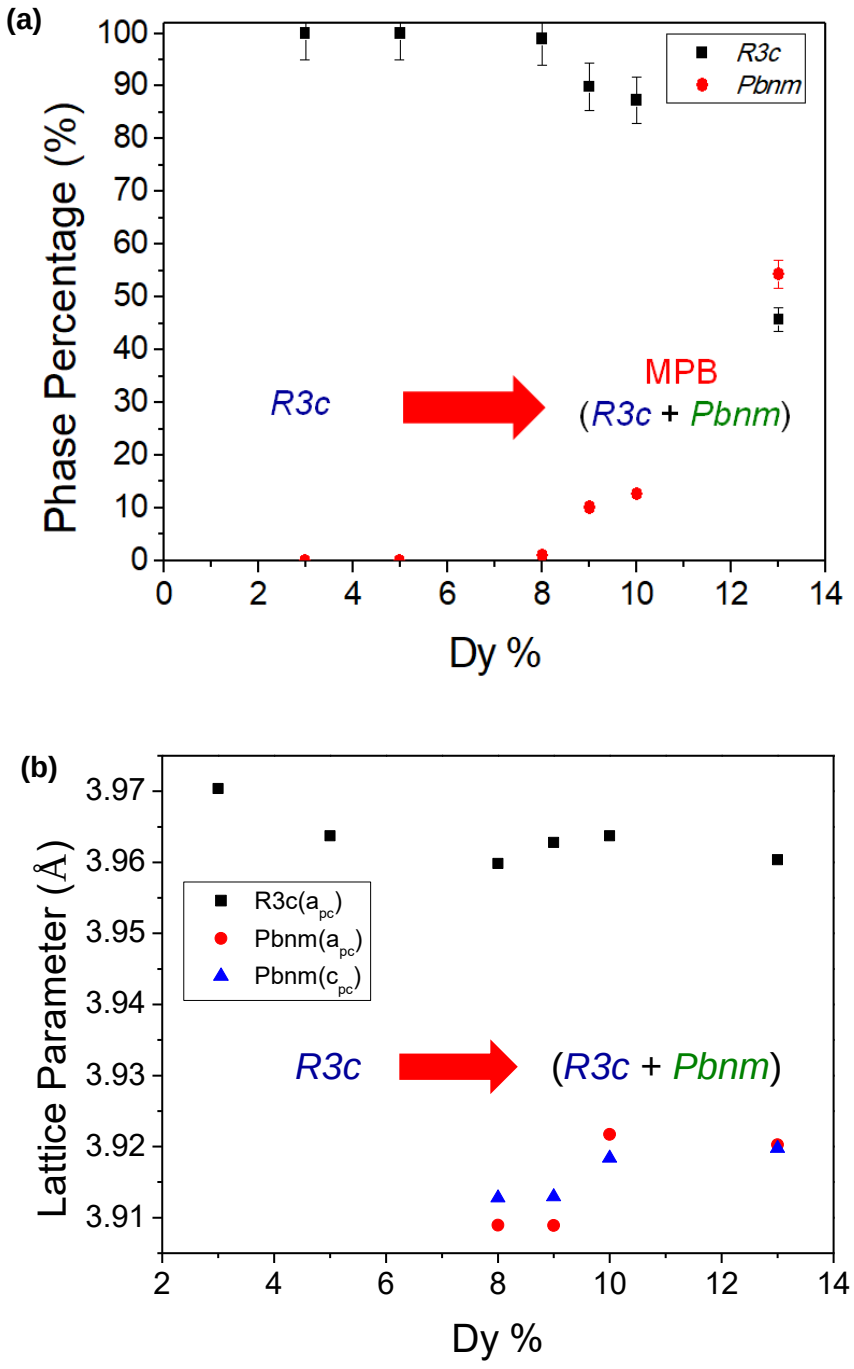

Figure 3.2 **(a) Rhombohedral (*R3c*) and orthorhombic (*Pbnm*) phase ratio as a function of composition for the BDF-*x* (*x* = 0.03 - 0.13) ceramics. (b) Variation of the lattice parameters of BDF-*x* (*x* = 0.03 - 0.13) ceramics as a function of composition in the pure rhombohedral (*R3c*) phase and MPB (rhombohedral *R3c* phase + orthorhombic *Pbnm* phase). The lattice parameters are described in a pseudocubic cell a_{pc} for the *R3c* phase, c_{pc} for the *Pbnm* phase.**

Figure 3.2 (a) shows the structure phase percentage for each composition of BDF-*x* (*x* = 0.03 - 0.13) solid solutions. The orthorhombic *Pbnm* phase increases with the increasing amount of Dy. The morphotropic phase boundary (MPB) is observed in the composition range of *x* = 0.08 - 0.15. Figure 3.2 (b) shows that the lattice parameter of the rhombohedral phase is decreased with increasing Dy content, which leads to the shrinkage of the unit cell due to the smaller ionic radius of Dy^{3+} (1.027 Å) compared with that of Bi^{3+} (1.17 Å). When *x* = 0.08, the pseudocubic cell parameter, a_{pc} for the *R*3*c* rhombohedral becomes smaller, indicating that the phase transition changes from the *R*3*c* rhombohedral phase to the *Pbnm* orthorhombic phase. In order to stabilize the perovskite structure, the BDF-*x* soild solution undergoes a transformation from the rhombohedral *R*3*c* to the orthorhombic *Pbnm* phase or to a bridging mixture of phases. This result is consistent with the XRD analysis. . Meanwhile, the lattice parameters of orthorhombic phase are increased gradually with the increasing amount of $DyFeO_3$.

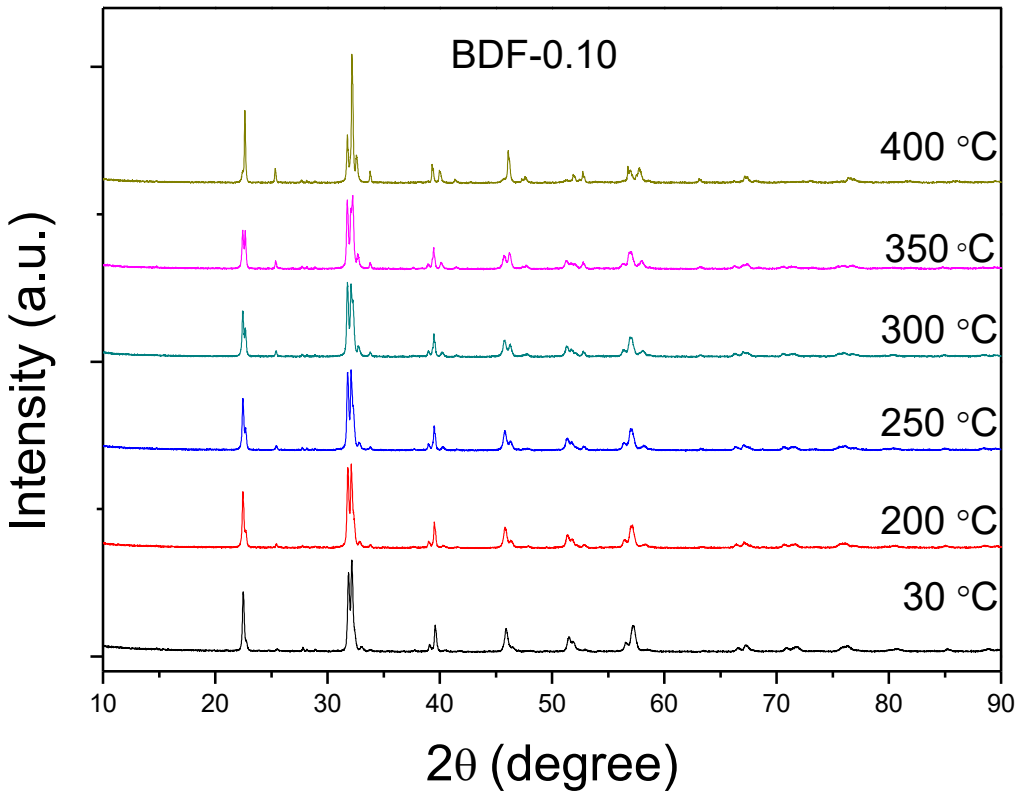

Figure 3.3 X-ray diffraction patterns of the BDF-0.10 ceramics measured at various temperatures.

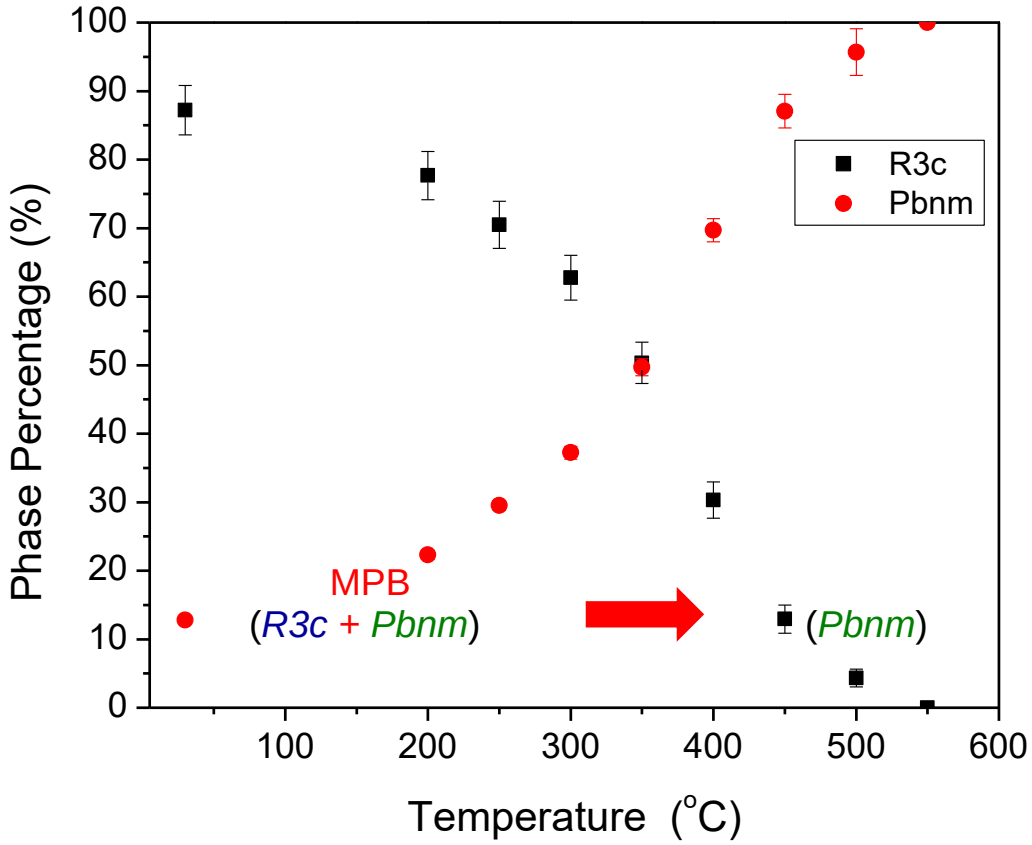

Figure 3.4 Phase percentage of BDF-0.10 ceramics measured at various temperatures.

Figure 3.3 and 3.4 show the XRD pattern and phase ratio of BDF-0.1, respectively, measured at different temperatures. The percentages of *R3c* and *Pbnm* are changed with increasing temperature. The structure of BDF-0.10 changes gradually from mixed phases of rhombohedral *R3c* and orthorhombic *Pbnm* to a single phase *Pbnm* with increasing temperature. The majority of the rhombohedral phase is converted to orthorhombic at around 350 °C. These results are consistent with the differential scanning calorimetry (DSC) measurements and the anomaly in the temperature-dependence of the dielectric constant, which will be discussed later in this chapter.

Table 3.1 Rietveld refinement results of the calculated lattice parameters and phase ratio for the BDF-0.10 ceramics at room temperature.

BDF-0.10 (RT)	a (Å)	b (Å)	c (Å)	a_{pc} (Å)	Angle (°)	Lattice Volume (Å^3)	Calculated polarization (μC/cm^2)
R3c (87.33%)	5.5647	5.5647	13.821	3.9531	α = 89.47	370.616	6.572
Pbnm (12.67%)	5.4219	5.6254	7.816	3.9065	γ = 87.89	238.397	N/A

The XRD patterns for the BDF-0.10 ceramics at different temperatures and different compositions were refined by Rietveld refinements. As an example, the room-temperature structural information for BDF-0.10 is shown in Table 3.1, with the values of the phase ratio, the lattice parameters, and the calculated spontaneous polarization.

The method of calculation of the spontaneous polarization was as follows:

The spontaneous polarization was calculated by using the *A*-site and *B*-site cation displacements in the rhombohedral unit cell. An example for such a calculation is

$$D_A \text{x } C_A \text{ x } N_A \text{ x } \frac{lattice\ parameter\ \text{c}}{Unit\ Cell\ Volume} = \text{polarization for } A \text{ site cation (along } c \text{ axis)}, \quad (3.2)$$

$$D_B \text{x } C_B \text{ x } N_B \text{ x } \frac{lattice\ parameter\ \text{c}}{Unit\ Cell\ Volume} = \text{polarization for } B \text{ site cation (along } c \text{ axis)}, \quad (3.3)$$

where D_A and D_B are A site and B site atom displacements, respectively, C_A and C_B is the ionic charges of A site and B site, respectively, N_A and N_B is numbers of atoms per unit cell for *A* site and *B* site cation, respectively. The total polarization is the sum of Equation (3.2) and Equation (3.3). The unit of total polarization is ($\frac{electrons\ charge}{Å^2}$). Electrons charge per Ångström square is converted to μC/cm^2. For example, to calculate the polarization of the BDF-0.10 (RT) solid solution, D_A = 0.4464 and D_B = 0.01648 are the ratio along *c* axis. C_A and C_B are both equal to 3. N_A and N_B are both equal to 6 in a perovskite unit cell. Lattice parameter c is equal to 13.821 Å and lattice volume equals to 370.616 Å^3. Plugging in all the numbers and convert the unit, the calculated polarization is 6.572 μC/cm^2.

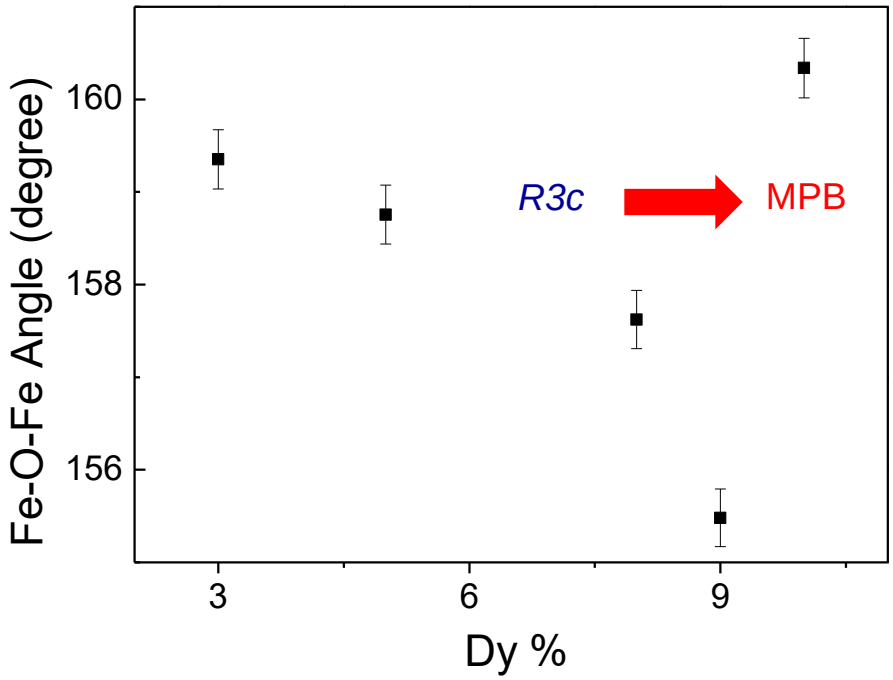

Figure 3.5 **The Fe^{3+}-O-Fe^{3+} superexchange angle of BDF-*x* (*x* = 0.03 - 0.10) ceramics with various Dy concentration.**

In order to study the origin of the magnetic interactions, the Fe^{3+}-O-Fe^{3+} superexchange angle was obtained from the atom positions. The superexchange angle for pure $BiFeO_3$ at room temperature was reported to be 153.5^o [88]. Figure 3.5 shows the Fe^{3+}-O-Fe^{3+} superexchange angle of BDF-*x* ceramics at various compositions. As a result, the Fe^{3+}-O-Fe^{3+} superexchange angle of the BDF-*x* solid solution decreases as the Dy concentration increases in the rhombohedral range. When the Dy concentration is increased to 10%, the solid solution enters the MPB range, showing a sudden increase of the Fe^{3+}-O-Fe^{3+} superexchange angle. The results of the XRD and Rietveld refinement revealed that the Dy-doping on the *A* site resulted in the structural distortions and corresponding changes in the Fe-O-Fe bond distances and bond angles [99], which is expected to enhance the magnetic and ferroelectric properties. Further discussion on the magnetic properties of BDF-*x*-*y* is given in Section 3.4.5 of this chapter.

3.4.2 Ferroelectric Properties

According to the conduction mechanism deduced in Ref. [139], one of the main sources for high electric conductivity in BFO was the concentration of oxygen vacancies. In order to decrease the electric conductivity in the BDF-*x* ceramics, *B*-site aliovalent ionic substitution of Ti^{4+} for Fe^{3+} was performed for all the BDF-*x* ($0.03 \leq x \leq 0.18$) compounds. Among these BDF-*x*-*y* ($0.03 \leq x \leq 0.18$, $y = 0.02$) compounds, the Ti^{4+}-doped ceramics with composition $x = 0.1$ showed a pure perovskite phase. This is attributed to the increase of perovskite tolerance factor by the substitution Ti^{4+} ion which has a smaller ionic radius than that of Fe^{3+}, leading to the stabilization of the perovskite phase. The substitution of Ti^{4+} for Fe^{3+}, however, requires a higher densification temperature for the ceramics, possibly due to the refractory character of TiO_2, which causes the decomposition of the solid solution. To decrease the sintering temperature, 2 wt% excess Bi_2O_3 was introduced as a sintering aid, which at the same time compensated for Bi_2O_3 evaporation. All of the ceramics of BDFT-*x*-*y* ($0.03 \leq x \leq 0.18$, $y = 0.02$) compositions sintered at 900 ~ 950 °C with excess of Bi_2O_3 exhibited a high relative density (> 93%) with a pure perovskite phase. This approach was proven to be effective in improving the dielectric and ferroelectric properties of the $BiFeO_3$-$PbTiO_3$ solid solution by reducing the conductivity [19, 139]. Moreover, the role of the substitution of Dy^{3+} on the Bi^{3+} site of the system could be better investigated.

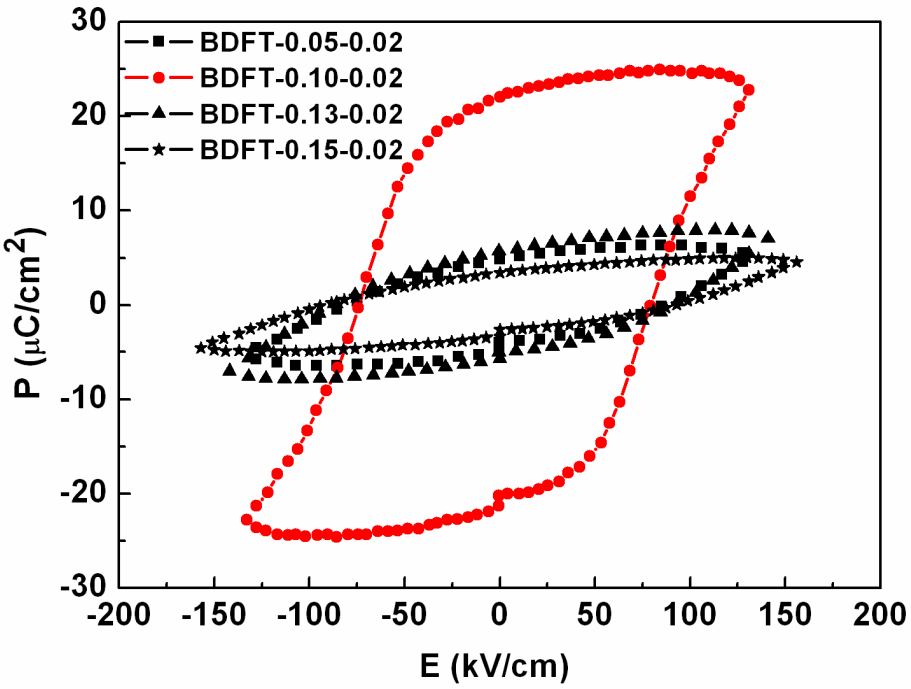

Figure 3.6 Dielectric hysteresis loops of the BDFT-*x*-*y* (*x* = 0.05 - 0.15, *y* = 0.02) ceramics displayed at room temperature.

The *P*-*E* measurements of BDFT-*x*-*y* (*x* = 0.05-0.15, *y* = 0.02) were performed, as shown in Figure 3.6. The results show that the substitution of Ti^{4+} for Fe^{3+} has significantly reduced the conductivity in the ceramics, which is due to the reduced oxygen vacancies and reduced electron hopping conduction from Fe^{2+} to Fe^{3+} by the *B*-site substitution. As mentioned earlier, due to the comparable thermodynamic stability of Fe^{3+} and Fe^{2+}, some Fe^{2+} ions are always formed during the synthetic process of $BiFeO_3$ and its solid solutions, giving rise to positively charged oxygen vacancies in the final products as a result of charge balance, which is responsible for the high electric conductivity [19, 139]. The substitution of Ti^{4+} for Fe^{3+} compensates the negative charge produced by the Fe^{2+} ions, reduces the concentration of oxygen vacancies, and thereby decreases the electric conductivity of the $BiFeO_3$–$DyFeO_3$ ceramics. By doping with the same percentage of the Ti^{4+} ions for various Dy concentrations, particularly, a saturated dielectric hysteresis loop without leakage feature was found in BDFT-0.10-0.02 of

morphotropic phase boundary (MPB) composition, which shows a promising remnant polarization of 23 $\mu C/cm^2$ (Fig. 3.6).

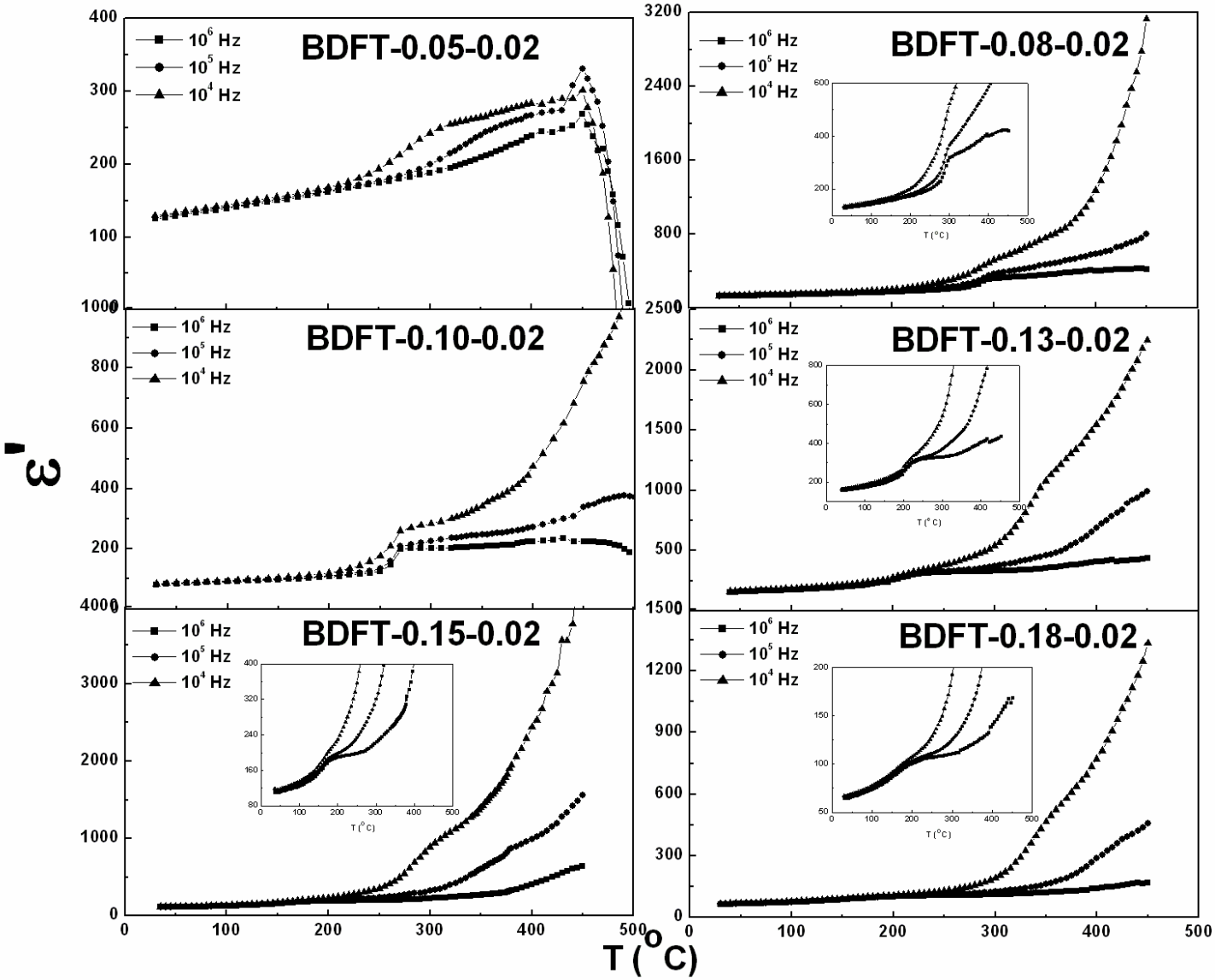

Figure 3.7 Temperature dependence of the dielectric constant (ε') for all of the BDFT-*x*-*y* (*x* = 0.05 - 0.18, *y* = 0.02) samples measured upon cooling at 10 kHz, 10^2 kHz, and 10^3 kHz.

Figure 3.7 shows the temperature dependence of the dielectric constant (ε') for all of the BDF-*x*-*y* ($0.05 \leq x \leq 0.18$, $y = 0.02$) samples measured upon cooling at 10 kHz,

10^2 kHz, and 10^3 kHz. A maximum value of the dielectric constant appeared at Curie temperature (T_C), which decreased from 450 °C to 200 °C with the increase of the $DyFeO_3$ concentration for different samples. The dielectric anomaly with the variation of Dy concentration was observed for all the samples, which is consistent with the results of the DSC measurements (see sec. 3.4.3). Incidentally, with the increase of $DyFeO_3$ concentration, the frequency-independent dielectric peaks changed into bumps with frequency relaxation behaviour (insets), indicating that the majority of the rhombohedral *R*3*c* phase transitions to the orthorhombic structure by the $DyFeO_3$ substitution.

3.4.3 Differential Scanning Calorimetry (DSC) Analysis

The phase transitions of the BDEF-*x*-*y* solid solution system were also studied by differential scanning calorimetry (DSC) in the heating and cooling processes, and the results are shown in Figure 3.8 and Table 3.2. A systematic change of transition temperature with respect to composition, as well as a large thermal hysteresis, was observed, which is related to the majority of rhombohedral (*R*3*c*) phase transitions to the orthorhombic structure. With the increase of the Dy^{3+} ions, the transition temperatures decreased from 538 °C to 223 °C in the heating process, and from 454 °C to 151 °C in the cooling process.

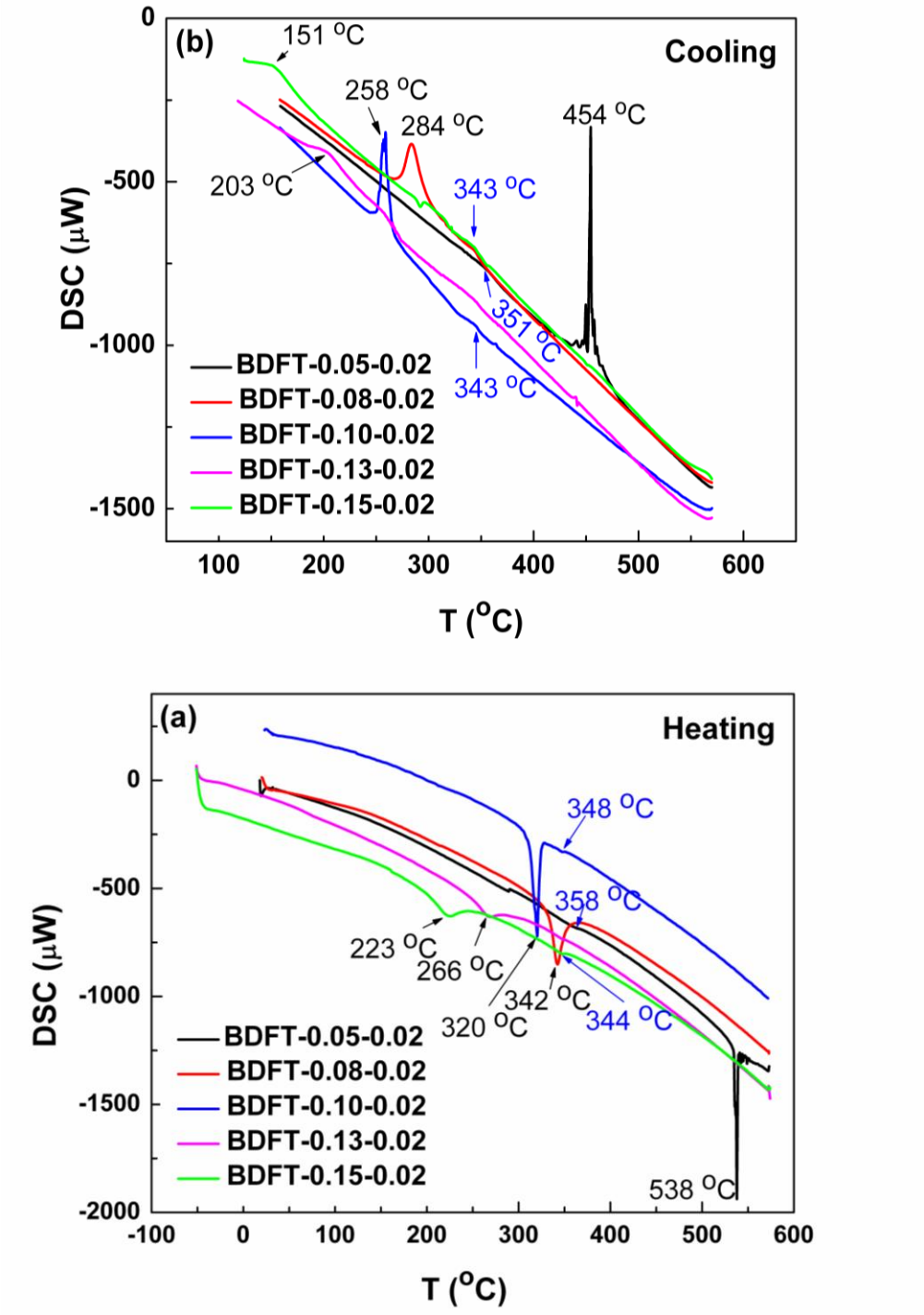

Figure 3.8 **(a) The phase transition detected as the endothermic peaks by DSC for all of the BDFT-*x*-*y* (*x* = 0.05 - 0.15, *y* = 0.02) samples measured on heating. (b) The phase transition detected as the exothermic peaks by DSC for all of the BDFT-*x*-*y* (*x* = 0.05 - 0.15, *y* = 0.02) samples measured on cooling.**

Table 3.2 The phase transition temperature by DSC for all of the BDFT-*x*-*y* (*x* = 0.05 - 0.15, *y* = 0.02) samples measured by DSC on heating and cooling.

Dysprosium Percentage	5%	8%	10%	13%	15%
DSC Heating (°C)	538	342	320	266	223
DSC Cooling (°C)	454	284	258	203	151

3.4.4 Temperature-Composition Phase Diagram

Based on the above structural analysis, dielectric characterization, ferroelectric measurements, and DSC analysis, a temperature-composition phase diagram for the (1-*x*)BFO-*x*DFO solid solution is established by combining the results of high temperature X-ray diffraction, differential scanning calorimetry (DSC), and dielectric measurements (Figure 3.9). The structure of BDF-*x* ceramic changes from the rhombohedral perovskite (*R3c*) to the orthorhombic orthoferrite (*Pbnm*), as the concentration of Dy (*x*) increases. In the range of morphotropic phase boundary (MPB), a mixture of two phases (rhombohedral and orthorhombic) is observed. With the increase of temperature, the structure of BDF-*x* solid solution ($0.03 \leq x \leq 0.10$) also undergoes the similar structure evolution, that is, from the rhombohedral perovskite *R3c* to the MPB, and then to the orthorhombic orthoferrite (*Pbnm*).

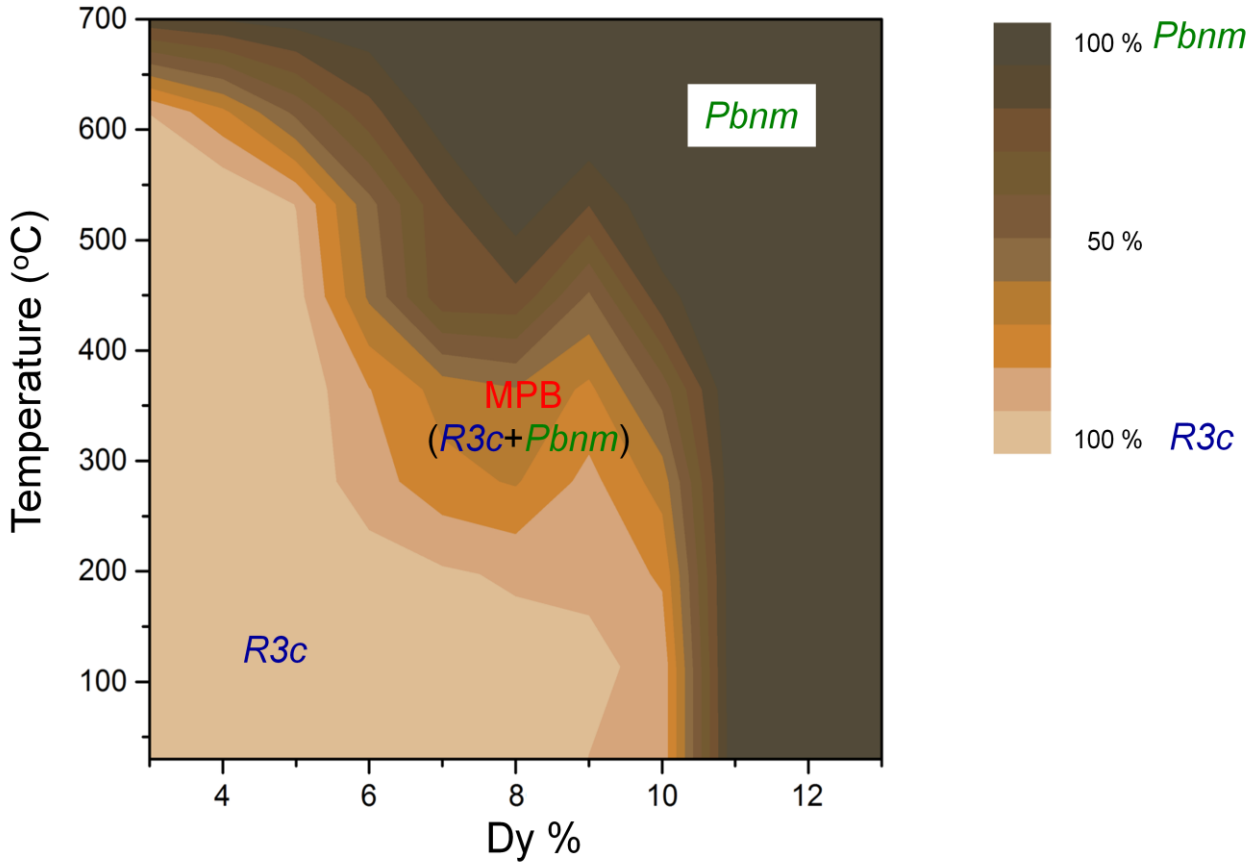

Figure 3.9 **Partial temperature-composition phase diagram of the (1-*x*)$BiFeO_3$-*x*$DyFeO_3$ (BDF-*x*) solid solution system, indicating the pure rhombohedral phase, the MPB with a mixture of rhombohedral and orthorhombic phases, and the pure orthorhombic phase.**

3.4.5 Magnetic Characterization of the BDFT-*x*-*y* Solid Soluiton

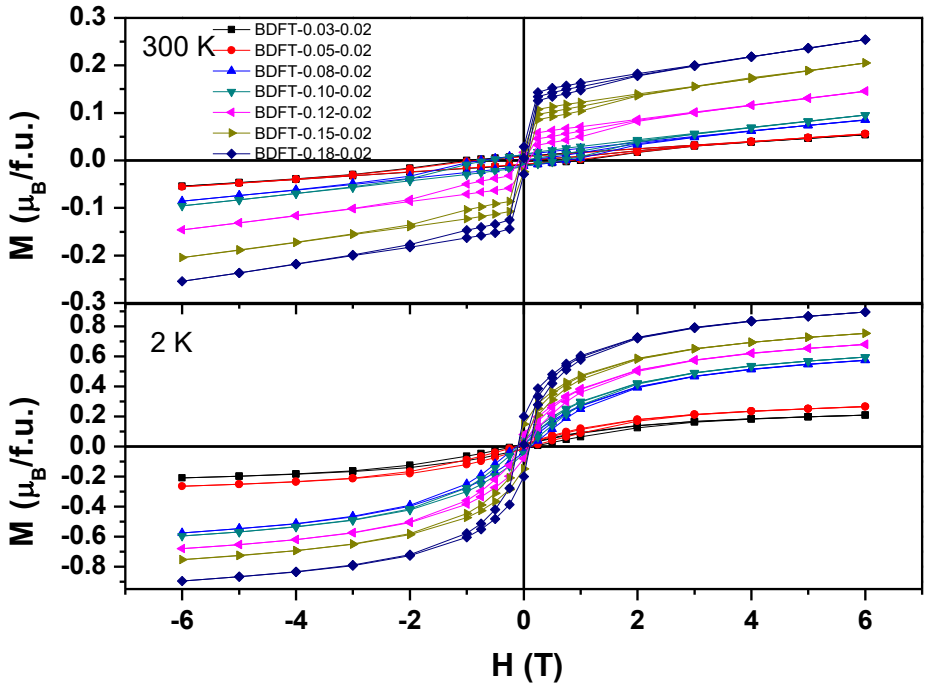

Figure 3.10 Magnetic hysteresis loops of the BDFT-*x*-*y* (*x* = 0.05-0.18, *y* = 0.02) ceramics measured at 300 K and 2 K.

It is known that the ferroelectricity of BFO originates from the structural distortion associated with $6s^2$ lone pair electrons of Bi^{3+} ions, whereas the magnetic property comes from the Fe^{3+}-O-Fe^{3+} superexchange interactions [88] related to the Fe^{3+}-O-Fe^{3+} superexchange angle of the BDF-x ceramics with various compositions. Pure BFO often shows a weak ferromagnetic order due to the G-Type antiferromagnetic spin structure, which is superimposed by a spiral spin structure with an incommensurate long-wave period of 62 nm in the lattice, including the canting of AFM sublattices. It will suppress the macroscopic ferromagnetic order and inhibit the observation of ME effect, so the Dy-doping was performed in order to suppress the spiral spin structure. Thus, it is expected that the Dy-doping on the perovskite *A* site will modify the magnetic properties of BFO. This hypothesis is proven by the variation of magnetization (M) with magnetic

field (H) (M-H curves) of the BDFT-*x*-*y* ($0.05 \leq x \leq 0.18$, $y = 0.02$) solid solutions at 300 K and 2 K, as shown in Figure 3.10. At room temperature, weak ferromagnetism was displayed in the compositions ($x \leq 0.18$) by a slim magnetic hysteresis loop with a residual magnetization of 0.015 μ_B/f.u for $x = 0.1$. However, at a low temperature of 2 K, all of the samples exhibited ferromagnetic behaviour and a large saturated magnetization of 0.8 μ_B/f.u. was displayed in BDFT-0.18-0.02. All the results show that the introduction of Dy^{3+} on the perovskite *A* site can enhance the magnetic properties of $BiFeO_3$. This is due to the effect of unpaired electrons on Dy^{3+}, which could result in additional magnetic interactions and ordering, and the modifications of the structure by the chemical substitution with ions of different sizes. Indeed, the weak ferromagnetism in BDFT-0.1-0.02 at room temperature is believed to arise from a structural distortion induced by the Dy^{3+} ion with a smaller ionic radius (1.027 Å) than that of Bi^{3+} (1.17 Å), which destroys the spiral spin modulation in $BiFeO_3$ and consequently induces the weak ferromagnetism. The magnetic Dy^{3+} ion has five unpaired electrons which can also increase the magnetism. Therefore the saturated magnetization is increased as the concentration of Dy increased. Since the concentration of the magnetic Dy^{3+} ion in BDFT-0.1-0.02 is too low to form a long range *A*-site magnetic ordering, the significantly enhanced magnetization at low temperatures must result from the interaction between the spins of the *A* site Dy^{3+} ion and the *B* site Fe^{3+} ion, which to some extent, decouples the antiferromagnetic interactions between the Fe^{3+} ions. A similar magnetic behaviour has also been found in (1-x)$BiFeO_3$-*x*$ErFeO_3$ solid solution which will be discussed in detail in Chapter 6.

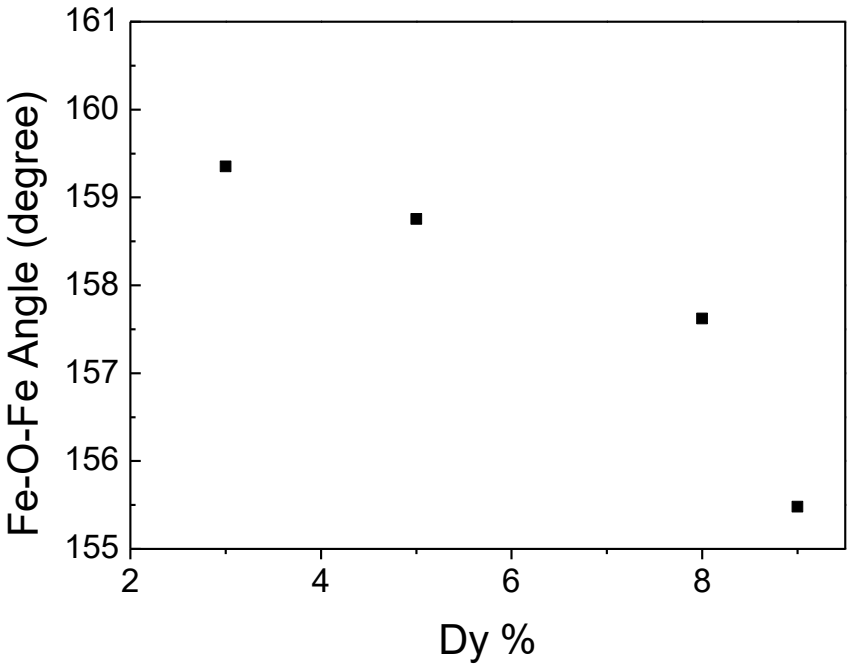

Figure 3.11 Fe-O-Fe angle as a function of Dy concentration of BDF-*x* (*x* = 0.03 - 0.09) solid solutions at 300 K.

The enhancement of ferromagnetism by Dy substitution can be explained by structure distortion which leads to suppression of the spiral spin magnetic order. The variation of superexchange angle (Fe-O-Fe) provides the evidence that structure distortion is induced by the Dy substitution. Fe-O-Fe angle has a direct effect on magnetism. The smaller the Fe-O-Fe angle leads to enhanced ferromagnetism. According to Kanamori-Goodenough Rule, for an antiferromagnetic, t_{2g}-p-t_{2g} is equal to 180°, whereas for ferromagnetic, t_{2g}-p-e_g is equal to 90° [18, 19]. When the material has a Fe-O-Fe angle of 180°, it is pure antiferromagnetic. When the Fe-O-Fe angle is 90°, the material is ferromagnetic due to the *d* orbital of Fe^{3+} hybridizing with 2*p* orbital of O^{2-}.. This is consistent with the magnetic hysteresis result.

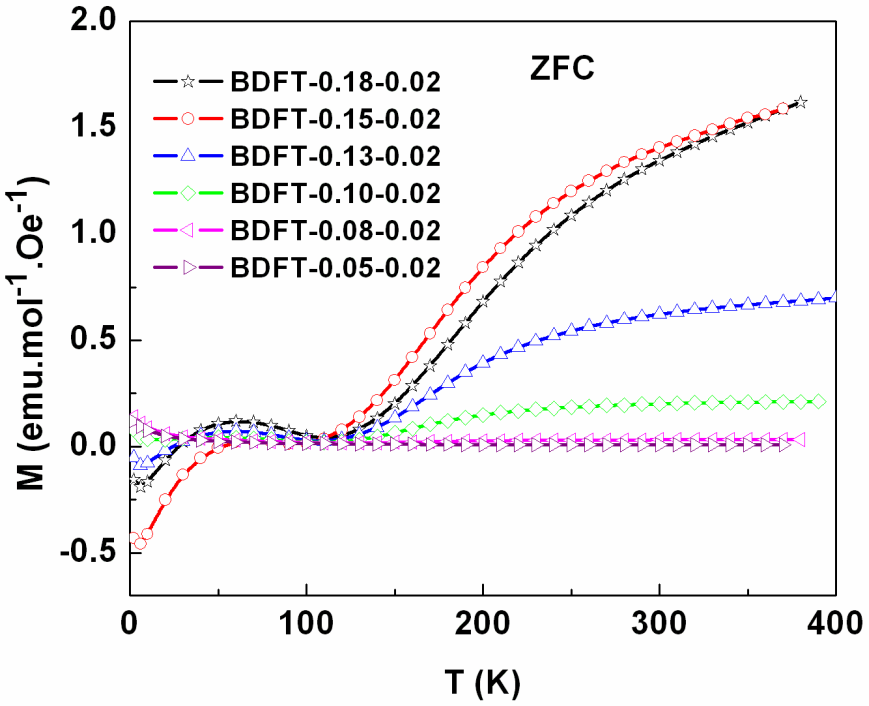

Figure 3.12 Temperature dependence of magnetization measured in zero-field-cooling (ZFC) process for BDFT-*x*-*y* (*x* = 0.05 - 0.18, *y* = 0.02).

Figure 3.12 shows the temperature dependence of the magnetization for the BFD-*x*-*y* ($0.05 \leq x \leq 0.18$, $y = 0.02$) ceramics. The magnetic anomalies at around 100 K in BDFT-*x*-*y* ($0.1 < x \leq 0.18$, $y = 0.02$) arise from the spin reorientation of the Fe^{3+} moments, as observed in $DyFeO_3$ and other orthoferrites with an orthorhombic structure (*Pbnm*) [19, 139]. No anomalies were observed in the solid solution with a $DyFeO_3$ content less than 10 mol%, which was possibly due to the rhombohedral *R*3*c* structure of these samples. This may be due to the low Dy concentration, which is not high enough to affect the interaction between Fe ions, leading to the feature of magnetization as a function of temperature remaining the characteristics of antiferromagnets. The results obtained from this work indicate that the (Dy, Ti)-co-doped ceramics exhibit larger magnetization than that of the pure BFO sample. As the (Dy, Ti)-co-doping concentration increases, the Fe-O-Fe bond angle decreases, followed by the variations decrease of Bi-O bond and Fe-O bond distance. A possible explanation is that the (Dy, Ti)-co-doping

might increase the structural distortion, resulting in a change of bond angle of Fe-O-Fe which enhances the magnetization [76]. The change in the Fe-O-Fe bond angle arises primarily due to the modulation in the rigid FeO_6 octahedra [140]. The variations of the Fe-O bond distance and bond angle due to the ionic substitution play a significant role in structure transformation [35], which will promote the suppression of the spin cycloid and the enhancement of the ferromagnetic and ferroelectric properties of BFO.

3.5 Conclusions

The (1-*x*)$BiFeO_3$-*x*$DyFeO_3$ solid solutions and the Ti-modified multiferroic (1-*x*)$BiFeO_3$-*x*$DyFeO_3$ solid solutions were successfully synthesized and their structural and multiferroic properties were systematically studied. A transition from the rhombohedral perovskite to MPB (mixture of rhombohedral and orthorhombic phases) was observed by XRD at *x* around 0.1. From differential scanning calorimetry (DSC) and dielectric measurements, an anomaly occurred at around room temperature for compositions of $x \leq 0.1$ and shifted to lower temperatures for $x > 0.1$, which is attributed to the related transition from the majority rhombohedral *R*3*c* phase to the orthorhombic structure. The temperature-composition phase diagram of (1-*x*)$BiFeO_3$-*x*$DyFeO_3$ solid solution was established. BDF-*x* solid solution and chemically modified BDFT-*x*-*y* ceramics exhibited weak ferromagnetism at room temperature and a large saturated magnetization (M_s = 0.8 μ_B/f.u.) at 2 K, as well as a typical ferroelectric hysteresis loop with a large remnant polarization of 23 $\mu C/cm^2$. Through this work, we have revealed that the Dy and Ti ions are effectively incorporated into the crystal structure of BFO, which provides an alternative strategy to enhance the multiferroic properties. These properties entitle the (1-*x*)$BiFeO_3$-*x*$DyFeO_3$ solid solution to novel applications as one of the few multiferroic materials that exhibit both decent magnetization and electric polarization.

In this chapter, we demonstrate that the magnetization of (1-*x*)$BiFeO_3$-*x*$DyFeO_3$ solid solution was enhanced by Dy *A*-site substitution. There are two reasons for such enhancement: the structure distortion and five unpaired electrons. In the next chapter, in

order to investigate the pure effect from structural distortion, Lu was incorporated into BFO to form (1-*x*)$BiFeO_3$-*x*$LuFeO_3$ solid solution. Lu has a smaller ionic radius compared with Bi^{3+}, and zero unpaired electrons. By such substitution of Bi^{3+} with Lu^{3+} on the *A*-site, the variation of magnetization is merely due to structure distortion.

Chapter 4.

Synthesis, Structure, and Characterization of the (1-*x*)$BiFeO_3$-*x*$LuFeO_3$ Solid Solution

4.1 Abstract

The coexistence of electric and magnetic order parameters in multiferroics offers new multifunctional devices based on the cross-control of magnetic moments and/or polarizations by the electric field and/or magnetic field. $BiFeO_3$ is one of the few single-phase multiferroics with both ferroelectricity and antiferromagnetism above room temperature. In many antiferromagnetic materials, the spin configuration of magnetic ions is determined by the superexchange through O 2*p* states, while in ferroelectric materials with perovskite structure, O^{2-} ions play an essential role in the lattice distortion. This motivated us to investigate the solid solution systems of (1−*x*)$BiFeO_3$-*x*$LuFeO_3$ (denoted as BLF-*x*), taking into consideration the possible spin-lattice couplings in the multiferroics. The pure $BiFeO_3$ crystallizes in a rhombohedral *R*3*c* structure and pure $LuFeO_3$ crystallizes in an orthorhombic *Pbnm* structure. Furthermore, in order to better understand the effects of rare-earth substitutions on the strucutral distortions and thereby on the ferromagnetism and ferroelectricity, Lu is chosen to substitute Bi because it has a zero unpaired electrons and smaller ionic raidii (0.977 Å) than that of Bi^{3+} (1.17 Å) and Dy $^{3+}$ (1.027 Å). Therefore, the solid solution system (1-x)$BiFeO_3$-x$LuFeO_3$, in which Lu substitutes for Bi^{3+} on the *A*-site, with the simultaneous chemical substitution of Ti^{4+} for Fe^{3+} on the *B*-site, was studied.

In this work, the solid solutions of BLF-*x* were prepared by the solid state reaction method. The substitution of Lu^{3+} for Bi^{3+} is found to significantly improve the magnetic properties of $BiFeO_3$. For the solid solution with $x < 0.10$, the structure remains a rhombohedral perovskite with *R*3*c* space group. With the further increase of $LuFeO_3$

content, a morphotropic phase boundary is found in the composition range of x = 0.10 – 0.15. The Lu^{3+} ion has no unpaired electron, therefore the enhancement of the magnetization in the BLF-x solid solution must arise purely from the crystal structural modification. This study provides a better understanding of the fundamentals of the structural distortions of $BiFeO_3$-based solid solutions with Lu-doping on the *A*-site, and the resulting effects on the multiferroic properties.

4.2 Introduction

Multiferroic materials with the coexistence of at least two ferroic orders (ferromagnetic, ferroelectric and ferroelastic) have drawn much interest over the past century [59, 73]. Among them, the coexistence of ferroelectricity (showing a spontaneous and switchable electrical polarization) and ferromagnetism (showing a spontaneous and switchable magnetization), which is expected to lead to magnetoelectric (ME) effects, is especially important in both academic research and technological applications because of their promising multifunctional applications in memory devices, sensors, and spintronics. However, few multiferroic materials (especially single-phase ones) have been found up to date because of the mutual exclusion between ferroelectricity and ferromagnetism (e.g. in perovskite materials). One of the best known multiferroic materials is $BiFeO_3$, which possesses the ABO_3 perovskite structure and is one of the few single-phase multiferroics with both ferroelectricity and anti-ferromagnetism above room temperature. Canonical multiferroic $BiFeO_3$ has low magnetization and weak switchable polarization and it is challenging to develop multiferroics materials with both large magnetization and polarization since ferroelectricity and ferromagnetism are mutually exclusive. Bismuth ferrite ($BiFeO_3$) bulk material has a few drawbacks such as low thermodynamic stability of the perovskite phase, the presence of a spiral spin arrangement, high electric coercive field, and high electric conductivity. Therefore, chemical modifications in the form of solid solution systems are needed to improve the magnetic and electrical properties. $BiFeO_3$ has an antiferromagnetic spin configuration with a canting of antiferromagnetic sublattices (the anti-parallel spins are not at 180° to each other). In order to increase the magnetic

properties of $BiFeO_3$, orthoferrite is being incorporated to improve the magnetic properties by introducing structure distortion and unpaired electrons. In the previous chapter, the $(1-x)BiFeO_3-xDyFeO_3$ solid solution was found to substantially increase the ferromagnetism of BFO by structural distortion and unpaired electrons. In order to have a better understanding of the ferromagnetism induced by structural distortion, the $(1-x)BiFeO_3$-$xLuFeO_3$ (BLF-*x*) solid solution is studied in this chapter. In BLF-*x* solid solution, there are three types of magnetic interactions: the $Fe^{3+}–O^{2-}–Fe^{3+}$ interaction (Dzyaloshinskii–Moriya, denoted as DM interaction), the Lu^{3+}-O^{2-}-Fe^{3+} interaction and the Lu^{3+}-O^{2-}-Lu^{3+} interaction. The interaction of Lu^{3+}-O^{2-}-Lu^{3+} is very weak and only exists below a very low temperature of 6 K [141], so, the magnetization of BLF-*x* at a higher temperature range is dominated by the DM interaction and the Lu^{3+}-O^{2-}-Fe^{3+} interaction. Furthermore, ceramic samples of $(1-x)BiFe_{(1-y)}Ti_{(y)}O_{(3+y/2)}$-$xLuFeO_3$ (denoted as BLFT-*x*-*y*) were also synthesized and characterized to investigate the ferroelectricity and ferromagnetism. By introducing Ti^{4+} on the B-site of $BiFeO_3$-base solid solutions, the electric conductivity can be decreased and new types of magnetic interactions, which arise from the Lu^{3+}-O^{2-}-Ti^{4+} interaction and the Fe^{3+}-O^{2-}-Ti^{4+}-O^{2-}-Fe^{3+} interaction, will be induced. In addition, the Ti^{4+} ion can also disrupt or break the long-range interaction of the spiral spin arrangement with a wavelength of 62 nm within the lattice of BFO [84]. Therefore, this *B*-site substitution can also have an impact on the magnetic behaviour of BLFT-*x*-*y*. In order to investigate the effect of structure distortion on spontaneous magnetization, Lu was used to synthesis the BLF-*x* solid solution because of its smaller ionic radius compared with Dy and its absence of unpaired electrons.

4.3 Experimental

4.3.1 Synthesis

The ceramic samples of $(1-x)BiFeO_3-xLuFeO_3$ (denoted as BLF-*x*) solid solution were prepared using conventional solid state reactions. The starting materials used were Bi_2O_3 (99.975%), Fe_2O_3 (99%) and Lu_2O_3 (99.9%) and they were weighed accurately to four significant digits according to the stoichiometric chemical formula:

$$\frac{(1-x)}{2}\mathrm{Bi_2O_3} + \frac{x}{2}\mathrm{Lu_2O_3} + \frac{1}{2}\mathrm{Fe_2O_3} \rightarrow (1-x)\mathrm{BiFeO_3} - x\mathrm{LuFeO_3} \quad (4.1)$$

Each composition was mixed stoichiometrically and ground by ball milling for 24 h. Ball milling container was setup as 25.0 ml bottle with 15.0 ml of ethanol and 40 zirconium oxide balls. The mixed powders were pressed into pellets, packed down into a platinum crucible and then calcined at 840 °C for 4 h. After the calcination, the sample disc was reground by ball milling for 24 h and then the sample powders were ground with 0.15ml of 5% polyvinyl alcohol (PVA) binder. The powders were pressed into pellets and then heated at 650 °C for 1 h for the binder to evaporate. After the elimination of the binder, the pellets were packed down into a platinum crucible which was then sealed in a larger Al_2O_3 crucible, followed by sintering at 900 °C for 1 h. The calcination temperature and sintering temperature are increased up to 850 °C and 950 °C, respectively with correspondence of increased concentration of Lu. In addition, ceramic samples of BLFT-*x*-*y* were also prepared by using the same solid state reaction method as for the BLF-*x* solid solution.

4.3.2 Structural Analysis

X-ray diffractions of as-sintered ceramics were performed on a Bruker D-8 diffractometer using Cu K_α radiation (40 mA, 40 kV, 0.01° steps and 2θ = 15 - 80°) to analyze the phase purity and to refine the crystal structure. $BiFeO_3$ single crystals were ground into powders. XRD data were collected and used as a structural reference for $BiFeO_3$. The resulting patterns were analyzed using TOPAS-Academic Software by Rietveld refinements to determine the symmetry, lattice parameters, and atomic positions of the solid solutions.

4.3.3 Ferroelectric and Magnetic Measurements

The sintered ceramics were mirror-polished with a series of silicon carbon sand papers to achieve parallel and flat surfaces on the circular faces of the ceramics, with various thickness (1000 - 200 μm). The polished ceramics were sputtered with gold

layers (Anatech Hummer Sputter-Coater 6.2, 12 min., 15 mA plasma discharge current). The gold wires were attached to both surfaces of the samples as electrodes. The ferroelectric hysteresis loops of the (1-*x*)$BiFeO_3$-*x*$LuFeO_3$ solid solution were displayed by a RT66A ferroelectric testing system (Radian Technology), connected to a Trek 609E-6 high voltage bipolar amplifier. The magnetization and magnetic field (M-H) relation were measured at different temperatures by using a Quantum Design MPMS-XL SQUID magnetometer.

4.4 Results and Discussion

4.4.1 Structural Analysis

Figure 4.1 shows the XRD patterns for BLF-*x* (*x* = 0.03 - 0.20) at room temperature, suggesting a rhombohedral perovskite *R*3*c* phase for all the compositions with *x* < 0.10. The MPB of BLF-*x* is found to be in the composition range of *x* = 0.10 - 0.15. Within the MPB, a mixture of two phases (rhombohedral *R*3*c* and orthorhombic *Pbnm*) is observed and the percentage of each phase was analyzed by Rietveld refinements. For the composition of *x* = 0.20, the solid solution is a pure orthorhombic perovskite phase with *Pbnm* space group. Because of the kinetics of the $BiFeO_3$ formation (Equation 4.2) and the evaporation of Bi_2O_3, a small amount of $Bi_2Fe_4O_9$ impurity phase was observed in the compounds with *x* < 0.1, according to the reaction described in Equation 4.4. In Equation 4.3, $Bi_xFe_yO_{1.5x+1.5y}$ (*x* > *y*) may be such phases as $Bi_{3.43}Fe_{0.57}O_6$, $Bi_{12}(Bi_{0.5}Fe_{0.5})O_{19.5}$, $Bi_{25}FeO_{39}$, $Bi_{36}Fe_2O_{57}$, and $Bi_{46}Fe_2O_{72}$. However, in our case, the XRD peaks do not match any of these phases.

$$Bi_2O_3 + Fe_2O_3 \rightarrow (1-z)BiFeO_3 + z(Bi_2O_3 + Fe_2O_3) \quad (4.2)$$

(volatile) (unreacted)

$$Bi_2O_3 + Fe_2O_3 \rightarrow (2/x)Bi_xFe_yO_{1.5x+1.5y} + (1-y/x)Fe_2O_3 (x > y) \quad (4.3)$$

(unreacted)

$$Bi_2O_3 + Fe_2O_3 \rightarrow Bi_xFe_yO_{1.5x+1.5y} + Bi_2O_3(x < y) \quad (4.4)$$

(volatile)

Oxygen vacancies will form due to the volatilization of Bi^{3+} ions and the conversion of Fe^{3+} into Fe^{2+} ions in pure BFO ceramics [136], as shown in the following equations,

$$2Fe^{3+} + O^{2-} \rightarrow Fe^{2+} + 0.5O^{2-}(\text{volatile}) + V_O^{2+} , \quad (4.5)$$

$$2Bi^{3+} + 3O^{2-} \rightarrow Bi_2O_3(\text{volatile}) + 2V_{Bi}^{3-} + 3V_O^{2+}. \quad (4.6)$$

When Lu substitutes Bi in BFO, it reduces the Bi_2O_3 volatilization, suppresses impurity phases and oxygen vacancy formation. This can be explained by the bond dissociation energy. The bond association energy of the Lu-O bond (669 $kJmol^{-1}$, standard dissociation energies at 298 K) is higher than that of Bi-O bond (337.2 $\pm$ 12.6 $kJmol^{-1}$, standard dissociation energies at 298 K), meaning that Lu firmly holds oxygen [142, 143]. In the rhombohedral phase region, the perovskite peaks shift to a smaller *d*-spacing with the increase of the $LuFeO_3$ amount, indicating the decrease of the lattice parameters with the increase of *x* values and the shrinkage of the unit cell due to the smaller ionic radius of the Lu^{3+} ion (0.977 Å) than that of Bi^{3+} (1.17 Å). As a result, the impurity phase disappeared with the increase of the $LuFeO_3$ amount, forming the BLF solid solution of pure perovskite phase.

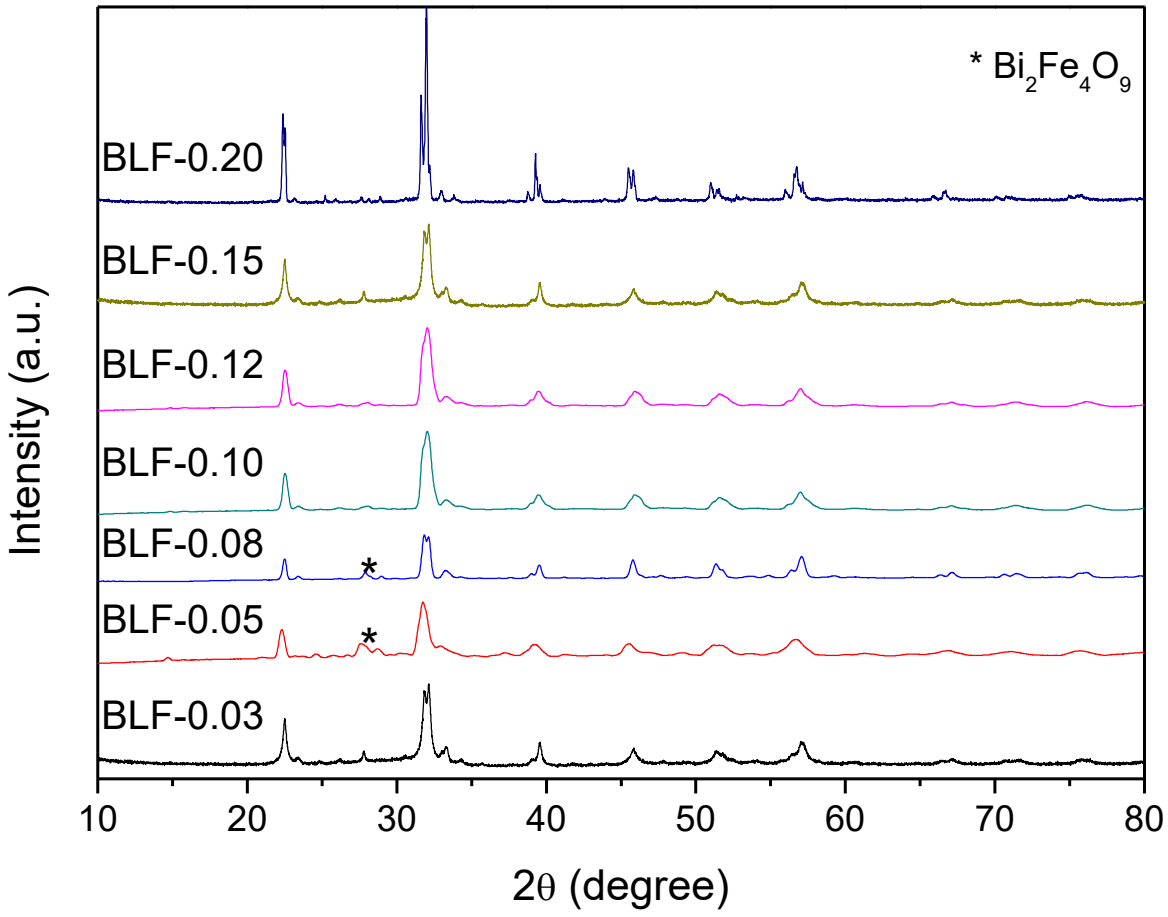

Figure 4.1 **X-ray diffraction patterns of the BLF-*x* (*x* = 0.03 - 0.20) ceramics prepared at optimal sintering temperatures. Stars indicate the peaks of the impurity phase $Bi_2Fe_4O_9$.**

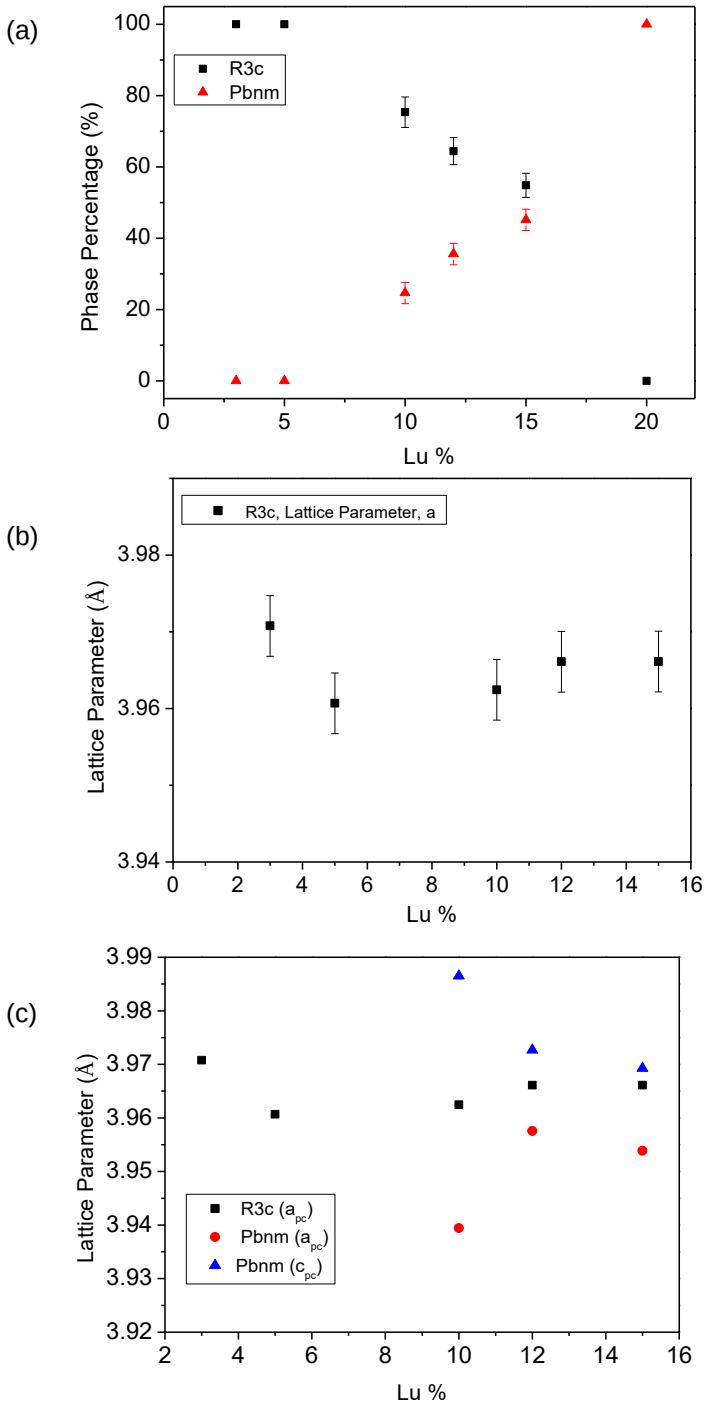

Figure 4.2 **(a) Rhombohedral (*R3c*) and orthorhombic (*Pbnm*) phase percentage as a function of composition of the BLF-*x* (*x* = 0.03 - 0.20) ceramics. (b) Variation of the lattice parameter, *a*, of the BLF-*x* (*x* =0.03-0.15) ceramics as a function of composition in the pure rhombohedral (*R3c*) phase. (c) The pseudocubic cell lattice parameters (a_{pc} = lattice parameters *a*, c_{pc} = lattice parameters *c*) as a function of the Lu concentration.**

Figure 4.2 (a) shows the structure phase percentage for each composition of the BLF-*x* (*x* = 0.03 - 0.20) ceramics. It shows that the orthorhombic phase percentage increases with increasing concentration of Lu^{3+} ions. The MPB is in the composition range of *x* = 0.10 - 0.15. Figure 4.2 (b) shows that the lattice parameter of rhombohedral phase decreases with increasing amount of Lu in the composition range of BLF-*x* (*x* = 0.03 -0.10). When x reaches 0.10, the pseudocubic cell parameter, a_{pc} for the *R*3*c* rhombohedral phase cannot decrease any further, as shown in Figure 4.2 (c), indicating that the phase of the solid solution partially transforms from the rhombohedral to the orthorhombic phase, remaining in the perovskite structure. The BLF-*x* soild solution undergoes a phase transformation from rhombohedral *R*3*c* to orthorhombic *Pbnm*, through the bridging MPB. Meanwhile, the lattice parameter of the orthorhombic phase is increased with increasing amount of Lu.

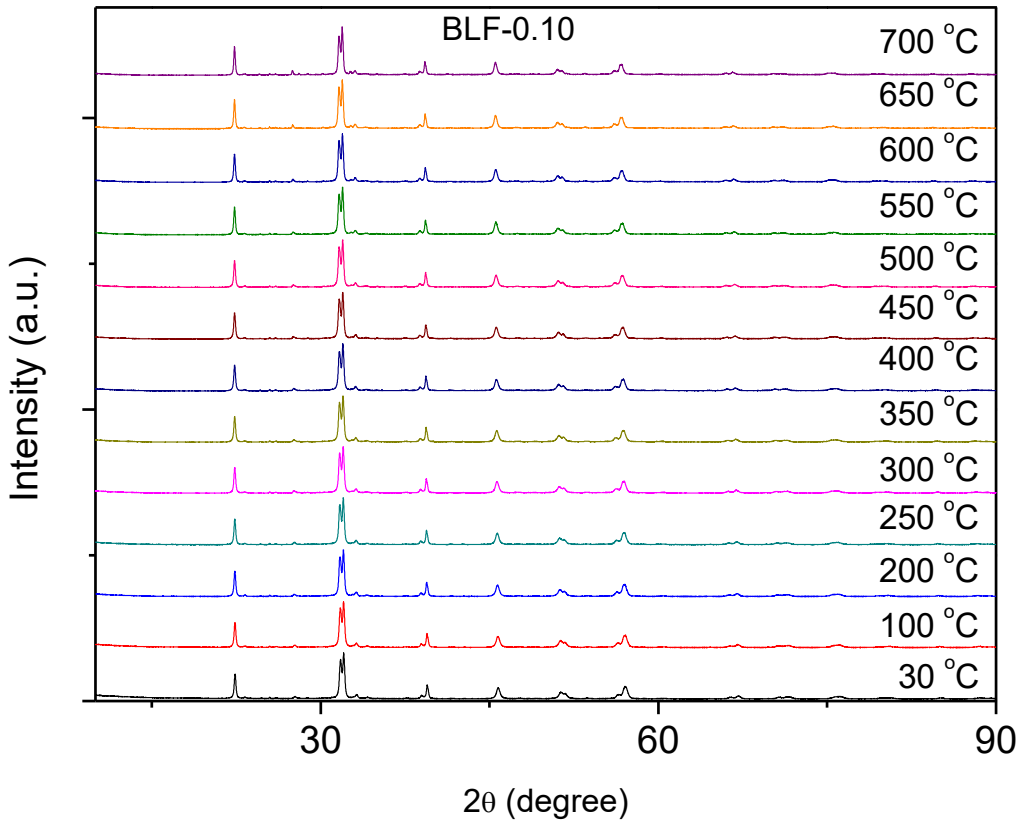

Figure 4.3 X-ray diffraction patterns of the BLF-0.10 ceramics at various temperatures.

Table 4.1 **Rietveld refinement results of the calculated lattice parameters and phase ratio for the BLF-0.10 at room temperature.**

BLF-0.10 (RT)	a (Å)	b (Å)	c (Å)	a_{pc} (Å)	Angle (°)	Calculated polarization (μC/cm2)
R3c (75.38%)	5.5781	5.5780	13.8513	3.9624	α = 89.47	4.9072
Pbnm (24.62%)	5.3895	5.7472	7.9730	3.9394	γ = 86.32	N/A

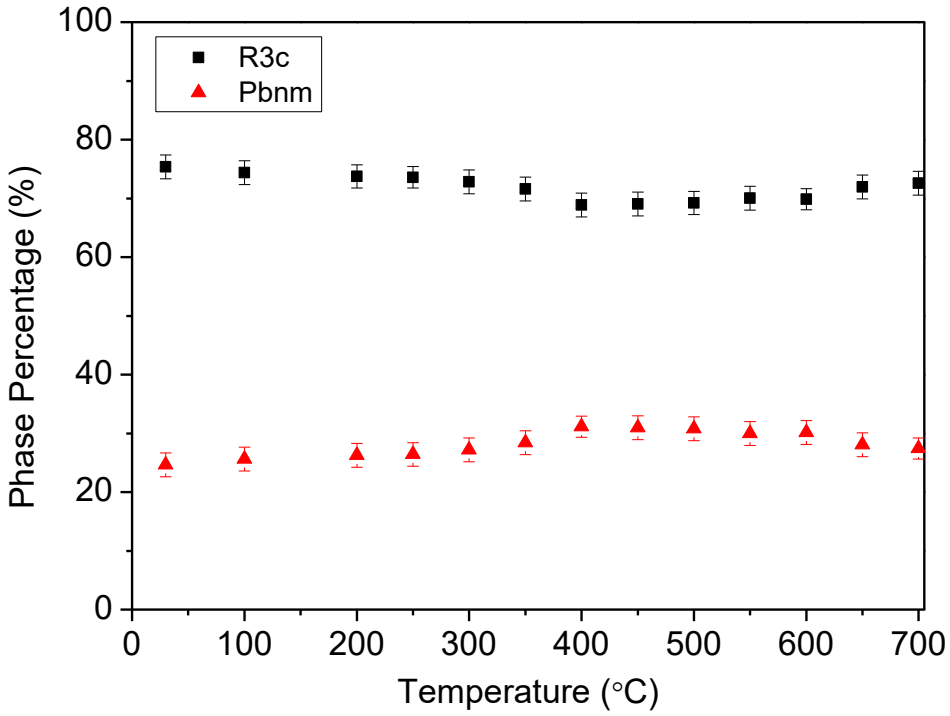

Figure 4.4 **Percentage of the rhombohedral (*R3c*) and orthorhombic phase (*Pbnm*) for the BLF-0.10 ceramics as a function of temperature.**

The structure evolution and phase transformations of BLF-*x* solid solution as a function of temperature was studied by high-temperature X-ray diffraction. Figure 4.3 shows the XRD patterns of BLF-0.10 at different temperatures (30 °C - 700 °C). It can be seen that the structure of BLF-0.10 is a mixture of rhombohedral and orthorhombic

phases within the whole studied temperature range and the percentages of *R*3*c* and *Pbnm* are only slightly changed with increasing temperature, as shown in Figure 4.4. There is no crossover of the majority phase from the rhombohedral phase to the orthorhombic at temperatures up to 700 ^{o}C. As an example, the Rietveld refinement results of the calculated lattice parameters and phase percentages for the BLF-0.10 at room temperature are shown in Table 4.1 and Figure 4.4.

4.4.2 Ferroelectric Properties

The off-centre ferroelectric distortion in BFO is mainly due to the stereochemical activity of the Bi 6S^2 lone pair electrons [73]. The substitution of Bi^{3+} by Lu^{3+} and Ti^{4+} for Fe^{3+} will affect the ferroelectric distortion and decrease the electric conductivity in the BLF-*x* ceramics. The calculated spontaneous polarization at various temperatures is shown in the Figures 4.5, which was obtained by using structural information of the *A*-site and *B*-site cation displacements in the rhombohedral unit cell.

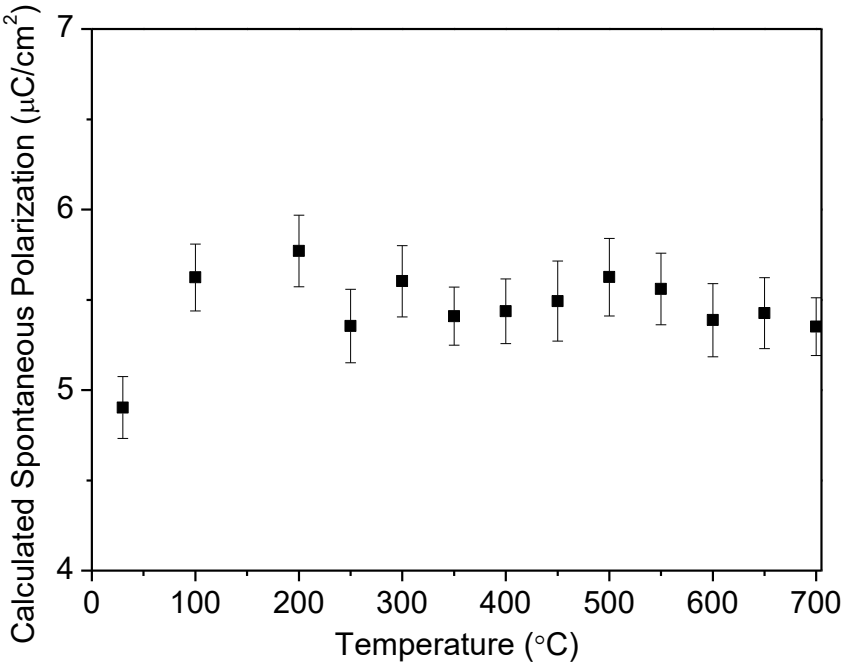

Figure 4.5 **The calculated spontaneous polarization as a function of various temperature for the BLF-0.10 solid solution.**

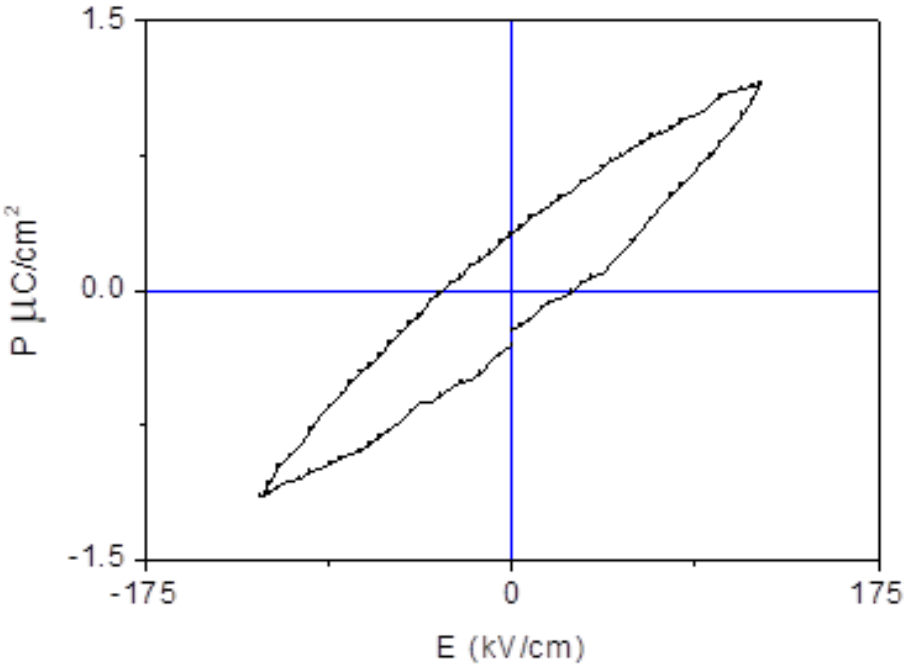

Figure 4.6 **Room temperature P-E hysteresis loop of the BLF-0.10-0.02 solid solution.**

Figure 4.5 shows the calculated spontaneous polarization for BLFT-0.10. The calculated P_s is around 4.90 $\mu C/cm^2$ at room temperature and it shows a slight increase and then remains almost constant upon heating up to 700 °C. Figure 4.6 presents an unsaturated P-E hysteresis loop without leakage feature in the BLFT-0.10-0.02 sample, which is of MPB composition, at room temperature. The ferroelectric property was improved by the aliovalent ionic substitution of Ti^{4+} for Fe^{3+} ions, which decreased the conductivity by reducing the concentration of oxygen vacancies. As mentioned earlier, due to the comparable thermodynamic stability of Fe^{3+} and Fe^{2+}, some Fe^{2+} ions always form during the synthetic process of $BiFeO_3$ solid solutions, giving rise to the positively charged oxygen vacancies in the final products as a result of charge balance, which is responsible for the high electric conductivity [142]. The substitution of Ti^{4+} for Fe^{3+} compensates the negative charges produced by the Fe^{2+} ions, reduces the concentration of oxygen vacancies, and thereby decreases the electric conductivity of the BLFT-0.10-0.02 ceramics. Hence, it is concluded that the incorporation of Ti^{4+} into the BFO ceramics is an effective technique to improve the ferroelectric properties at room temperature.

4.4.3 Temperature-Composition Phase Diagram for the $BiFeO_3$-$LuFeO_3$ System

Based on the results obtained above, a partial phase diagram for BLF-*x* solid solutions is established in terms of temperature and composition, by using high temperature X-ray diffraction and Rietveld refinements, as shown in Figure 4.7. It depicts the effects of Lu-substitution on the phase symmetry and phase transition temperature of BLF-*x*. With the increase of Lu concentration, the structure changes from the rhombohedral perovskite *R3c* phase to the orthorhombic orthoferrite *Pbnm* phase. For $x \leq 0.8$, the structure remains a rhombohedral perovskite with *R*3*c* space group. While in the composition range of $0.10 \leq x < 0.15$, an MPB region is identified in which the rhombohedral *R3c* and orthorhombic *Pbnm* phases coexist in a comparable amount. The pure orthorhombic *Pbnm* phase appears with $x \geq 0.20$. When the temperature is increased, the feature of the MPB compositions remains a nearly unchanged mixture of the *R*3*c* and *Pbnm* phases, leading to an almost vertical MPB region.

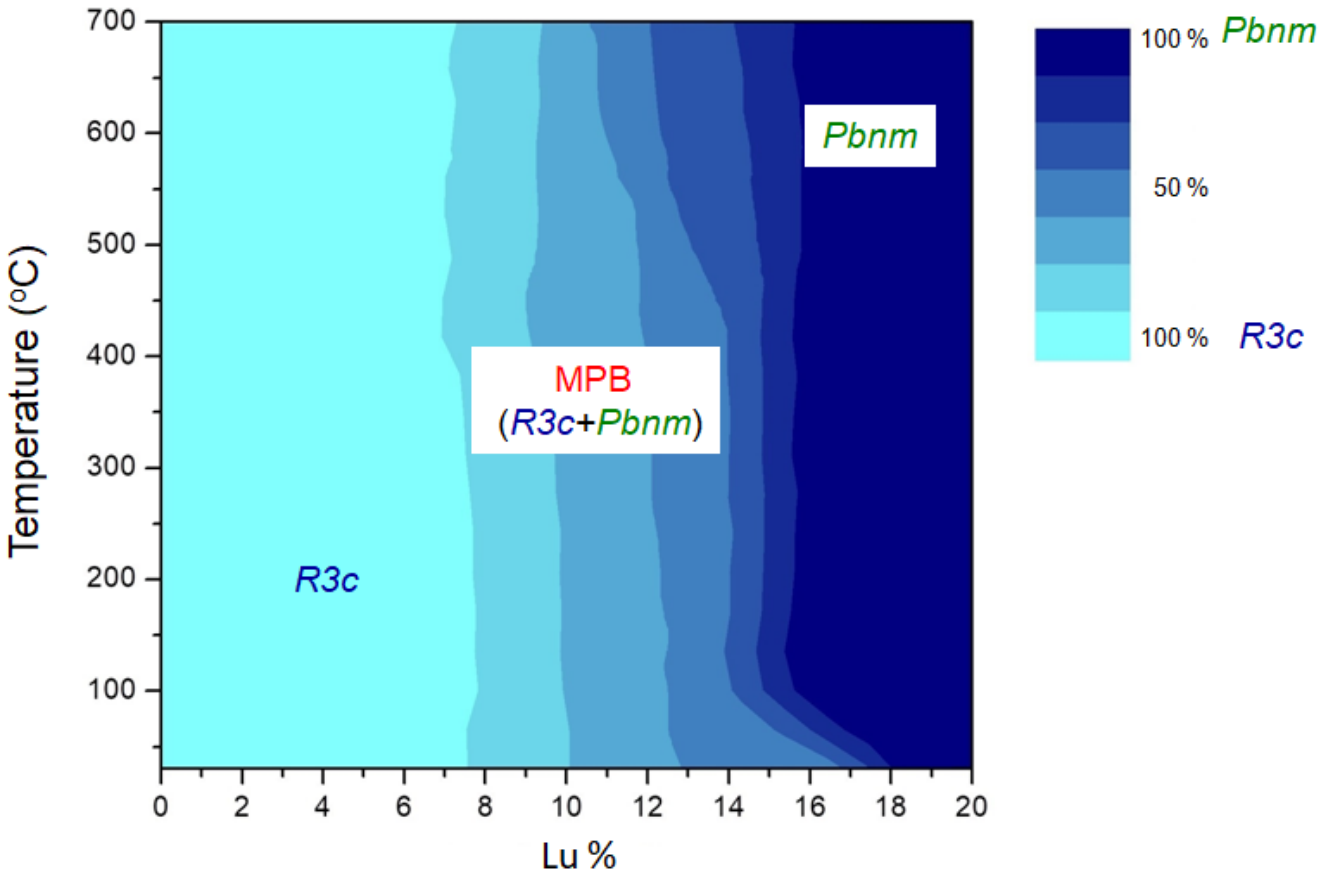

Figure 4.7 **Partial phase diagram of the (1-*x*)$BiFeO_3$-*x*$LuFeO_3$ solid solution system, indicating the pure rhombohedral phase region, MPB as a mixture of rhombohedral and orthorhombic phase, and the pure orthorhombic phase.**

4.4.4 Magnetic Characterization of BLF-*x* Solid Solution

BFO is known to be antiferromagnetic with a G-type magnetic structure, which is expected to exhibit a linear variation of the magnetization as a function of the magnetic field [144]. The magnetic hysteresis (*M*-*H*) curves of the BLF-*x* ($0.03 \leq x \leq 0.30$) solid solutions at 300 K and 5 K are shown in Figure 4.8. A noticeable change from a straight line to a slim loop is found in the *M*-*H* loops with the increase of Lu concentration, indicating that the substitution of Lu for Bi has enhanced the magnetic properties of BFO. At room temperature, weak ferromagnetism was displayed for the compositions of $x \leq 0.1$ by a slim magnetic hysteresis loop, with a residual magnetization of 0.005 μ_B/f.u for $x = 0.1$. At lower temperature (5 K), all the substituted samples exhibit ferromagnetic behavior, with a saturated magnetization of 0.05 μ_B/f.u. displayed for BLF-0.30. Therefore, as expected, the introduction of Lu^{3+} on the perovskite *A*-site can improve the magnetic properties of $BiFeO_3$ solid solutions due to the effect of structural distortions. Indeed, the weak ferromagnetism in BLF-0.1 at room temperature is believed to arise from a structural distortion introduced by the Lu^{3+} ion with a smaller ionic radius (0.977 Å) than that of Bi^{3+} (1.17 Å), which destroys the spiral spin modulation in $BiFeO_3$.

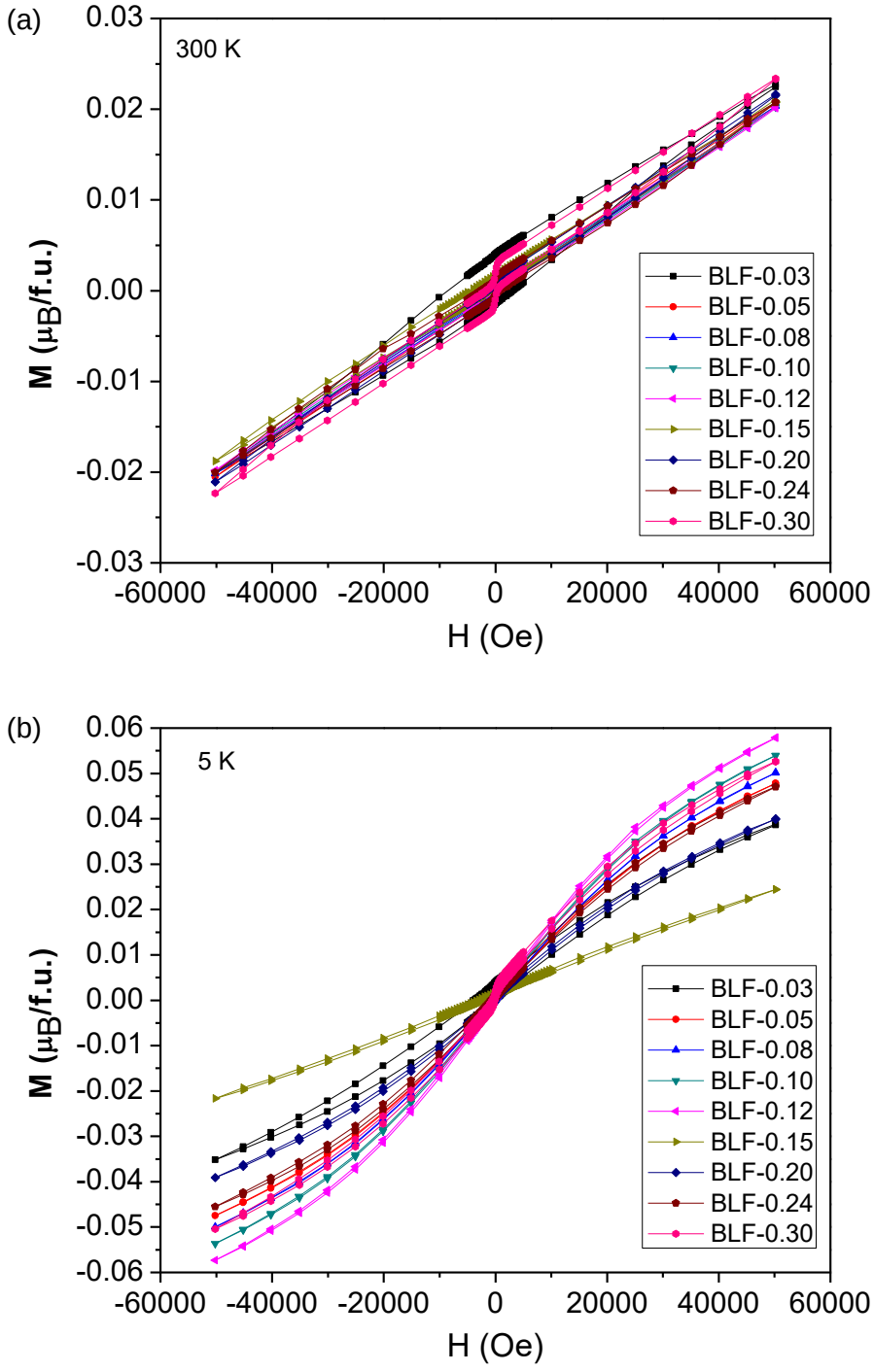

Figure 4.8 **Magnetic hysteresis loops of the BLF-*x* (*x* = 0.03 - 0.30) ceramics measured at (a) 300 K and (b) 5 K.**

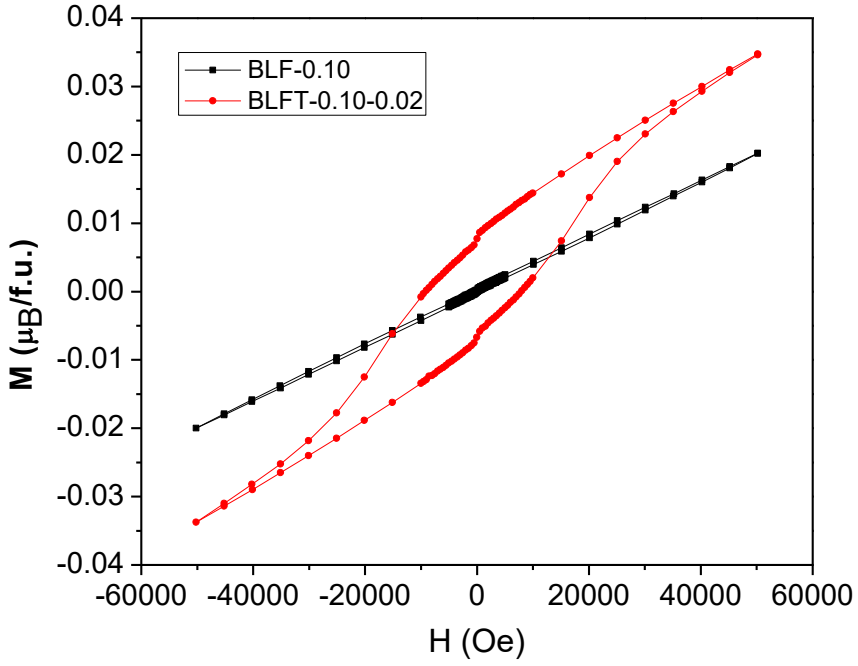

Figure 4.9 Magnetic hysteresis loops of BLF-0.10 and BLFT-0.10-0.02 solid solutions measured at 300 K.

Furthermore, the Ti^{4+}-modified BLFT-0.10-0.02 solid solution was also prepared in order to investigate the modification of magnet properties by *A*-site and *B*-site co-substitution. The magnetic hysteresis (*M-H*) curves of BLF-0.10 and BLFT-0.10-0.02 solid solutions at 300 K are shown in Figure 4.9. At room temperature, a weak ferromagnetism was displayed in BLF-0.10 by a slim magnetic hysteresis loop with a remnant magnetization of 0.005 μ_B/f.u. whereas a much higher remnant magnetization of 0.010 μ_B/f.u. was displayed for BLFT-0.10-0.02 with a decent hysteresis loop. In this figure, a slim magnetic hysteresis is presented for BLF-0.10 solid solution, which indicates the weak ferromagnetic property of the BLF ceramics. This shows that a low concentration of Lu substitution makes a very small enhancement of magnetization. However, an evident ferromagnetic behaviour is shown in the BLFT-0.10-0.02 ceramics, which means that the G-type antiferromagnetism in BFO is turned into a ferromagnetic ordering with a non-zero net magnetic moment due to the cosubstitution. By introducing Ti^{4+} on the *B*-site, new types of magnetic interactions, Lu^{3+}-O^{2-}-Ti^{4+} and Fe^{3+}-O^{2-}-Ti^{4+}-O^{2-}-Fe^{3+} are created. The Ti^{4+} ion can also break the long range interaction of a spiral spin

arrangement with a wavelength of 62 nm within the lattice [84]. Therefore, the chemically modified BLFT-0.10-0.02 ceramics with Lu- and Ti-co-substitutions exhibit ferromagnetism at room temperature and a large saturated magnetization *M*s = 0.03 μ_B/f.u., as well as a clear ferroelectric hysteresis loop with a remnant polarization of 0.30 $\mu C/cm^2$ as shown in Figure 4.6. These results demonstrate that the enhanced magnetic properties have been achieved by the co-substitution of Lu^{3+} for Bi^{3+} and Ti^{4+} for Fe^{3+} in the BLFT-*x*-*y* solid solution.

Figure 4.10 shows the temperature dependence of the magnetization for the BLF-0.10 and BLFT-0.10-0.02 solid solutions. The BLF-0.10 sample exhibits a monotonic increase of magnetization with temperature decreasing from 300 K to 5 K, indicating the enhanced ordering of Fe spins along the magnetic field with the decrease of temperature. Also, the BLFT-0.10-0.02 sample exhibits a significant increase in magnetic moment compared with BLF-0.10. These results are consistent with the results of magnetic hysteresis loops of BLF-0.10 and BLFT-0.10-0.02 solid solutions at 300 K, as shown in Figure 4.9.

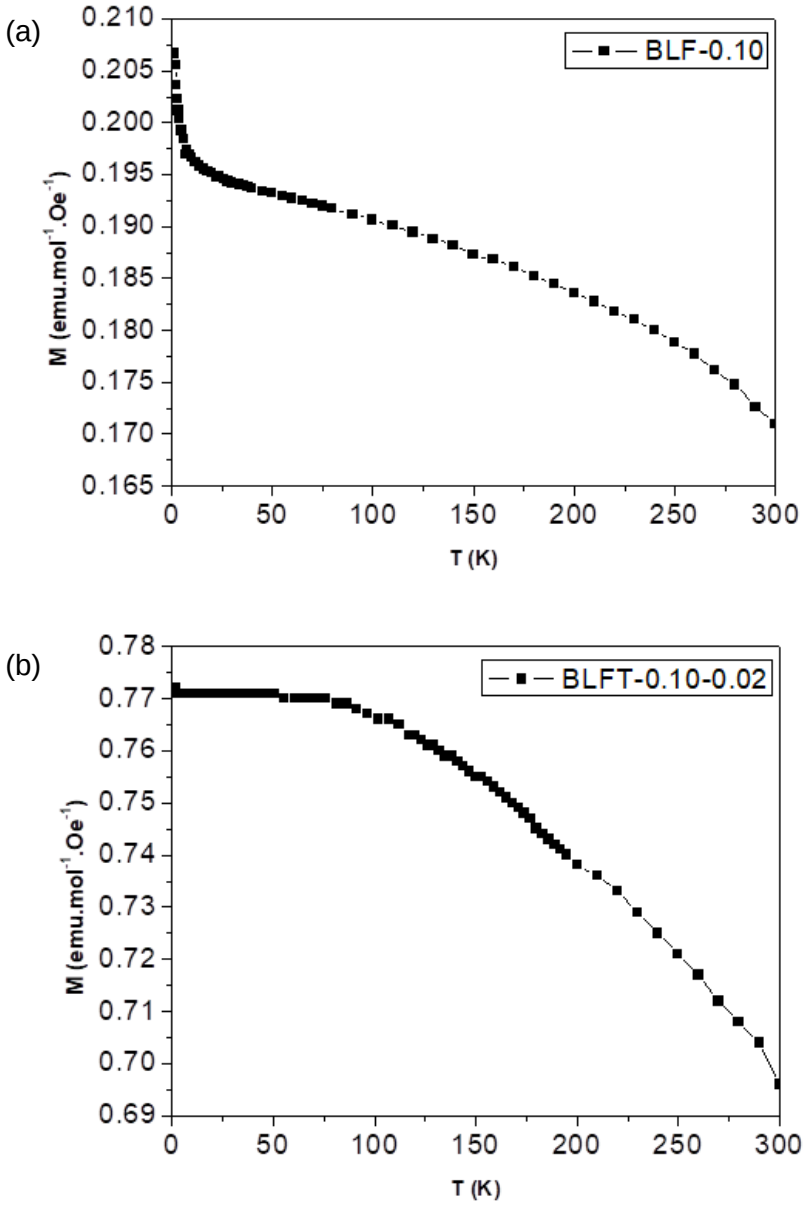

Figure 4.10 Temperature dependence of magnetization measured in field-cooling (FC, 100 Oe) for (a) BLF-0.10, and (b) BLFT-0.10-0.02.

Figure 4.11 shows the temperature dependence of the magnetization for the BLF-*x* (*x* = 0.05 - 0.30) solid solutions. The BLF-x (*x* = 0.05 - 0.15) samples exhibit a monotonic increase of magnetization with decreasing temperature from 300 K to 5 K. In this composition range, the magnetic behaviour is observed in the samples of the rhombohedral (*R*3*c*) compositions and MPB region. The enhanced magnetization in the

temperature range of 50 K to 300 K, results from the interactions between the spins of the *A*-site Lu^{3+} ion and the *B*-site Fe^{3+} ion, which, to some extent, decouples the antiferromagnetic interactions between the Fe^{3+} ions. The magnetic anomalies at around 70 K in the BLF-*x* ($0.24 < x \leq 0.30$) compositions could arise from the spin reorientation of the Fe^{3+} moments and the structural distortion induced by Lu substitution, as observed in $LuFeO_3$ and other orthoferrites with orthorhombic phase (*Pbnm*) [145]. Upon cooling, the Fe^{3+} uncompensated antiferromagnetic structure spin reoriented to another antiferromagnetic structure axis by Morin type transition [149]. This also explains the slight decrease in the magnetic moments at a lower temperature which was observed in the BLF-*x* (x = 0.20 - 0.30), as the concentration of $LuFeO_3$ increases. The net magnetization shows a significant increase upon cooling to $T < 30$ K due to the paramagnetic Lu^{3+} and Fe^{3+} ions that are aligned (oriented parallel) with the external magnetic field (100 Oe). The schematic spin configurations for the BLF-0.30 ceramics are shown in Figure 4.12, corresponding to specific temperature ranges.

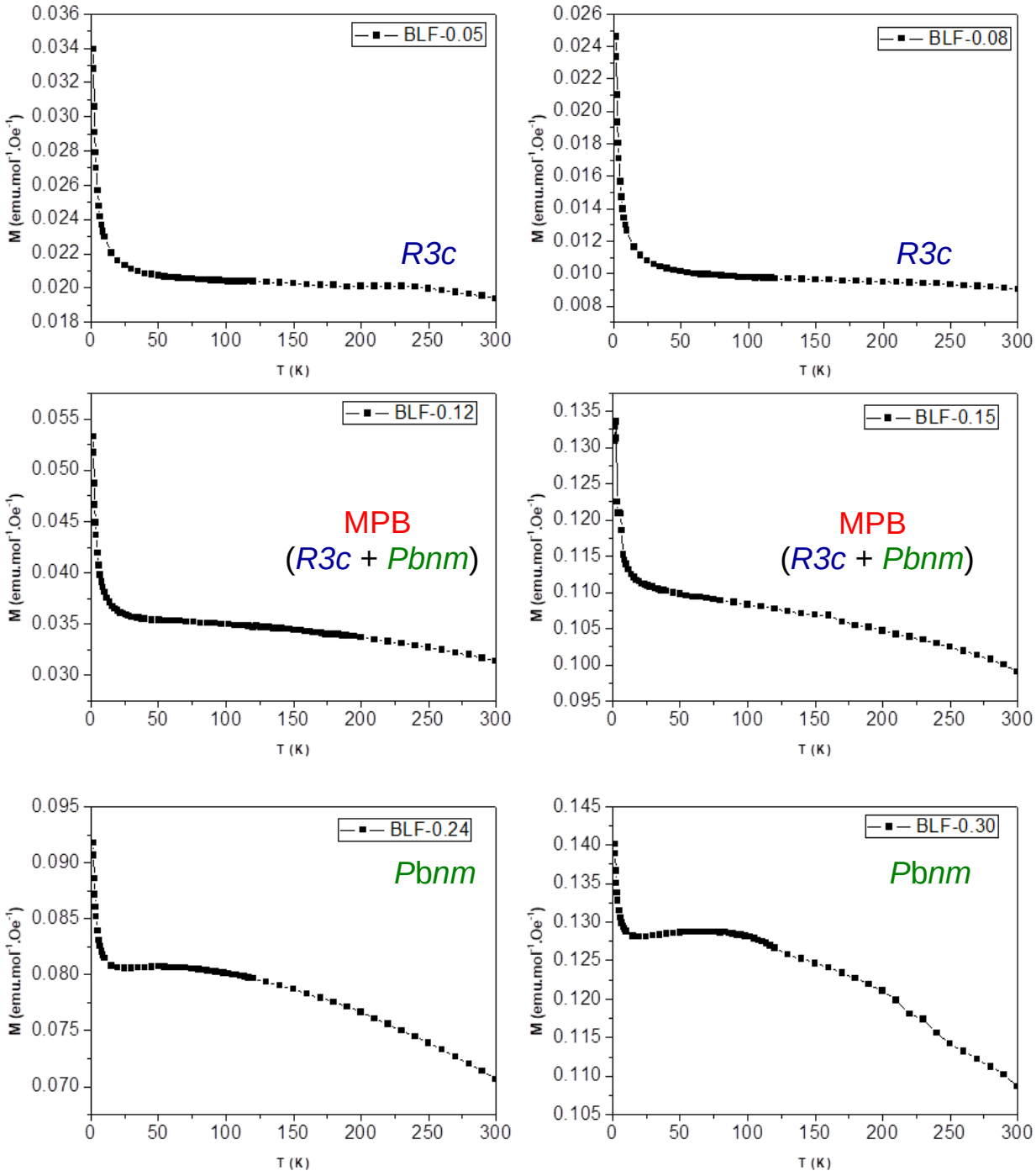

Figure 4.11 **Temperature dependence of magnetization measured in field-cooling (FC, 100 Oe) for (a) BLF-0.05, (b) BLF-0.08, (c) BLF-0.12, (d) BLF-0.15, (e) BLF-0.24 and (f) BLF-0.30.**

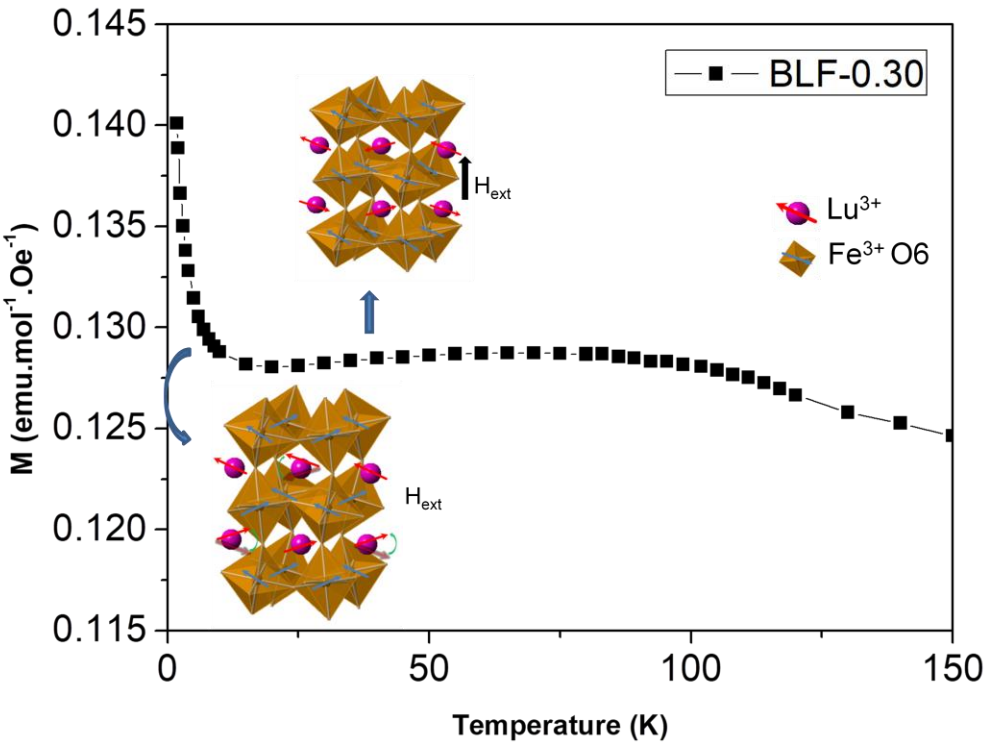

Figure 4.12 Temperature dependence of magnetization measured in field-cooling (FC, 100 Oe) for BLF-0.30, with schematic spin structures corresponding to different temperature ranges.

The measured spontaneous magnetization and calculated spontaneous polarization for different BLF-*x* compositions at 300 K are shown in Figure 4.13. It is clear that the coexistence of ferromagnetic and ferroelectric orders is present in these BLF-*x* solid solutions, making these materials room-temperature multiferroic. The values of spontaneous magnetization and polarization decrease with the increase of Lu content in the rhombohedral *R*3*c* structure range, which is probably due to the decreasing lattice parameter in the rhombohedral phase as shown in Figure 4.2. The spontaneous magnetization and polarization then increase as the concentration of Lu further increases and enters the MPB region of $0.10 \leq x \leq 0.15$, in which both enhanced ferromagnetic and ferroelectric orderings are observed for the BLF-*x* solid solutions

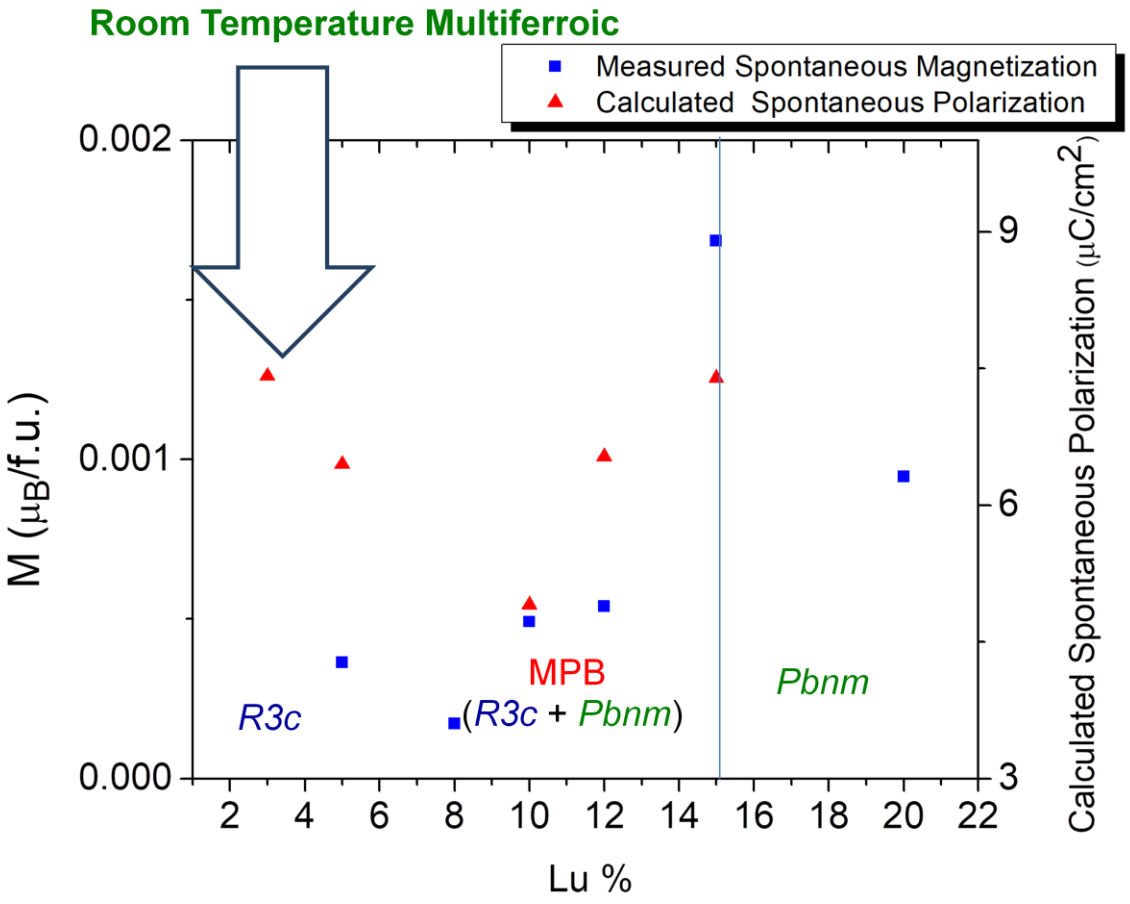

Figure 4.13 **The spontaneous magnetization and calculated spontaneous polarization of BLF-*x* solid solutions as a function of various Lu compositions at 300 K.**

4.5 Conclusions

The solid solution of (1-*x*)$BiFeO_3$-*x*$LuFeO_3$ (BLF-*x*) and the Ti-modified BLFT-*x*-*y* solid solutions have been successfully synthesized. The temperature-composition phase diagram of the BFO-LFO solid solution system is constructed and the structural and multiferroic properties of these solid solutions are systematically studied. A phase transition from rhombohedral perovskite (*R*3*c*) to orthorhombic orthoferrite (*Pbnm*) was observed by XRD for the BLF-*x* ceramics with Lu concentration increasing to *x* = 0.10 - 0.15. The Bi- and Ti-co-substituted BLFT-0.10-0.02 ceramics exhibit ferromagnetism at

room temperature with a large saturated magnetization *M*s = 0.03 μ_B/f.u., and a decent ferroelectric hysteresis loop with a remnant polarization of 0.30 $\mu C/cm^2$. The calculated spontaneous polarization is 4.90 $\mu C/cm^2$ at room temperature. Thus, these results indicate that the substitution of Lu for Bi in BFO is a possible approach to improve the multiferroic properties of BFO-based solid solutions, and the simultaneous presence of the ferromagnetism and ferroelectricity in the Lu-substituted $Bi_{1-x}Lu_xFeO_3$ solid solution entitles it a new room-temperature multiferroic material, potential useful for magnetoelectric and spintronic device applications.

In this chapter, the magnetization of BLF-*x* and the Ti-modified BLFT-*x*-*y* solid solutions were enhanced by Lu *A*-site substitution and *B*-site co-substitution. The magnetization enhancement for BLF-*x* is due to the structure distortion. The magnetization enhancement for *B*-site co-substitution is because that Ti^{4+} ion substitution can break the long range interaction of a spiral spin arrangement. In the next chapter, in order to investigate the effect of structure distortion and unpaired electrons on Bi-based solid solution, (1-*x*)$BiFeO_3$-*x*$YbFeO_3$ solid solutions were synthesized. Yb has a larger ionic radius with one unpaired electron than Lu. By comparative study of these solid solutions, the effect of unpaired electrons on magnetization can be systematically studied.

Chapter 5.

Synthesis, Structure, and Characterization of the (1-*x*)$BiFeO_3$-*x*$YbFeO_3$ Solid Solution

5.1 Abstract

To systematically study the effects of rare earth substitution on the *A*-site of the BFO-base solid solutions, Yb-substituted solid solutions of (1-*x*)$BiFeO_3$ -*x*$YbFeO_3$ (denoted BYF-*x*) have been synthesized and characterized. With a slightly larger ionic radius and 1 unpaired electron, Yb^{3+} (r = 0.985 Å) is chosen to be studied to compared with Lu^{3+} (0.977 Å, 0 number of unpaired electrons). As such, the effect of different number of unpaired electrons and ionic radius on the structure, ferroelectric, and ferromagnetic properties of the (1-*x*)$BiFeO_3$-*x*$YbFeO_3$ solid solution was studied.

The phase diagram of the solid solutions has been constructed. The pure $BiFeO_3$ crystallizes in a rhombohedral *R*3*c* structure and the pure $YbFeO_3$ crystallizes in an orthorhombic *Pbnm* structure [141]. In this work, the solid solutions of BYF-*x* were prepared by solid state reaction. The high temperature X-ray diffraction measurements showed that the substitution of Yb has induced noticeable lattice distortion in the ceramics. For the BYF-*x* ($x < 0.11$) solid solutions, the structure remains rhombohedral with *R*3*c* space group. With further increase of the concentration of Yb, a morphotropic phase boundary with coexisting rhombohedral *R*3*c* phase and orthorhombic *Pbnm* phase is found in the composition range of $0.11 \leq x < 0.15$. The calculated spontaneous polarization for the BYF-0.11 ceramics is 7.7 $\mu C/cm^2$ at room temperature, and the solid solution ceramics also exhibit a weak ferromagnetism at room temperature along with a saturated magnetization of M_s = 0.025 μB/f.u.. The Yb-substituted samples show good ferroelectric properties, which may be attributed to suppressed formation of oxygen vacancies by the Yb substitution for Bi. The disruption of the spin cycloidal structural

caused by the structural distortion can be an important factor for the improvement of magnetic properties.

5.2 Introduction

Despite the very interesting properties and promising applications of $BiFeO_3$ (BFO), there are some drawbacks for the pure $BiFeO_3$, such as high electric conductivity, high electric coercive field and G-type antiferromagnetism, which have greatly limited the potential applications of bulk BFO [34]. Many researchers have tried to overcome these problems in BFO by improving the synthetic techniques such as rapid liquid phase sintering and leaching out the impurity phase with dilute nitric acid, but little improvement on multiferroic properties has been obtained [101, 102]. Recently, the introduction of rare-earth ferrite into BFO is proven to be an effective method to improve the performance of bulk BFO [19, 23, 25, 34]. In this work, the formation of (1-*x*)$BiFeO_3$-*x*$YbFeO_3$ (denoted BYF-*x*) solid solution by the substitution of Yb^{3+} for Bi^{3+} on the perovskite *A*-site leads to significant improvement of the magnetic properties. It is found that the enhancement of the magnetization in the BYF-*x* solid solutions arises from the crystal structural distortion and an unpaired electron on the substituting Yb^{3+} ion. From our previous work [23] and the results presented in Chapter 3, it is shown that the BDF-*x* solid solution substantially increases the ferromagnetism due to structural distortion and unpaired electrons. In order to systematically understand the enhancement of ferromagnetism in BFO by structural distortion with one unpaired electron, the BYF-*x* solid solution has been studied. There are three types of magnetic interactions in the BYF-*x* solid solution (similar to the BLY-*x* system presented in Chapter 4), which are the Fe^{3+}-O^{2-}-Fe^{3+} (Dzyaloshinskii–Moriya, denoted as DM interaction), the Yb^{3+}-O^{2-}-Fe^{3+} interaction and the Yb^{3+}-O^{2-}-Yb^{3+} interaction. The magnetization of BYF-*x* at a higher temperature range (50 K - 300 K) is dominated by the DM interaction and the Yb^{3+}-O^{2-}-Fe^{3+} interaction. The spin reorientation between Yb^{3+}-O^{2-}-Yb^{3+} is found at 8 K [146], which is characteristic of $YbFeO_3$. This study provides a better understanding of the fundamentals of the structure-property relation in BFO. In this chapter, the effects of structure distortion and unpaired electrons on Bi-

based solid solution were studied. Yb has larger ionic radii with one unpaired electron than Lu. By comparative study of these solid solutions, the effect of unpaired electrons on magnetization can be systematically studied.

5.3 Experimental

5.3.1 Synthesis

The ceramic samples of the (1−*x*)$BiFeO_3$ –*x*$YbFeO_3$ (denoted as BYF-*x*) solid solution were prepared by using solid state reactions. The starting materials Bi_2O_3 (99.975%), Fe_2O_3 (99%) and Yb_2O_3 (99.9%) were weighed accurately to four significant digits according to the stoichiometirc chemical formula:

$$\frac{(1-x)}{2}\mathrm{Bi_2O_3} + \frac{x}{2}\mathrm{Yb_2O_3} + \frac{1}{2}\mathrm{Fe_2O_3} \rightarrow (1-x)\mathrm{BiFeO_3} - x\mathrm{YbFeO_3} \quad (5.1)$$

The reagents for each composition were mixed and ground by ball milling for 24 h. Ball milling container was setup as 25.0 ml bottle with 15.0 ml of ethanol and 40 zirconium oxide balls. The mixed powders were pressed into pellets, packed down into platinum crucible and then calcined in furnace at 840 °C for 4 h. After the calcinations, the sample discs were reground by ball milling for 18 h, then the sample powders were mixed with 0.15 ml of 5% polyvinyl alcohol (PVA) as binder. The powders were pressed into pellets again and then subsequently heated at 650 °C for one hour to evaporate the binder. The calcination temperature and sintering temperature are increased up to 850 °C and 950 °C, respectively with correspondence of increased concentration of Yb. Afterwards, the pellets were packed down into platinum crucible which was sealed inside a lager Al_2O_3 crucible, and then sintered at 900 °C for 4 h.

5.3.2 Structural Analysis

X-ray diffractions of as-sintered ceramics were performed on a Bruker D-8 diffractometer using Cu K_α radiation (40 mA, 40 kV, 0.01° steps and 2θ = 15 - 80°) to analyze the phase purity and to determine the crystal structure. $BiFeO_3$ single crystals

were ground into a powder and XRD data were collected and used as a structural reference. The resulting patterns were analyzed using TOPAS-Academic Software by Rietveld refinements to determine the symmetry, lattice parameters, and atomic positions of the solid solutions.

5.3.3 Ferroelectric and Magnetic Measurements

Ferroelectric hysteresis loops were displayed using a RT66A ferroelectric testing system (Radian Technology), connected to a Trek 609E-6 high voltage bipolar amplifier. Magnetic measurements were performed using a Quantum Design MPMS-XL SQUID magnetometer.

5.4 Results and Discussion

5.4.1 Structural Analysis

The structure of the BYF-*x* (*x* = 0.05 - 0.20) solid solutions was analyzed by X-ray diffraction. Figure 5.1 shows the XRD patterns for BYF-*x* (*x* = 0.05 - 0.20) at room temperature. A noticeable change of lattice parameter is observed in the Yb-substituted samples. For $x < 0.11$, the solid solutions are of rhombohedral *R*3*c* symmetry. In the composition range of *x* = 0.12 - 0.15, a morphotropic phase boundary (MPB) was formed, with a mixture of the rhombohedral *R*3*c* phase and the orthorhombic *Pbnm* phase. The percentages of each phase were analyzed by the Rietveld refinements. When $x > 0.15$, the solid solution is orthorhombic perovskite with *Pbnm* space group. In both the rhombohedral and orthorhombic phase regions, the perovskite peaks are shifted toward higher 2-theta angles with increasing Yb content, implying a shrinkage of the unit cell due to the fact that the ionic radius of the Yb^{3+} (0.985 Å) is smaller than that of Bi^{3+} (1.17 Å). Due to the kinetics of the $BiFeO_3$ formation and the evaporation of Bi_2O_3, the $Bi_2Fe_4O_9$ impurity phase was observed in the samples for *x* < 0.09. Oxygen vacancies will form due to the volatility of Bi^{3+} ions and the conversion of Fe^{3+} into Fe^{2+}

ions in pure BFO ceramics [142]. With the substitution of Yb for Bi in BFO, Bi_2O_3 volatilization is reduced and the formations of oxygen vacancy and impurity phases are suppressed, leading to the disappearance of impurity phase with the further increase of Yb content to $x \geq 0.09$.

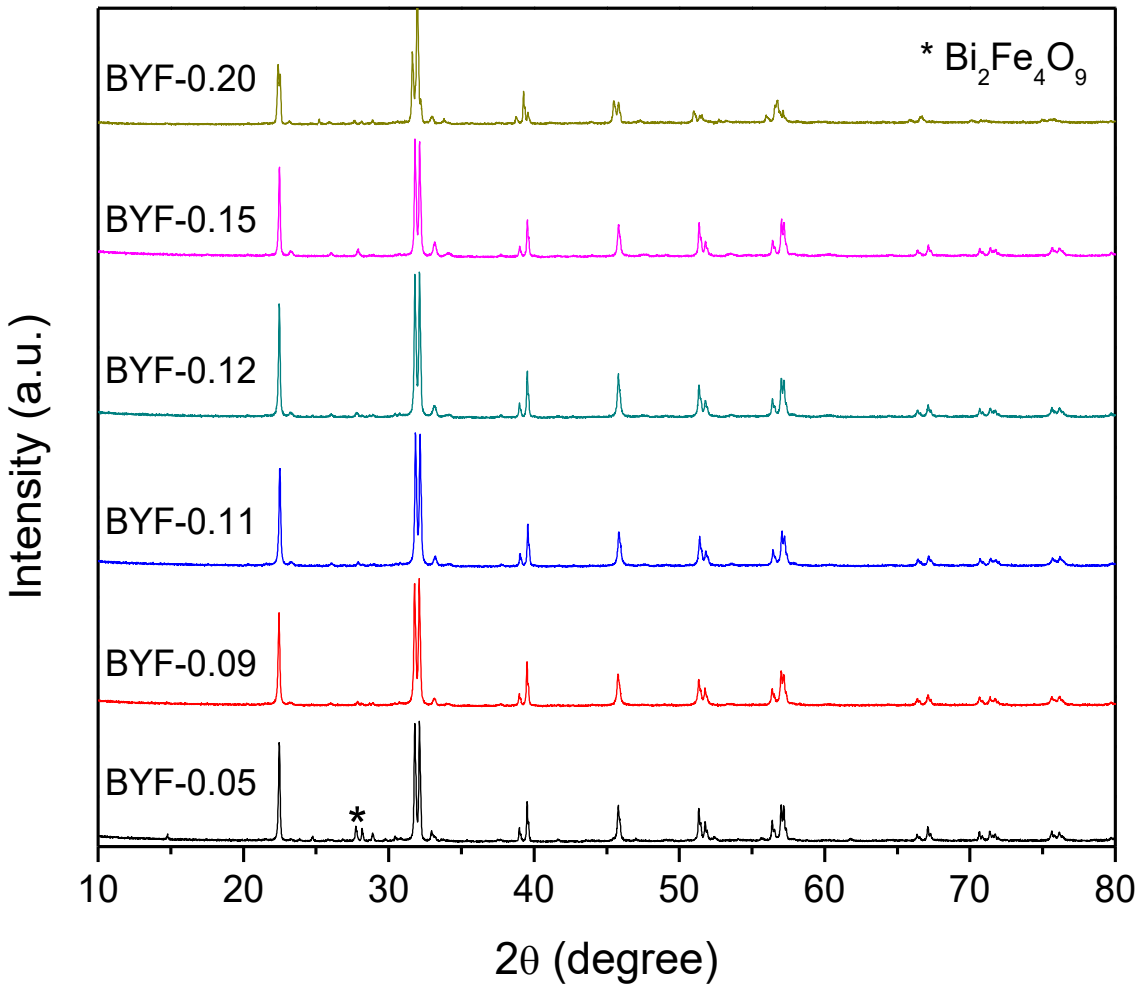

Figure 5.1 **X-ray diffraction patterns of the BYF-*x* (*x* = 0.05 - 0.20) ceramics prepared at sintering temperatures (T = 900 °C). Stars indicate the peaks of $Bi_2Fe_4O_9$ impurity phase.**

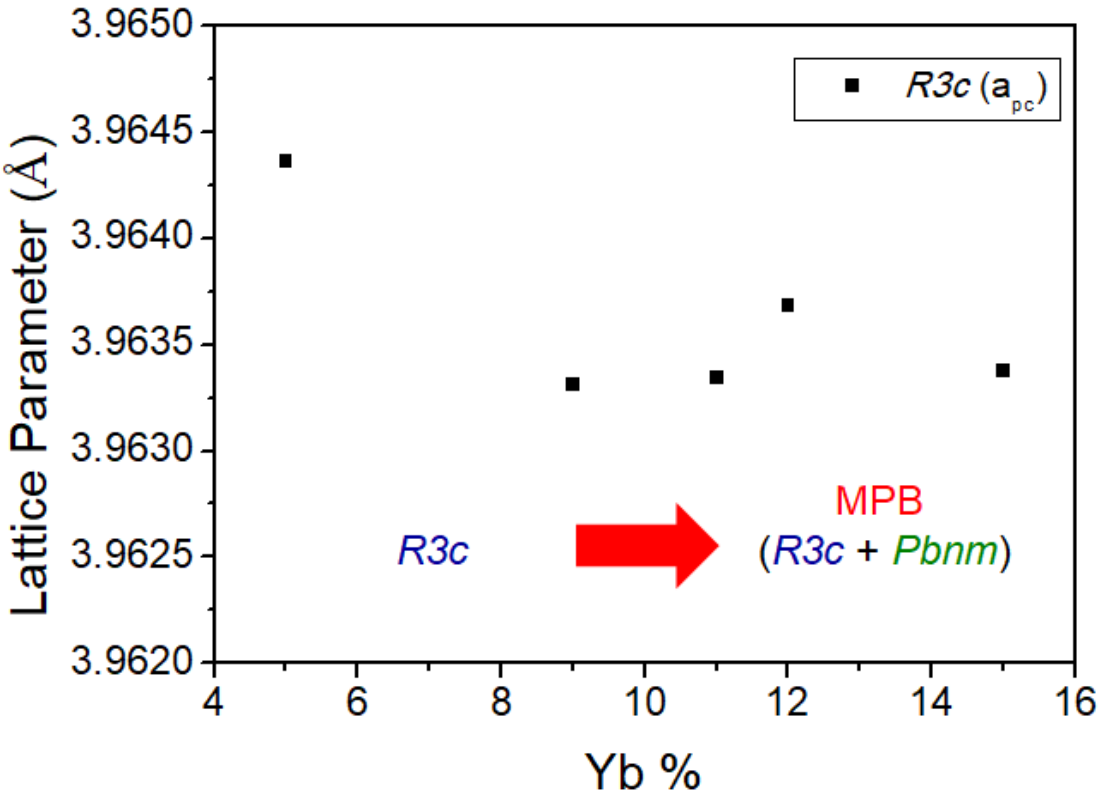

Figure 5.2 **Variation of the lattice parameter of the BYF-*x* (*x* = 0.05 - 0.15) ceramics as a function of composition in the pure rhombohedral (*R*3*c*) phase with lattice parameter a_{pc}.**

The structure evolution of the BYF-*x* solid solution at various temperatures was studied by high temperature X-ray diffraction. Figure 5.3 shows the XRD pattern of BYF-0.11 measured at various temperatures. The structure of BYF-0.11 changes from a pure rhombohedral phase to a mixture phases of rhombohedral and orthorhombic phases as temperature increases. The phase percentage of the *R*3*c* and *Pbnm* phases are as shown in Figure 5.4, which indicates that the structure of BYF-0.11 changes from a pure rhombohedral phase to a mixture of rhombohedral and orthorhombic phases as temperature increases. The major structure change from the rhombohedral phase to orthorhombic phases is observed at around 700 °C. When *x* = 0.12, the pseudocubic lattice parameter, a_{pc} for the R3c rhombohedral structure slightly changes to the pseudocubic lattice parameters a_{pc} and c_{pc} for the Pbnm orthorhombic phase appear,

indicating that the phase transition from the *R*3*c* rhombohedral phase to the Pbnm orthorhombic phase which is induced by the substitution of Yb for Bi, as shown in Figure 5.5

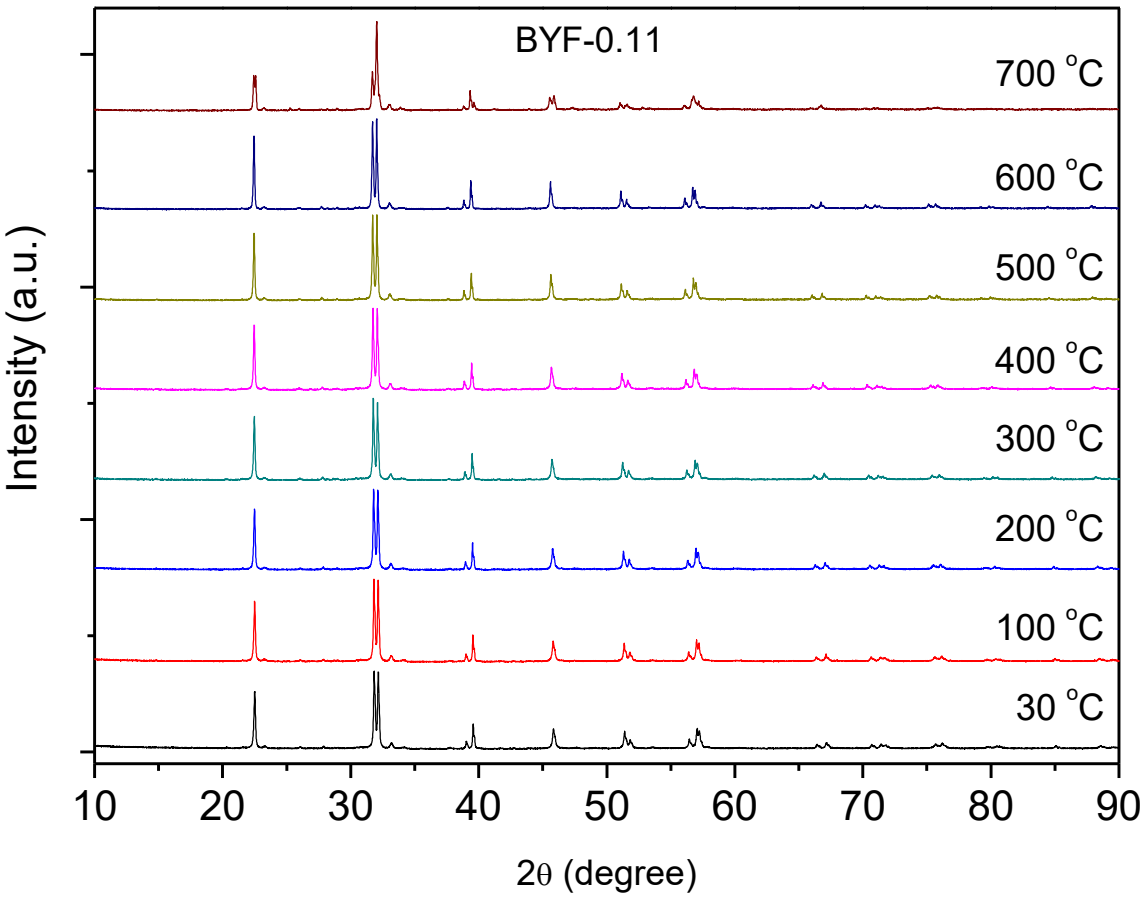

Figure 5.3 **X-ray diffraction patterns of the BYF-0.11 ceramics measured at various temperatures.**

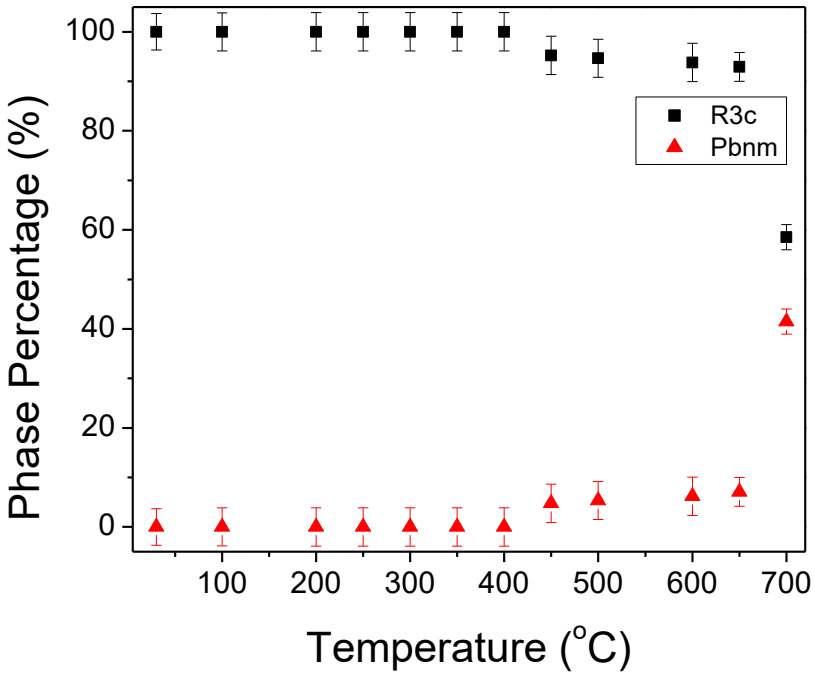

Figure 5.4 **Phase percentage of BYF-0.11 ceramics as a function of temperature.**

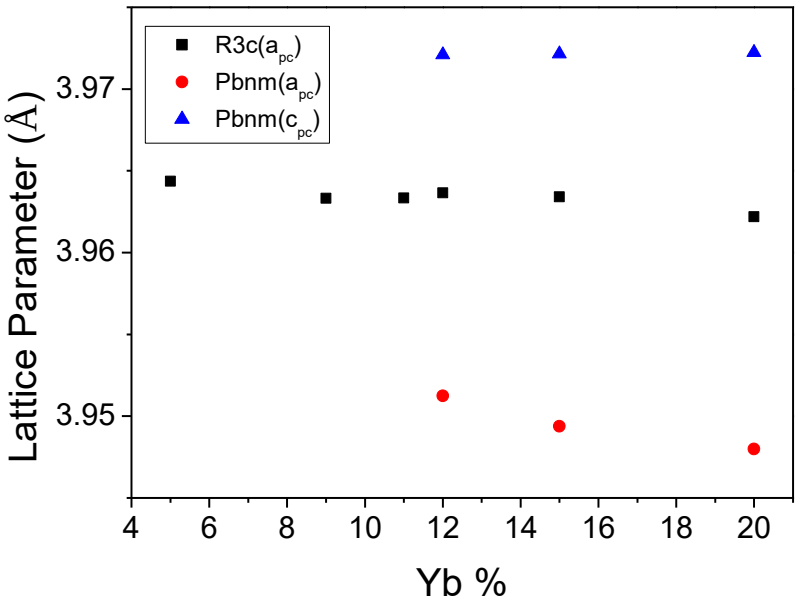

Figure 5.5 **(a) Rhombohedral (*R*3*c*) and orthorhombic (*Pbnm*) phase percentage as a function of composition for the BYF-*x* (*x* = 0.05 - 0.20) ceramics. (b) Variation of the lattice parameter of BYF-*x* (*x* = 0.05 - 0.20) ceramics as a function of composition in the pure rhombohedral (*R*3*c*) phase, and in the MPB (rhombohedral *R*3*c* phase + orthorhombic *Pbnm* phase). The cell parameters are described in a pseudocubic cell, a_{pc} for the *R*3*c* phase, and c_{pc} for the *Pbnm* phase.**

5.4.2 Ferroelectric Properties

Figure 5.6 shows the ferroelectric hysteresis (P-E) loop of the BYF-0.11 samples displayed at room temperature. A partially saturated P-E loop with a small leakage feature is observed for the Yb-substituted BFO (x = 0.11) of rhombohedral (*R3c*) composition, with a remnant polarization of 4.0 $\mu C/cm^2$. The calculated spontaneous polarizations of BYF-x (x = 0.05 - 0.15) at room temperature are shown in Figure 5.7. With the increase of the Yb concentration, the polarization is significantly enhanced as the composition enters the MPB region. The enhanced ferroelectric properties can be attributed to the stronger tendency of the coexistence of rhombohedral and orthorhombic phases. The BYF-0.11 ceramics has a calculated spontaneous polarization of 7.7 $\mu C/cm^2$ at room temperature, which is slightly higher than the experimental value extracted from the unsaturated P-E loop.

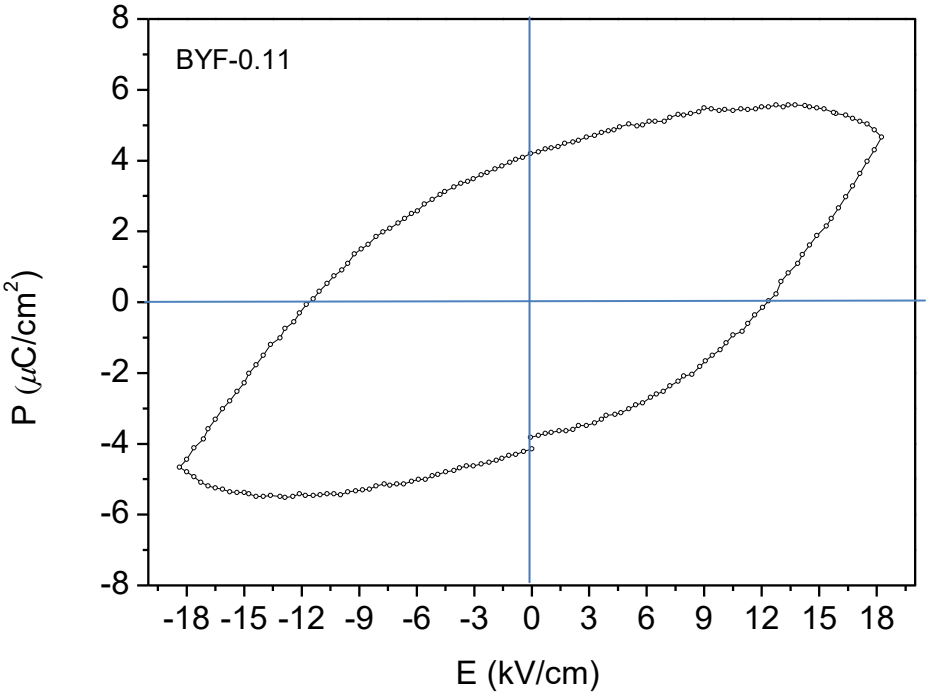

Figure 5.6 Polarization electric field (P-E) loop of the BYF-0.11 solid solution displayed at room temperature.

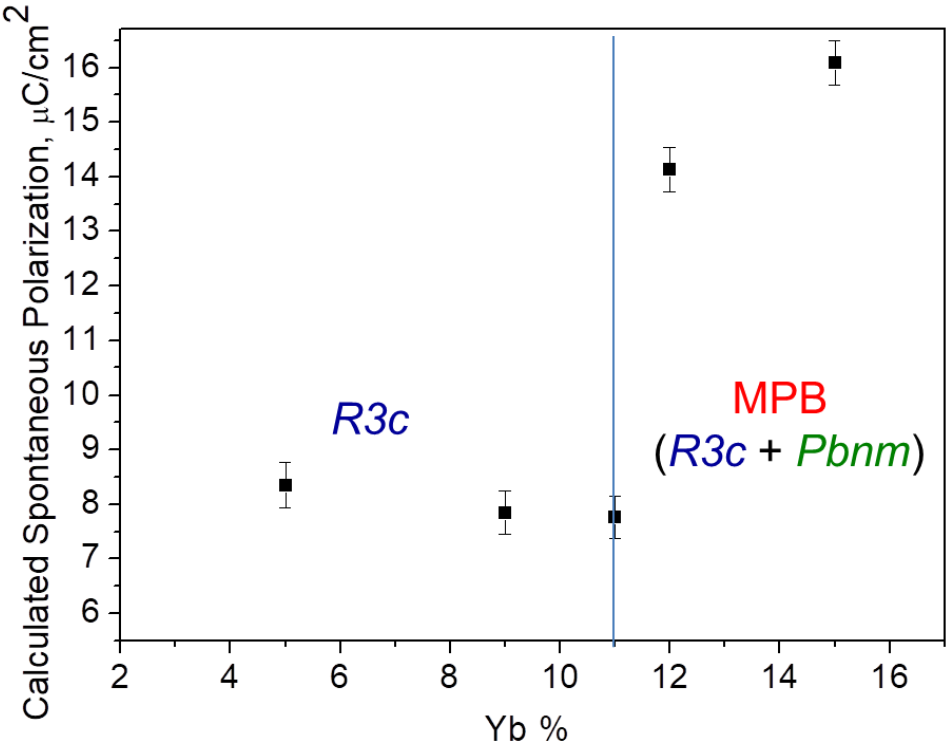

Figure 5.7 **The calculated spontaneous polarization as a function of the composition for the BYF-*x* (*x* = 0.05 - 0.15) solid solutions.**

5.4.3 Temperature-Composition Phase Diagram for the $BiFeO_3$-$YbFeO_3$ System

Based on the results obtained above, a phase diagram is established for the BYF-*x* solid solution in terms of temperature and composition, based on the high-temperature X-ray diffraction and Rietveld refinements, as shown in Figure 5.8. The Yb-substituted BFO ceramics undergo a phase transition from the rhombohedral *R*3*c* to the MPB, and then to the orthorhombic *Pbnm* phase with the increasing $YbFeO_3$ concentration at room temperature. In the composition region of $0.11 \leq x < 0.15$, an MPB is identified, in which the rhombohedral *R3c* and orthorhombic *Pbnm* phases in a comparable amount are resolved. In the composition region of $0.11 \leq x < 0.15$, the structure undergoes a phase transition from the mixed phase of MPB to the pure

orthorhombic orthoferrite *Pbnm* phase with temperature increased at and above 700 °C, this is different from the phase diagram of the (1-x)$BiFeO_3$-x$LuFeO_3$ solid solution system which exhibits an almost vertical MPB region within the same temperature range (Chapter 4).

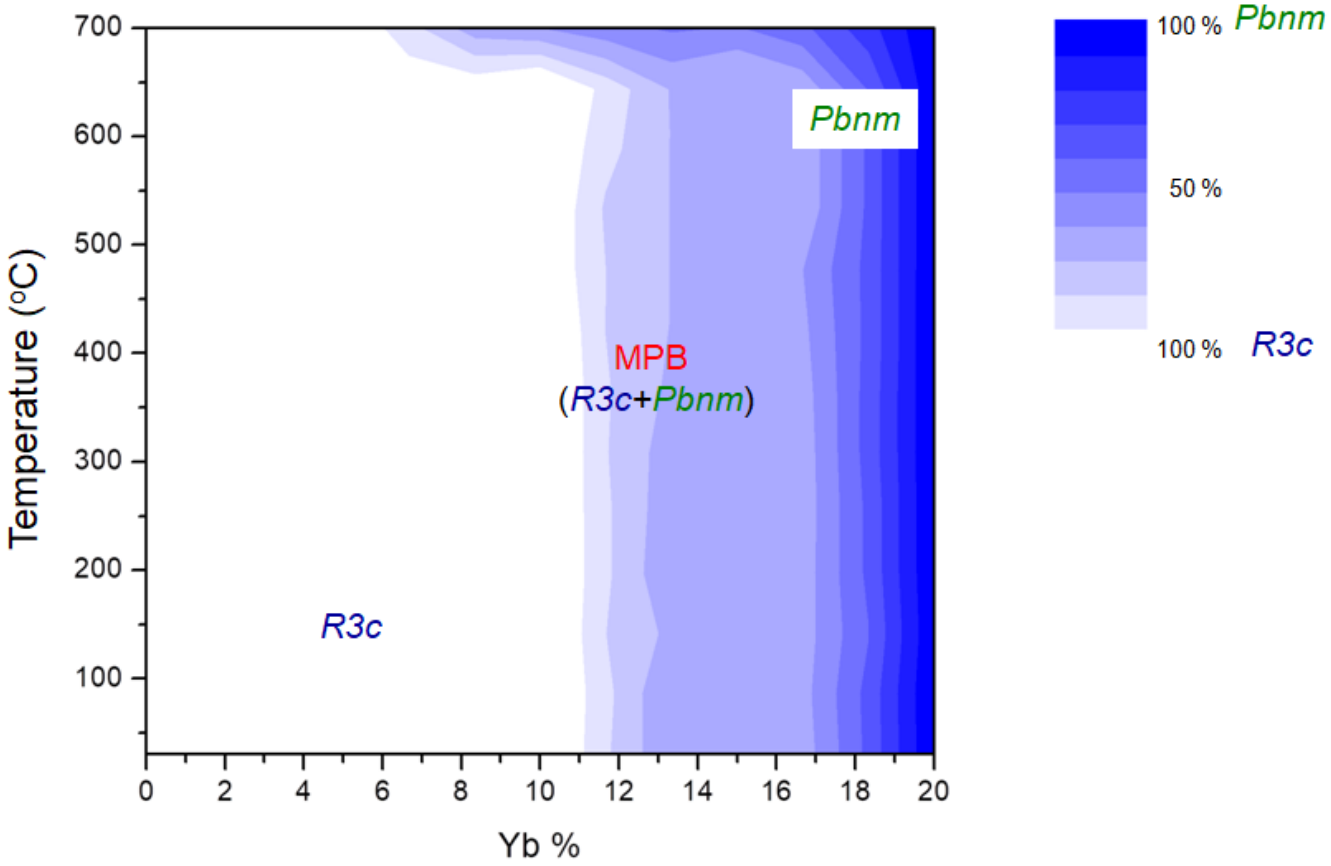

Figure 5.8 **Partial phase diagram of the (1-*x*)$BiFeO_3$-*x*$YbFeO_3$ (BYF-*x*) solid solution system, indicating the pure rhombohedral phase, the MPB with a mixture of the rhombohedral and orthorhombic phases, and the pure orthorhombic phase.**

5.4.4 Magnetic Characterization of the BYF-*x* Solid Solution

The temperature dependence of the magnetization measured upon field-cooling under 100 Oe for the BYF-*x* (*x* = 0.05 - 0.30) samples is shown in Figure 5.9. The BYF-0.05 sample exhibits a monotonic increase of magnetization with decreasing temperature from 300 K to 5 K. Because the concentration of the magnetic Yb^{3+} ion in BYF-0.05 is too low to form a long range *A*-site magnetic ordering, the Yb^{3+} spin reorientation was not observed.

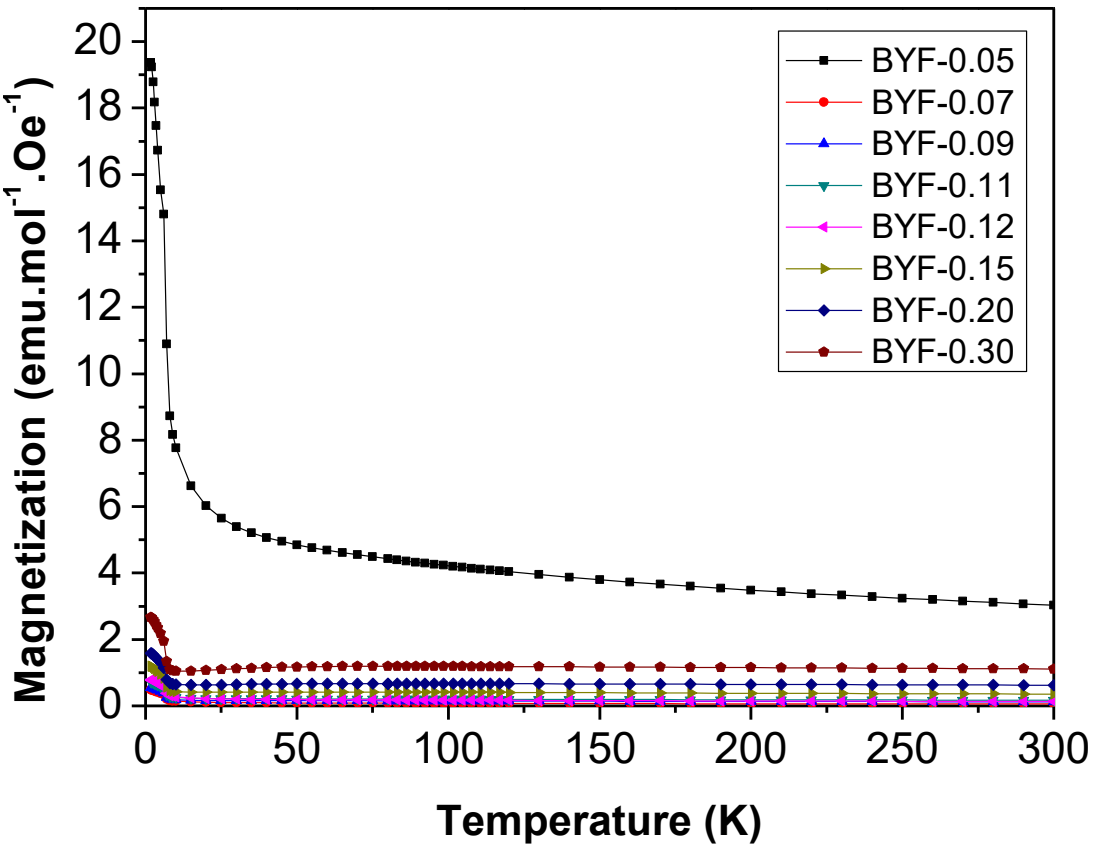

Figure 5.9 Temperature dependence of magnetization measured in field-cooling (FC, 100Oe) for the BYF-*x* (*x* = 0.05 - 0.30) samples.

Upon cooling, the canted antiferromagnetism of the Fe sublattices is antiparallel by coupled to the spin moment of the Yb sublattice. During cooling, the magnetic moment of the Yb sublattice start to order and it is anti-aligned to the Fe sublattices, and

this is the reason why at higher concentration of $YbFeO_3$ (x = 0.20 - 0.30) slightly decreased magnetic moments was observed at a lower temperature range. The magnetic anomalies at around 8 K in BYF-x (x = 0.07 - 0.30) could arise from the spin reorientation of the Yb^{3+} moments, as observed in $YbFeO_3$ and other orthoferrites with the orthorhombic phase (*Pnma*) [19]. The schematic spin structures for BYF-x are in the corresponding temperature ranges, are shown in Figure 5.10. The net magnetization starts to increase at 8 K because the paramagnetic Yb^{3+} aligned (oriented parallel) with the external magnetic field (100 Oe), corresponding to the onset of the (weak) ferromagnetic ordering.

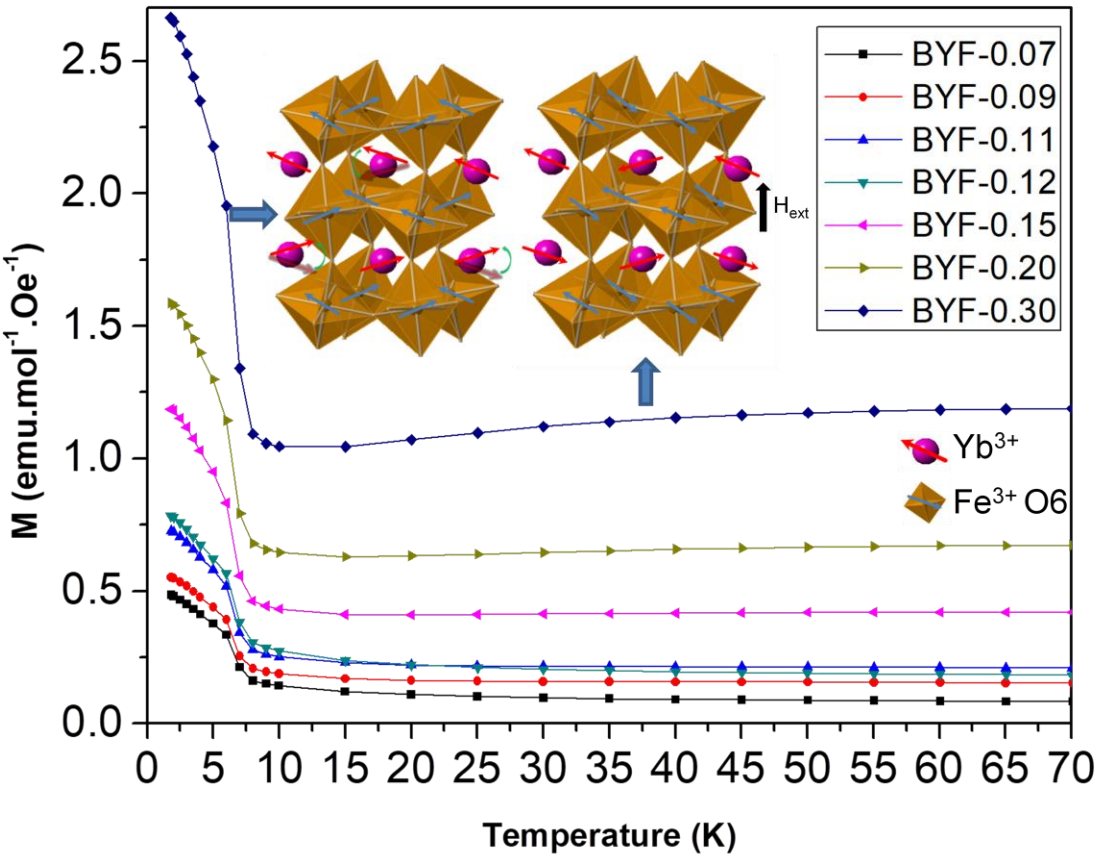

Figure 5.10 **Temperature dependence of the magnetization measured in field-cooling (FC) for BYF-x (x = 0.07 - 0.30), with the schematic spin structures shown for the different temperature ranges.**

BFO is known to be antiferromagnetic with a G-type magnetic structure which exhibits a typical linear variation of the magnetization as a function of the magnetic field [144]. The magnetic hysteresis (*M-H*) curves of the BYF-*x* ($0.05 \leq x \leq 0.30$) solid solutions measured at 300 K and 5 K are shown in Figure 5.11 (a) and (b), respectively. With the decrease of temperature, a noticeable change occurred from a straight line to a ferromagnetic *M-H* hysteresis loops, indicating the presence of spontaneous magnetization that is induced by the Yb^{3+} substitution for Bi^{3+}. Even at room temperature, a weak ferromagnetism was displayed in the compositions of $x \leq 0.15$ by a slim magnetic hysteresis loop, with a residual magnetization of 0.025 μ_B/f.u for $x = 0.15$. At a lower temperature (5 K), all of the substituted samples exhibit ferromagnetic behaviour, and a large saturated magnetization of 0.05 μ_B/f.u. was observed in BLF-0.30 composition. These results show that the introduction of Yb^{3+} on the perovskite *A*-site has enhanced the magnetic properties of $BiFeO_3$ because of the effect of structural modifications and the one unpaired electron on Yb^{3+}. Indeed, the weak ferromagnetism in BYF-0.15 at room temperature is believed to arise from a structural distortion introduced by the Yb^{3+} ion with a smaller ionic radius (0.985 Å) than that of Bi^{3+} (1.17Å), which disrupts the spiral spin modulation in $BiFeO_3$. Their hysteresis loops exhibited ferromagnetic hysteretic behaviour with saturation, in which the Yb-doped samples have a larger saturation magnetization compared with the pure BFO ceramics. Therefore, the enhanced ferromagnetic property may be attributed to Yb substitution, which could disrupt the spin cycloid structure, and trigger a variation in the canting angles of the Fe-O-Fe bonds [147], giving rise to a net magnetization and the enhanced ferromagnetism.

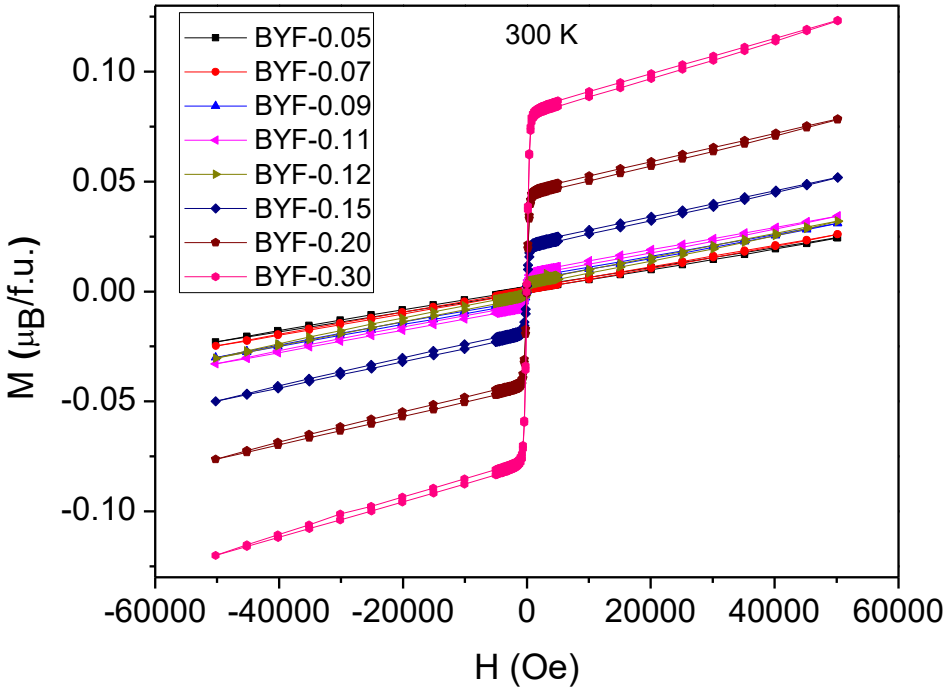

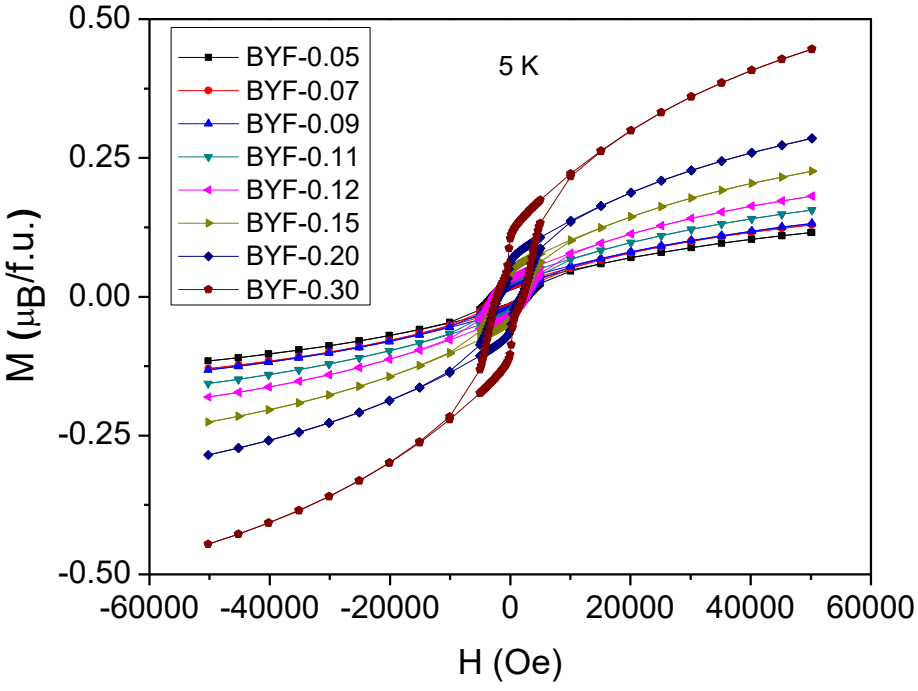

Figure 5.11 **(a) Magnetic M (H) hysteresis loops of the BYF-*x* (*x* = 0.05 - 0.30) ceramics measured at (a) 300 K, (b) 5 K.**

The calculated spontaneous polarization and the measured spontaneous magnetization of BYF-*x* (*x* = 0.05 - 0.15) are shown in Figure 5.12. The electric and magnetic properties both show an increase in the MPB region. This phenomenon is due to the introduction of Yb^{3+} which leads to the formation of the morphotrophic phase boundary, where the rhombohedral and orthorhombic phases coexist, trigging structural distortion and enhancing the ferromagnetic interactions. These properties entitle the BYF-*x* solid solutions a multiferroic material. The results obtained in this part indicate that magnetic properties of the Yb-substituted samples are improved compared with the BFO ceramics. Therefore, the influence of the structural distortion upon the magnetic properties of the Yb-substituted samples seems to play an important role. The distortions of the lattice structure and the change of crystal field symmetry induced by Yb-substitution at Bi-sites destroy the cycloidal spin magnetic ordering and release the (weak) ferromagnetism, resulting in the enhancement of the ferromagnetism in the BYF-*x* solid solutions [148].

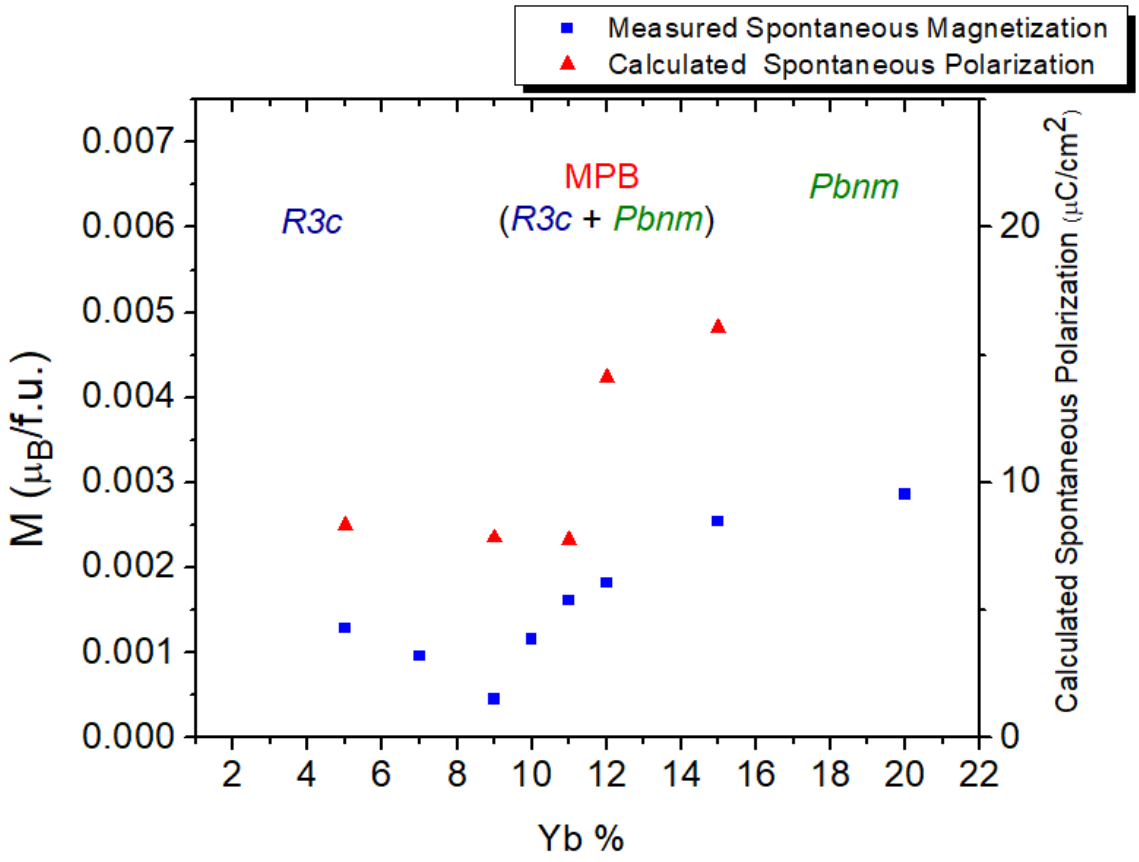

Figure 5.12 The spontaneous magnetization and calculated spontaneous polarization of (1-*x*)$BiFeO_3$-*x*$YbFeO_3$ (BYF-*x*) solid solutions as a function of Yb concentration at 300 K.

5.5 Conclusions

The solid solution of (1-*x*)$BiFeO_3$-*x*$YbFeO_3$ (BYF-*x*) have been successfully synthesized in the perovskite structure in the form of ceramics using the solid state reaction method. The temperature-composition phase diagram of BLF-*x* is constructed and their structure and multiferroic properties are systematically studied. When x < 0.11, the structure remains a rhombohedral perovskite phase with *R*3*c* space group. With an increasing substitution amount of $YbFeO_3$, an morphotropic phase boundary (MPB) region appears in the composition range of *x* = 0.11 - 0.15. With the further increase of the substitution amount of $YbFeO_3$, the structural phase transition from rhombohedral

perovskite *R*3*c* phase to the orthorhombic orthoferrite *Pbnm* phase is observed at $x \geq 0.20$. The polarization-electric field (P-E) hysteresis loop of ferroelectric properties was displayed in the BYF-0.11 ceramics, with the remnant polarization of 4 $\mu C/cm^2$ at room temperature**.** The chemically modified BYF-*x* (x = 0.05 - 0.30) exhibit weak ferromagnetism at room temperature. The BYF-0.30 solid solution exhibit a large saturated magnetization (M_s = 0.5 μB/f.u.) at 5 K. The simultaneous ferroelectric and ferromagnetic properties make the BYF-*x* solid solution one of the few single-phase multiferroic materials that exhibit both magnetization and electric polarization at room temperature. The present results provide an alternative way to improve the ferromagnetic and ferroelectric properties for BFO-based solid solutions. This work confirms the beneficial role of the rare-earth substitution in enhancing the multiferroic properties of BFO, making it a more viable material for potential applications as magnetoelectric and spintronics devices.

In this chapter, the spontaneous magnetization of (1-*x*)$BiFeO_3$-*x*$YbFeO_3$ solid solution was further improved compared with the (1-*x*)$BiFeO_3$-*x*$LuFeO_3$ solid solution. This is due to the unpaired electrons in the Yb^{3+} ions. In the next chapter, in order to further investigate the effect of unpaired electrons, the (1-*x*)$BiFeO_3$-*x*$ErFeO_3$ solid solutions were synthesized. Er^{3+} has larger ionic radii and two more unpaired electrons than Yb. By comparative study of these solid solutions, the effect of unpaired electrons on magnetization can be systematically studied.

Chapter 6.

Synthesis, Structure, and Characterization of the (1-*x*)$BiFeO_3$-*x*$ErFeO_3$ Solid Solution: A Multiferroic System Exhibiting Magnetic Pole Inversion

6.1 Abstract

The (1-x)$BiFeO_3$-*x*$YbFeO_3$ multiferroic solid solution system in Chapter 5 shows enhanced ferromagnetic and ferroelectric properties. Therefore, the effects with different number of unpaired electrons and ionic radii are systematically studied in this chapter. Er^{3+} is chosen and studied in this chapter because it has a larger ionic radius (1.004 Å) and a larger number of unpaired electrons (3) than that of Yb^{3+} (0.985 Å, 0 numbers of unpaired electrons). An interesting magnetic phenomenon called "magnetic pole inversion" is observed in the (1-*x*)$BiFeO_3$-*x*$ErFeO_3$ solid solution.

The (1-x)$BiFeO_3$-*x*$ErFeO_3$ (denoted as BErF-*x*) solid solutions have been synthesized by solid state reaction method and characterized by various techniques. The crystal structure and multiferroic properties of various compositions were systematically investigated. The high temperature phase diagram of the solid solutions has been established. Rietveld refinements showed that the sample crystallized in a rhombohedral *R*3*c* structure. With the increasing concentration of Er, the crystal structure transforms from the rhombohedral *R*3*c* phase to an orthorhombic *Pbnm* phase. The structure remains rhombohedral with *R*3*c* space group for $x < 0.12$. With further increase of the Er concentration, an morphotropic phase boundary (MPB) region is found to exist in the composition range of $0.12 \leq x < 0.15$. A single phase orthorhombic *Pbnm* structure was observed for $x \geq 0.20$. It is found that the magnetic properties of BErF-*x* exhibit an unusual behaviour, i.e. the magnetic pole inversion. In most of the

ferromagnets, the magnetic moment directions can be changed by applying a sufficiently high magnetic field, but not by temperature, since temperature usually only affects the magnitude of a magnetic moment, rather than its magnetic directions. Upon cooling below the magnetic phase transition temperature, most magnets exhibit a monotonic increase in magnetization. In this BErF-*x* system, the magnetic pole is found to change sign (inversion) at low temperatures. In addition, the magnetic pole inversion behaviour can be tuned by changing the concentration of the magnetic ion Er^{3+} in the BErF-*x* (*x* = 0.12 - 0.20) solid solutions. This study provides a better understanding of the enhanced multiferroic properties in the $BiFeO_3$-based multiferroic materials.

6.2 Introduction

In most of the ferromagnets, the magnetic moment directions can be significantly changed by applying sufficiently high external magnetic field rather than varying temperature. The temperature usually affects the magnitude of a magnetic moment, rather than its magnetic directions. Upon cooling below the magnetic phase transition temperature, most magnets exhibit a monotonic increase rather than the magnetic pole inversion. The terminology ‘‘magnetic pole inversion’’ (or magnetic reversal) is defined as a crossover of dc magnetization from a positive value to a negative value as a function of temperature in materials below their magnetic ordering temperature in my previous work [149]. The objective of this work is to design and prepare new magnetic materials that exhibit magnetic pole inversion with a change in temperature, and also to show that the temperature at which the magnetization changes its polarity (T_m) can be tuned by the change of composition. In this work, the (1-*x*)$BiFeO_3$-*x*$ErFeO_3$ (denoted BErF-*x*) solid solution is found to be one of the promising multiferroics with an unusual magnetic pole inversion. The magnetic pole inversion behaviour can be tuned by changing the concentration of the magnetic ion Er^{3+} in the BErF-*x* (*x* = 0.12 - 0.20) solid solution, and can be observed in relatively high Er^{3+} concentrations. Because of these complex interactions phenomenon, magnetic pole inversion may occur, leading to the reduced net magnetic moment in the BErF-*x* solid solution with the decrease of temperature. Furthermore, the magnetic pole inversion temperature can also be tuned by changing the concentration of Er. The results of this work reveal the effects of the

substitution of Er on the structural symmetry and properties of the $BiFeO_3$-based multiferroic solid solution.

6.3 Experimental

6.3.1 Synthesis

The ceramic samples of the (1-*x*)$BiFeO_3$-*x*$ErFeO_3$ (BErF-*x*) solid solution were prepared by using solid state reactions. The starting materials: Bi_2O_3 (99.975%), Fe_2O_3 (99%) and Er_2O_3 (99.9%) were weighed accurately to four significant digits according to the chemical reaction:

$$\frac{(1-x)}{2}\mathrm{Bi_2O_3} + \frac{x}{2}\mathrm{Er_2O_3} + \frac{1}{2}\mathrm{Fe_2O_3} \rightarrow (1-x)\mathrm{BiFeO_3} - x\mathrm{ErFeO_3} \qquad (6.1)$$

Each composition was mixed and ground by ball milling for 24 h. Ball milling container was setup as 25.0 ml bottle with 15.0 ml of ethanol and 40 zirconium oxide balls.The mixed powders were pressed into pellets, packed into platinum crucible, and calcined at 840 °C for 4 h. After the calcination, the sample discs were reground by ball milling for 24 h and then the powders were mixed with 0.15 ml 5% polyvinyl alcohol (PVA) binder. The powders were pressed into pellets again and then heated at 650 °C for 1 h to evaporate the binder. After the elimination of the binder, the pellets were packed into platinum crucible which was sealed in a lager Al_2O_3 crucible, followed by sintering at 900 °C for 2 h. The calcination temperature and sintering temperature are increased up to 850 °C and 950 °C, respectively with correspondence of increased concentration of Er.

6.3.2 Structural Analysis and Magnetic Measurements

X-ray diffractions were performed on as-sintered ceramics on a Bruker D-8 diffractometer using Cu K_α radiation (40 mA, 40 kV, 0.01° steps and 2θ = 15 - 80°) to analyze the phase purity and to determine the crystal structure. $BiFeO_3$ single crystals

were ground into a powder and XRD data were collected and used as a structural reference for $BiFeO_3$. The resulting patterns were analyzed using TOPAS-Academic Software by Rietveld refinements to determine the symmetry, the lattice parameters, the average structure, and the atomic positions of the solid solutions. Magnetic measurements were performed as a function of temperature using a Quantum Design MPMS-XL SQUID magnetometer.

6.4 Results and Discussion

6.4.1 Structural Analysis

Figure 6.1 shows the XRD patterns for BErF-*x* (*x* = 0.03 - 0.20) at room temperature. A noticeable lattice parameter change can be observed in the Er-substituted samples. By increasing the Er concentration *x* from 0.03 to 0.20, the positions of all the peaks shift towards higher 2θ values. This tendency is the result of the different ionic radii between Er^{3+} ions (1.004 Å) and that of the Bi^{3+} ion (1.17 Å). For x < 0.10, the solid solution is of rhombohedral perovskite *R*3*c* structure. As the concentration of Er increased, a morphotropic phase boundary (MPB) is found to exist in the composition range of $0.10 \leq x < 0.15$. A mixture of two phases, the rhombohedral *R*3*c* and the orthorhombic *Pbnm*, is observed in the MPB region and the percentage of each phase was analyzed by the Rietveld refinements. With $x \geq 0.20$, the solid solution is of pure orthorhombic perovskite with the *Pbnm* space group. Therefore, three different structural regions are observed: the single rhombohedral structure for BErO-*x* ($x \leq 0.10$, the mixed rhombohedral and orthorhombic structures for BErO-*x* (*x* = 0.10 - 0.15), and the single orthorhombic structure for BErO-x ($x \geq 0.20$). Due to the kinetics of the $BiFeO_3$ formation and the evaporation of Bi_2O_3, the $Bi_2Fe_4O_9$ impurity phase was observed in trace amount in the samples for *x* < 0.1. Oxygen vacancies usually form due to the volatility of the Bi^{3+} ions and the reduction of Fe^{3+} into Fe^{2+} ions in pure BFO ceramics [142]. When Bi is substituted with Er in BFO, the Er-substitution reduces the Bi_2O_3 volatilization and suppresses the impurity phases and the oxygen vacancy formation. Eventually, the impurity disappeared as the amount of Er-substitution is increased to *x* = 0.08. A in the previous studies of the Dy-, Lu-, and Yb-substitutied $BiFeO_3$ solid

solutions, the subsitution of $ErFeO_3$ for $BiFeO_3$ up to the solubility limit is proven to be beneficial to the formation of pure and stable perovskite phase for the BFO-based solid solutions.

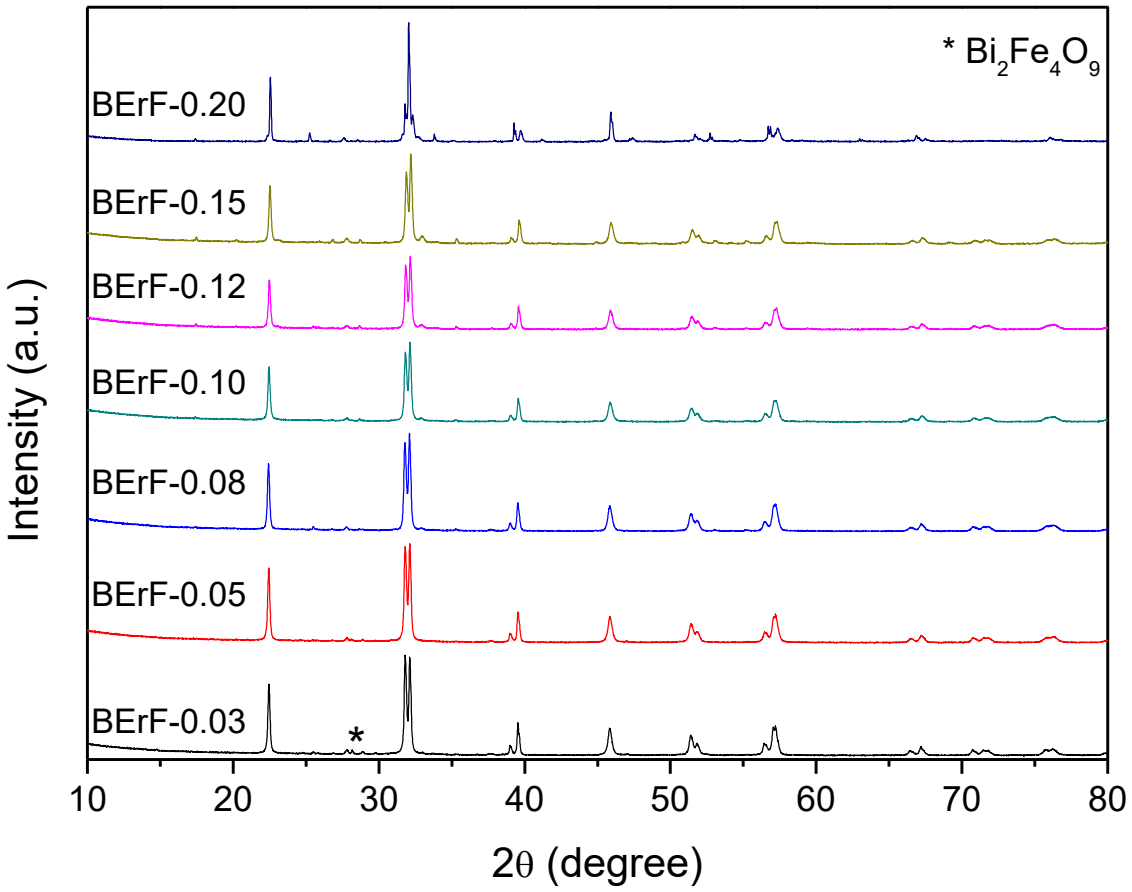

Figure 6.1 **X-ray diffraction patterns of the BErF-*x* (*x* = 0.03 - 0.20) ceramics prepared at optimal sintering temperatures (T = 900 °C). Stars indicate the peaks of the impurity phase of $Bi_2Fe_4O_9$.**

Figure 6.2 (a) shows the structure phase percentage for each composition of the BErF-*x* (*x* = 0.03 - 0.20) ceramics. The *R*3*c* phase fraction is gradually reduced while the amount of the orthorhombic phase is gradually increased with the increase of $EuFeO_3$ concentration from *x* = 0.03 to 0.15. At *x* = 0.15, the pseudocubic cell parameters, a_{pc} and c_{pc} for *Pbnm* orthorhombic phase, start to appear, as shown in Figure 6.2 (b), indicating that the phase of the solid solution partially transforms from the rhombohedral phase to the orthorhombic phase. With increasing Er concentration, the lattice parameter

is reduced, which is caused by the smaller ionic radius of Er^{3+} than that of Bi^{3+}. In order to remain in the perovskite structure, the BErF-*x* soild solution undergoes the transformation from the rhombohedral *R*3*c* to the orthorhombic *Pbnm,* through the bridging MPB with mixture of phases.

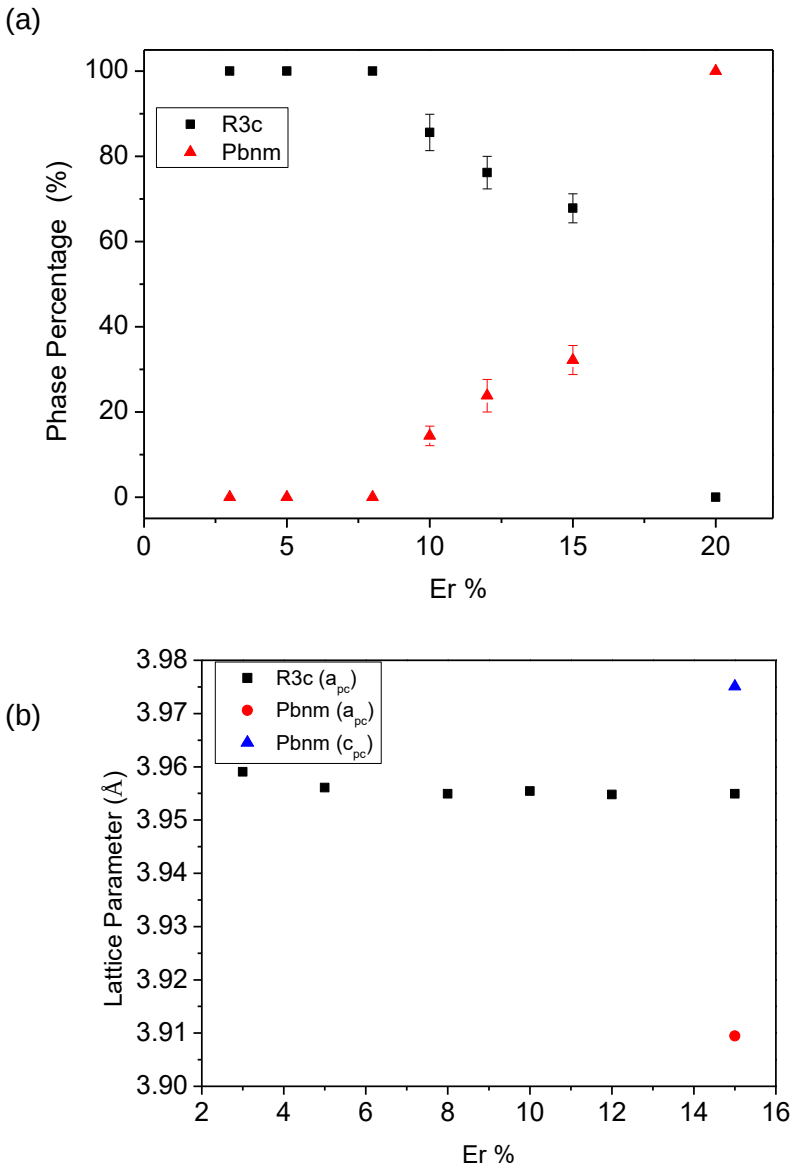

Figure 6.2 **(a) Rhombohedral (*R3c*) and orthorhombic (*Pbnm*) phase percentages as a function of composition for the BErF-*x* (*x* = 0.03-0.20) ceramics. (b) Compositional dependence of the unit cell parameters a of the BErF-*x* (*x* = 0.03-0.15) ceramics. The pseudocubic cell lattice parameters (a_{pc} = lattice parameters *a*, c_{pc} = lattice parameters *c*) as a function of Er compositions.**

The structure of the BErF-0.10 solid solution was studied by high-temperature X-ray diffraction. The high temperature X-ray diffraction was used to study the phase transition temperatures (*T*c) and to monitor the structural evolution of the BErF-*x* solid solution with temperature. Figure 6.3 shows the XRD patterns of BErF-0.10 at different temperatures (30 °C - 700 °C). Ar room temperature, the solid solution is in the MPB region with the coexistence of the rhombohedral *R*3*c* and orthorhombic *Pbnm* phases. The percentages of the *R*3*c* and *Pbnm* are slightly changed with increasing temperature up to 500 °C, as shown in Figure 6.4. A change in the phase percentages occurs at 550 °C with a crossover from the rhombohedral majority phase to the orthorhombic majority phase, abrupt indicating a transformation of phase components from the mixture of phases of MPB to a pure orthorhombic phase with the increase of temperature.

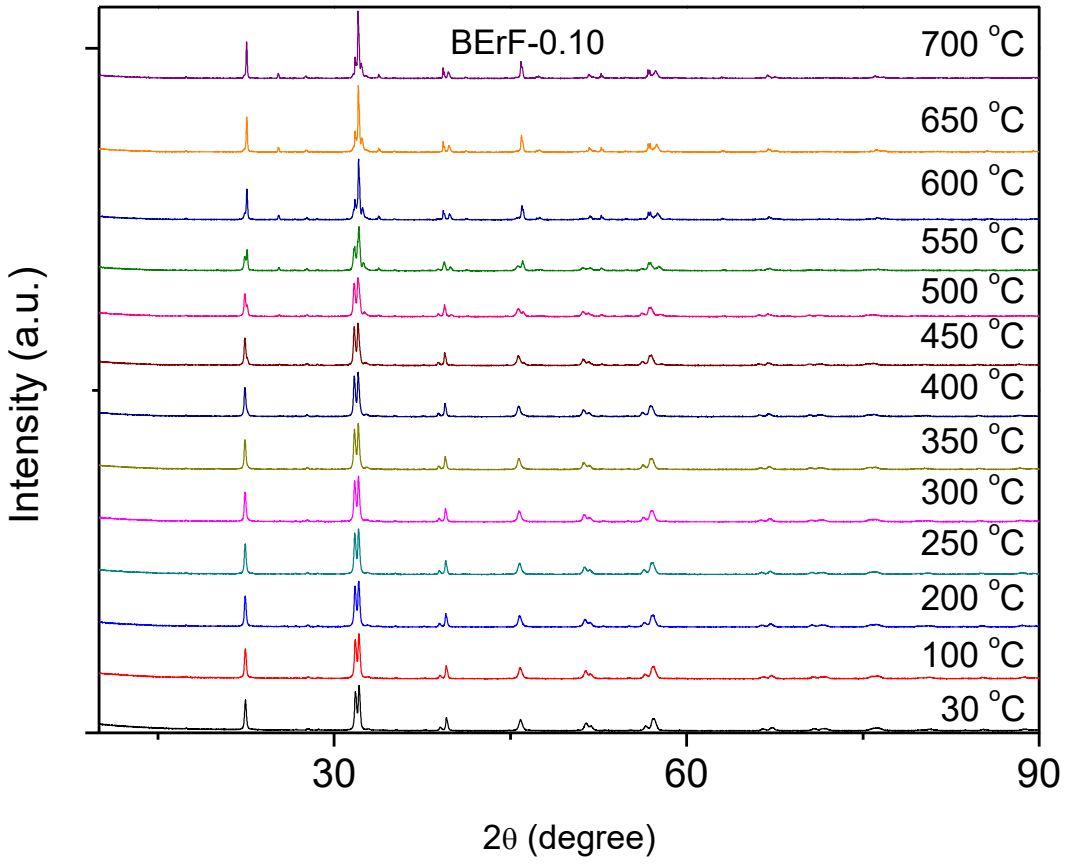

Figure 6.3 X-ray diffraction patterns of the BErF-0.10 ceramics at various temperature.

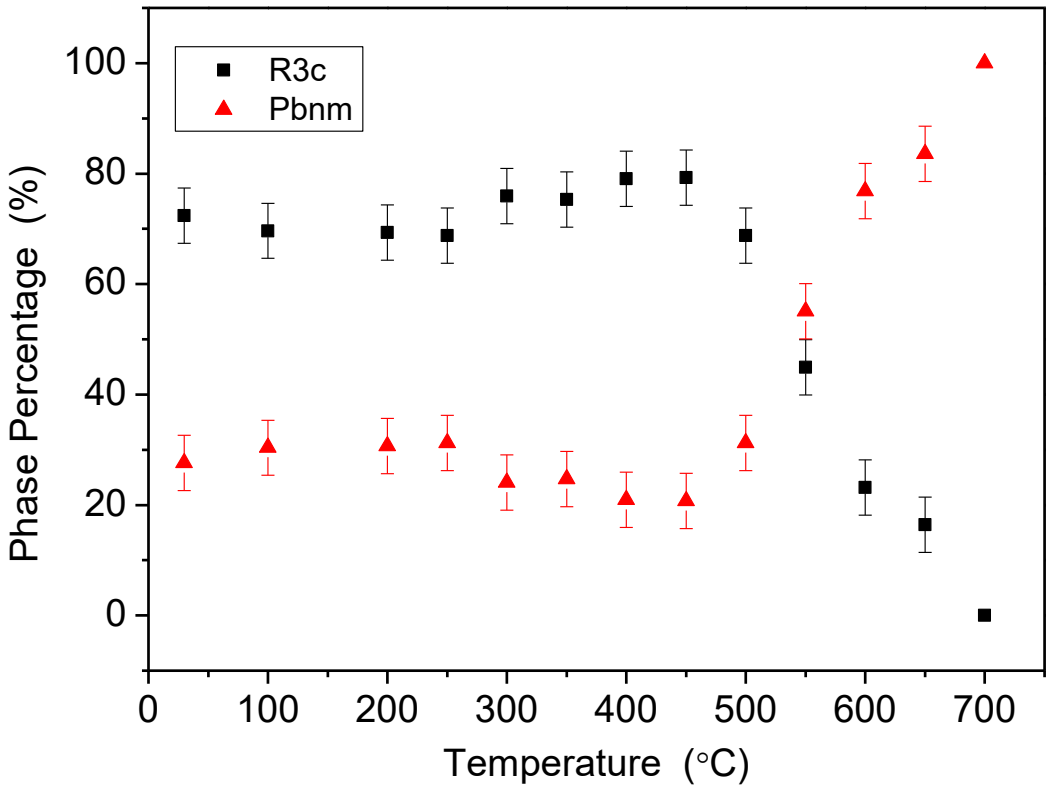

Figure 6.4 **Phase percentage for the BErF-0.10 ceramics with the variation of temperature.**

6.4.2 Temperature-Composition Phase Diagram for the (1-*x*)$BiFeO_3$-*x*$ErFeO_3$ Solid Solution

Based on the results obtained above, the high-temperature phase diagram of the BErF-*x* solid solution is established in terms of temperatures and composition, based on the X-ray diffraction and Rietveld refinement results, as shown in Figure 6.5. It depicts the effects of Er-substitution on the phase symmetry, phase components and phase transitions in the BErF-*x* system. The structure of BErF-*x* changes from the rhombohedral perovskite (*R3c*) to the orthorhombic orthoferrite (*Pbnm*) with the increasing amount of Er-substitution. The compositions of $x \leq 0.10$ with a dominant *R3c* phase undergo a phase transition from the rhombohedral *R3c* to the orthorhombic *Pbnm* upon heating as a result of a curved MPB region. The morphotropic phase boundary (MPB) is found to exist in the composition range of $0.10 \leq x < 0.15$ at room temperature.

With further increase of Er concentration, the phase components change from the MPB with a mixture of phases to the pure orthorhombic *Pbnm* phase. With the increase of temperature, the MPB region with mixed phases transforms to the pure Pbnm phase.

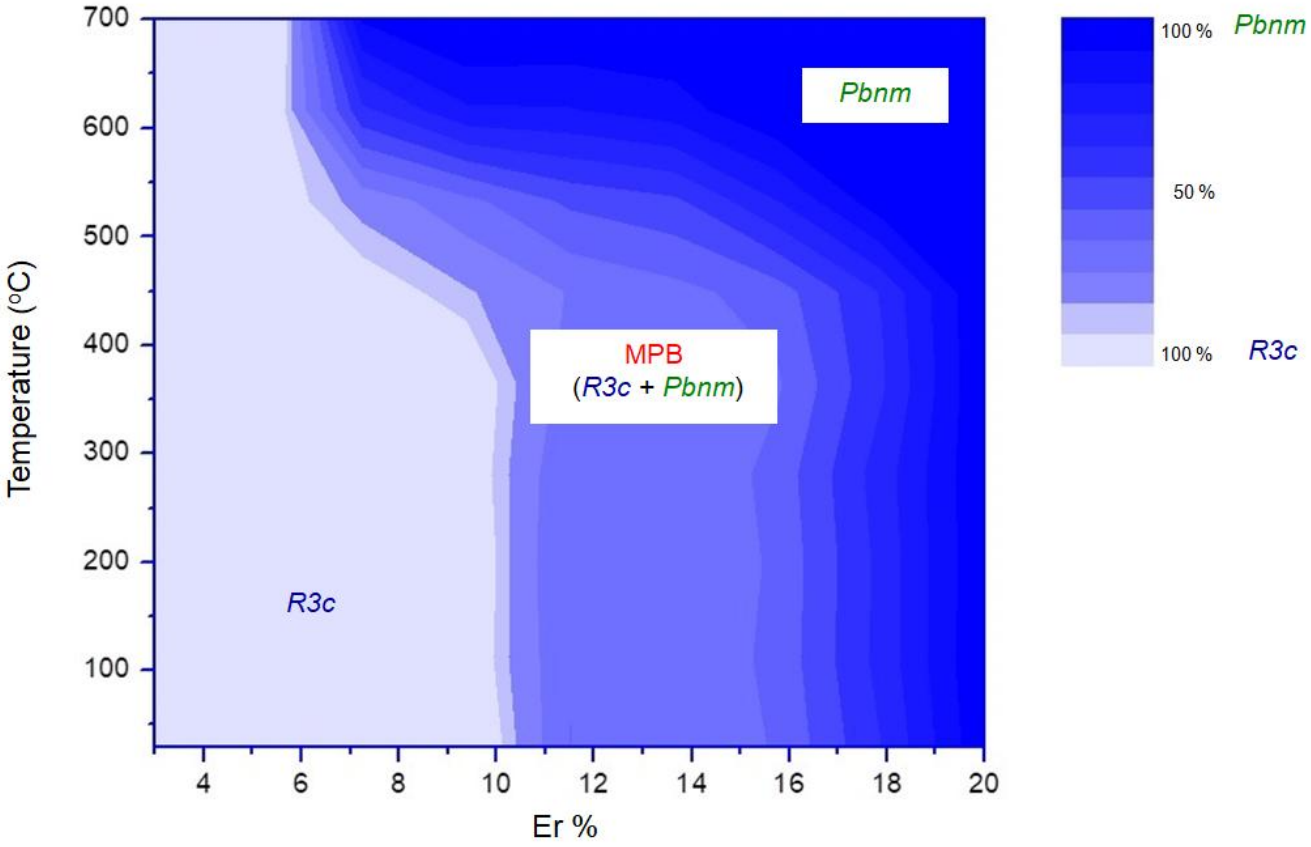

Figure 6.5 **Partial phase diagram of the (1-*x*)$BiFeO_3$-*x*$ErFeO_3$ solid solution system, indicating the pure rhombohedral phase region, the MPB region with a mixture of the rhombohedral and orthorhombic phases, and the pure orthorhombic phase region.**

6.4.3 Magnetic Characterization of the BErF-*x* Solid Solution

Figure 6.6 (a) presents the temperature dependence of magnetization for the BErF-*x* (*x* = 0.03 - 0.20) samples under the field-cooling (FC) process with an applied magnetic field of 100 Oe. Figure 6.6 (b) presents the enlarge section of the BErF-*x* (*x* = 0.05 - 0.12) samples under the field-cooling (FC, 100 Oe). In BFO, the Fe^{3+}

sublattice is in a canted G-type antiferromagnetic ordering below its Néel temperature (T_N ~ 640 K), resulting in anti-ferromagnetism [34]. Interestingly, the temperature dependences of the magnetization for BErF-*x* show a minimum value around 30 K, and moreover, the field-cooling magnetization of BErF-0.20 becomes negative, indicating a magnetic pole inversion phenomenon.

To understand the magnetic minimum and the unusual magnetic pole inversion, it is necessary to discuss the magnetic interactions in BErF-*x* system. BErF-*x* solid solution has three types of magnetic interaction, similar to Yb-substituted BFO solid solutions (Chapter 5), which are known as Fe^{3+}-O^{2-}-Fe^{3+} (Dzyaloshinskii–Moriya, denoted as DM interaction), Er^{3+}-O^{2-}-Fe^{3+} and Er^{3+}-O^{2-}-Er^{3+}. In the rare-earth orthoferrites, the Fe^{3+}-O^{2-}-Fe^{3+} usually orders magnetically at Néel temperature T_N = 620 - 740 K with a slightly canted antiferromagnetic structure, yielding a very small residual ferromagnetic moment. The interaction between Er^{3+}-O^{2-}-Er^{3+} was observed at very low temperatures 4.5 K. Therefore, the net magnetization of the BErF-*x* solid solution between 20 K and 300 K can be approximately estimated by using the paramagnetic sublattice of Er and the DM interaction from Fe^{3+} ions, shown as the following equation [104]:

$$M_{net} = [\mathrm{Fe}] \times M_{Fe} + [Er] \times (H_{int} + H_{ext}) \times C_{Er}/T \qquad (6.2)$$

where M_{Fe} is the magnetization of the canted antiferromagnetism of the Fe^{3+}-O^{2-}-Fe^{3+} (the DM interaction), C_{Er} is the Curie constant for Er^{3+} ions, *T* is the temperature in Kelvin, H_{int} is the internal magnetic fields (due to Fe sublattice ordering) of Er^{3+} sublattice, which is negatively coupled to the Fe sublattice, with the magnetization opposite to M_{Fe}, and H_{ext} is the external magnetic fields. [Fe] and [Er] are the concentrations of the Fe^{3+} and Er^{3+} ions, respectively [104]. Upon cooling, the magnetic moment of the Er sublattice is increased and it is anti-aligned to the magnetic moment Fe sublattices with the DM interaction.

Thus, the competitions between these interactions may give rise to interesting and complexed magnetic properties [150]. Fe^{3+}-O-Fe^{3+} superexchange interaction is dominant in $ErFeO_3$, with the bond angle around 144° [151]. Such Fe^{3+}-O-Fe^{3+}

superexchange interactions are responsible for the antiferromagnetic ordering with a weak ferromagnetic spin component. As introduced in Chapter 6.2, this canted ferromagnetism is attributed to the antisymmetric Dzyaloshinskii-Moriya (DM) exchange interaction between neighboring spins induced by the spin-orbit interaction:

$$\overrightarrow{D_\iota} \cdot \overrightarrow{S_\iota} \times \overrightarrow{S_J} \quad , \tag{6.3}$$

where $\overrightarrow{D_\iota}$ is the exchange interaction intensity, and $\overrightarrow{S_\iota}$ and $\overrightarrow{S_J}$ are the two nearest spins [150, 152]. It is worth mentioning that the Er-substituted samples exhibit interesting magnetic behaviour when the temperature is decreased from 300 K to 5 K. A sudden change of net magnetism from a positive value to a negative value was observed around 30 K to 50 K, which is depended on the Er^{3+} concentration. This interesting phenomenon is defined as magnetic pole inversion. Upon cooling, the canted antiferromagnetism of the Fe^{3+} sublattices is negatively coupled to the moment of the Er^{3+} sublattice. During the cooling process, the magnetic moment of the Er^{3+} sublattice, which is anti-aligned to the Fe^{3+} sublattices, is increasing more quickly in its magnitude. With further decreasing temperature, the magnetic moment decreases sharply and approaches zero at 30 K to 50 K. This is because when the magnetic moment of the Er^{3+} sublattice overweighs that of the DM interaction produced by the Fe^{3+}-O^{2-}-Fe^{3+}, the net magnetization becomes a negative value, which also means that the spin reorientation of the DM interaction provides extra degrees of freedom in changing the sign of the net magnetic moment [150].

Moreover, the net magnetization of BErF-*x* (*x* = 0.03 - 0.10) solid solution significantly decreases in the temperature range of 30 K to 50 K and the net magnetization does not become negative. This is due to the concentration of Bi^{3+} in BFO which is a G-type antiferromagnetic and has the $6s^2$ lone-pair electrons forming a strong covalent bonding with the Fe^{3+} ion, which prevents any rotation of the moment on Fe^{3+}. As a result, the samples with $x < 0.10$ do not show any effect of spin reorientation and exhibit only a single change of magnetic pole at T_{min} within the measured temperature range. Therefore the concentration of Bi^{3+} can also have an effect on the magnitude of magnetization and the temperature of magnetic minimum (denoted as T_{min}) which is the minimal or most-negative magnetic values. Moreover, the spin reorientation of Fe^{3+}

becomes active, when the concentration of Er^{3+} is further increased. This is one of the reasons that the pole inversion occurs in the BErF-*x* (*x* = 0.12 - 0.20) ceramics.

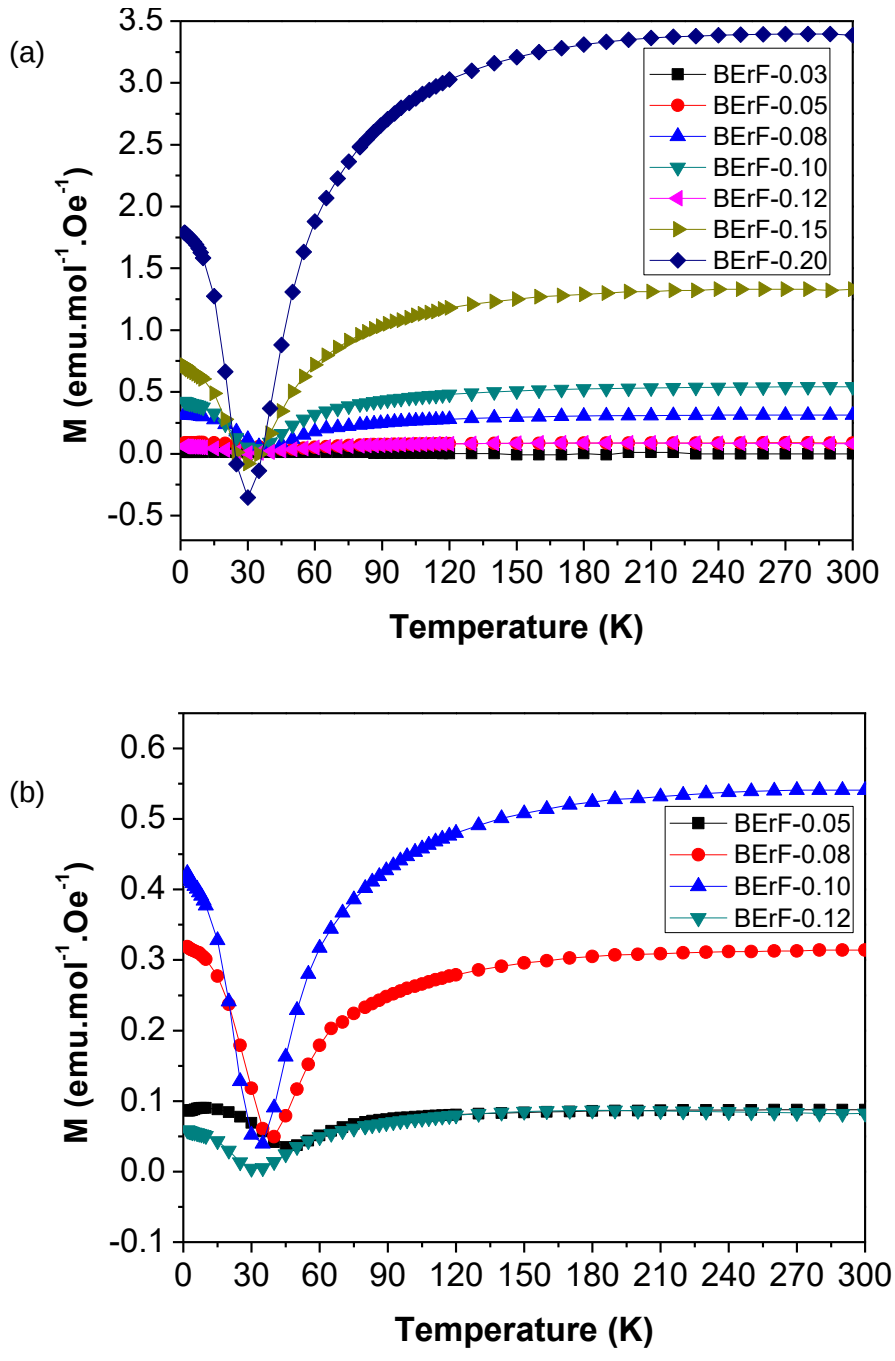

Figure 6.6 **(a) Temperature dependence of the magnetization measured in the field-cooling process (FC, 100 Oe) for BErF-*x* (*x* = 0.03 - 0.20), and (b) Temperature dependence of the magnetization measured in the zero-field-cooling process (FC,100 Oe) for BErF-*x* (*x* = 0.05 - 0.12).**

Figure 6.7 (a) shows composition dependence of the minimum values of magnetization within the temperature range of 5 K - 300 K and the temperature (T_{min}) corresponding to the minimum magnetization. It can be seen that with the increase in the $ErFeO_3$ concentration, T_{min} is continuously decreased until x = 0.12, while the minimum magnetization is decreased within the whole composition range studied because the spin moments of Er^{3+} is oriented in the antiparallel direction with the Fe^{3+} spins. When the net magnetization reaches zero, the magnetizations of the two different magnetic ions have antiparallel directions and the total moments of the Fe^{3+} and Er^{3+} sublattices are cancelled out at a point called the compensation point [150]. The net magnetization then starts to increase with the decrease of temperature below 30 K, which is because the paramagnetic Er^{3+} aligned (oriented parallel) with the external magnetic field (100 Oe) and the Fe^{3+} ions reoriented from a canted antiferromagnetic structure toward a pure antiferromagnetic structure by Morin type transition [149]. As the temperature decreases, the magnetization of Er^{3+} increases, and the magnetization of Fe^{3+} also increases and these two magnetic ions are antiparallelly aligned. The paramagnetic characteristics of the curve mainly originate from the larger magnetic moment of Er^{3+} (9.59 μB/Er^{3+}, 5.9 μB/Fe^{3+}), which is gradually enhanced with decreasing temperature [150]. The schematic spin structures for the BErF-0.20 in the corresponding temperature ranges are illustrated in Figure 6.7(b).

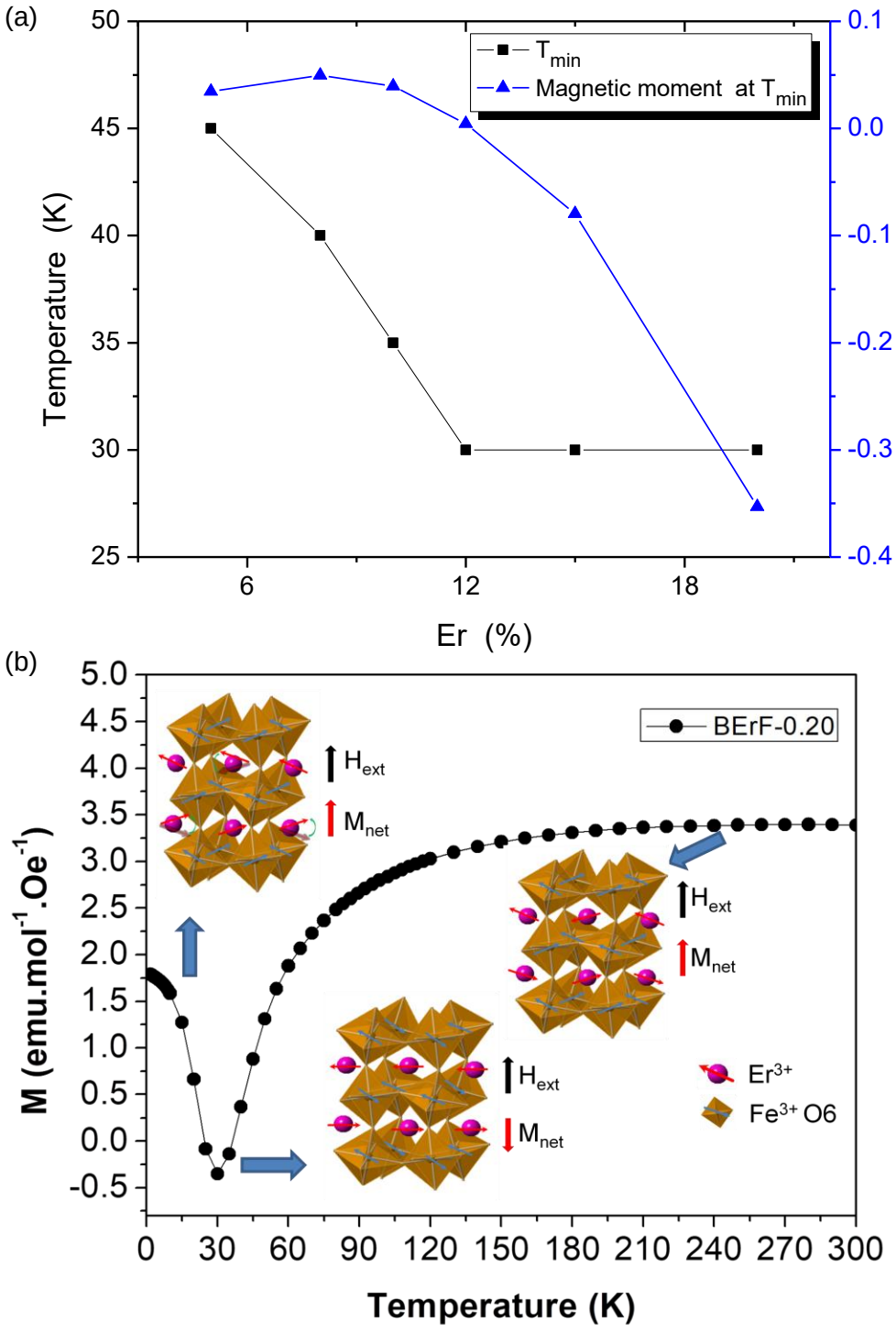

Figure 6.7 **(a) Values of minimal magnetization at T_{min} and the temperature of T_{min} as a function of the concentration of Er for the BErF-0.20 solid solution, and (b) Schematic spin structures for the BErF-0.20 solid solution at various temperature ranges.**

Figure 6.8 (a) and (b) shows the magnetic hysteresis (M-H) curves of the BErF-*x* ($0.03 \leq x \leq 0.20$) solid solutions measured at 300 K and 5 K, respectively. At room temperature, a weak ferromagnetism was displayed for some compositions (x = 0.05 - 0.20) as shown by a slim magnetic hysteresis loop with a saturated magnetization. At a lower temperature (5 K), all of the samples exhibited ferromagnetic behaviour and a large saturated magnetization of 0.8 μB/f.u. was displayed for the BErF-0.20 composition. The chemical modification for introducing Er^{3+} into $BiFeO_3$ is shown to enhance the magnetic properties. Indeed, the weak ferromagnetism is found in BErF-0.15 at room temperature, which is believed to arise from a structural distortion introduced by the Er^{3+} ion with a smaller ionic radius (1.004 Å) than that of Bi^{3+} (1.17 Å), which disrupts the spiral spin modulation in $BiFeO_3$, giving rise to a net non-zero magnetization, and thereby the (weak) ferromagnetism at room temperature.

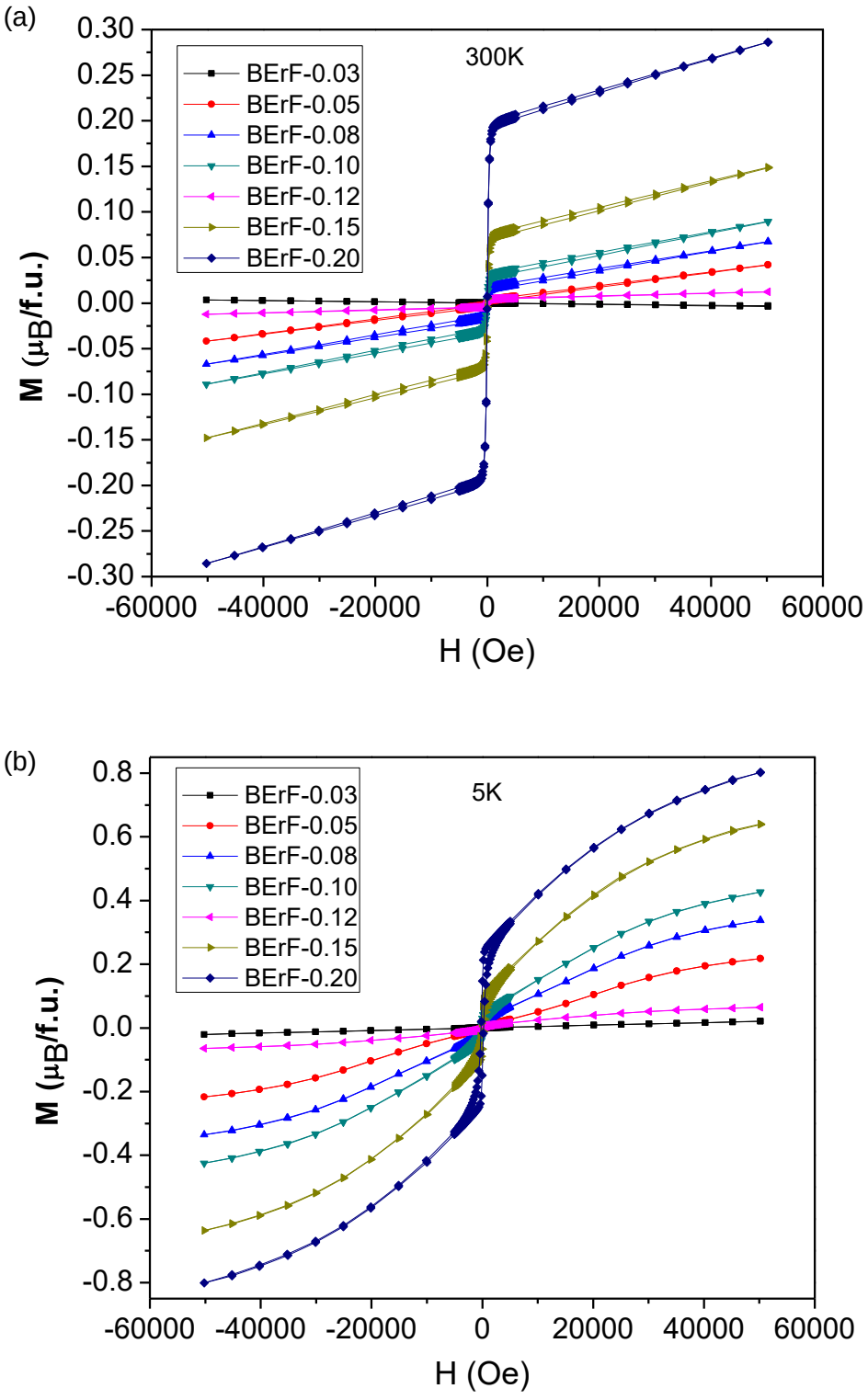

Figure 6.8 **Magnetic hysteresis loops of the BErF-*x* (*x* = 0.03 - 0.20) ceramic measured at (a) 300 K and (b) 5 K.**

The measured spontaneous magnetization and the calculated spontaneous polarization of the BErF-*x* (*x* = 0.03 - 0.20) solid solutions at 300 K are shown in Figure 6.9. It can be seen that ferromagnetism and ferroelectricity coexist in these solid solutions. The best candidate for multiferroics applications among all the compositions is BErF-0.15, which is within the MPB composition range and exhibits both a decent magnetization and an electric polarization at room temperature. These results support that the Er-substitution is able to improve the magnetic properties of $BiFeO_3$ and therefore its multiferroic properties. The room temperature ferromagnetism is increased with the increasing concentration of $ErFeO_3$.This phenomenon is due to the substitution of Er^{3+} for Bi^{3+}, which induces structural distortion and unpaired electrons into the $BiFeO_3$-base solid solutions. The structural distortion can have an effect on the Fe^{3+}-O-Fe^{3+} angles and disrupted the long range spiral spin interactions, which can enhance the ferromagnetism properties.

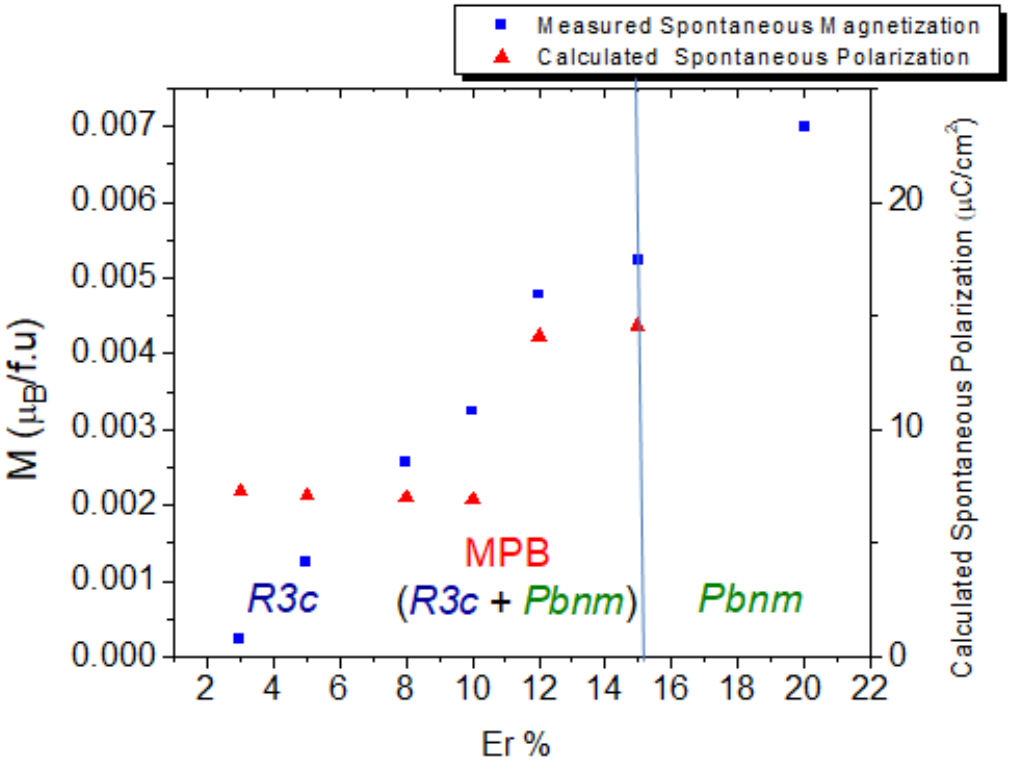

Figure 6.9 **The measured spontaneous magnetization and the calculated spontaneous polarization of the BErF-*x* (*x* = 0.03 - 0.20) solid solutions as a function of Er concentration at 300 K.**

6.5 Conclusions

The multiferroic solid solutions of (1-*x*)$BiFeO_3$-*x*$ErFeO_3$ (BErF-*x*) have been successfully synthesized using a solid state reaction method. The high temperature phase diagram of BErF-*x* is established and the structure and multiferroic properties are systematically studied. For $x < 0.10$, the structure at room temperature remains rhombohedral perovskite with *R*3*c* space group. With the increase of the $ErFeO_3$ concentration, a morphotropic phase boundary is found to exist in the composition range of BErF-*x* ($x = 0.10 - 0.15$). With the further increase the $ErFeO_3$ concentration, the structure undergoes a phase transition to a single phase orthorhombic orthoferrite *Pbnm* for BErF-x ($x \geq 0.20$). Moreover, interesting magnetization reversal behaviour is discovered by the introduction of Er^{3+} ions into $BiFeO_3$ to form the BErF-*x* solid solutions. For a specific composition, the magnetic pole direction can be tuned by the variation of temperature. For BErF-0.12, the temperature dependent magnetic pole inversion occurs at 30 K, which is due to the negative coupling between the magnetization of the Er^{3+} sublattice and the canted antiferromagnetism of the Fe^{3+} sublattice, and the different temperature dependences of these two magnetic sublattices. The concentration of Er^{3+} also has an effect on the magnitude of minimal magnetization and its temperature T_{min}. Furthermore, the spin reorientation of Fe^{3+} becomes more active as the concentration of Er^{3+} is further increased.

These results show that the partial substitution of Er^{3+} for Bi^{3+} in BFO can also enhance the magnetic properties, making the $Bi_{1-x}Er_xFeO_3$ solid solutions an interesting class of multiferroic materials. The best properties are found in BErF-0.15 which exhibits the coexistence of good magnetic and ferroelectric properties at room temperature, potentially useful for magnetoelectric and spintronic devices applications. In addition to the multiferroic properties, the chemically modified BErF-x solid solutions show the concentration and temperature-induced magnetic pole inversion a new phenomenon that will incite more fundamental theoretical and that may point to new application. Furthermore, with increasing the number of unpaired electrons, a trend for enhancing spontaneous magnetization can be observed. In order to further study the effect of unpaired electrons on magnetization, Eu^{3+} was chosen and the (1-*x*)$BiFeO_3$-*x*$EuFeO_3$ solid solution was studied in the next chapter. Eu^{3+} has six unpaired electrons, one more

unpaired electrons than Dy^{3+} and it has the largest ionic radius compared with Dy^{3+}, Lu^{3+}, Yb^{3+}, and Er^{3+}.

Chapter 7.

Synthesis, Structure, and Characterization of the (1-*x*)$BiFeO_3$-*x*$EuFeO_3$ Solid Solution

7.1 Abstract

The single-phase multiferroic bismuth ferrite $BiFeO_3$ has attracted considerable interest in the past decades because of the coexistence of the ferroelectricity and anti-ferromagnetism, which has an exceptional potential for technological applications. The rare-earth substituted $BiFeO_3$-based solid solutions can offer complex electric and magnetic interactions which are still poorly understand. According to the results in the previous chapters, the ferromagnetism of $BiFeO_3$ can be improved by rare-earth substitutions on the *A*-site. In Chapter 3, the (1-*x*)$BiFeO_3$-*x*$DyFeO_3$ solid solution studied in Chapter 3 is a promising room temperature multiferroic material, however, in order to find a better room temperature multiferroic material, Eu^{3+} is chosen and the (1-*x*)$BiFeO_3$-*x*$EuFeO_3$ solid solution is studied in this chapter. Eu^{3+} has 6 unpaired electrons, one more than Dy^{3+} (5 unpaired electrons) and it has the largest ionic radius (1.066 Å) compared with Dy^{3+} (1.027 Å), Lu^{3+} (0.977 Å), Yb^{3+} (0.985 Å), and Er^{3+} (1.004 Å).

In this work, the single-phase multiferroic (1-x)$BiFeO_3$ -*x*$EuFeO_3$ (denoted as BEuF-*x*) solid solution was synthesized to study the effects of Eu substitution for Bi on the crystal structure and ferromagnetic behaviour. The X-ray diffraction patterns of BEuF-*x* were analyzed by the Rietveld refinements. A structural transformation from the rhombohedral *R*3*c* phase to the orthorhombic *Pbnm* phase occurred with increasing Eu concentration. The high-temperature phase diagram of the solid solutions has been established. The pure $BiFeO_3$ crystallizes in the rhombohedral *R*3*c* structure and the pure $EuFeO_3$ crystallizes in the orthorhombic *Pbnm* structure [153]. For the BEuF-*x* ($0 \leq x \leq 0.12$) solid solutions, the structure remains a rhombohedral perovskite with the

*R*3*c* space group. With the further increase of the $EuFeO_3$ content, a morphotropic phase boundary (MPB) is found to exist in the composition range of x = 0.12 - 0.15. A single-phase orthorhombic *Pbnm* structure was found for compositions $x \geq 0.20$ at room temperature.

7.2 Introduction

Multiferroic materials possess simultaneous ferroelectric, ferromagnetic, and ferroelastic orderings, and exhibit promising applications in memories, spintronics, and magnetoelectric sensor devices [19, 20, 23, 24, 89]. Among these known multiferroics, $BiFeO_3$ (BFO) has attracted extensive attention due to the coexistence of ferroelectric and magnetic orderings above the room temperature. It is a G-type antiferromagnet below the Néel temperature ($T_N \sim 640K$) with a spiral spin arrangement (the canted anti-parallel spins are not exactly at 180° to each other) with an incommensurate wavelength period of 62 nm through the lattice [154]. It is also a ferroelectric material below the Curie temperature ($Tc \sim 1103$ K) [61]. As mentioned in Chapter 1 (sec.1.6.4), it is in general quite rare for a material to possess a large magnetization and a large polarization since ferroelectricity and ferromagnetism are mutually exclusive. Therefore, it is challenging to develop multiferroic materials with both large magnetization and electrical polarization. High leakage current, weak magnetoelectric coupling, and low remnant polarizations are some of the drawbacks of BFO that prevent it from being used in applications. [34, 73, 92, 97]. One of the approaches to improve the properties of BFO is by the substitution of rare-earth elements for the *A*-site (Bi-site) of the perovskite unit cell. As reported in Chapters 3 - 7, an enhanced ferromagnetic behaviour has been observed in the *A*-site substituted BREF-*x* solid solutions RE = Dy, Lu, Tb, and Er. The canted antiferromagnetic spins by the modification of the antiparallel sublattice magnetization of Fe^{3+} due to the RE^{3+} substitution are responsible for the weak ferromagnetism on the *A* sites of the perovskite unit cell [59, 95].

In order to explore alternative way to enhance the magnetic properties of $BiFeO_3$, in this work, Eu^{3+} is introduced into the $BiFeO_3$ system to form the solid solution of

$Bi_{1-x}Eu_xFeO_3$ (BEuF-*x*) to improve the magnetic properties by introducing structural distortion and unpaired electrons. The partial substitution of Eu^{3+} for Bi^{3+} results in two effects. First, the ionic radius (1.066 Å) of the Eu^{3+} ion is smaller than that of Bi^{3+} (1.17 Å), which leads to the decreasing lattice volume. The shrinkage of the lattice parameters can disrupt the cycloidal spin structure of the antiferromagnetic interactions in $BiFeO_3$, creating ferromagnetism. Second, the incorporation of magnetic Eu^{3+} ions will introduce additional magnetic moments related to the Eu spins. In previous chapters, the magnetic properties of $BiFeO_3$-based system were improved by introducing of rare earth elements, RE = Dy^{3+}, Yb^{3+}, Er^{3+} and Lu^{3+}, on the perovskite *A*-site. In comparison, Eu^{3+} (1.066 Å) has a larger ionic radius than the Dy^{3+} (1.027 Å), Er^{3+} (1.004 Å), Yb^{3+} (0.985 Å) and Lu^{3+} (0.977 Å) ions. In order to achieve the same magnitude of structural distortion, the concentration of Eu^{3+} has to be higher. The BEuF-*x* (*x* = 0.05 - 0.20) samples exhibit an interesting magnetization behaviour when the temperature is decreased from 300 K to 5 K. As the concentration of $EuFeO_3$ increases, the magnetization maximum decreases from above 300 K to 290 K for the samples in the composition range of *x* = 0.03 - 0.12. When the concentration of Eu^{3+} is further increased to *x* = 0.15 - 0.20, the solid solutions exhibit ferromagnetic behaviour. Indeed, the structural distortion induced by the substitution of Eu^{3+} ions for Bi^{3+} on the *A*-site can has a significant impact on the ferromagnetism of $BiFeO_3$. This study provides a better understanding of the fundamental magnetic properties of the rare-earth substituted $BiFeO_3$-based multiferroics solid solution systems.

7.3 Experimental

7.3.1 Synthesis

Ceramics of (1-*x*)$BiFeO_3$-*x*$EuFeO_3$ (BEuF-*x*) solid solutions were prepared by using solid state reaction method. High purity powers of Bi_2O_3 (99.975%), Fe_2O_3 (99%) and Eu_2O_3 (99.9%) were used as starting materials. After weighting accurately to four significant digit according to the chemical reaction:

$$\frac{(1-x)}{2}\mathrm{Bi_2O_3} + \frac{x}{2}\mathrm{Eu_2O_3} + \frac{1}{2}\mathrm{Fe_2O_3} \rightarrow (1-x)\mathrm{BiFeO_3} - x\mathrm{EuFeO_3} \quad (7.1)$$

Each composition was mixed and ground by ball milling for 24 h. Ball milling container was setup as 25.0 ml bottle with 15.0 ml of ethanol and 40 zirconium oxide balls. The mixed powders were pressed into pellets, packed into platinum crucible, and calcined at 840 °C for 4 h. After the calcination, the sample discs were reground by ball milling for 24 h and then the powders were mixed with five drops of 5% polyvinyl alcohol (PVA) as binder. The powders were pressed into pellets again and then heated at 650 °C for 1 h to evaporate the binder. After the elimination of the binder, the pellets were packed into platinum crucible which was sealed in a lager Al_2O_3 crucible then sintered at 900◦C for 1 h. The calcination temperature and sintering temperature are increased up to 870 °C and 950 °C, respectively with correspondence of increased concentration of Eu.

7.3.2 Structural Analysis and Magnetic Measurements

Crystallographic structure and phase purity analysis of as-sintered ceramics was performed by X-ray diffractions using a Bruker D-8 diffractometer with Ni-filtered Cu K_α radiation (40 mA, 40 kV, 0.01° steps and 2θ = 15 - 80°). $BiFeO_3$ single crystals were ground into a powder and XRD data were collected and used as a structural reference for $BiFeO_3$. Simulation of crystal structure based on the measured XRD data was performed using Rietveld crystal structure refinement software (TOPAS-Academic) in order to determine the symmetry, lattice parameters, the average structure, and atomic positions of the solid solution. Magnetic properties of the samples were performed as a function of temperature using a Quantum Design MPMS-XL SQUID magnetometer.

7.4 Results and Discussion

7.4.1 Structural Analysis and Phase Transformation

Figure 7.1 shows the XRD patterns for (1-*x*)$BiFeO_3$-*x*$EuFeO_3$ (*x* = 0.03 – 0.20) solid solutions at room temperature. The XRD patterns for the samples reveal the characteristic well-crystallized pattern of $BiFeO_3$-based perovskite phase along with some impurity peaks due to the formation of $Bi_2Fe_4O_9$ for *x* < 0.08. However, the impurity phase vanished with the increase of the $EuFeO_3$ amount, which indicated that the $EuFeO_3$ can suppress the formation of the impure $Bi_2Fe_4O_9$ phase [155], favouring the formation of pure perovskite phase. The diffraction peaks in the BEuF-*x* solid solutions of *x* ≤ 0.12 can be identified as the rhombohedral perovskite *R*3*c* structure. As the concentration of Eu increased, a morphotropic phase boundary (MPB) is found to exist in the range of 0.12 ≤ *x* < 0.15. A mixture of two phases: the rhombohedral *R*3*c* and the orthorhombic *Pbnm*, is observed in the MPB region and the percentage of each phase was analyzed by the Rietveld refinements. For *x* > 0.15, the solid solution is of orthorhombic perovskite with the *Pbnm* space group. The BEuF-*x* solid solutions exhibit a wider rhombohedral perovskite phase range than the other rare-earth (RE = Dy, Er, Yb and Lu)-substituted systems discussed in the previous chapters. This is because the Eu^{3+} ionic radius is the largest one compared with the Dy^{3+} ,Er^{3+} ,Yb^{3+} and Lu^{3+} ions. In order to achieve the same magnitude of structural distortion, the concentration of Eu^{3+} has to be higher. Indeed, the composition that displays pure rhombohedral perovskite phase in other BREF-*x* systems are around *x* = 0.10 or less.

In the rhombohedral phase region, the perovskite peaks shift to higher 2θ angles with the increase of the $EuFeO_3$ amount, indicating the decrease of the lattice parameters with the increase of the *x* values. The resultant shrinkage of the unit cell caused by the formation of the solid solution is due to the smaller ionic radius of the Eu^{3+} ion compared with that of Bi^{3+} ion. The structural transformation from the rhombohedral phase *R*3*c* phase to the orthorhombic *Pbnm* phase induced by the Eu-substitution can be attributed to the size effect. It is known that the $6s^2$ lone-pair orbital of Bi^{3+} stereochemically activates a hybridization of the Bi 6*p* and O 2*p* states, and causes the off-centering displacement of Bi^{3+} toward O^{2-} to induce ferroelectricity [36]. The *R*3*c*

structure of BFO can be regarded as being evolved from the ideal cubic perovskite structure. The Eu^{3+} ion possesses a smaller radius (1.066 Å) compared with the Bi^{3+} ion (1.17 Å). With the substitution of the smaller Eu^{3+} for the Bi^{3+} ions, the tolerance factor (*t*) decreases as shown in Equation 1.1. As the tolerance factor is smaller, the Fe-O bonds are under compression and the Bi^{3+}-O and Eu^{3+}-O bonds are under tension. The relative rotation angle of the two oxygen octahedra around the polarization [111] axis in the *R*3*c* unit cell increased with the substituted amount of Eu^{3+} for Bi^{3+} in BFO. With further increasing of Eu concentration, the induced distortions make the rhombohedral phase less stable, leading to the more stable the orthorhombic phase with decreased lattice parameters and reduced overall volume of the unit cell, as shown in Figure 7.2.

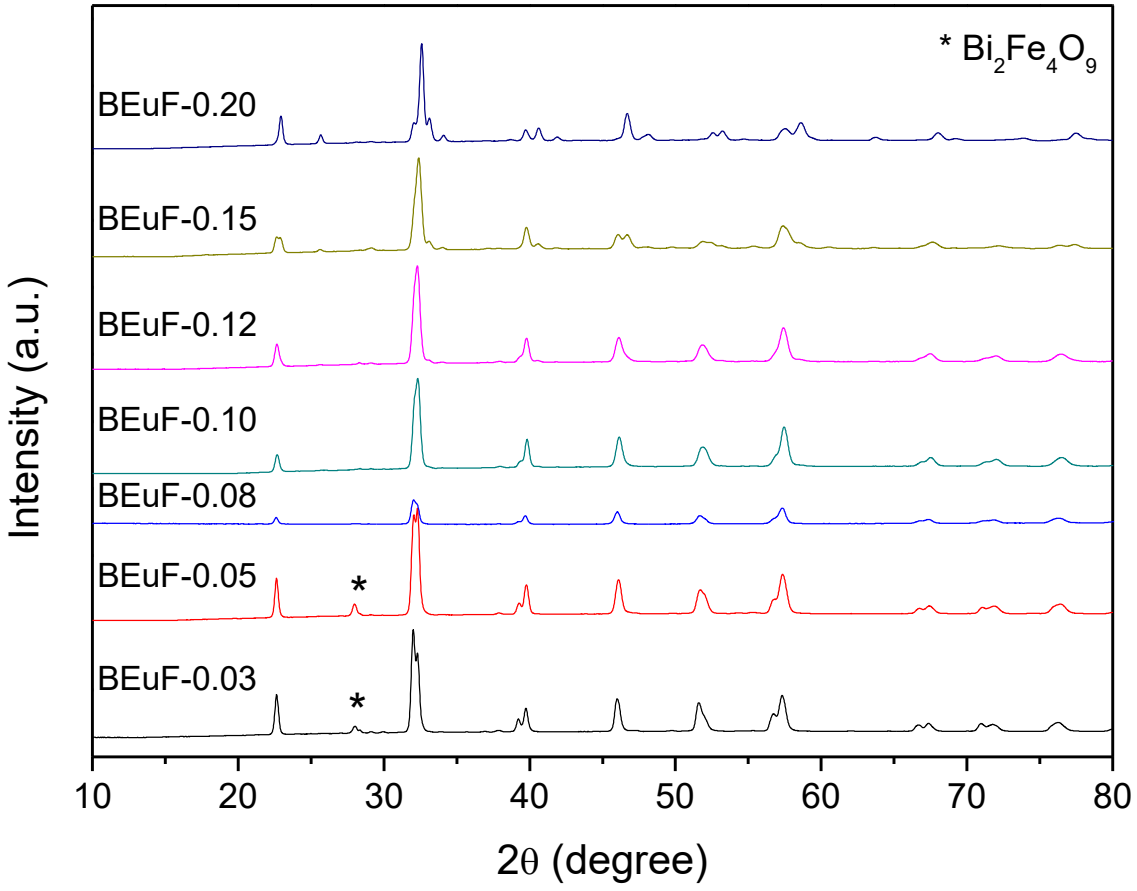

Figure 7.1 **X-ray diffraction patterns of the BEuF-*x* (*x* = 0.03 - 0.20) ceramics prepared at optimal sintering temperatures (T = 900 °C). Stars indicate the peaks of the impurity phase $Bi_2Fe_4O_9$.**

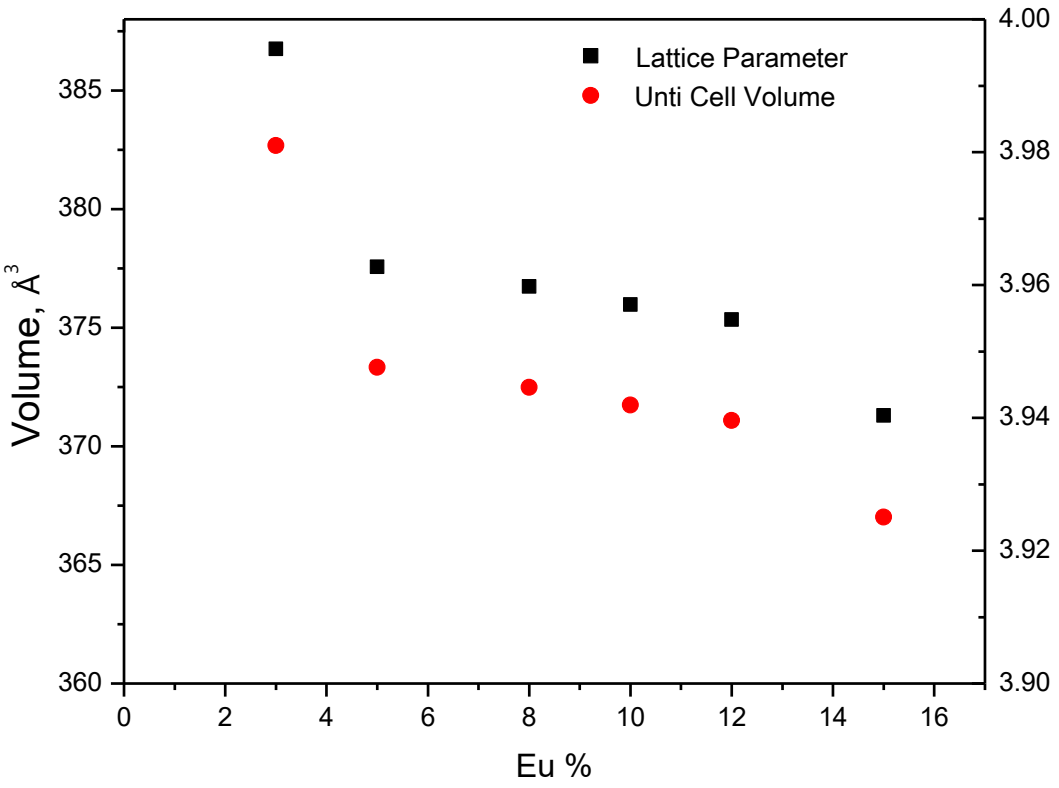

Figure 7.2 **Lattice parameter, a, and unit cell volume of the BEuF-*x* (*x* = 0.03 - 0.15) ceramics as a function of the concentration of Eu.**

Figure 7.3 (a) shows the phase percentage for various compositions of the BEuF-*x* (*x* = 0.03 - 0.20) ceramics. The structure gradually changed from the rhombohedral perovskite *R*3*c* to a mixture of rhombohedral and orthorhombic perovskite (MPB) for *x* = 0.12 - 0.15, followed by a structural transformation into a pure orthorhombic perovskite *Pbnm* with increasing amount of $EuFeO_3$ at $x \geq 0.15$. These results are consistent with the decreasing trend of the lattice parameter of a_{pc} for the *R*3*c* phase as a function of Eu concentration, as shown in Figure 7.3 (b). When *x* = 0.15, the pseudocubic lattice parameter, a_{pc} for *R*3*c* displays an abrupt drop, which triggers the solid solution to undergo a phase transition from the rhombohedral phase to the orthorhombic phase.

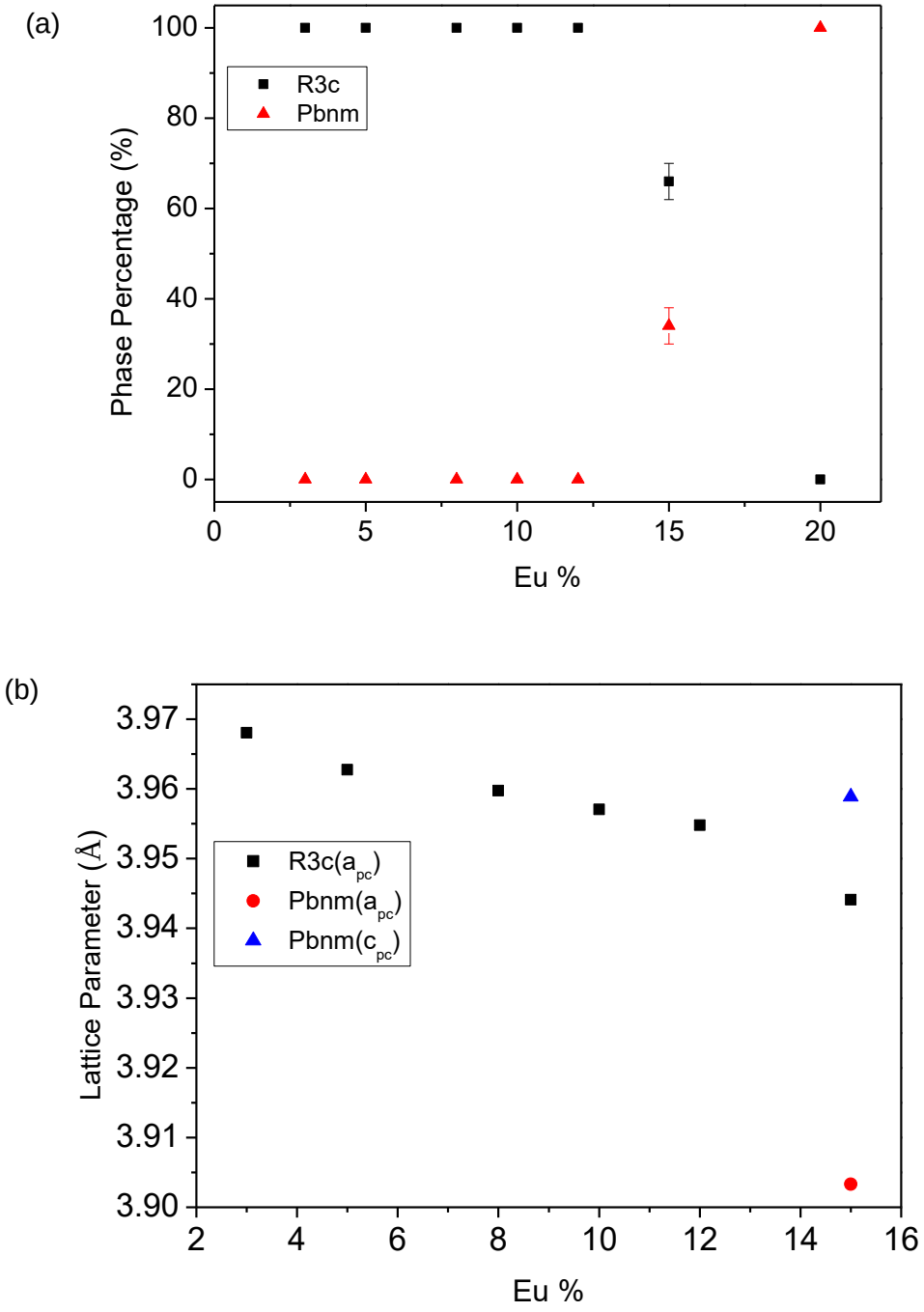

Figure 7.3 **(a) Phase percentage of the BEuF-*x* (*x* = 0.03 - 0.20) ceramics with various concentrations of Eu. (b) The composition dependence of the unit cell parameters *a* and *c* of the BEuF-*x* (*x* = 0.03 - 0.15) ceramics. The pseudocubic cell: a_{pc} = lattice parameters *a*, c_{pc} = lattice parameters *c*) as a function of the Eu concentrations.**

We take the BEuF-0.10 solid solution as an example to study the phase transition temperature (*T*c) and the structure of the BEuF-*x* solid solutions by high-temperature X-ray diffraction, as shown in Figure 7.4. At room temperature, the pure rhombohedral structure was observed. Upon heating at 400 ^{o}C, the BEuF-0.10 solid solution transforms into the MPB region with of a mixture phases. The percentages of rhombohedral and the orthorhombic phases are changed with increasing temperature. The majority phase changes from the rhombohedral phase to the orthorhombic phase at 450 ^{o}C. Then the system transforms into a pure orthorhombic phase at 550 ^{o}C. In addition, this phase transformation can be described by the changes of phase percentages as a function of temperatures as shown in Figure 7.5.

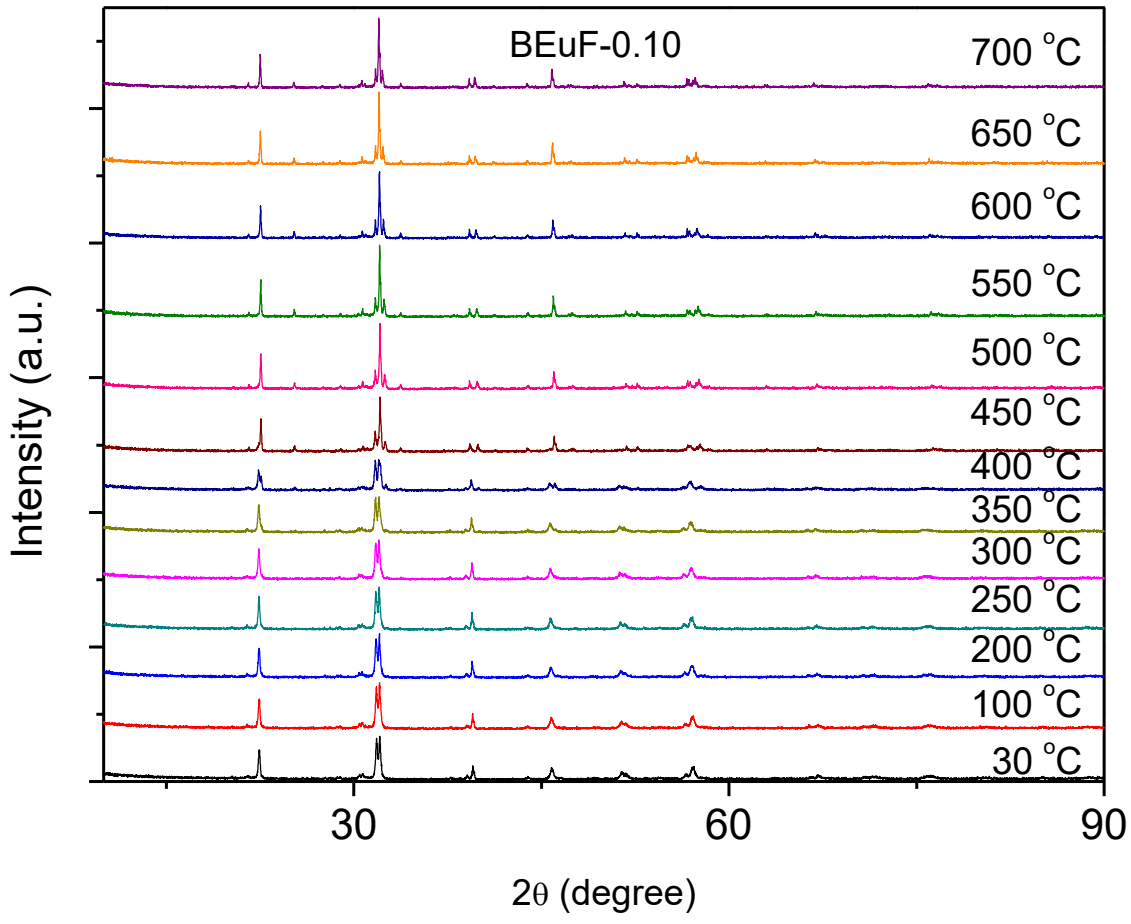

Figure 7.4 X-ray diffraction patterns of the BEuF-0.10 ceramics at various temperatures.

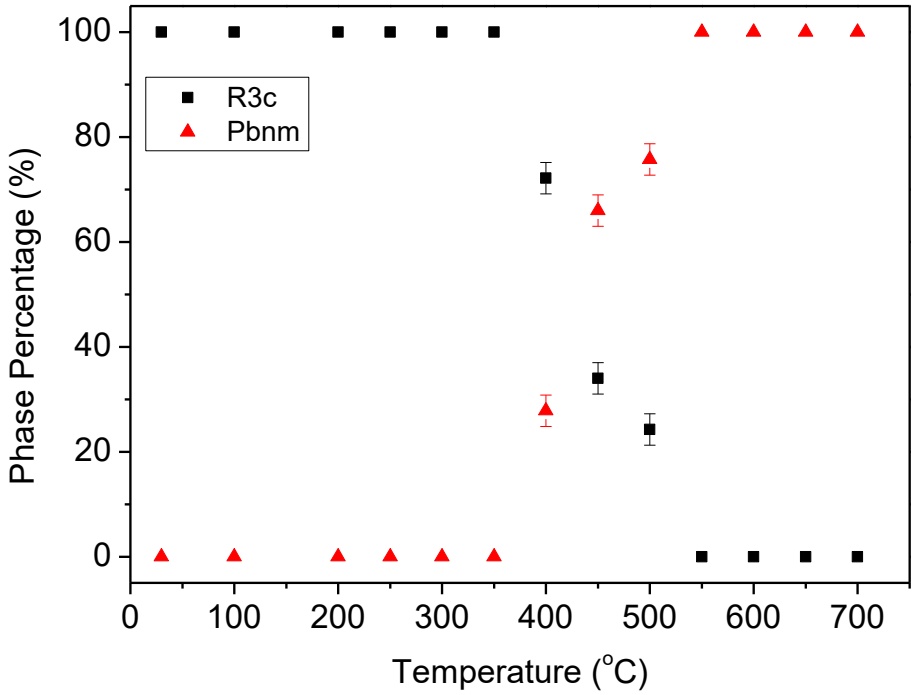

Figure 7.5 **Phase percentages of the rhombohedral (*R3c*) and orthorhombic (*Pbnm*) phase of the BEuF-0.10 ceramics as a function of temperature.**

7.4.2 Temperature-Composition Phase Diagram for the $BiFeO_3$-$EuFeO_3$ System

Based on the above structural analysis, the temperature-composition phase diagram of (1-*x*)$BiFeO_3$-*x*$EuFeO_3$ solid solution is established using X-ray diffraction data and Rietveld refinements, as shown in Figure 7.6. For $x < 0.12$, the structure remains in the rhombohedral perovskite phase with *R*3*c* space group. The structure of BEuF-*x* changes from the rhombohedral *R3c* to the orthorhombic *Pbnm* as the Eu concentration increases. An MPB region is found to exist in the composition range of $x = 0.12 - 0.15$, where a mixture of the rhombohedral *R3c* and the orthorhombic *Pbnm* phases is observed. The pure orthorhombic *Pbnm* phase appears for $x \geq 0.20$. As the temperature increases, the BEuF-*x* solid solution undergoes a phase transition from the rhombohedral *R3c*, to MPB, then to the pure orthorhombic *Pbnm* phase.

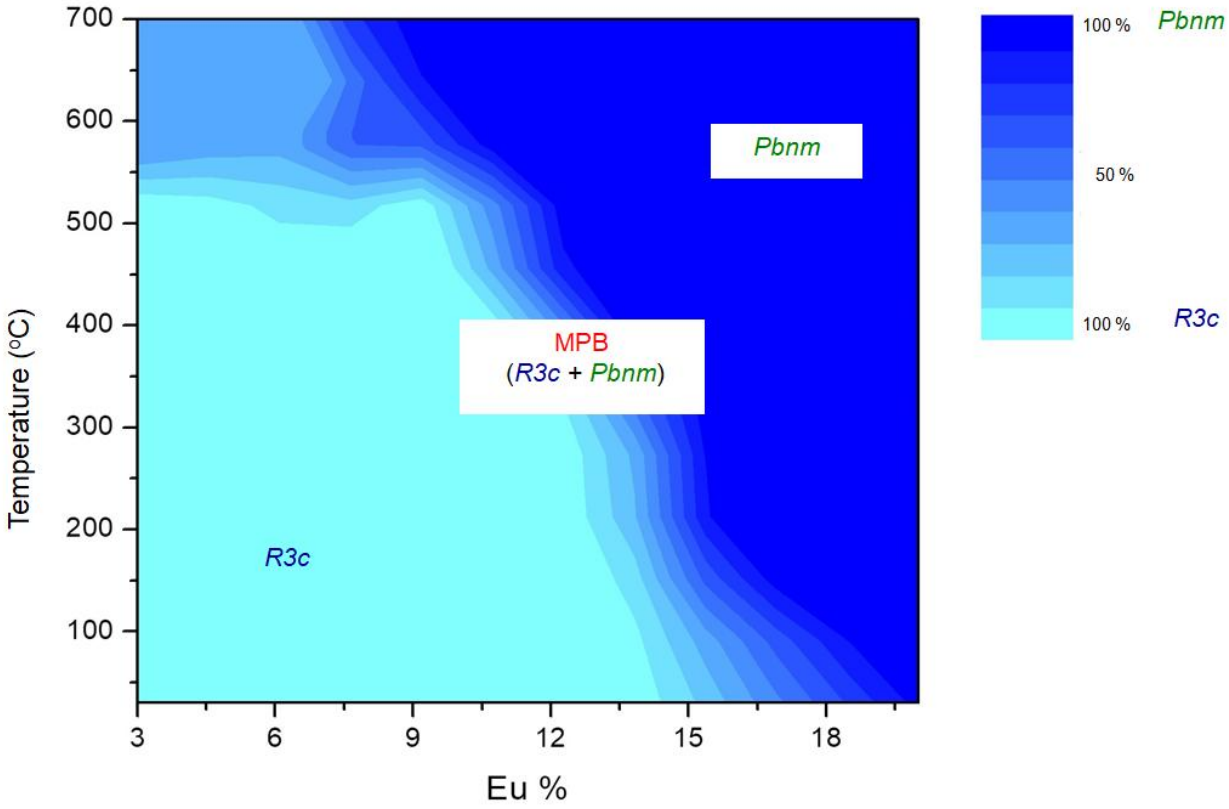

Figure 7.6 **Partial temperature-composition phase diagram of the (1-*x*)$BiFeO_3$-*x*$DyFeO_3$ (BEuF-*x*) solid solution system, demonstrating the pure rhombohedral phase region, the MPB region with a mixture of the rhombohedral and orthorhombic phases, and the pure orthorhombic phase, as the concentration of $EuFeO_3$ is increased.**

7.4.3 Magnetic Characterization of BEuF-*x* Solid Solution

The temperature dependences of the magnetization measured in field-cooling (FC, 100Oe) process for the BEuF-*x* (*x* = 0.03 - 0.20) samples were shown in Figure 7.7 and 7.8. The BEuF-x (*x* = 0.05 - 0.20) samples exhibit an interesting magnetization behaviour when the temperature is decreased from 300 K to 5 K. As the concentration of $EuFeO_3$ increases, the magnetization maximum decreases from above 300 K to 290 K for the samples in the composition of x = 0.03 - 0.12. The magnetization maximum of BEuF-0.08 and BEuF-0.12 samples was observed at 300 K and 290 K, respectively. This indicates that the introduction of Eu^{3+} on the perovskite *A*-site has modified the magnetic properties of $BiFeO_3$. This arises from a structural distortion introduced by the

Eu^{3+} ion with a smaller ionic radius (1.066 Å) than that (1.17 Å) of the Bi^{3+} ions, which has affects the spiral spin of the DM interaction produced by the Fe^{3+}-O^{2-}-Fe^{3+}. The net magnetization for BEuF-0.08 and BEuF-0.12 at room temperature is increased from 0.056 to 0.200 $emu.mol^{-1}.Oe^{-1}$. Upon cooling, the canted antiferromagnetism of the Fe sublattices exhibits the spin reorientation of DM interaction at 70 K, as shown in Figure 7.8. When the concentration of Eu^{3+} is further increased, the solid solution enters the MPB region and ferromagnetism is demonstrated within the composition range of x = 0.15 - 0.20. With the increase of the magnetic Eu^{3+} concentration, the introduced structural distortion disrupts the spiral spin modulation in $BiFeO_3$. Therefore, it is observed that the BEuF-0.15 and BEuF-0.20 samples exhibit a monotonic increase of magnetization with decreasing temperature from 300 K to 5 K. Moreover, the magnetic properties of $BiFeO_3$ can also be affected by the unpaired electrons in Eu^{3+} ions. In the case of BEuF-0.15 and BEuF-0.20, as shown in Figure 7.8, the net magnetization also increases by introducing more unpaired electrons into the solid solution system.

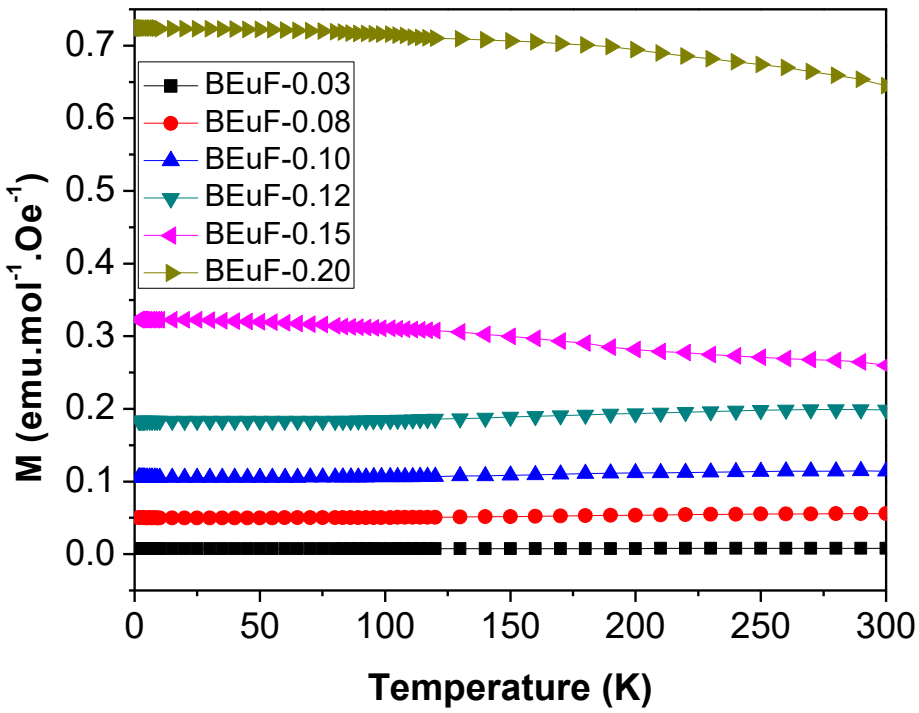

Figure 7.7 **Temperature dependences of the magnetization measured in field-cooling (FC, 100 Oe) process for BEuF-*x* (*x* = 0.03 - 0.20).**

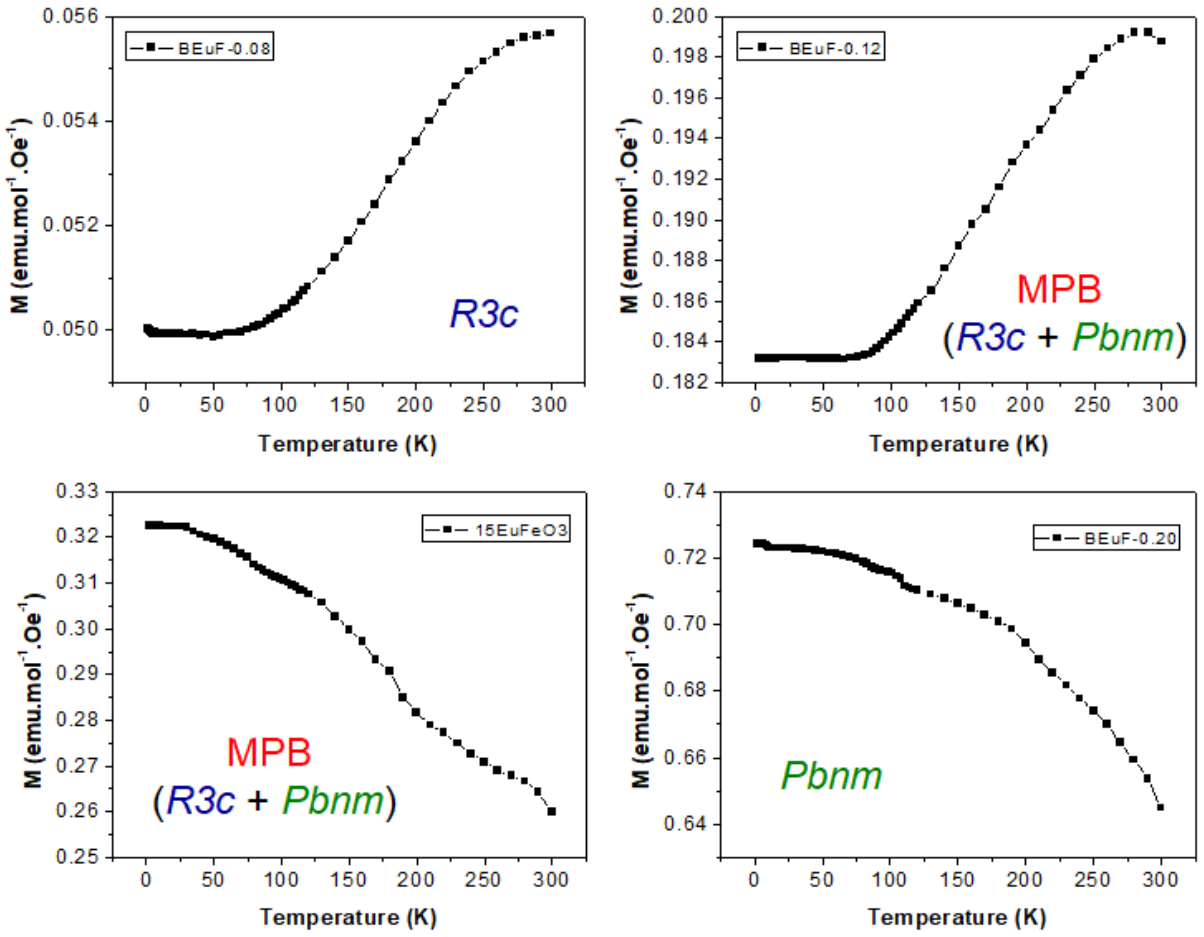

Figure 7.8 **Enlarged temperature dependences of the magnetization measured in field-cooling (FC 100 Oe) for (a) BEuF-0.08, (b) BLF-0.12, (c) BLF-0.15, and (d) BLF-0.20.**

The magnetic hysteresis (M-H) loops of the BEuF-*x* ($0.03 \leq x \leq 0.20$) solid solutions at 300 K and 5 K are shown in Figure 7.9. Weak ferromagnetism is demonstrated for the solid solution systems of BEuF-*x* (x = 0.03, 0.08, and 0.10) by a slim magnetic hysteresis loop with a saturated magnetization of 0.015 μB/f.u, 0.025 μB/f.u, and 0.035 μB/f.u, respectively, at room temperature (300 K). It has been reported that the weak ferromagnetism in BFO is related to the rhombohedrally distorted perovskite *R*3*c* structure, in which both ferroelectric atomic displacements and weak ferromagnetism are allowed [62]. With increasing concentration of Eu^{3+}, the introduction of structural distortion into the BEuF-*x* solid solutions disrupts the spiral spin modulation in $BiFeO_3$. As a result, for x = 0.12 - 0.20, the magnetic hysteresis loops exhibit

ferromagnetic behaviour with a non-zero saturated magnetization and the BEuF-0.12 exhibits the highest saturated magnetization of 0.045 μB/f.u at 300 K. Furthermore, at a very low temperature of 5 K, the BEuF-0.15 sample exhibits a saturated ferromagnetic hysteretic behaviour and a saturated magnetization of 0.05 μB/f.u., which is consistent with the temperature dependence of magnetization of the BEuF-0.15 solid solution, as shown in Figure 7.8. These results indicate that the change in the crystal structure caused by the Eu substitution for Bi results in the modification on the anisotropic superexchange interaction [156] and the suppression of the spiral spin modulation [157] in BFO, leading to the (weak) ferromagnetism in BEuF-*x*. When the concentration of Eu^{3+} is further increased, the solid solution enters the MPB region and ferromagnetism is demonstrated within the composition range of x = 0.12 - 0.20. With the increase of magnetic Eu^{3+} concentration, the introduced structural distortion destroys the spiral spin modulation in $BiFeO_3$. Indeed, the ferromagnetism in BEuF-0.12 and BEuF-0.15 at room temperature is further enhanced and it also exhibited ferroelectric properties. Therefore, the above results demonstrate that the ferromagnetic properties were improved in the Eu-substituted BFO solid solutions.

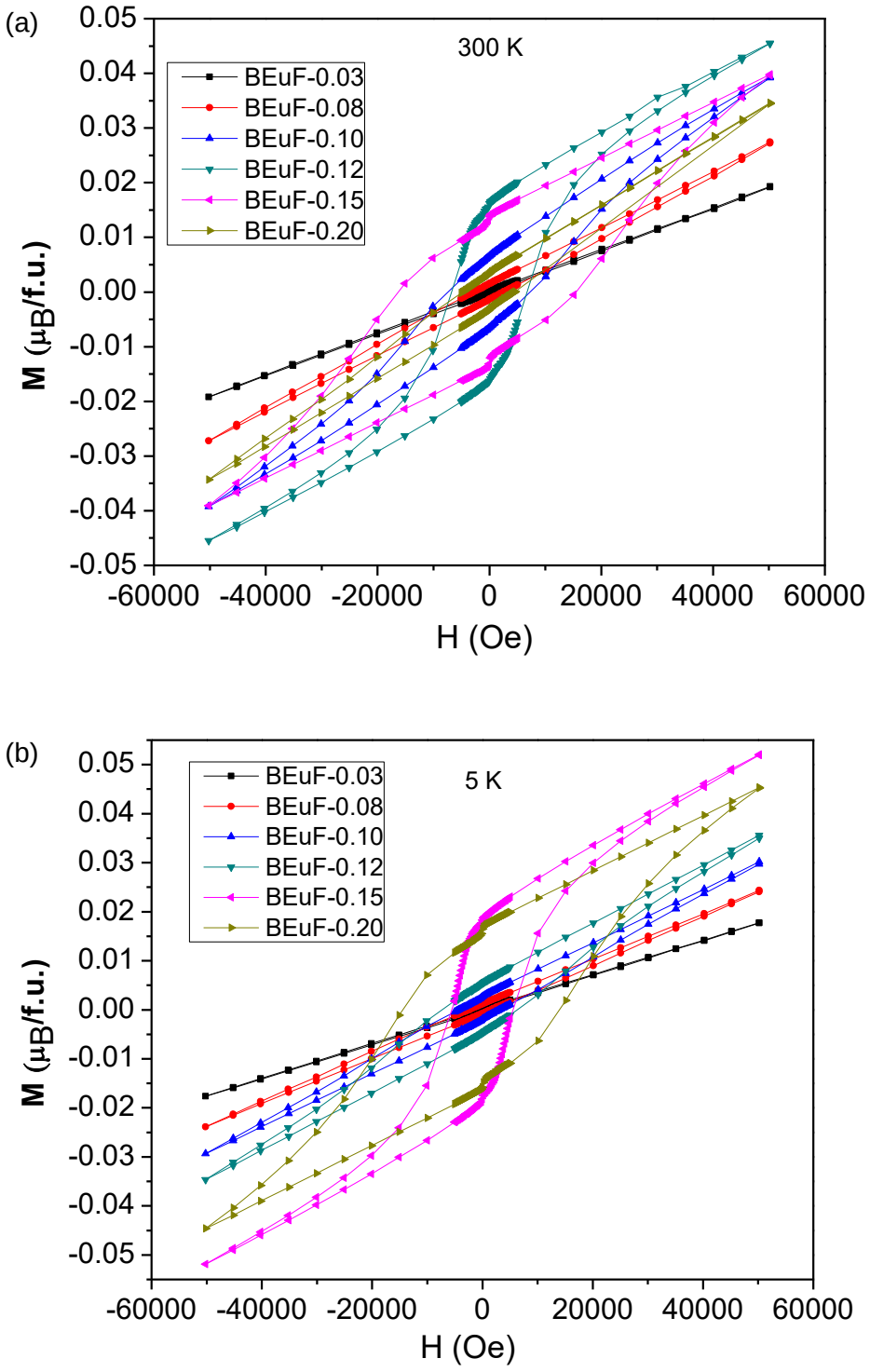

Figure 7.9 **Magnetic hysteresis loops of the BEuF-*x* (*x* = 0.03 - 0.20) ceramics measured at (a) 300K and (b) 5 K.**

The spontaneous magnetization and the calculated spontaneous polarization (example calculation see sec. 3.4.1) of BEuF-*x* (*x* = 0.03 - 0.20) solid solutions at 300 K are shown in Figure 7.10. It can be seen that the coexisted ferromagnetism and ferroelectricity in the solid solutions with *x* = 0.03 - 0.15. The room temperature ferromagnetic moment is increased with the increasing $EuFeO_3$ concentration. This phenomenon is due to the introduction of Eu^{3+} which induces structural distortion and unpaired electrons into the $BiFeO_3$-based solid solutions. The BEuF-0.15 the solid solution is the turning point for the weak ferromagnetic to change into a ferromagnetic state. As a result, the best candidate for multiferroics applications in this system is BEuF-0.15, which exhibits both decent magnetization and electric polarization at room temperature.

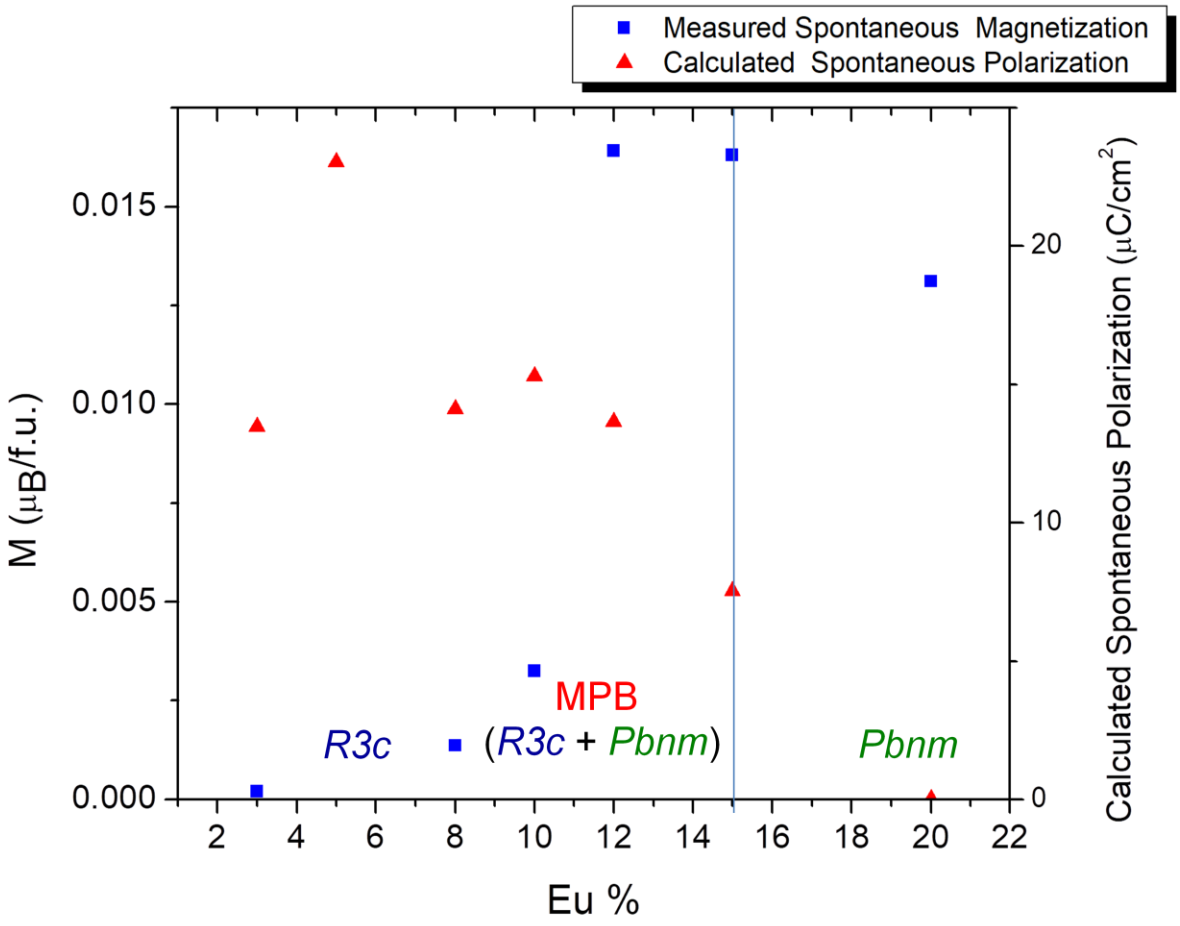

Figure 7.10 The measured spontaneous magnetization and calculated spontaneous polarization of BEuF-*x* (*x* = 0.03 - 0.20) solid solutions as a function of Eu concentration at 300 K.

7.5 Conclusions

The room temperature multiferroic BEuF-*x* solid solutions were successfully synthesized by the solid state reaction method. A morphotropic phase boundary (MPB) was found to exist in the composition range of $x = 0.12 – 0.15$. For $x \geq 0.20$, the solid solution transforms to the single-phase orthorhombic *Pbnm* structure. Furthermore, the interesting magnetization behaviour is discovered by the substitution of Eu^{3+} ion for the Bi^{3+} ion in multiferroic $BiFeO_3$. The concentration of Eu^{3+} and the resultant ionic size effect can affect the ferromagnetic behaviour. For $x = 0.08$, the solid solution exhibit weak ferromagnetism with a magnetization maximum at 300 K. When the concentration of the Eu^{3+} ion is increased, the enhanced structural distortion in the BEuF-*x* solid solutions disrupts the spiral spin modulation in $BiFeO_3$. Consequently, the ferromagnetic behaviour was observed in the BEuF-0.15 sample at room temperature. The BEuF-*x* solid solutions have a wider rhombohedral perovskite phase range than the other rare-earth (RE = Dy, Er, Yb and Lu)-substituted systems (reported in chapters 3 - 7) because Eu^{3+} has the largest ionic radius compared to the Dy^{3+}, Er^{3+}, Yb^{3+} and Lu^{3+} ions. This size effect explains the particular magnetic behaviour of the BEuF-*x* solid solutions with various amounts of Eu substituted, as shown in Figure 7.8. The weak ferromagnetic behaviour was observed with small amounts of Eu ($x \leq 0.12$), whereas the ferromagnetism was induced in samples with larger amounts of Eu ($x = 0.15$ and 0.20). The best multiferroic candidate in this BEuF-*x* solid solution system is BEuF-0.15, as it exhibits both decent magnetization and electric polarization at room temperature. This work provides an additional example of the rare-earth-substitution that leads to the formation of $BiFeO_3$-based solid solutions, and it demonstrates that the Eu-substitution for Bi is effective in enhancing the multiferroic properties of the BFO, making the $Bi_{1-x}Eu_xFeO_3$ solid solutions interesting multiferroic materials for potential applications.

Chapter 8.

General Overview, Comparative Analysis and Further Studies

8.1 General Conclusions

Multiferroics, showing the coexistence of magnetic, ferroelectric and ferroelastic properties within a single phase, have attracted much attention due to their potential applications in data-storage systems, multiple-state memories, spintronics, sensors, etc [73]. Among the most studied multiferroic materials, the perovskite bismuth ferrite $BiFeO_3$ (BFO) is one of the few single-phase multiferroics exhibiting both ferroelectricity and antiferromagnetism above room temperature with high ferroelectric Curie temperature, (*Tc* = 830 °C) and a moderate Néel temperature (T_N = 370 °C). The coexistence of electric and magnetic order parameters in multiferroics offers new possibilities for device functionalities based on the cross-control of magnetization and/or polarization by the electric field and/or magnetic field (magnetoelectric coupling) [73, 89]. BFO has a rhombohedral perovskite structure with the space group *R*3*c*. However, it is difficult to display large polarization in BFO due to its high leakage arising from the secondary phases and charge defects (such as oxygen vacancies). Besides, a spiral spin modulation with an incommensurate wavelength period of ~ 62 nm, which is superimposed on the G-type antiferromagnetic ordering, leads to a cancellation effect on the macroscopic magnetization [84]. Therefore, to overcome these drawbaks, chemical modifications by partial substitution of Bi-site (*A*-site) by rare-earth (RE) elements (RE = Dy^{3+}, La^{3+}, Er^{3+}, $Gd^{3+,}$ etc), or alkaline earth elements (Ca^{2+}, Ba^{2+}, Sr^{2+}, etc) were performed and proven to be an effective method to improve the performance of bulk BFO. Also, *B*-site co-substitution of Fe^{3+} by Ti^{4+}, Nb^{5+}, and Mn^{4+} was carried out [94-97,101,102,104]. Despite the large amount of researches on BFO in recent years, little attention has been focused on the structure and properties of the rare-earth modified

$BiFeO_3$, which is the main motivation of this work. In this work, the effects of *A*-site substitution by Dy^{3+}, Lu^{3+}, Yb^{3+}, Er^{3+} and Eu^{3+}, substitutions of *A*-site with Dy^{3+} and *B*-site with Ti^{3+}, and the co-substitution of *A*-site with Lu^{3+}, *B*-site with Ti^{3+}, on the crystal structure, ferroelectric and magnetic properties of the BFO-based solid solutions in a wide range of compositions have been systematically investigated.

The first part of this work was focused on the development and characterization of a new series of multiferroic materials $(1-x)BiFeO_3$ -$xDyFeO_3$ (denoted as BDF-*x*) and $(1-x)BiFe_{(1-y)}Ti_{(y)}O_{(3+y/2)}$-$xDyFeO_3$ (denoted as BDFT-*x*-*y*). The solid solution of BDF-*x* with a stable perovskite phase was synthesized by the solid state reaction method. The defects presented in the lattice of BDF-x ceramics are responsible for the electronic conduction and ionic conduction. These defects could arise from the volatilization of Bi_2O_3 during the material preparation process, resulting in oxygen vacancies and bismuth vacancies. In addition Fe^{2+} would occupy the octahedral site in the perovskite and the electric conductivity arises mainly from the electrons hopping from Fe^{2+} to Fe^{3+}. To resolve these issues, *B*-site aliovalent substitution by Ti^{4+} was performed to improve the dielectric and ferroelectric properties. The concentration of oxygen vacancies was reduced by substitution of Ti^{4+} for Fe^{3+} on the *B* site because Ti^{4+} has higher ionic charge compared to Fe^{3+} and it is about the same size as Fe^{3+}. A large remnant polarization of 23 $\mu C/cm^2$ was displayed of at room temperature in the BDFT-*x*-*y* ceramics, which is higher than the polarization of the pure $BiFeO_3$ ceramics (8.9 $\mu C/cm^2$) [99].

In this first part, the structure of the BDF-*x* solid solution was analyzed by temperature-variable X-ray diffraction and refined by the Rietveld refinements. For *x* below 8%, the solid solution is of a pure rhombohedral perovskite *R*3*c* phase. When the Dy concentration is increased, a morphotropic phase boundary (MPB) is found to exist in the composition range of $x = 0.08 - 0.12$, in which a mixture of rhombohedral *R3c* phase and orthorhombic *Pbnm* phase is observed. The solid solution is of pure orthorhombic perovskite (*Pbnm*) space group with $x > 0.12$. Upon heating, BDF-*x* undergoes a structural evolution from the rhombohedral perovskite *R3c*, to the MPB, and then to the orthorhombic orthoferrite *Pbnm.* The magnetic properties of the BDF-*x* system are characterized in detail by SQUID magnetomery. The weak ferromagnetism is found in BDF-*x* system at room temperature, which is believed to arise from the

structural distortion introduced by the Dy^{3+} ion with a smaller ionic radius than that of Bi^{3+} ion, which disrupts the spiral spin modulation in $BiFeO_3$, giving rise to non-zero net magnetization and thereby the ferromagnetism. The ferromagnetism with a large saturated magnetization of M_s = 0.5 μ_B/f.u. and the ferroelectricity with a remnant polarization of 23 $\mu C/cm^2$ are displayed in the BDFT-0.10-0.02 ceramics at room temperature. These properties entitle the BDFT-*x*-*y* solid solution one of the few multiferroic materials that exhibit both decent magnetization and electric polarization.

In the second part of this work, the ceramics of the $(1-x)BiFeO_3$ -$xLuFeO_3$ (denoted as BLF-x) solid solutions, and the ceramics of $(1-x)BiFe_{(1-y)}Ti_{(y)}O_{(3+y/2)}$-$xLuFeO_3$ (denoted as BLFT-*x*-*y*) solid solutions have been successfully synthesized with a stable perovskite structure by the solid state reaction method. The structure of the BLF-*x* solid solution was also studied by temperature-variable X-ray diffraction and the structure of each composition was refined by the Rietveld refinements. According to the established temperature-composition phase diagram, the structure of the BLF-*x* solid solution is of pure rhombohedral perovskite *R3c* phase for $x \leq 0.08$, and it was found to change from the rhombohedral perovskite *R3c* to the orthorhombic orthoferrite *Pbnm* with the increase of the Lu concentration, with a mixture of the rhombohedral *R3c* phase and the orthorhombic *Pbnm* phase in the MPB region (x = 0.10 - 0.15). A single pure orthorhombic *Pbnm* phase was identified for $x \geq 0.20$.

The magnetic properties of the BLF-x system were characterized in detail by SQUID magnetometry. Three types of magnetic interactions: Fe^{3+}-O^{2-}-Fe^{3+} Dzyaloshinskii–Moriya interaction (denoted as DM interaction), Lu^{3+}-O^{2-}-Fe^{3+} interaction and Lu^{3+}-O^{2-}-Lu^{3+} interaction are believed to be responsible for the magnetic properties of the BLF-*x* solid solutions. The magnetization of BLF-x at a higher temperature range (30 K – 300 K) is dominated the by DM interaction and the Lu^{3+}-O^{2-}-Fe^{3+} interaction. BLFT-*x*-*y* ceramic samples were also prepared by solid state reactions to improve the ferroelectricity and ferromagnetism of the $BiFeO_3$-based solid solution. By introducing Ti^{4+} on the *B*-site, the electric conductivity was reduced and new types of magnetic interactions, Lu^{3+}-O^{2-}-Ti^{4+} and Fe^{3+}-O^{2-}-Ti^{4+}-O^{2-}-Fe^{3+}, were introduced. As a result, the long-range interaction of a spiral spin arrangement in the lattice was disrupted. The BLF-x (*x* = 0.05 - 0.15) samples exhibit a monotonic increase of magnetization with

decreasing temperature from 300 K to 5 K in the rhombohedral *R*3*c* phase and the MPB region of these solid solutions. The magnetization anomalies at around 70 K for BLF-*x* ($0.24 < x \leq 0.30$) could arise from the spin reorientation of the Fe^{3+} moments and the Lu^{3+} moments, as observed in $LuFeO_3$ and other orthoferrites with orthorhombic phase (*Pbnm*). For BLF-*x* with a relatively high Lu^{3+} concentration, a slight decrease in magnetic moments upon cooling was observed, which is due to the negative coupling between the canted antiferromagnetism of the Fe sublattices and the spin moment of the Lu-sublattice. The ferromagnetism has been improved by the disruption of the spiral spin modulation in $BiFeO_3$. At room temperature, weak ferromagnetism was displayed in BLF-0.10 by a slim magnetic hysteresis loop with a saturated magnetization of 0.018 μ_B/f.u, and in the BLFT-0.10-0.02 ceramics with a saturated magnetization of 0.035 μ_B/f.u.

In order to systematically study the effects of rare-earth *A*-site substitutions on the $BiFeO_3$-based solid solutions, the (1-*x*)$BiFeO_3$ -*x*$YbFeO_3$ (denoted BYF-*x*) solid solution has been successfully synthesized by solid state reaction. The structure of the BYF-*x* solid solutions was studied by temperature-variable X-ray diffraction and refined by the Rietveld refinements. For the BYF-*x* ($x < 0.11$) solid solutions, the structure exhibits a rhombohedral perovskite with *R*3*c* space group. With the further increase of the $YbFeO_3$ content, an MPB was found to exist in the composition range of $x = 0.11$ - 0.15. The orthorhombic orthoferrite (*Pbnm*) phase is found at $x \geq 0.20$. The chemically modified BYF-*x* is found to exhibit weak ferromagnetism at room temperature with a large saturated magnetization (M_s = 0.5 μB/f.u.) at 5 K, as well as a ferroelectric hysteresis loop with a remnant polarization of 4 $\mu C/cm^2$ at room temperature.

A systematic study has been carried out of the structure and ferromagnetic properties of Er-substitutied BFO ceramics, in order to understand the origin of the enhanced magnetic properties in rare earth element-substituted $BiFeO_3$-based solid solutions. Ceramics of the (1-*x*)$BiFeO_3$-*x*$ErFeO_3$ (denoted BErF-*x*) solid solutions have been synthesized and characterized. For $x \leq 0.12$, the structure of BErF-*x* is of rhombohedral perovskite with *R*3*c* space group. With the increase of the $ErFeO_3$ content, an MPB is found to exist in the composition range of $x = 0.12$ - 0.15, which is followed by a single phase orthorhombic *Pbnm* structure at $x = 0.20$. As for the magnetic properties,

BErF-*x* is found to exhibit an unusual behaviour of magnetic pole inversion. In most of the ferromagnets, the magnetic moment directions can be changed by applying sufficiently high external magnetic field rather than decreasing temperature. Temperature usually affects the magnitude of the magnetic moment, rather than its magnetization directions. In this BErF-*x* system, however, the magnetic pole inversion has been observed with the variation of temperature, which is a rare and interesting phenomenon. This magnetic pole inversion behaviour can be tuned by changing the concentration of the magnetic ion Er^{3+} in the BErF-*x* (*x* = 0.12 - 0.20) solid solutions. Therefore, this study provides an alternative way to improve the multiferroic properties of $BiFeO_3$-based ceramics and points out the new phenomenon of magnetic pole inversion in BFO-based multiferroics.

Furthermore, the (1-*x*)$BiFeO_3$ -*x*$EuFeO_3$ (denoted BEuF-*x*) solid solutions have been successfully synthesized and studied. The structure remains in the rhombohedral perovskite with *R*3*c* space group for x ≤ 0.12. With increase of $EuFeO_3$ content, an MPB region is found to exist in the composition range of *x* = 0.12 - 0.15, followed by a single phase orthorhombic *Pbnm* structure at *x* = 0.20. It is found that that the BEuF-*x* solid solutions have a wider rhombohedral perovskite range than the other rare earth (RE = Dy, Er, Yb, and Lu)-substituted systems studied in this work. Eu^{3+} has the largest ionic radius (1.066 Å) compared to the Dy^{3+} (1.027 Å), $Er3^{+}$ (1.004 Å), Yb_3^{+} (0.985 Å) and Lu^{3+} (0.977 Å) ions. In order to achieve the same magnitude of the structural distortion, a higher concentration of Eu^{3+} is required. As a result, the partial substitution of Eu^{3+} for Bi^{3+} results in two effects. First, the smaller ionic radius of the Eu^{3+} ions can decrease the unit cell lattice parameter and increase the magnetic moment of the Eu^{3+} sublattice. Second, the shrinkage of the cell volume can disrupt the cycloidal spin structure, which is the characteristic of the antiferromagnetic spin configuration in $BiFeO_3$. With the increase of Eu^{3+} content from *x* = 0.03 to 0.12, the BEuF-*x* solid solutions exhibit a decreased antiferromagnetic phase transition temperature compared with pure BFO, which indicates a decreased stability of antiferromagnetism. As the concentration of the Eu^{3+} ion is further increased, more structural distortion is induced into the BEuF-*x* solid solutions, which disrupts the antiferromagnetic characteristics of spiral spin modulation in $BiFeO_3$, resulting in the ferromagnetic behaviour in the BEuF-0.15 solid solution.

8.2 Comparison of the Structural Features and the Multiferroic Properties of the (1-*x*)$BiFeO_3$-*x*$REFeO_3$ (RE = Dy, Lu, Yb, Er, Eu) Solid Solutions

The chemically modified BFO with the *A*-site substitution of RE^{3+} (RE = Dy, Lu, Yb, Er, Eu) for Bi^{3+} is found to display improved electrical and magnetic properties compared with the pure $BiFeO_3$ ceramics. These chemical modifications have two effects. First, the smaller ionic radius of the RE^{3+} ions can induce the structure distortion and increase the magnetic moment. Second, the shrinkage of the lattice parameters can disrupt the characteristic cycloidal spin structure in the antiferromagnetic $BiFeO_3$. In this work, $BiFeO_3$ is substituted with different rare-earth metal ions: Dy^{3+}, Lu^{3+}, Yb^{3+}, Eu^{3+}, and Er^{3+}, which have different ionic radii and numbers of unpaired electrons. The ionic radii for Dy^{3+}, Lu^{3+}, Yb^{3+}, Er^{3+}, and Eu^{3+} ions are 1.027 Å, 0.977 Å, 0.985 Å, 1.004 Å and 1.066 Å, respectively and the numbers of unpaired electrons for Eu^{3+}, Dy^{3+}, Er^{3+}, Yb^{3+}, and Lu^{3+} are 6, 5, 3, 1 and 0, respectively. From the results presented in chapters 3 - 7, it is possible to compare structural characteristics and multiferroic properties of the various RE-substituted BFO-solid solution system in order to gain a better understanding of the effects of chemical substitutions on the structure and properties.

The composition-temperature phase diagrams of the BREF-*x* solid solution studies constructed based on X-ray diffraction and Rietveld refinements are assemble in Fig. 8.1 (the 3D Figure). For the BREF-*x* solid solutions, in general, the rhombohedral perovskite with *R*3*c* space group appears in the composition range of $x \leq 0.10$. The structure of BREF-*x* changes from the rhombohedral perovskite (*R3c*) to the orthorhombic orthoferrite (*Pbnm*) with increasing amount of $REFeO_3$. An MPB is found to exists in the composition range at $x = 0.10 - 0.15$, where a mixture of the rhombohedral *R3c* phase and the orthorhombic *Pbnm* phase is observed. A single pure-phase orthorhombic *Pbnm* phase is found in BREF-*x* at $x > 0.15$. Figure 8.2 presents the combined phase diagrams of the BREF-x (RE = Dy, Lu, Yb, Er and Eu) solid solutions, which indicates the MPB region for the different RE elements. As the ionic radius and the number of unpaired electrons decreased, the curved MPB region gradually changed to vertical MPB region in the temperature range of 30 °C to 700 °C.

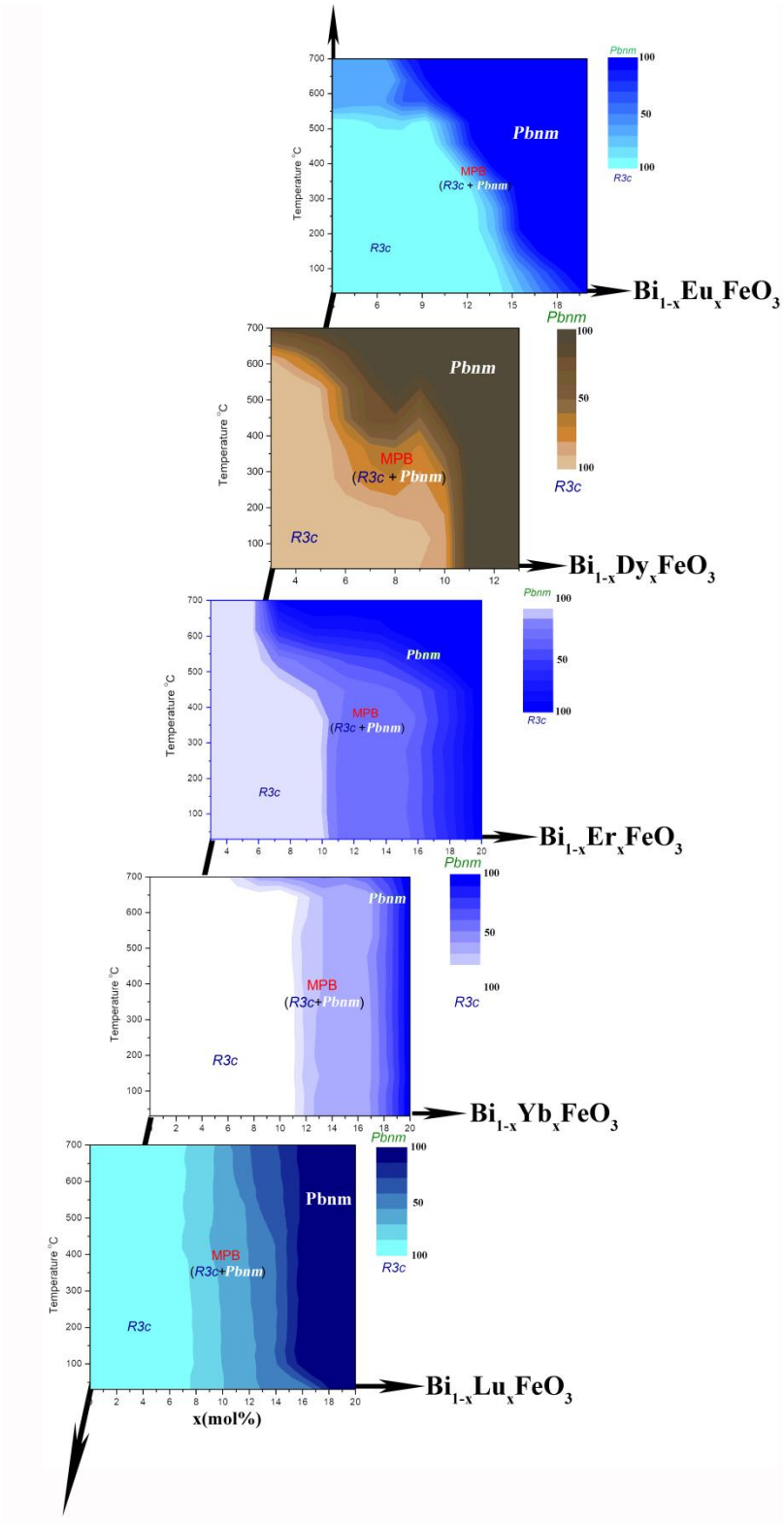
Pbnm
MPB
(R3c + Pbnm)
R3c
Temperature °C
Bi1-xEuxFeO3
Bi1-xDyxFeO3
Bi1-xErxFeO3
Bi1-xYbxFeO3
Bi1-xLuxFeO3
x(mol%)

Figure 8.1 **The composition-temperature phase diagrams of the BREF-*x* (RE = Dy, Lu, Yb, Er, and Eu) Solid Solutions based on X-ray diffraction and Rietveld refinements.**

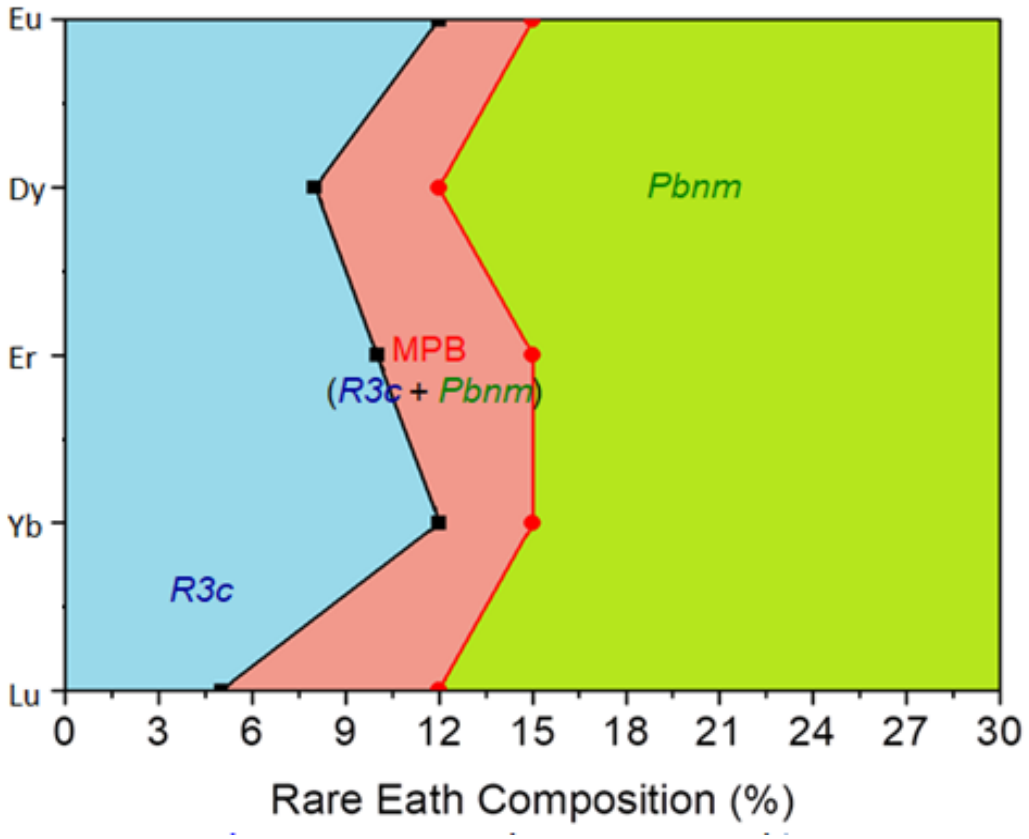

Figure 8.2 **Combined phase diagrams of the BREF-*x* (RE = Dy, Lu, Yb, Er, and Eu) Solid Solutions showing the different MPB regions at room temperature.**

Figure 8.3 shows the magnetic hysteresis (M-H) curves of the BREF-0.10 (RE = Dy, Lu, Yb, Er, Eu) solid solutions at 300 K. The spontaneous magnetization and the calculated spontaneous polarization of the BREF-0.10 solid solutions at 300 K are shown in Figure 8.4. The ferromagnetism of BREF-0.10 samples for various compositions was displayed by a slim magnetic hysteresis loop with a saturated magnetization and BErF-0.10 ceramics has the highest saturated magnetization 0.08 μ_B/f.u at room temperature (300 K). The highest spontaneous magnetization is observed in BDF-0.10 with the value of 0.0115 μ_B/f.u (see Fig. 8.4). For the BEuF-*x* ceramics, Eu^{3+}

has the most unpaired electrons, which BEuF-0.10 samples exhibit antiferromagnetic behaviour with Néel Temperature at 290 K. The reason for the BEuF-*x* ceramics to exhibit antiferromagnetic behaviour is due to the ionic radii of Eu^{3+} ion. Eu^{3+} has the largest ionic radius (1.066 Å) compared to that of Dy^{3+} (1.027 Å), Er^{3+} (1.004 Å), Yb^{3+} (0.985 Å) and Lu^{3+} (0.977 Å) ions. In order to achieve the same magnitude of structural distortion, the concentration of Eu^{3+} has to be higher. This indicates that in order to transform the magnetic properties of $BiFeO_3$ from G-type antiferromagnetic to ferromagnetic, both structural distortion and unpaired electrons are needed. Furthermore as shown in Figure 8.4 (a), by comparing the ferroelectric and ferromagnetic properties of all the BREF-*x* solutions, BDF-0.10 is revealed to have the best properties at room temperature, with the spontaneous magnetization of 0.0115 μ_B/f.u and a spontaneous polarization of 23 $\mu C/cm^2$. Figure 8.4 (b) shows the comparison of the best calculated spontaneous polarization and measured spontaneous magnetization properties for each BREF-*x* solid solutions, i.e., BEuF-0.12, BDF-0.12, BErF-0.15, BYF-0.15, and BLF-0.15, and as a result, BDF-0.12 solid solution system has the best multiferroic properties than other solid solution systems. In experimental data, BDF-10 solid solution system has higher spontaneous polarization of 23 $\mu C/cm^2$ than BDF-12 solid solution system (17.5 $\mu C/cm^2$). Thus, as one of the few and new multiferroic materials, the BDF-0.10 solid solution, which exhibits both decent magnetization and electric polarization, can be a good candidate for novel applications. The results of this work show that the substitution of rare-earth metal ion (Dy, Lu, Yb, Er, and Eu) can affect the structural symmetry and the phase component of the $BiFeO_3$-based multiferroic solid solutions, and thereby enhance their multiferroic properties.

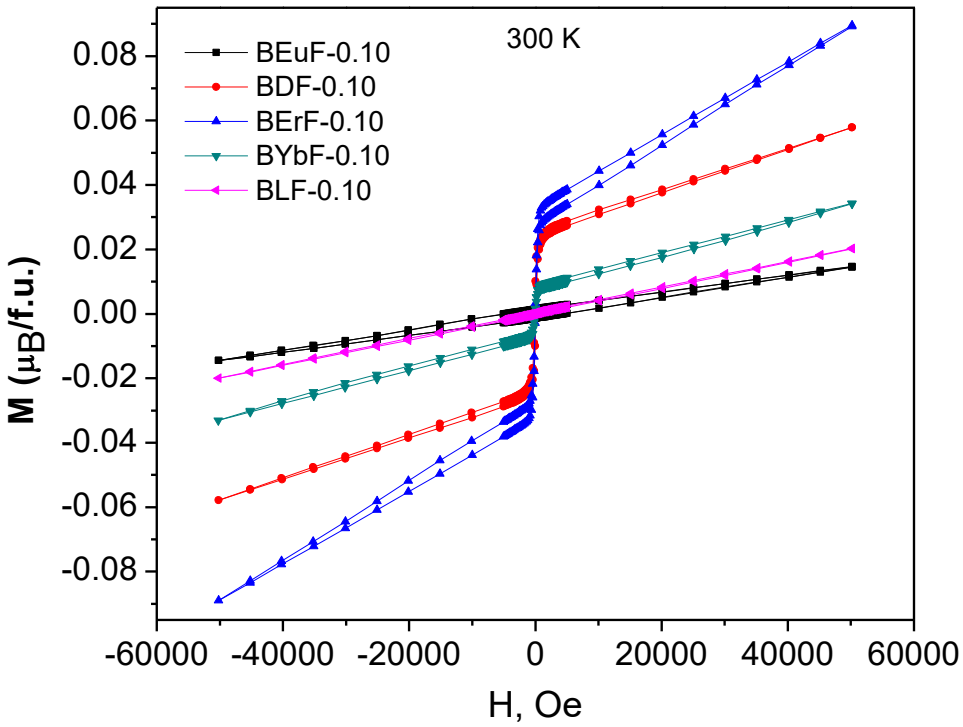

Figure 8.3 **Comparison of the magnetic hysteresis loops of the BREF-0.10 (RE = Dy, Lu, Yb, Er, and Eu) ceramics measured at 300 K.**

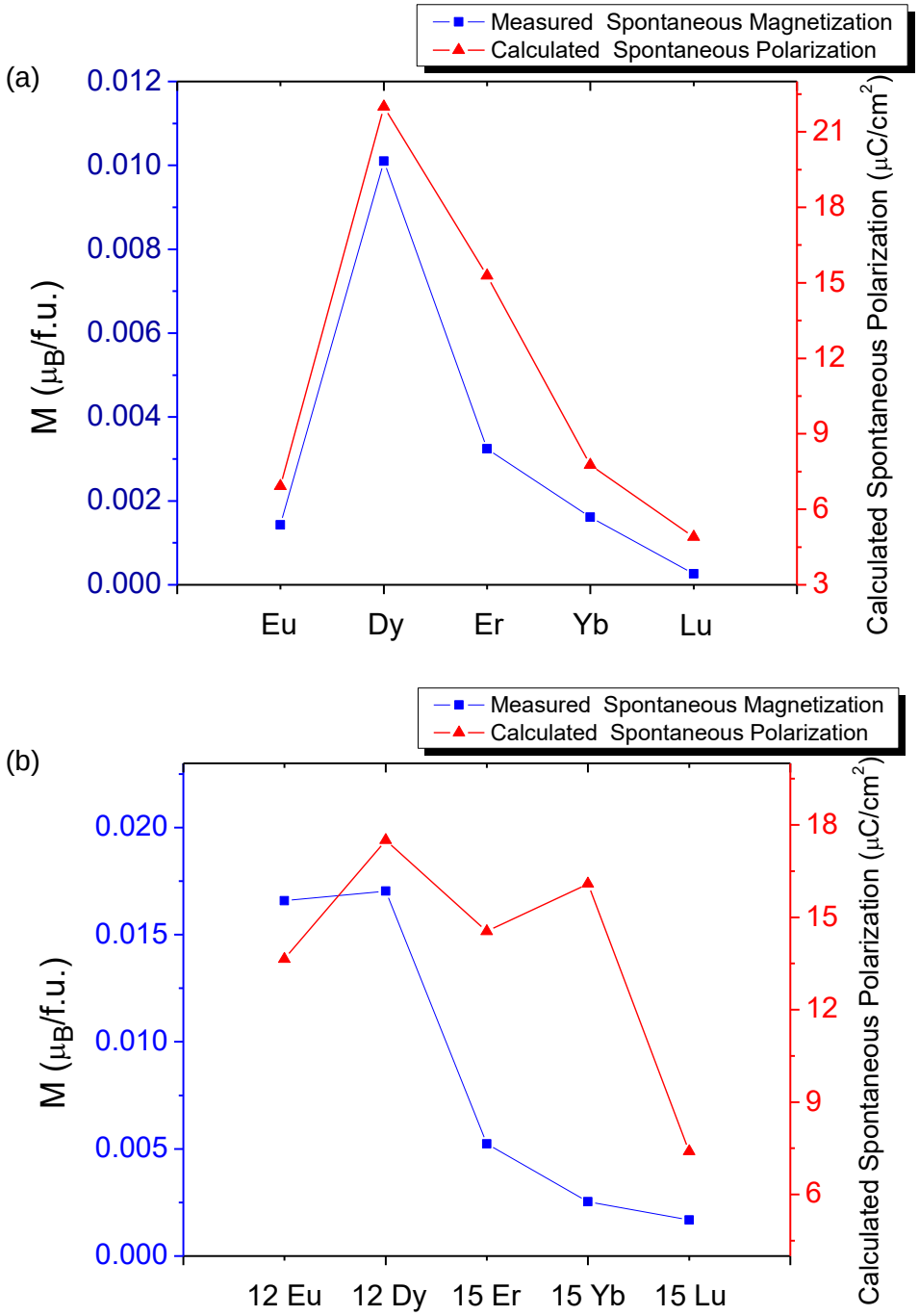

Figure 8.4 **(a) Comparison of the calculated spontaneous polarization and measured spontaneous magnetization for the BREF-0.10 (RE = Dy, Lu, Yb, Er, and Eu) ceramics at 300 K. (b) Comparison of the best calculated spontaneous polarization and measured spontaneous magnetization properties for each BREF-*x* solid solutions (BEuF-0.12, BDF-0.12, BErF-0.15, BYF-0.15, and BLF-0.15).**

8.3 On-going Work: Synchrotron Spectroscopic Studies

X-ray Absorption Spectroscopy (XAS) technique has been widely used to determine the local geometric and/or electronic structure of materials [121]. The Fe *K*-edge synchrotron X-ray absorption near edge structure (XANES) and extended X-ray absorption fine structure (EXAFS) are obtained in transmission mode at the 01C1 beam line of the National Synchrotron Radiation Research Center (NSRRC) in Taiwan (in collaboration with Dr. Chi-Shun Tu) [149,158]. Also, the soft X-ray absorption spectra (XAS) of the Fe $L_{2,3}$-edges and oxygen *K*-edge were studied in total electron yield via current mode at the 20A1 beam line of the NSRRC. The Fe $L_{2,3}$-edge XAS spectra of BDF-0.10 BLF-0.08 and BLF-0.10 are shown in Figure 8.5, in which the Fe $L_{2,3}$-edge XAS spectra correspond to the transition from the Fe 2*p* core level to the unoccupied Fe 3*d* states. The splitting of the $L_{2,3}$ absorptions can be identified as the t_{2g} and e_g orbital bands that are separated by the ligand-field (LF) splitting. The Fe $L_{2,3}$ bands are similar to the $L_{2,3}$-edge band structures of α-Fe_2O_3 [149]. This result suggests the dominant oxidation states of the Fe ion are Fe^{3+} in all three solid solutions.

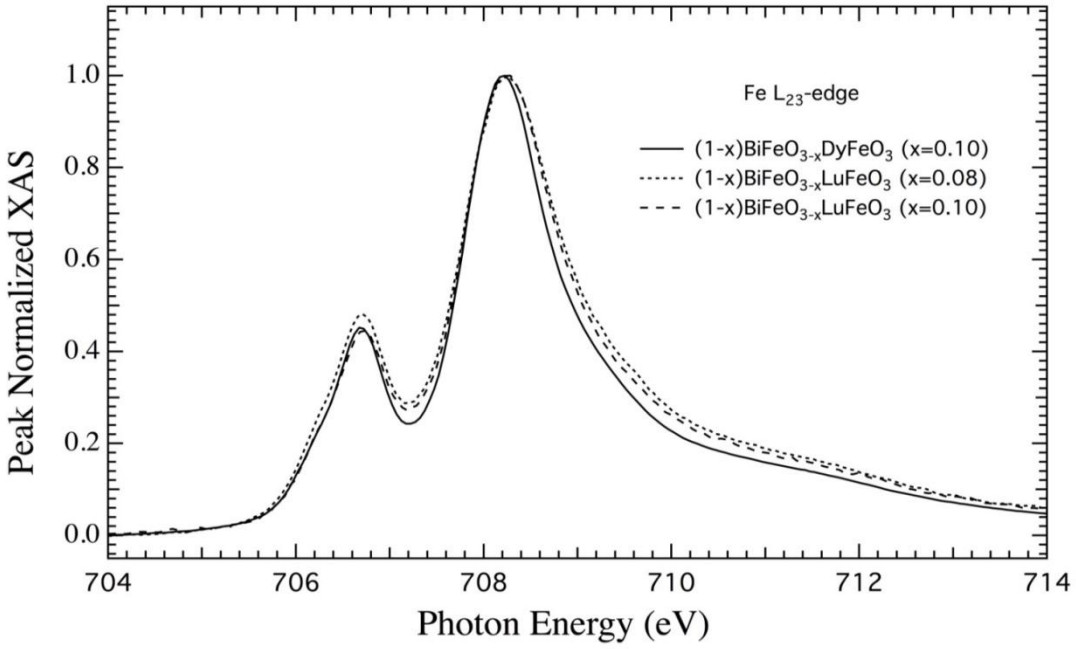

Figure 8.5 The Fe $L_{2,3}$-edge XAS spectra of the BDF-0.10, BLF-0.08, and BLF-0.10 solid solutions.

Figure 8.6 shows the O *L*-edge XAS spectra of the BDF-0.10, BLF-0.08, and BLF-0.10 samples. The pre-edge peaks occurring at ~ 529 *e*V are correlated to the dipole transition from O 1*s* to O 2*p* up-spin states hybridized with the unoccupied Fe^{3+} 3*d* up-spin states. This implies that the Fe^{3+} $3d^5$ orbitals are in the high-spin polarization electron configuration. The A and B peaks can be identified as the t_{2g} and e_g orbital bands separated by the ligand-field (LF) splitting and the LF splitting between the t_{2g} and e_g bands are ~1.6 *e*V for the samples. The broad C band in the region of 535–545 *e*V can be attributed to the mixture of the Bi 6*p*, Dy/Lu 6*s*, Fe 4*s*/4*p*, and O 2*p* configurations. In addition, the broader C band indicates the higher disordered configuration of electronic states. The broadness of XAS lines has been considered as an intrinsic property of oxygen vacancies. The conductivity is higher for the Lu Doped sample. The results of the XANES and XAS spectroscopy provide some insights into the local structure and electronic configuration of the BREF-*x* solid solutions. They are being analyzed in more detail to provide a better understanding of the origins of the structural changes and the mechanism of the enhanced magnetic and electric properties in the BFO-based solid solutions.

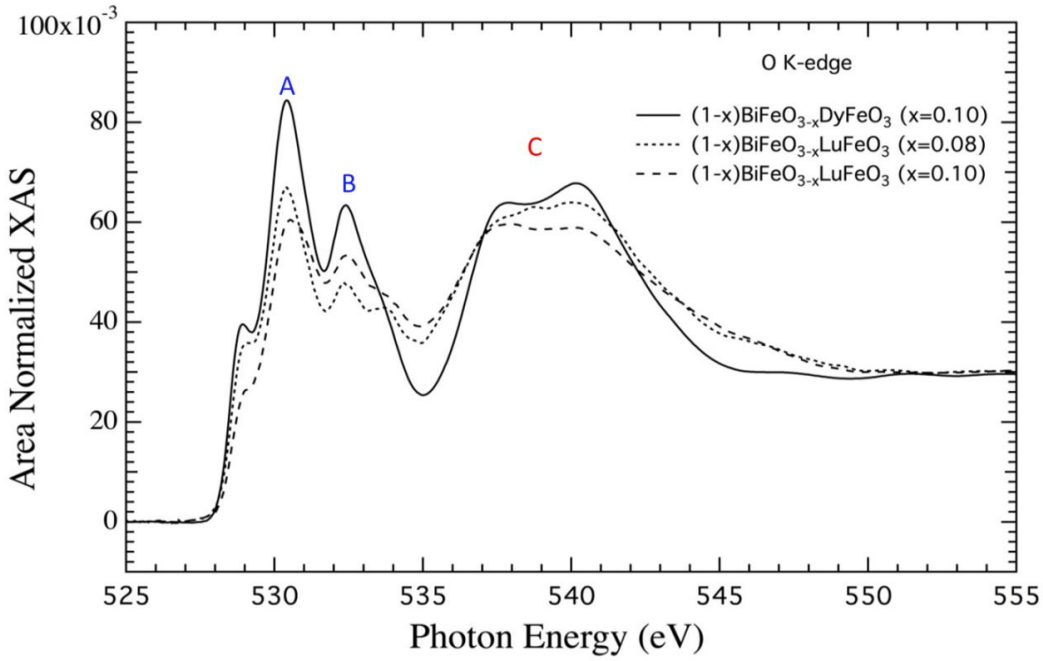

Figure 8.6 The O L-edge XAS spectra of the BDF-0.10, BLF-0.08 and BLF-0.10 solid solutions.

8.4 Future Directions

The BREF-*x* solid solutions have helped address the drawbacks of BFO which are G-type antiferromagnetism, weak magnetism coupling, and large leakage current density. Although BREF-*x* solid solutions form a promising class of multiferroic materials, further optimization and improvement of the properties of BFO are needed. The magnetoelectric effect in (1-x)$BiFeO_3$-x$REFeO_3$ remains to be investigated. This can be realized by combing a SQUID magnetometer with an electrometer (e.g., Keithley 6517) which can measure the charge accumulated on the electrodes of the sample due to the change of polarization induced by a magnetic field, or using a SQUID magnetometer to detect the magnetization induced on the sample by the application of an electric field. The extension of the binary BREF-*x* solid solutions into ternary systems is a possible approach to be adopted in the future work. In addition, the growth of the BREF-*x* single crystals is another area that is worth investigating for a comprehensive understanding of fundamentals and origins of the ferroelectric and ferromagnetic properties. Moreover, magnetic neutron diffraction can be used to solve the magnetic structure, and to illustrate the superexchange coupling and the magnetic structures.

8.5 Concluding Comments

In this thesis, a series of $BiFeO_3$-based perovskite solid solutions have been synthesized via the chemically modification using various rare earth elements: Eu, Dy, Er, Yb, and Lu. Their crystal structures are analyzed, their phase diagrams are constructed, and their properties are systematically characterized. This work constitutes an important step forward in providing a comprehensive understanding of the crystal chemistry and physics of bismuth ferrite-based in ferroelectric and ferromagnetic perovskite systems. The knowledge gained in this thesis is crucial for developing new multiferroic materials with muti-functionality, which is very promising for new technological applications as multi-state memory spintronics devices and magnetoelectric sensors and actuators.

References

[1] T. Screen, Platinum group metal perovskite catalysts-Preparation and Application, Plat. Met. Rev. 51 (2007) 87-92.

[2] Z. Liu, A.R. Paterson, H. Wu, P. Gao, W. Ren, Z.-G. Ye, Synthesis, structure and piezo-/ferroelectric properties of a novel bismuth-containing ternary complex perovskite solid solution, J. Mater. Chem. C.5 (2017) 3916-3923.

[3] M.T. Weller, Inorganic Materials Chemistry, Oxford Science Publications, Oxford, UK, 1994.

[4] A.R. West, Solid State Chemistry and its Applications, Second Ed., John Wiley & Sons Ltd., Chichester, West Sussex, UK, 2014.

[5] B. Jaffe, W.R. Kook, H. Jaffe, Piezoelectric Ceramics, Academic Press, London, 1971.

[6] A.R. West, Basic Solid State Chemistry, Second Ed., John Wiley & Sons Ltd.,Chichester, West Sussex, UK, 1999.

[7] D. Damjanovic, Ferroelectric, dielectric and piezoelectric properties of ferroelectric thin films and ceramic, Reports Prog. Phys. 61 (1998) 1267-1324.

[8] S.W. Choi, T.R. Shrout, S.J. Jang and A.S. Bhalla, Dielectric and pyroelectric properties in the (1-x)$Pb(Mg_{1/3}Nb_{2/3})O_3$-x$PbTiO_3$ system, Ferroelectric 100 (1989) 29-38.

[9] R. Blinc, B. Zeks, Soft Modes in Ferroelectric and Antiferroelectrics, North-Holland Publishing Company, Amsterdam, 1974.

[10] S.C. Abraha, Ferroelasticity, Materials Research Bulletin 6 (1971) 881-890.

[11] J.C. Philips, M.F. Thorpe, Phase Transitions and Self-Organization in Electronic and Molecular Networks, Springer, Boston, MA, 2001.

[12] C. Kittel, Introduction to Solid State Physics, John Wiley & Sons Ltd, Hoboken, NJ, 8th Ed., 2005.

[13] L. E. Smart and E. A. Moore, Solid State Chemistry: An Introduction, CRC Press Taylor & Francis Group, Boca Raton, USA, 3rd Ed., 2005.

[14] S. Elliott, The Physics and Chemistry of Solids, John Wiley & Sons, Chichester, United Kingdom, 1998.

[15] N. A. Hill, Why are there so few magnetic ferroelectrics?, J. Phys. Chem. B 104 (2000) 6694-6709.

[16] R. Shankar, Principles of Quantum Mechanics, Second Ed., Plenum Press, Germany, 2013.

[17] K. Aizu, Determination of the state parameters and formulation of spontaneous strain for ferroelastics, J. Phys. Soc. Jpn. 28 (1970) 706.

[18] P. W. Anderson, Antiferromagnetism. Theory of superexchange interaction, Phys. Rev. 79 (1950) 350.

[19] W.-M. Zhu, L.W. Su, Z.-G. Ye, W. Ren, Enhanced magnetization and polarization in chemically modified multiferroic (1-x)$BiFeO_3$-x$DyFeO_3$ solid solution, Appl. Phys. Lett. 94 (2009) 142908.

[20] R. Rai, S.K. Mishra, N.K. Singh, S. Sharma, A.L. Kholkin, Preparation, structures, and multiferroic properties of single-phase $BiRFeO_3$, Current Applied Physics 11 (2011) 508-512.

[21] T. Kimura, T. Goto, H. Shintani, K. Ishizaka, T. Arima, Y. Tokura, Magnetic control of ferroelectric polarization, Nature 426 (2003) 55.

[22] N. Hur, S. Park, P.A. Sharma, J.S. Ahn, S. Guha, S.-W. Cheong, Electric polarization reversal and memory in a multiferroic material induced by magnetic fields, Nature 429 (2004) 392.

[23] W.-M.Zhu, L.W. Su, Z.-G. Ye, W. Ren, Effect of chemical modification on the structure and dielectric and magnetic properties of multiferroic (1-x)$BiFeO_3$-x$DyFeO_3$ solid solution, Eur. Phys. J.B. 71 (2009) 377-381.

[24] J. Zhuang, J. Zhao, L.W. Su, H. Wu, A. A. Bokov, W. Ren, Z.-G. Ye, Structure and local polar domains of Dy-modified $BiFeO_3$-$PbTiO_3$ multiferroic solid solutions, J. Mater. Chem. C 3 (2015) 12450.

[25] Z. Ren, N. Zhang, L.W. Su, Z.-G. Ye, Softening of antiferroelectricity in $PbZrO_3$-$Pb(Mn_{1/2}W_{1/2})O_3$ complex perovskite solid solution, J. Appl. Phys. 116 (2014) 024103.

[26] D.V. Efremov, J. van den Brink, D. I. Khomskii, Bond-versus site-centered ordering and possible ferroelectricity in manganite, Nat. Mater. 3 (2004) 853.

[27] S.W. Cheong, M.V. Mostovoy, Multiferroics: a magnet twist for ferroelectricity, Nat. Mater. 6 (2007) 13.

[28] F. Bertaut, F. Forrat, and P.-H. Fang, A new class of ferroelectrics: rare earth and yttrium manganites, Compt. Rend. 256 (1963) 1958-1961.

[29] V. A. Bokov, S. A. Kizhaev, and I. E. MyI'nikova, A.G. Tutov, Antiferroelectric and magnetic properties of $PbCo_{1/2}W_{1/2}O_3$, Fizika Tverdogo Tela 6 (1964) 3038-3044.

[30] I. G. Ismailzade and S. A. Kizhaev, Determination of the Curie point of the ferroelectric $YMNO_3$ and $YBMNO_3$, Sov. Phys. Solid State 7 (1965) 236.

[31] J. Chappert, Moessbauer effect study on the partial replacement of manganese by iron in rare earth manganites, Phys. Lett. 18 (1965) 229-230.

[32] M. Eibschütz and H. J. Guggenheim, Antiferromagnetic-piezoelectric crystals: $BaMF_4$ (M = manganese, iron, cobalt, and nickel), Solid State Commun. 6 (1968) 737-739.

[33] L. Holmes, M. Eibschüetz, and H. J. Guggenheim, Spin-flop transition in $BaMnF_4$ [barium manganese fluoride], Solid State Commun. 7 (1969) 973-976.

[34] D.C. Arnold, Composition-driven structural phase transitions in rare-earth-doped $BiFeO_3$ ceramics: a review, IEEE Transaction on Ultrasonics, Ferroelectric, and Frequency Control 62 (2015) 62-82.

[35] J. Wang, J.B. Neaton, H. Zheng, V. Nagarajan, S.B. Ogale, B. Liu, D. Viehland, V. Vaithyanathan, D.G. Schlom, U.V. Waghmare, N.A. Spaldin, K.M. Rabe, M. Wuttig, R. Ramesh, Epitaxial $BiFeO_3$ multiferroic thin film heterostructures, Science 299 (2003) 1719-1722.

[36] P. Ravindran, R. Vidya, A. Kjeshus, H. Fjellvag, O. Eriksson, Theoretical investigation of magnetoelectric behavior in $BiFeO_3$, Phys. Rev. B 74 (2006) 224412.

[37] K.Y. Yun, M. Noda, M. Okuyama, H. Seki, H. Tabata and K. Saito, Structural and multiferroic properties of $BiFeO_3$ thin films at room temperature, J. Appl. Phys. 96 (2004) 3399.

[38] Yu. F. Popov, A. M. Kadomtseva, G. P. Vorobev, A. K. Zvezdin, Discovery of the linear magnetoelectric effect in magnetic ferroelectric $BiFeO_3$ in a strong magnetic field, Ferroelectrics, 162 (1994) 135-140.

[39] J. R. Teague, R. Gerson, W. J. James, Dielectric hysteresis in single crystal $BiFeO_3$, Solid State Commun. 8 (1970) 1073-1074.

[40] V. A. Murashav, D. N. Rakov, V. M. Ionov, I. S. Dubenko, Y. U. Titov, Magnetoelectric (Bi, Ln)FeO_3 compounds: Crystal growth, structure and properties, Ferroelectrics 162 (1994) 11.

[41] W. Eerenstein, N.D. Mathur, J.F. Scott, Multiferroic and magnetoelectric materials, Nature 422 (2006) 759-765.

[42] N. Cai, C.-W. Nan, J. Zhai, Y. Lin, Large high-frequency magnetoelectric response in laminated composites of piezoelectric ceramics, rare-earth iron alloys and polymer, Appl. Phys. Lett. 84 (2004) 3516.

[43] G. Srinivasan, E.T. Rasmussen, B.J. Levin, R. Hayes, Magnetoelectric effects in bilayers and multilayers of magnetostrictive and piezoelectric perovskite oxides, Phys. Rev. B 65 (2002) 134402.

[44] M.K. Lee, T.K. Nath, C.B. Eom, Strain modification of epitaxial perovskite oxide thin films using structural transitions of ferroelectric $BaTiO_3$ substrate, Appl. Phys. Lett. 77 (2000) 3547.

[45] J. Van Suchtelen, Product properties: a new application of composite materials, Philips Res. Rep. 27 (1972) 28-37.

[46] J. V. D. Boomgaard, D. R. Terrelll, R. A. J. Born, H. F. J. I. Giller, An in situ grown eutectic magnetoelectric composite material, J. Mater. Sci. 9 (1974) 1705-1709.

[47] A. Hanumaiah, T. Bhimasankaram, S.V. Suryanaryana, and G.S. Kumar, Dielectric behavior and magnetoelectric effect in cobalt ferrite-barium titanate composites, Bull. Mater. Sci. 17 (1994) 405.

[48] J.V.D. Boomgaard, A.M.J.G. Van Run, J. Van Suchtelen, Piezoelectric-piezomagnetic composites with magnetoelectric effect, Ferroelectrics 14 (1976) 727-728.

[49] W. E. Kramer, R. H. Hopkins, M. R. Danel, Growth of oxide in situ composites: the systems lithium ferrite-lithium niobate, lithium ferrite-lithium tantalite, and nickel ferrite-barium titanate, J. Mater. Sci. Lett. 12 (1977) 409-414.

[50] G. Harshe, J. P. Dougherty, and R. E. Newnham, Theoretical modelling of multilayer magnetoelectric composites, Int. J. Appl. Electromagn. Mater. 4 (1993) 145.

[51] M. Avellaneda, G. Harshe, Magnetoelectric effect in piezoelectric/magnetostrictive multilayer (2-2) composites, J. Intell. Mater. Syst. Struct. 5 (1994) 501.

[52] S. Dong, J.-F. Li, and D. Vieland, Ultrahigh magnetic field sensitivity in laminates of TERFENOL-D and $Pb(Mg_{1/3}Nb_{2/3})O_3 – PbTiO_3$ crystals, Appl. Phys. Lett. 83 (2003) 2265-2267.

[53] L.D. Landau, E. Lifshitz, Electrodynamics of Continuous Media, Perfamon, Oxford, 1960.

[54] C.W. Nan, M.I. Bichurin, S.X. Dong, D. Viehland, G. Srinivasan, Multiferroic magnetoelectric composites: Historical perspective, status, and future directions, J. Appl. Phys. 103 (2008) 031101.

[55] J.-M. Kiat, Y. Uesu, B. Dkhil, M. Matsuda, C. Maliberta, G. Calvarin, Effect of composition and poling field on the properties and ferroelectric phase-stability of $Pb(Mg_{1/3}Nb_{2/3})O_3 – PbTiO_3$ crystals, Phys. Rev. B 65 (2002) 064106.

[56] B. Ruette, S. Zvyagin, A.P. Pyatakov, A. Bush, J.F. Li, V.I. Belotelov, A.K. Zvezdin, D. Viehland, Magnetic-field-induced phase transition in $BiFeO_3$ observed by high-field electron spin resonance: Cycloidal to homogeneous spin order, Phys. Rev. B 69 (2004) 064114.

[57] T. Mizokawa, D.I. Khomskii, G.A. Sawatzky, Interplay between orbital ordering and lattice distortions in $LaMnO_3$, YVO_3, and $YTiO_3$, Phys. Rev. B 60 (1999) 7309-7313.

[58] J. Zhuang, L.-W. Su, H. Wu, A. A. Bokov, M. Liu, W. Ren, Z.-G. Ye, Coexisting ferroelectric and magnetic morphotropic phase boundaries in Dy-modified $BiFeO_3$-$PbTiO_3$ multiferroics, Applied Physics Letters 107 (2015) 182906.

[59] L.-Y. Chang, C.-S. Tu, P.-Y. Chen, C.-S. Chen, V.H. Schmidt, H.-H. Wei, D.-J. Huang, T.-S. Chan, Raman vibrations and photovoltaic conversion in rare earth doped $(Bi_{0.93}RE_{0.07})FeO_3$ (RE = Dy, Gd, Eu, Sm) ceramics, Ceramics International 42 (2016) 834-842.

[60] W.P. Mason, Piezoelectricity, its history and applications, J. Acoust. Soc. Am. 70 (1981) 1561-1566.

[61] G. Gautschi, Piezoelectric Sensorics: Force, Strain, Pressure, Acceleration and Acoustic Emission Sensor, Materials and Amplifier, Springer, German, 2002.

[62] J.F. Nye, Physical Properties of Crystals, Second Ed., Clarendon Press, London, 1985.

[63] Pizeo Systems, INC, Introduction to piezoelectricity, Piezoceramic Application Data Catalog 8 (2011) 59-61.

[64] A.L. Kholkin, N.A. Pertsev, A.V. Goltsev, Piezoelectric and Acoustic Materials for Transducer Applications, Springer, U.S., 2008.

[65] M.E. Lines, A.M. Glass, Principle and Applications of Ferroelectrics and Related Materials, Clarendon Press, Oxford, 1977.

[66] J.-H. Lee, M.-A. Oak, H.J. Choi, J.Y. Son, H.M. Jang, Rhombohedral-orthorhombic morphotropic phase boundary in $BiFeO_3$-based multiferroics: first-principles prediction, J. Mater. Chem. 22 (2012) 1667.

[67] R. Guo, L. E. Cross, S.-E. Park, B. Noheda, D. E. Cox and G. Shirane, Origin of the high piezoelectric response in $PbZr_{1-x}Ti_xO_3$, Phys. Rev. Lett. 84 (2000) 5423-5426.

[68] B. Noheda, D.E. Cox, G. Shirane, J.A. Gonzalo, L.E. Cross, S.E. Park, A monoclinic ferroelectric phase in the $Pb(Zr_{1-x}Ti_x)O_3$ solid solution, Appl. Phys. Lett. 74 (1999) 2059.

[69] A.A. Bokov, Z.-G. Ye, Universal relaxor polarization in $Pb(Mg_{1/3}Nb_{2/3})O_3$ and related materials, Phys. Rev. B. 66 (2002) 064103.

[70] A.A. Bokov, Z.-G. Ye, Field-induced shift of morphotropic phase boundary and effect of overpoling in (1-x)$Pb(Mg_{1/3}Nb_{2/3})O_3$-x$PbTiO_3$ piezocrystals, Appl. Phys. Lett. 92 (2008) 82901.

[71] C. Michel, J.-M. Moreau, G.D. Achenbach, R. Gerson, W.J. James, The atomic structure of $BiFeO_3$, Solid State Communications 7 (1969) 701-704.

[72] F. Kubel, H. Schmid, Structure of a ferroelectric and ferroelastic monodomain crystal of the perovskite $BiFeO_3$, Acta Cryst. B 46 (1990) 698.

[73] G. Catalan, F. Scott, Physics and applications of bismuth ferrite, Adv. Mater. 21 (2009) 2463-2485.

[74] J. D. Bucci, B.K. Robertson, W.J. James, The precision determination of the lattice parameters and the coefficients of thermal expansion of $BiFeO_3$, J. Appl. Cryst. 5 (1972) 187-191.

[75] J.R. Chen, W.L. Wang, J.-B. Li, G.H. Rao, X-ray diffraction analysis and specific heat capacity of $(Bi_{1-x}La_x)FeO_3$ perovskites, J. Alloys Compd. 459 (2008) 0925-8388.

[76] R. D. Shannon, Revised effective ionic radii and systematic studies of interatomic distances in halides and chalcogenides, Acta. Cryst. A 32 (1976) 751.

[77] V.V. Shvartsman, W. Kleemann, R. Haumont, J. Kreisel, Large bulk polarization and regular domain structure in ceramic $BiFeO_3$, Appl. Phys. Lett. 90 (2007) 172115.

[78] H. Schmid, Multi-ferroic magnetoelectrics, Ferroelectrics 162 (1994) 317-338.

[79] J. Li, J. Wang, M. Wuttig, R. Ramesh, N. Wang, B. Ruette, A.P. Pyatakov, A.K. Zvezdin, D. Viehland, Dramatically enhanced polarization in (001), (101), and (111) $BiFeO_3$thin films due to epitaxial-induced transitions, Appl. Phys. Lett. 84 (2004) 5261.

[80] Y. H. Chu, T. Zhao, M.P. Cruz, Q. Zhan, P.L. Yang, L.W. Martin, M. Huijben, C.H. Yang, F. Zavaliche, H. Zheng, R. Ramesh, Ferroelectric size effects in multiferroic $BiFeO_3$ thin films, Appl. Phys. Lett. 90 (2007) 252906.

[81] H.W. Jang, S.H. Beak, D. Ortiz, C.M. Folkman, R.R. Das, Y.H. Chu, P. Shafer, J.X. Zhang, S. Choudhury, V. Vaithyanathan, Y.B. Chen, D.A. Felker, M.D. Biegalski, M.S. Rzchowski, X.Q. Pan, D.G. Schlom, L.Q. Chen, R. Ramesh, C.B. Eom, Strain-induced polarization rotation in epitaxial (001) $BiFeO_3$ thin films, Phys. Rev. Lett. 101 (2008) 107602.

[82] S.R. Das, R.N.P. Choudhary, P. Bhattacharya, R.S. Katiyar, P. Dutta, A. Manivannan, M. S. Seehra, Structural and multiferroic properties of La-modified $BiFeO_3$ ceramics, J. Appl. Phys. 101 (2007) 034104.

[83] T. Moriya, Anisotropic superexchange interaction and weak ferromagnetism, Phys. Rev. 120 (1960) 91.

[84] I. Sosnowska, T. Peterlin-Neumaier, E. Streichele, Spiral magnetic ordering in bismuth ferrite, J. Phys. C. 15 (1982) 4835.

[85] D. Lebeugle, D. Colson, A. Forget, M. Viret, A.M. Bataille, A. Gukasov, Electric-field-induced spin flop in $BiFeO_3$ single crystal at room temperature, Phys. Rev. Lett. 100 (2008) 227602.

[86] I. Sosnowska, W. Schäfer, W. Kockelmann, K.H. Andersen, I.O. Troyanchuk, Crystal structure and spiral magnetic ordering of $BiFeO_3$, Appl. Phys. A: Mater. Sci. Process. 74 (2002) S1040.

[87] F. Bai, J. Wang, M. Wuttig, J.F. Li, N. Wang, A.P. Pyatakov, A.K. Zvezdin, L.E. Cross, D. Viehland, Destruction of spin cycloid in $(111)_c$-orientated $BiFeO_3$ thin films by epitaxial constraint: Enhanced polarization and release of latent magnetization, Appl. Phys. Lett. 86 (2005) 32511.

[88] J. Wang, J.B. Neaton, H. Zheng, V. Nagarajan, S.B. Ogale, B. Liu, D. Viehland, V. Vaithyanathan, D. G. Schlom, U.V. Waghmare, N.A. Spaldin, K.M. Rabe, M. Wuttig, R. Ramesh, Epitaxial $BiFeO_3$ multiferroic thin film heterostructures, Science 299 (2003) 1719.

[89] M. Fiebig, T. Lottermoser, D. Meier, M. Trassin, The evolution of multiferroics, Nature Reviews Materials 1 (2016) 16046.

[90] M. Khodabakhsh, C. Sen, H. Kassaf, M.A. Gulun, I.B. Misirligolu, Strong smearing and disappearance of phase transitions into polar phases due to inhomogeneous lattice strains induced by A-site doping in $Bi_{(1-x)}A_{(x)}FeO_3$ (A: La, Sm, Gd), J. Alloys Compd. 604 (2014) 117-129.

[91] S.R. Das, R.N.P. Choudhary, P. Bhattacharya, R.S. Katiyar, P. Dutta, A. Manivannan, M. S. Seehra, Structural and multiferroic properties of La-modified $BiFeO_3$ ceramics, J. Appl. Phys. 101 (2007) 034104.

[92] T. Higuchi, T. Hattori, W. Sakamoto, N. Itoh, T. Shimura, T. Yogo, P. Yao, Y.-S. Liu, P.-A. Glans, C. Chang, Z. Wu, J. Guo, Effect of Mn substitution for multiferroic $BiFeO_3$ probed by high-resolution soft X-ray spectroscopy, Japanese Journal of Applied Physics 47 (2008) 7570-7573.

[93] C.-S. Tu, C.-S. Chen, P.-Y. Chen, Z.-R. Xu, Y.U. Idzerda, V.H. Schmidt, M.-Q. Lyu, T.-S. Chan, C.-Y. Lin, Raman vibrations, domain structures, and photovoltaic effects in A-site La-modified $BiFeO_3$ multiferroic ceramics, J. Am. Ceram. Soc. 99 (2016) 674-681.

[94] S.-T. Zhang, Substitution-induced phase transition and enhanced multiferroic properties of $Bi_{1-x}La_xFeO_3$ ceramics, Appl. Phys. Lett. 88 (2006) 162901.

[95] Q.H. Jiang, C.W. Nan, Synthesis and properties of multiferroic La-modified $BiFeO_3$ ceramics, J. Am. Ceram. Soc. 89 (2006) 2123-2127.

[96] G.L. Bras, P. Bonville, D. Colson, A. Forget, N. Genand-Riondet, R. Tourbot, Effect of La doping in the multiferroic compound $BiFeO_3$, Phys. B. 406 (2011) 1492-1495.

[97] Y.H. Lin, Q. Jiang, Y. Wang, C.W. Nan, L. Chen, J. Yu, Enhancement of ferromagnetic properties in $BiFeO_3$ polycrystalline ceramic by La doping, Appl. Phys. Lett. 90 (2007) 172507.

[98] G.L. Yuan, S.W. Or, J.M. Liu, Z.G. Liu, Structural transformation and ferroelectromagnetic behavior in single-phase $Bi_{1-x}Nd_xFeO_3$ multiferroic ceramics, Appl. Phys. Lett. 89 (2006) 052905.

[99] Y.P. Wang, G.L. Yuan, X.Y. Chen, J.-M. Liu, Z.G. Liu, Electrical and magnetic properties of single-phased and highly resistive ferroelectromagnet $BiFeO_3$ ceramic, J. Phys. D: Appl. Phys. 39 (2006) 2019.

[100] D. Lebeugle, D. Colson, A. Forge, M. Viret, Very large spontaneous electric polarization in $BiFeO_3$ single crystals at room temperature and its evolution under cycling fields, Appl. Phys. Lett. 91 (2007) 022907.

[101] M.M. Kumar, V.R. Palkar, K. Srinivas, S.V. Suryanarayana, Ferroelectricity in a pure $BiFeO_3$ ceramic, Appl. Phys. Lett. 76 (2000) 2764-2766.

[102] G.L. Yuan, S.W. OR, J.M. Liu, Z.G. Liu, Structural transformation and ferroelectromagnetic behavior in single-phase $Bi_{1-x}Nd_xFeO_3$ multiferroic ceramics, 89 (2006) 052905-1-052905-3.

[103] J. Zhuang, L.-W. Su, H. Wu, A. A. Bokov, M. Liu, W. Ren, Z.-G. Ye, Coexisting ferroelectric and magnetic morphotropic phase boundaries in Dy-modified $BiFeO_3$-$PbTiO_3$ multiferroics, Appl. Phys. Lett. 107 (2015) 182906.

[104] R. Rai, S.K. Mishra, N.K. Singh, S. Sharma, A.L. Kholkin, Preparation, structures, and multiferroic properties of single-phase $BiRFeO_3$, R=La and Er ceramics, Current Applied Physics 11 (2011) 508-512.

[105] S. Chauhan, M. Kumar, S. Chhoker, S. Katyal, M. Jewariya, B. Suma, G. Kunte, Structural modification and enhanced magnetic properties with two phonon modes in Ca-Co codoped $BiFeO_3$ nanoparticles, Ceram. Int. 41 (2015) 14306-14314.

[106] B. Ramachandran, A. Dixit, R. Naik, G. Lawes, M.S. Ramachandra Rao, Dielectric relaxation and magneto-dielectric effect in polycrystalline $Bi_{0.9}Ca_{0.1}FeO_{2.95}$, Appl. Phys. Lett. 100 (2012) 252902.

[107] S. Chauhan, M. Arora, P.C. Sati, S. Chhoker, S.C. Katyal, M. Kumar, Structural, vibrational, optical, magnetic and dielectric properties of $Bi_{1-x}Ba_xFeO_3$ nano-particles, Ceram. Int. 39 (2013) 6399-6405.

[108] A.S. Naeimi, E. Dehghan, D. Sanavi Khoshnoud, A. Gholizadeh, Enhancement of ferromagnetism in Ba and Er co-doped $BiFeO_3$ nanoparticles, J. Magn. Magn. Mater. 393 (2015) 502-507.

[109] G.F. Cheng, Y.H. Huang, J.J. Ge, B. Lv, X.S. Wu, Effects of local structural distortion on magnetization in $BiFeO_3$ with Pr, Ba co-doping, J. Alloy. Compd. 635 (2015) 272-277.

[110] C. Quan, Y. Ma, Y. Han, X. Tang, M. Lu, W. Mao, J. Zhang, J. Yang, X. Li, W. Huang, Effect of Nd substitution for Ca on crystal structure, optical and magnetic properties of multiferroic $Bi_{0.9}Ca_{0.1}FeO_3$, J. Alloy. Compd. 635 (2015) 272-277.

[111] H.M. Rietveld, A profile refinement method for nuclear and magnetic structures, J. Appl. Crystallogr. 2 (1969) 65-71.

[112] B. Jiménez, J.M. Vicente, Oxygen defects and low-frequency mechanical relaxation in Pb-Ca and Pb-Sm titanates, Journal of Physics D: Applied Physics 31 (1998) 446-452.

[113] A. A. Bokov, Z.-G. Ye, Dielectric relaxation in relaxor ferroelectrics, J. Adv. Dielect. 2 (2012) 1241010.

[114] I. Coondoo, Ferroelectrics, InTech, New York, 2010.

[115] Novocontrol Technologies, Alpha-A High Resolution Dielectric, Conductivity, Impedance and Gain Phase Modular Measurement System User's Manual, (2010).

[116] Quantum Design, Magnetic Property Measurement System (MPMS® XL) System Brochure, (2010).

[117] J. Clarke, A.I. Braginski, The SQUID Handbook, Vol. I Fundamentals and Technology of SQUIDs and SQUIDs Systems, Wiley-VCH, Germany, 2006.

[118] W.-M. Zhu (2007). Synthesis, structure, and properties of perovskite materials for multiferroism and piezoelectricity (Doctoral dissertation). http://summit.sfu.ca/item/8157 (accessed Oct 28, 2017).

[119] M.E. Lines, A.M. Glass, Principles and Applications of Ferroelectrics and Related Materials, Clarendon Press, Oxford, 1977.

[120] E.A. Pecherskaya, Radio measurements: The use of the Sawyer-Tower method and its modifications to measure the electrical parameters of ferroelectric materials, Measurement Techniques 50 (2007) 1101.

[121] D.C. Koningsberger, R. Prins, X-ray Absorption: Principles, Applications, Techniques of EXAFS, SEXAFS and SANES, Wiley, New York, 1988.

[122] G. Bunker, Introduction to XAFS, Cambridge University Press, Cambridge, 2010.

[123] C.S. Schnohr, M.C. Ridgway, Introduction to X-Ray Absorption of Semiconductors, Springer, Berlin, Heidelberg, 2015.

[124] J.E. Penner-Hahn, X-ray Absorption Spectroscopy, John Wiley & Sons, New York, 2005.

[125] H.G.J. Moseley, The reflexation of the X-rays, Phil. Mag. 26 (1913) 210-232.

[126] K. Clark-Baldwin, D.L. Tierney, N. Govindaswamy, E.S. Gruff, C. Kim, J. Berg, S.A. Koch, J.E. Penner-Hahn, The limitations of X-ray absorption spectroscopy for determining the structure of zinc sites in proteins, J. Am. Chem. Soc. 120 (1998) 8401-8409.

[127] J.E. Hahn, R.A. Scott, K.O. Hodgson, D. Doniach, S.R. Desjardins, E.I. Solomon, Observation of an electric quadrupole transition in the X-ray absorption spectrum of a Cu(II) complex, Chem. Phys. Lett. 88 (1982) 595-598.

[128] A.L. Roe, D.J. Schneider, R.J. Maver, J.W. Pyrz, J. Widom, L. Que, X-ray absorption spectroscopy of iron-tyrosinate proteins, J. Am. Chem. Soc. 106 (1984) 1676-1681.

[129] S.E. Shadle, J.E. Penner-Hahn, H.J. Schugar, B. Hedman, K.O. Hodgson, E.I. Solomon, X-ray absorption spectroscopy studies of the blue copper site: metal and ligand K-edge studies to probe the origin of the EPR hyperfine splitting in plastocyanin, J. Am. Chem. Soc. 115 (1993) 767-776.

[130] G.N. George, W.E.J. Cleland, J.H. Enemark, B.E. Smith, C.A. Kipke, S.A. Roberts, S.P. Cramer, L-Edge spectroscopy of molybdenum compounds and enzymes, J. Am. Chem. Soc. 112 (1990) 2541-2548.

[131] G.J. Colpas, M.J. Maroney, C. Bagyinka, M. Kumar, W.S. Willis, S.L. Suib, N. Baidya, P.K. Mascharak, X-ray spectroscopic studies of nickel complexes, with application to the structure of nickel sites in hydrogenases, Inorg. Chem. 30 (1991) 920-928.

[132] J.B. Neaton, C. Ederer, U.V. Waghmare, N.A. Spaldin, K.M. Rabe, First-principles study of spontaneous polarization in multiferroic $BiFeO_3$, Phys. Rev. B 71 (2005) 014113.

[133] National Synchrotron Radiation Research Center Beamline 01C1. http://www.nsrrc.org.tw/english/index.aspx (accessed Oct 28, 2017).

[134] Y.B. Li, T. Sritharan, S. Zhang, X.D. He, Y. Liu, T.P. Chen, Multiferroic properties of sputtered $BiFeO_3$ thin films, Appl. Phys. Lett. 92 (2008) 132908.

[135] J. Xu, G. Wang, H. Wang, D. Ding, Y. He, Synthesis and weak ferromagnetism of Dy-doped $BiFeO_3$ powders, Mater. Lett. 63 (2009) 855.

[136] P. Uniyal, K. Yadav, Pr doped bismuth ferrite ceramics with enhanced multiferroic properties, J. Phys.: Condens. Matter 21 (2009) 012205.

[137] R. Mishra, D. Pradhan, R. Choudhary, A. Banerjee, Effect of yttrium on improvement of dielectric properties and magnetic switching behavior in $BiFeO_3$, J. Magn. Magn. Mater. 270 (2008) 2602.

[138] M. Al-Haj, X-ray diffraction and magnetization studies of BiFeO3 multiferroic compounds substituted by Sm^{3+}, Gd^{3+}, Ca^{2+}, Cryst. Res. Technol. 45 (2010) 89-93.

[139] W.M. Zhu, Z.-G. Ye, Effects of chemical modification on the electrical properties of $0.67BiFeO_3$-$0.33PbTiO_3$ ferroelectric ceramics, Ceram. Int. 30 (2004) 1435-1422.

[140] J.B. Good Enough, Localized to itinerant electronic transition in perovskite oxides, Springer, New York, 2001.

[141] W. Zhu, L. Pi, S. Tan, Y. Zhang, Anisotropy and extremely high coercivity in weak ferromagnetic $LuFeO_3$, Appl. Phys. Lett. 100 (2012) 052407.

[142] I. Coondoo, N. Panwar, I. Bdikin, V.S. Katiyar, A.L. Kholkin, Structural, morphological and piezoresponse studies of Pr and Sc co-substituted $BiFeO_3$ ceramics, J. Phys. D: Appl. Phys. 45 (2012) 055302.

[143] Y.R. Luo, Comprehensive Handbook of Chemical Bond Energies, CRC press, Boca Raton, FL, 2007.

[144] Y.T. Li, H.G. Zhang, X.G. Dong, X.P. Ge, X.H. Yan, Q. Li, The study of electronic structures for $Bi_{0.95}R_{0.05}$ FeO_3 (R = Ce, Eu, Er) multiferroic material, J. Electron Spectrosc. Relat. Phenom. 196 (2014) 121.

[145] S. Cao, X. Zhang, T.R. Paudel, K. Sinha, X. Wang, X. Jiang, W. Wang, S. Brutsche, J. Wang, P.J. Ryan, J.-W. Kim, X. Cheng, E.Y. Tsymbal, P.A. Dowben, X. Xu, On the structural origin of the single-ion magnetic anisotropy in $LuFeO_3$, J. Phys.: Condens. Matter 28 (2016) 156001.

[146] K.B. Aring, A.J. Sievers, Role of the Ytterbium spins in the spin reorientation in $YbFeO_3$, J. Appl. Phys. 41 (1970) 1197.

[147] W.H. Kim, J.Y. Son, The effects of La substitution on ferroelectric domain structure and multiferroic properties of epitaxially grown $BiFeO_3$ thin films, Appl. Phys. Lett. 103 (2013) 132907.

[148] Y.-T. Li, H.-G. Zhang, X.-G. Dong, X.-P. Ge, X.-H. Yan, Q. Li, The study of electronic structures for $Bi_{0.95}R_{0.05}FeO_3$ (R = Ce, Eu, Er) multiferroic material, Journal of Electron Spectroscopy and Related Phenomena 196 (2014) 121-124.

[149] J. Wu, Z. Liao, T. Sun, L.-W. Su, J. Bi, G. Fan, D. Gao, Z. Xie, Z.-G. Ye, Tunable magnetic pole inversion in multiferroic $BiFeO_3$-$DyFeO_3$ solid solution, J. Mater. Chem. C 5 (2017) 4063.

[150] H. Shen, Z. Cheng, F. Hong, J. Xu, S. Yuan, Magnetic field induced discontinuous spin reorientation in $ErFeO_3$ single crystal, Appl. Phys. Lett. 103 (2013) 192404.

[151] S.-J. Kim, G. Demazeau, I. Presniakov, J.-H. Choy, Structural distortion and chemical bonding in $TiFeO_3$: comparison with $AFeO_3$ (A = Rare Earth), J. Solid State Chem. 161 (2001) 197.

[152] B. Berini, A. Fouchet, E. Popova, J. Scola, Y. Dumount, N. Franco, R.M. C. Da Silva, N. Keller, High temperature phase transitions and critical exponents of samarium orthoferrite determined by in situ optical ellipsometry, J. Appl. Phys. 111 (2012) 053923.

[153] S.W. Hyun, K.R. Choi, C.S. Kim, The magnetic properties for Europium-doped BiFeO3, J. Supercond. Nov. Magn. 24 (2011) 635-639.

[154] X. Zhang, Y. Sui, X. Wang, Y. Wang, Z. Wang, Effect of Eu subsitution on the crystal structure and multiferroic properties of $BiFeO_3$, Journal of alloys and compounds 507 (2010) 157-161.

[155] T. Munoz, J.P. Rivera, A. Monnier, H. Schmid, Measurement of the quadratic magnetoelectric effect on single crystalline $BiFeO_3$, Jpn. J. Appl. Phys. Part 1 24 (1985) 2051.

[156] T. Moriya, Anisotropic superexchange interaction and weak ferromagnetism, Phys. Rev. 120 (1960) 91.

[157] P. Uniyal, K.L. Yadav, Room temperature multiferroic properties of Eu doped BiFeO3, J. Appl. Phys. 105 (2009) 07D941.

[158] C.-S. Tu, C.-S. Chen, P.-Y. Chen, H.-H. Wei, V.H. Schmidt, C.-Y. Lin, J. Anthoniappen, J.-M. Lee, Enhanced photovoltaic effects in A-site samarium doped BiFeO3 ceramics: The roles of domain structure and electronic state, Journal of the European Ceramic Society 36 (2016) 1149-1157.

[159] C. Ederer, N. A. Spaldin, Weak ferromagnetism and magnetoelectric coupling in bismuth ferrite, Phys. Rev. B, 71 (2005) 060401